



# Recrystallization of L-605 cobalt superalloy during hot-working process

Julien Favre

## ► To cite this version:

Julien Favre. Recrystallization of L-605 cobalt superalloy during hot-working process. Other. INSA de Lyon; Tōhoku Daigaku (Sendai, Japon), 2012. English. NNT : 2012ISAL0112 . tel-00876664

**HAL Id: tel-00876664**

**<https://theses.hal.science/tel-00876664>**

Submitted on 25 Oct 2013

**HAL** is a multi-disciplinary open access archive for the deposit and dissemination of scientific research documents, whether they are published or not. The documents may come from teaching and research institutions in France or abroad, or from public or private research centers.

L'archive ouverte pluridisciplinaire **HAL**, est destinée au dépôt et à la diffusion de documents scientifiques de niveau recherche, publiés ou non, émanant des établissements d'enseignement et de recherche français ou étrangers, des laboratoires publics ou privés.



# Recrystallization of L-605 Cobalt Superalloy during Hot-Working Process



Julien Favre

MATEIS Laboratory, INSA de Lyon

Institute for Materials Research, Graduate School of Engineering, Tohoku University

A thesis submitted for the degree of

*Doctor of Philosophy*

July 2012

## Jury

---

### Reviewers

Christopher Hutchinson	Associate Professor, Faculty of Engineering, Monash University
Toyohiko Konno	Professor, Institute for Materials Research, Tohoku University
<hr/>	
Tadashi Furuhashi	Professor, Institute for Materials Research, Tohoku University
Akihiko Chiba	Professor, Institute for Materials Research, Tohoku University
Damien Fabrigère	Associate Professor, MATEIS Laboratory, INSA de Lyon
Eric Maire	Professor, MATEIS Laboratory, INSA de Lyon

---







## Acknowledgements

I would like to thank people at the origin of collaboration between Tohoku University and INSA de Lyon: I am very grateful to Pr. Jean-Yves Cavaillé and to Pr. Tetsuo Shoji for their kind support during all these three years, and for their efforts to promote the creation of this joint PhD program between the two institutes. I thank Pr. Akihiko Chiba and his team for welcoming me in their group to study superalloys, and for financial support. I am grateful to Pr. Yuichiro Koizumi, Hiroaki Matsumoto, Yunping Li and Shingo Kurosu for discussions and help during experiments. I thank all the PhD and Master students of Chiba Laboratory for their support and friendship. I am very grateful to Pr. Kazuhisa Sato for his very kind help for TEM observations and for scientific discussion. I would like to thank Pr. Toyohiko J. Konno and Pr. Tadashi Furuhashi for discussions and for their precious advice. I thank them very much for accepting to join my dissertation committee and for reviewing this report.

I thank very much Eric Maire, my French PhD supervisor, for his kind help and his advice during these three years. I would like to thank very much Damien Fabrègue for his wholehearted support all along these three years of PhD, for his scientific advice, his assistance for experimental parts carried out in France, and his dedicated help during difficult times. I will never forget his involvement during the events of 2011, nor his support and friendship during the moments of doubts or hopelessness. I hope we will continue to work together in the future on exciting topics. I thank very much all the members of MATEIS Laboratory in INSA de Lyon for their kind support. I especially thank Florian Mercier for his great help on hot deformation experiments on the Gleeble machine, and Mohammad Razzak for his kind support and for discussions on physical modelling. I thank also Coline Béal, Anis Hor, Aurélien Buteri, Joël Lachambre, Itziar Serrano, and all the PhD students of MATEIS for their friendship and cheerful support.

I would like to give a special dedication to Christopher Hutchinson: without his help the modeling part of this study would simply not exist. I found in his work and explanations the same fervent fascination to understand the underlying physics that motivates me since ever for research work. I thank him so much for fascinating discussions, and for teaching me the spirit of modeling applied to material sciences. I thank a lot his PhD student Darren Cram for sharing results and providing me the source code of his model, that was the basement of my modeling work. I thank very much Pr. Yves Bréchet for his involvement in the project, for finding the time to advise me and coming to Tohoku University. His pioneer work on the physics of metals constitutes a large part of the theoretical basis of this current study, and I would like to thank him not only for his contribution to this project, but also for all his dedicated work on the metallurgy field. I hope we will continue to work together, I still have so many things to learn from him. I thank very much Frank Montheillet and his colleague David Piot for constructive discussions and suggestions, and I am very excited to pursue my research work together with them.

I thank very much Emi Agatsuma for her kindness and understanding during this period, and for her support in daily life. I thank my family for their comprehension, their patience and tolerance, and I apologize for making some worries. I would like to thank also the French community in Sendai, especially Philippe Brachet for his friendship and for his involvement to help new comers to Sendai. Finally, I thank all the people whom has helped after I arrived to Japan for their support.

This work was supported by the Ministry of Education, Science and Culture of Japan and the Région Rhône-Alpes in France, and was performed within the frame of the Japanese-French joint laboratory ELyT lab.

*Theory is when you know everything, but nothing works.  
Practice is when everything works, but you don't know why.  
Here, we combine practice and theory: nothing works, and nobody knows why!  
Albert Einstein*

*La science remplace du visible compliqué par de l'invisible simple  
Jean Perrin*







# Abstract

Co-20Cr-15W-10Ni alloy (L-605) is a cobalt-based superalloy combining high strength, high ductility, biocompatibility and corrosion resistance. It has been used successfully for heart valves for its chemical inertia, and this alloy is a good candidate for stent elaboration. The control of grain size distribution can lead to significant improvement of mechanical properties: in one hand grain refinement enhance the material strength, and on the other hand large grains provide the ductility necessary to avoid the rupture in use. Therefore, tailoring the grain size distribution is a promising way to adapt the mechanical properties to the targeted applications. The grain size can be properly controlled by dynamic recrystallization during the forging process. Therefore, the comprehension of the recrystallization mechanism and its dependence on forging parameters is a key point of microstructure design approach. Thus this work aims at determining the optimal conditions for the occurrence of dynamic recrystallization, and investigating the link between microstructure evolution and mechanical behavior.

Compression tests are carried out at high-temperature on Thermec-master Z and Gleeble thermomechanical deformation devices, followed by gas or water quench. Mechanical behavior of the material at high temperature is analyzed in detail, and innovative methods are proposed to determine the metallurgical mechanisms at stake during the deformation process. Mechanical properties of the material after hot-working and annealing treatments is investigated. The grain growth kinetics of L-605 alloy is determined, and experimental results are compared with the static recrystallization process. Microstructures after hot deformation are evaluated using SEM-EBSD and TEM. Significant grain refinement occurs by dynamic recrystallization for high temperature and low strain rate ( $T \geq 1100^\circ\text{C}$ ,  $\dot{\epsilon} < 0.1\text{s}^{-1}$ ), and at high strain rate ( $\dot{\epsilon} \geq 10\text{s}^{-1}$ ). Dynamic recrystallization is discontinuous and takes place from the grain boundaries, leading to a necklace structure. The nucleation mechanism is most likely to be bulging of grain boundaries. However, recrystallization occurs also by rotation of annealing twins, thereafter the twin boundaries can bulge as well.







# Contents

<b>Abstract</b>	<b>iii</b>
<b>1 Literature review</b>	<b>1</b>
1.1 Metallic biomaterials for stent applications . . . . .	2
1.1.1 Stent structures and materials selection . . . . .	2
1.1.1.1 Development of metallic structures for vascular endoprosthesis . . .	2
1.1.1.2 Specifications on metallic biomaterials for vascular implants . . . .	6
1.1.1.3 Selection of materials for stent applications . . . . .	10
1.1.2 Manufacture process of stents . . . . .	12
1.1.2.1 Manufacture of pipes for semi-finished products . . . . .	12
1.1.2.2 Finalization of the stent product . . . . .	16
1.2 Cobalt-based superalloys: microstructure and mechanical properties . . . . .	20
1.2.1 Phase diagrams and typical microstructures of cobalt superalloys . . . . .	20
1.2.1.1 Phase diagrams of usual cobalt superalloys . . . . .	20
1.2.1.2 Stacking fault energy of cobalt alloys . . . . .	25
1.2.1.3 Martensitic transformation . . . . .	28
1.2.1.4 Precipitation in cobalt alloys . . . . .	29
1.2.1.5 Effect of grain refinement on mechanical properties . . . . .	29
1.2.2 Properties of L-605 superalloy . . . . .	30
1.2.2.1 Microstructure and mechanical properties . . . . .	31
1.2.2.2 Precipitation behavior . . . . .	32
1.2.2.3 Effect of grain refinement on mechanical properties . . . . .	35
1.3 Physics of high-temperature plasticity . . . . .	37
1.3.1 Mechanical behavior of metals at high temperature . . . . .	37
1.3.2 Dynamic materials model and thermodynamics of plasticity . . . . .	37
1.3.3 Physics of hardening and recovery mechanisms . . . . .	39
1.3.4 A single-parameter based description of work hardening . . . . .	41
1.3.5 Effect of strain rate on the dislocation structure: the Cottrell-Stokes law . . .	42



1.3.6	Plasticity of polycrystals . . . . .	43
1.3.7	Conclusions . . . . .	44
1.4	High-temperature microstructure evolution and recrystallization process . . . . .	46
1.4.1	Grain boundary migration . . . . .	46
1.4.1.1	Boundary migration in a relaxed material . . . . .	46
1.4.1.2	Grain growth during the deformation process . . . . .	47
1.4.1.3	General expression of grain growth . . . . .	49
1.4.1.4	Effect of solute-drag and precipitation on grain boundary mobility . . . . .	49
1.4.2	Modeling of discontinuous dynamic recrystallization . . . . .	51
1.4.2.1	Nucleation mechanisms of recrystallization . . . . .	52
1.4.2.2	Onset and transitory regime . . . . .	54
1.4.2.3	Stationary regime . . . . .	55
1.4.3	Other mechanisms of recrystallization . . . . .	56
<b>2</b>	<b>Materials and experimental procedure</b>	<b>59</b>
2.1	Initial materials: microstructure and properties . . . . .	60
2.1.1	Chemical composition . . . . .	60
2.1.2	Initial microstructure . . . . .	60
2.1.3	Mechanical properties . . . . .	62
2.2	High-temperature thermomechanical treatments and mechanical tests . . . . .	65
2.2.1	High-temperature thermomechanical treatments . . . . .	65
2.2.2	Tensile tests and Vickers hardness measurement at room temperature . . . . .	69
2.3	Microstructure characterization . . . . .	72
2.3.1	Microscopy observations . . . . .	72
2.3.2	X-ray diffraction . . . . .	74
2.3.3	Measurement of Thermoelectric Power . . . . .	74
<b>3</b>	<b>High-temperature mechanical behavior of L-605 alloy</b>	<b>77</b>
3.1	High-temperature compression tests . . . . .	78
3.1.1	Uniaxial hot compression tests: experimental data . . . . .	78
3.1.1.1	Evolution of flow stress with forging conditions . . . . .	78
3.1.1.2	Empirical description of flow stress . . . . .	79
3.1.1.3	Kocks-Mecking model: determination of constitutive equations . . . . .	81
3.1.2	Estimation of dislocation density from flow stress . . . . .	84
3.1.3	Effect of initial grain size . . . . .	85
3.1.4	Interrupted compression tests . . . . .	86
3.1.5	Speed jump experiments . . . . .	89



3.1.6	Vickers hardness after hot deformation . . . . .	91
3.1.7	Forging of large samples under non-isotherm conditions: the industrial reality . . . . .	92
3.1.8	Conclusions . . . . .	94
3.2	Analysis of flow stress and flow softening . . . . .	95
3.2.1	Processing maps . . . . .	95
3.2.2	Softening maps: a new representation of flow stress contributions . . . . .	96
3.2.3	Conclusions . . . . .	97
<b>4</b>	<b>High-temperature microstructure evolution of L-605 alloy</b>	<b>99</b>
4.1	Precipitation behavior of L-605 alloy . . . . .	100
4.1.1	Observation of precipitation by microscopy . . . . .	100
4.1.2	Detection of precipitation by X-ray diffraction . . . . .	100
4.1.3	Chemical composition of carbides . . . . .	103
4.1.4	Study of precipitation kinetics by thermoelectric power measurement . . . . .	103
4.1.5	Conclusion . . . . .	105
4.2	Grain growth after annealing . . . . .	107
4.2.1	Evolution of grain size during annealing treatment . . . . .	107
4.2.2	Modeling of grain growth process . . . . .	109
4.2.3	Evolution of mechanical properties with grain size . . . . .	111
4.2.4	Conclusion . . . . .	113
4.3	Static recrystallization . . . . .	115
4.3.1	Evolution of grain size during fast-annealing treatment after cold-rolling . . . . .	115
4.3.2	Evolution of Vickers hardness during static recrystallization . . . . .	118
4.3.3	Is grain growth model applicable to static recrystallization? . . . . .	119
4.3.4	Conclusion . . . . .	120
4.4	Dynamic recrystallization . . . . .	122
4.4.1	Plasticity gradient in compression tests . . . . .	122
4.4.2	Microstructure evolution by hot deformation . . . . .	125
4.4.3	Microstructural interpretation of processing maps . . . . .	127
4.4.4	Observation of dynamic recrystallization mechanism on partially compressed samples . . . . .	129
4.4.5	Microstructure gradient inside compression samples . . . . .	133
4.4.6	Observation of deformed substructure by transmission electron microscopy . . . . .	141
4.4.7	Conclusions . . . . .	143



<b>5</b>	<b>Modeling of discontinuous dynamic recrystallization</b>	<b>147</b>
5.1	Determination of grain boundary mobility at steady-state . . . . .	148
5.1.1	Determination of the steady-state flow stress and microstructure . . . . .	148
5.1.2	Principle of the determination of boundary mobility . . . . .	150
5.1.3	Grain boundary mobility of L-605 and of some pure metals . . . . .	155
5.2	Determination of nucleation criterion and nucleation frequency . . . . .	159
5.2.1	Nucleation criterion . . . . .	159
5.2.2	Gibbs energy hysteresis during recrystallization . . . . .	163
5.2.3	Frequency of nucleation . . . . .	165
5.3	Class modeling of dynamic recrystallization . . . . .	168
5.3.1	Principle . . . . .	168
5.3.2	Evolution of nucleation frequency . . . . .	169
5.3.3	Compression curves . . . . .	170
5.3.4	Mean grain size and grain size distribution . . . . .	171
5.3.5	Prediction of the conditions for half and full recrystallization . . . . .	174
5.3.6	Microstructure generation from the size distribution . . . . .	174
5.3.7	Conclusion . . . . .	176
<b>6</b>	<b>Conclusions</b>	<b>177</b>
	<b>Conclusions</b>	<b>179</b>
	<b>Appendix 1</b>	<b>183</b>
	<b>Appendix 2</b>	<b>187</b>
	<b>Appendix 3</b>	<b>197</b>
	<b>Bibliography</b>	<b>209</b>



# List of Figures

1.1	Coil graft stent (Patent US6488700B2). a: Metallic helix structure b: Stent with graft material c: placing method outline [1] . . . . .	3
1.2	Palmaz stent described in the patent EP1359865B1 a: Initial shape, a pipe with parallel slots and grooves b: Stent after expansion c: Integration of the stent inside the arterial wall [2] . . . . .	4
1.3	Strecker stent, as detailed in the patent US5662713 a: knitted structure made from metallic wire b: insertion of the stent in a vessel c: stent after expansion [3] . . . .	4
1.4	Gianturco self-expanding stent described in 1985 in the patent EP0177330A2 [4] . .	5
1.5	Wallstent <sup>®</sup> self-expanding prosthesis described in 1991 in the patent US5061275 [5]	5
1.6	Finite elements analysis of a Palmaz stent deployment until 12mm diameter [6] . . .	7
1.7	Cell proliferation and dissolution after 3 and 6 days on pure metals [7] . . . . .	9
1.8	Percentage of mean cell activity of Balb/C 3T3 fibroblasts on dental alloys [8] . . . .	10
1.9	Percentage of allergy caused by metallic elements [9] . . . . .	10
1.10	Ashby maps indicating the ultimate tensile stress, the maximal deformation and the yield stress (0.2%) based on datasheets from Aubert&Duval (Eramet) . . . . .	13
1.11	Roll-forming and continuous welding of strips to produce pipes . . . . .	14
1.12	Extrusion process of hollow products [10] . . . . .	15
1.13	Rotary rolling mill and ironing process [10] . . . . .	15
1.14	Drawing process of pipes with a plug [10] . . . . .	16
1.15	Laser cutting of a tube to produce a stent [11] . . . . .	17
1.16	Film contact imaging method [12] . . . . .	18
1.17	Laser scanning method [13] . . . . .	18
1.18	Composition of usual cobalt alloys based on datasheets from Deloro Stellite Inc., Haynes Intl Inc., Aubert&Duval (Eramet), Carpenter Tech. Corp. and Matthey SA	21
1.19	Binary phase diagram of Co-C system [14] . . . . .	22
1.20	Phase diagrams of 1.20a Co-Cr, 1.20b Co-Ni, 1.20c Co-W and 1.20d Mo-Co systems	24
1.21	Microstructure of MP35N and M64BC by optical microscopy . . . . .	24
1.22	Stacking sequence of close packed planes in FCC stacking fault structures [15] . . . .	25



1.23	Dependence of the SFE of cobalt superalloys and steels with temperature calculated from thermodynamics modeling [16], and SFE of pure cobalt from experimental observations [17] . . . . .	26
1.24	Calculation of the stacking fault width evolution with shear stress . . . . .	27
1.25	Effect of alloying elements on the FCC→HCP transformation temperature as a function of solubility in FCC cobalt . . . . .	28
1.26	stress-strain curves for nanocrystalline cobalt (12nm) and microcrystalline cobalt (4.8μm)	30
1.27	Mechanical properties of Co-29Cr-6Mo after hot deformation process [18] . . . . .	31
1.28	Microstructure of L-605 superalloy after annealing . . . . .	32
1.29	Processing of long products made of L-605 alloy in Carpenter © . . . . .	32
1.30	Mechanical properties of L-605 at room and high temperature . . . . .	33
1.31	Phase diagram of L-605 alloy with variable carbon content (Thermocalc with database Ni7) . . . . .	33
1.32	Time-Temperature-Precipitation diagram of L-605 from ORNL data (2007) [19] . . .	34
1.33	Dependence of mechanical properties of L-605 with grain size, data from Haynes 25 datasheet . . . . .	36
1.34	Schematic representation of the partition of total power P into two contributions J and G for: (a) $m < 1$ and (b) $m=1$ [20] . . . . .	39
1.35	Processing map of ETP copper for strain=0.5[21] . . . . .	39
1.36	Dislocation density and flow stress of pure copper, data from Kocks and Mecking [22, 23] . . . . .	41
1.37	Evolution of hardening rate and flow stress of (0.03 C, 0.3 Mn) steel at 950°C strain rate $1s^{-1}$ [24] . . . . .	41
1.38	Evolution of normalized flow stress with g parameter for different materials [22] . . .	42
1.39	Strain rate jump on pure copper for determining m [25] . . . . .	43
1.40	Dislocation density profile at the grain boundary interface . . . . .	48
1.41	Effect of solute drag on the grain boundary motion and on grain refinement . . . . .	50
1.42	Nucleation of dynamic recrystallization at grain boundaries in pure copper . . . . .	52
1.43	Schematic representation of nucleation mechanism [26, 27, 28] . . . . .	53
1.44	Bulging of a new grain from a pre-existing subgrain: mechanism diagram and subgrain size distribution[29, 30] . . . . .	53
1.45	Formation of necklace microstructure during dynamic recrystallization [31] . . . . .	54
1.46	Onset of recrystallization and evolution of microstructure during the transient regime	55
1.47	Relationship between dynamically recrystallized grain size and flow stress at steady-state [32] . . . . .	56
1.48	Continuous dynamic recrystallization of titanium and aluminum alloys . . . . .	57



2.1	Initial microstructure of Ø15.87mm Carpenter L-605 alloy . . . . .	61
2.2	Initial microstructure of Ø15.87mm Carpenter L-605 alloy observed by EBSD . . . . .	61
2.3	XRD diagram of L-605: Intensity (counts) as a function of $2\theta$ angle . . . . .	62
2.4	Initial grain size distribution of the different materials used for experiments . . . . .	62
2.5	Mechanical properties of L-605 alloy . . . . .	63
2.6	Tensile test samples surface after rupture (grading size=1 mm) . . . . .	64
2.7	Microstructure change of L-605 swaged at $\epsilon = 50\%$ by annealing treatment . . . . .	65
2.8	Thermecmaster-Z thermomechanical device . . . . .	66
2.9	Gleeble thermomechanical device . . . . .	67
2.10	Thermomechanical treatment applied for hot-working experiments . . . . .	68
2.11	Thermomechanical treatment applied for hot-working experiments . . . . .	69
2.12	Microstructure of L-605 Ø35mm Kamaishi after annealing 18h at 1200°C . . . . .	69
2.13	Tensile test sample dimensions and apparatus . . . . .	70
2.14	Vickers hardness test . . . . .	70
2.15	Optical and electron microscopes for microstructure characterization . . . . .	72
2.16	TEP measurement schema based on the Seebeck effect, and TEP measurement device [33] . . . . .	74
3.1	Stress - plastic strain curves of L-605 at high temperature . . . . .	79
3.2	Evolution of steady-state flow stress with deformation conditions . . . . .	80
3.3	Linear decrease of hardening rate with stress following the Voce law at $T=1150^{\circ}\text{C}$ : experimental curve (black) and linear fit (red) . . . . .	81
3.4	Evolution of steady-state extrapolated stress $\sigma_V$ , steady-state flow stress $\sigma_{SS}$ and yield stress $\sigma_y$ with g parameter . . . . .	82
3.5	Evolution of normalized hardening rate $\theta/\mu$ with deformation conditions . . . . .	83
3.6	Comparison of experimental curves (solid) and Voce law fits (dashed) . . . . .	84
3.7	Map of the estimated dislocation density at the steady-state versus temperature and strain rate . . . . .	85
3.8	Stress - plastic strain curves of L-605 at high temperature . . . . .	87
3.9	Relaxation of 10 seconds during compression deformation . . . . .	88
3.10	Determination of extrapolated steady-state stress and normalized hardening rate for Gleeble data . . . . .	89
3.11	Strain rate jumps and induced stress jumps with changing temperature . . . . .	90
3.12	Stress jump calculated by Kocks-Mecking model . . . . .	91
3.13	Vickers hardness of samples after hot compression at $\epsilon = 0.8$ versus temperature and strain rate . . . . .	92



3.14	Compression of 33mm diameter L-605 samples at $T < 1280^{\circ}\text{C}$ : on the left compression at speed $33\text{mm.s}^{-1}$ $\epsilon = 1$ , on the right compression at speed $0.33\text{mm.s}^{-1}$ until rupture	93
3.15	Tensile test stress-strain curves of L-605 initial (Carpenter $\varnothing 15.87\text{mm}$ ) and of L-605 forged at $T < 1280^{\circ}\text{C}$ $33\text{mm.s}^{-1}$	93
3.16	Processing maps of L-605 alloy in the range $1000\text{-}1200^{\circ}\text{C}$ $0.001\text{-}10\text{s}^{-1}$	95
3.17	Softening map of L-605 alloy in the range $1000\text{-}1200^{\circ}\text{C}$ $0.001\text{-}10\text{s}^{-1}$	97
4.1	Microstructure of L-605 after 5h aging treatment at $1000^{\circ}\text{C}$ , by optical microscopy	101
4.2	SEM observation of microstructure after aging at $1000^{\circ}\text{C}$	101
4.3	TTP diagram for carbides in L-605 alloy	102
4.4	XRD diagram of L-605 aged 15h at $1000^{\circ}\text{C}$ : only $\text{M}_6\text{C}$ carbide is formed in FCC matrix	102
4.5	Decomposition of the area analyzed by EPMA or EDX in 2 phases	103
4.6	Evolution of thermoelectric power (TEP) with aging time	104
4.7	Evolution of TEP normalized variation with time	105
4.8	Grain growth of L-605: grain size distribution and average grain size evolution with time	108
4.9	IPF map of microstructure after annealing 3h at $1100^{\circ}\text{C}$ , and grain size distribution	108
4.10	Grain boundary map for increasing annealing time at $1000^{\circ}\text{C}$	109
4.11	Fit of grain size distribution by the Hillert model	110
4.12	Tensile test stress-strain curves of L-605 before annealing (grain size $3.5\text{ }\mu\text{m}$ ), and after annealing 16min and 3 hours at $1100^{\circ}\text{C}$	112
4.13	Evolution of Vickers hardness during grain growth	112
4.14	Sample preparation and procedure for static recrystallization experiment	115
4.15	Temperature evolution measured in two different points during annealing $10\text{s}$ at $1000^{\circ}\text{C/s}$	116
4.16	Static recrystallization of L-605: grain size distribution and average grain size evolution with time	117
4.17	Evolution of Vickers hardness during static recrystallization	118
4.18	Fit of grain size distribution by the Hillert model	120
4.19	Calculation of Von-Mises strain and effective stress by finite elements method during deformation at $1100^{\circ}\text{C}$ $0.1\text{s}^{-1}$	124
4.20	Strain profile along the radial axis of the sample: the core corresponds to the left (higher strain), and the edge to the right of the plot (lower strain)	124
4.21	Maps of recrystallized grain size and fraction evolution with temperature and strain rate	126
4.22	Maps of boundaries fractions after deformation at $\epsilon=0.8$	126
4.23	Comparison of power efficiency map and softening map with the recrystallized fraction	129



4.24	Partial compression at strain $\epsilon = 0.11$ , $\epsilon = 0.36$ and $\epsilon = 0.69$ . . . . .	130
4.25	Calculation of strain gradient by Finite Elements Method, and determination of the area to observe by EBSD . . . . .	130
4.26	IPF maps of microstructure after partial compression at $1000^{\circ}\text{C}$ $1\text{s}^{-1}$ . . . . .	131
4.27	IPF maps of microstructure after partial compression at $1100^{\circ}\text{C}$ $0.001\text{s}^{-1}$ . . . . .	131
4.28	IPF maps of microstructure after partial compression at $1200^{\circ}\text{C}$ $10\text{s}^{-1}$ . . . . .	132
4.29	Formation of lens-shaped nucleus on annealing twins: surface tension equilibrium and boundaries angles . . . . .	133
4.30	Mosaic of 33 pictures taken by optical microscopy at 50x after compression at $1100^{\circ}\text{C}$ $0.01\text{s}^{-1}$ $\epsilon = 0.8$ . Width of the picture = 13.3mm . . . . .	134
4.31	Microstructure after deformation at $1200^{\circ}\text{C}$ $10\text{s}^{-1}$ observed at low magnification (250x) near the sample edge . . . . .	134
4.32	Strain gradient profile along the longitudinal axis calculated by Finite Elements Method	136
4.33	Grain size and KAM parameter as a function of strain along the longitudinal axis of the sample, after gas quench at $-50^{\circ}\text{C.s}^{-1}$ . . . . .	136
4.34	Evolution of grain and twin boundaries fractions with strain gradient for temperature between $1000$ and $1200^{\circ}\text{C}$ and strain rate $0.1\text{s}^{-1}$ . . . . .	137
4.35	Microstructure after deformation at $1200^{\circ}\text{C}$ $10\text{s}^{-1}$ with Thermecmaster-Z device, fol- lowed by $-50^{\circ}\text{C.s}^{-1}$ gas quench . . . . .	138
4.36	Microstructure after deformation at $1200^{\circ}\text{C}$ $10\text{s}^{-1}$ with Gleeble device, followed by $-2000^{\circ}\text{C.s}^{-1}$ water quench . . . . .	139
4.37	Comparison of grain size and KAM gradients after gas quench at $-50^{\circ}\text{C.s}^{-1}$ (Ther- mecmaster) or water quench at $-2000^{\circ}\text{C.s}^{-1}$ (Gleeble) . . . . .	140
4.38	Grain boundaries map in the center of the sample after deformation at $1200^{\circ}\text{C}$ $10\text{s}^{-1}$ : HAG (black lines), LAG (red lines) and twins (blue lines), and corresponding grain size distribution . . . . .	140
4.39	Observation by TEM after deformation at $1000^{\circ}\text{C}$ $1\text{s}^{-1}$ $\epsilon = 0.36$ . . . . .	141
4.40	Observation by TEM after deformation at $1100^{\circ}\text{C}$ $0.001\text{s}^{-1}$ $\epsilon = 0.36$ . . . . .	142
4.41	TEM observation of substructure in Co-Cr-Mo (CCM) and Co-Ni-Cr-Mo (SPRON) alloys . . . . .	143
5.1	Grain boundary mobility of L-605 alloy calculated from experimental data . . . . .	149
5.2	Grain size change with mobility at $1100^{\circ}\text{C}$ $0.1\text{s}^{-1}$ . . . . .	153
5.3	Schematic view of the modeling procedure to determine the mobility by fitting exper- imental grain size . . . . .	153
5.4	Evolution of grain size with time for different temperatures at strain rate $\dot{\epsilon} = 0.1\text{s}^{-1}$ .	154
5.5	Grain boundary mobility of L-605 alloy calculated from experimental data . . . . .	156



5.6	Evolution of mobility in L-605 superalloy, pure cobalt and pure copper as a function of $1000/T$ , and Turnbull estimation . . . . .	156
5.7	Determination of the $\alpha$ factor, and comparison between the Turnbull estimation and the Cahn low branch . . . . .	157
5.8	The different models of nucleation: 5.8a Bailey-Hirsch, 5.8b At a plane grain boundary (conventional), 5.8c At a triple boundary, 5.8d Complex nucleation on a combination of plane and triple boundaries . . . . .	160
5.9	Comparison of criterion sizes and selection of the suitable criterion depending on the grain size and dislocation density . . . . .	162
5.10	Comparison of the different nucleation criteria with the volumic average grain size as a function of dislocation density . . . . .	162
5.11	Gibbs free energy hysteresis loop during the lifetime of a grain at steady-state . . . .	164
5.12	Evolution of Gibbs free energy during the lifetime of a grain . . . . .	164
5.13	Effect of the critical size on the nucleus density . . . . .	165
5.14	Nucleation of a single grain per parent grain during the shrinkage step at steady-state	166
5.15	Normalized nucleation frequency $N.d^{*2}/\Delta t.d^2$ as a function of nucleation incubation frequency $1/\Delta t^*$ . . . . .	167
5.16	Schematic view of the dynamic recrystallization modeling steps . . . . .	168
5.17	Nucleation frequency as a function of strain . . . . .	170
5.18	Experimental compression curves of L-605 alloy . . . . .	171
5.19	Calculated compression curves of L-605 alloy . . . . .	171
5.20	Average grain size and recrystallized fraction maps calculated for $\epsilon = 0.8$ . . . . .	172
5.21	Grain size distribution: experimental distribution from EBSD (red), and calculated distribution (blue) . . . . .	173
5.22	Maps of the strain required to obtain a recrystallized fraction of 50% and 100% . . .	174
1	Phase diagrams of 1a Cr-W, 1b Cr-Mo and 1c Ni-W systems . . . . .	185
2	Ternary phase diagrams of Co-Cr-W-Mo-Ni systems: 2a Co-Cr-Mo at $1200^\circ\text{C}$ , 2b Co-Cr-W at $1350^\circ\text{C}$ , 2c Co-Cr-Ni at $800^\circ\text{C}$ , 2d Co-Ni-W at $1100^\circ\text{C}$ . . . . .	186
3	Raw stress-strain curves of L-605 from Thermecmaster-Z experiments before treatment	188
4	Conversion of load-stroke to stress-strain curve at $1100^\circ\text{C}$ $\dot{\epsilon} = 1\text{s}^{-1}$ , and determination of yield stress $\sigma_y$ . . . . .	188
5	Smooth of the compression curve by adjacent-averaging smoothing method to remove the variations due to friction . . . . .	188
6	Plastic stress-strain curves of L-605 from Thermecmaster-Z experiments . . . . .	189
7	Plastic stress-strain curves of L-605 from Gleeble experiments . . . . .	191
8	Observation of microstructure after deformation of $\epsilon = 0.8$ at $1000^\circ\text{C}$ $1\text{s}^{-1}$ . . . . .	192



9	Observation of microstructure after deformation of $\epsilon = 0.8$ at $1000^\circ \text{C}$ $1\text{s}^{-1}$ . . . . .	193
10	Microstructure after deformation at $1000^\circ \text{C}$ $0.1\text{s}^{-1}$ with Thermecmaster-Z device . .	194
11	Microstructure after deformation at $1100^\circ \text{C}$ $0.1\text{s}^{-1}$ with Thermecmaster-Z device . .	194
12	Microstructure after deformation at $1200^\circ \text{C}$ $0.1\text{s}^{-1}$ with Thermecmaster-Z device . .	194
13	Microstructure after deformation at $1100^\circ \text{C}$ $0.1\text{s}^{-1}$ with Gleeble device . . . . .	195
14	Microstructure after deformation at $1100^\circ \text{C}$ $0.1\text{s}^{-1}$ with Gleeble device . . . . .	195
15	Microstructure after deformation at $1200^\circ \text{C}$ $0.1\text{s}^{-1}$ with Gleeble device . . . . .	195
16	Microstructure gradient after compression at $1100^\circ \text{C}$ with a variable strain rate $\dot{\epsilon} = 0.1 \rightarrow 0.01 \rightarrow 0.001\text{s}^{-1}$ . . . . .	196
17	Microstructure gradient after compression at $1100^\circ \text{C}$ with a variable strain rate $\dot{\epsilon} = 0.001 \rightarrow 0.01 \rightarrow 0.1\text{s}^{-1}$ . . . . .	196
18	Stress-strain curves of pure ETP copper deformed in compression, and average grain size as a function of Zener-Hollomon parameter . . . . .	198
19	Treatment of compression curves: determination of $\sigma_V$ , $\sigma_y$ , and extrapolation of curves by the Voce law using the calculated parameters . . . . .	199
20	Fit of the average grain size with flow stress by the Derby law [32] . . . . .	200
21	Determination of the average grain size as a function of flow stress, and comparison with the Zener-Hollomon dependent grain size . . . . .	201
22	Determination of mobility and estimation of adiabatic heat from experimental data .	202
23	Determination of mobility and nucleation frequency from experimental data and modeling . . . . .	202
24	Compression curves and steady-state grain size of pure cobalt . . . . .	204
25	Determination of extrapolated steady-state stress $\sigma_V$ , and fit by the g parameter with $\dot{\epsilon}_0 = 10^{-3}\text{s}^{-1}$ . . . . .	205
26	Yield stress as a function of temperature, and grain size dependence with normalized stress . . . . .	205
27	Grain boundary mobility map of pure cobalt as a function of deformation condition	206
28	Determination of mobility and nucleation frequency from experimental data and modeling . . . . .	206
29	Microstructure generation process by growth of a compact layout of spheres . . . .	207







# Chapter 1

## Literature review



## 1.1 Metallic biomaterials for stent applications

The present report presents the results of a study on microstructural evolution of L-605 cobalt alloy for stent application. The following section is a literature review introducing a state-of-the art of the current knowledge in stents technology and on cobalt superalloys. After a presentation of the different stents structures and the specific materials requirements, it will be demonstrated that L-605 is a relevant material for this specific application. Common knowledge and metallurgical features concerning cobalt alloys are introduced in a second part. Finally, a part is dedicated to the basic facts on the metals plasticity and microstructure evolution during thermomechanical processing. The theoretical basis presented will be employed during experimental data processing in the last part of this report.

### 1.1.1 Stent structures and materials selection

Stents are tubular meshed metallic structures inserted in human body cavities to maintain it open. The neologism *stent* was first used to designate a dental system developed by Charles Stent during the XIX<sup>th</sup> century. The first real application of *stents* as vascular endoprosthesis was set up by Charles Dotter in 1983, based on canine experiments carried out in 1969 [34]. After 1983, some self-expanding and heat expanding stents were proposed by Maass (1983), Gianturco (1985), Rousseau and Sigwart (1987). The first balloon-expandable stent was created by Palmaz (1985). The first human implantation was carried out in 1986 by Puel using a self-expansible stent. However, it is only after 1991 that new stent designs and new implantation procedures made the treatment safer for the patient. The consideration of the restenosis issue and the development of efficient anticoagulant and antiplatelet poststenting therapies reduced dramatically the risks after the operation [34]. After 1995, the implant of stents became usual in angioplasty procedures. The emergence of drug-eluting stents was a significant breakthrough for the biocompatibility enhancement and the reduction of restenosis. Nowadays this technique is continually improved and constitutes the main development axis of stents technology [35]. Currently, more than one million drug-releasing stents are implanted every year just in United States, and the market exceeds \$7 billion per year [36]. During the last decades, various kind of stents models were developed, and the most common structures are presented hereafter.

#### 1.1.1.1 Development of metallic structures for vascular endoprosthesis

##### Spiral stents

The first stents developed by Charles Dotter in 1969 were simple spiral-shape implants for the treatment of aneurysms (local dilatation of blood vessels) and arteriovenous fistulas (abnormal connections between an artery and a vein) [37]. The device was improved in the early 80s by Maass



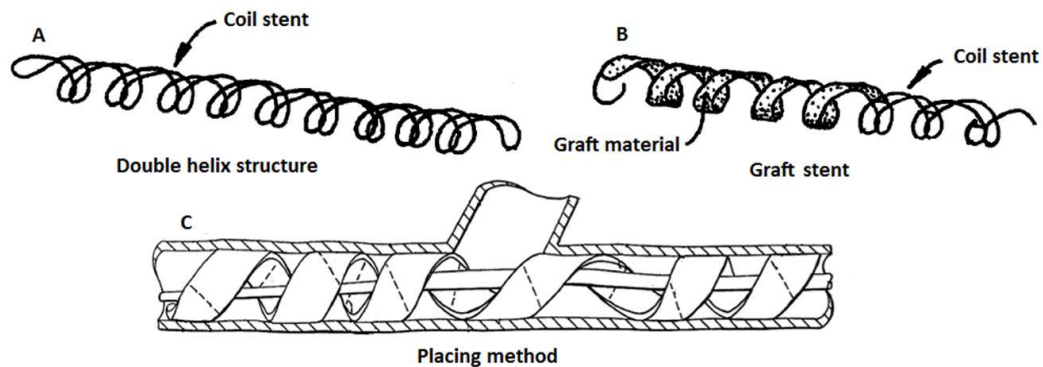


Figure 1.1: Coil graft stent (Patent US6488700B2). a: Metallic helix structure b: Stent with graft material c: placing method outline [1]

in a double helix shape. This design was the first expandable endoprosthesis, and was used for implantations in large blood vessels such as aorta or vena cava. This model was employed during 1982-1983, but was then abandoned. Some double helix stents grafted with polyurethane/polyester were developed, but did not reach clinical stages.

Several coil designs were investigated after 1985, single or double helix grafted stents are summarized in the patent US6488700B2 (2002) [1]. In this patent, the double helix structure is embedded in a graft polymer material (Figure 1.1) .

Some simple spiral-shape stents were developed from nitinol shape memory alloys. In this case, the shape at low temperature (about 0°C) is a straight wire, and the shape over 37°C becomes a coil. This technique was employed by Dotter during the 80s on animal experiments. However interactions between nitinol and the vessel are limited and the biocompatibility of this alloy is weak [37]. Moreover this technique requires relatively long wire pieces to form sufficient coils, and remains a problem for the insertion of such prosthesis.

### Balloon-expanded stents

Balloon-expanded stents are metallic mesh structures or slotted tubes. The initial stent device contains in its core an expandable angioplasty balloon, and the device is guided by a wire during its insertion in the artery. In a second step the stent is expanded by inflation of the balloon until it takes on the shape of the artery. Finally, the balloon and the guiding wire are removed, leaving the expanded stent inside the artery. The Palmaz stent[38] (Figure 1.2) is a seamless tube with staggered parallel slots edged through the wall (Johnson&Johnson Corp.). This stent has been extensively used for iliac and coronary arteries diseases since 1987. The description and the manufacture process are detailed in the patent EP1359865B1 (WO 2001/089420) [2]. In this patent the stent design was improved by adding grooves to promote the migration of endothelial cells.



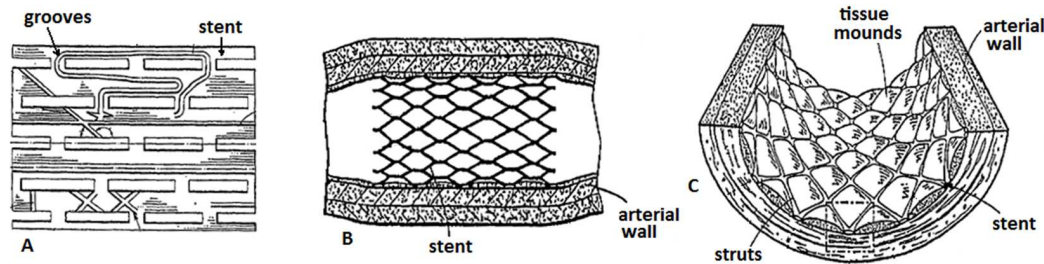


Figure 1.2: Palmaz stent described in the patent EP1359865B1 a: Initial shape, a pipe with parallel slots and grooves b: Stent after expansion c: Integration of the stent inside the arterial wall [2]

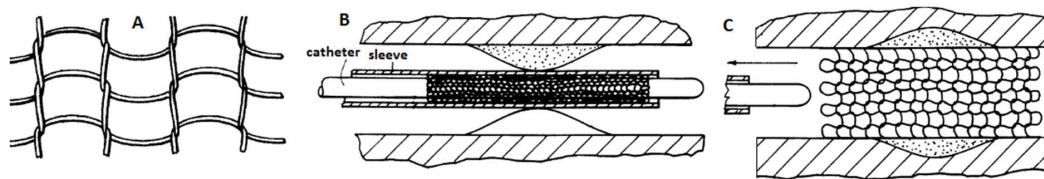


Figure 1.3: Strecker stent, as detailed in the patent US5662713 a: knitted structure made from metallic wire b: insertion of the stent in a vessel c: stent after expansion [3]

The Strecker stent (Figure 1.3) is simply made by knitting a single metallic wire in a series of faintly connected loops. The knitted structure is very flexible and elastic, and can be expanded by an angioplasty balloon. This stents have been used for the iliac arteries, but also for the renal arteries and the venous system [37]. The high flexibility of the structure enables the implantation in peristaltic lumens, like esophagus. This stent and its manufacture are developed in the patent US5662713 [3].

### Self-expanding stents

The Gianturco expandable stent is a simple zigzag pattern made from bent stainless steel wire [37, 4]. This stent was first described by Gianturco in the patent EP0177330A2 (US656261) [4]. The structure is compressed and placed in a catheter. After implantation, the zigzag structure expands itself in the vessel. Such stents are short, it is therefore possible to implant several stents in the same vessel (Figure 1.4). The stents can be connected together by wire loops and form a multiple stent (patent EP0622088A1).

The Wallstent<sup>®</sup> [5] is a tube made from stainless steel filaments woven in a criss-cross pattern (Figure 1.5). The crosspoints are not welded, making the stent very flexible and easily self-expandable [37]. After release in the vessel, the stent returns to its initial diameter by elastic forces. This stent has been used for the vascular and biliary systems, but also in the trachea and esophagus [37]. This stent is described by the patent US5061275 [5].



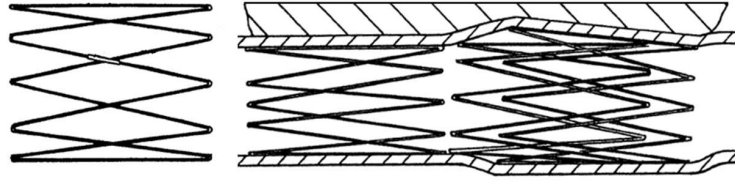


Figure 1.4: Gianturco self-expanding stent described in 1985 in the patent EP0177330A2 [4]

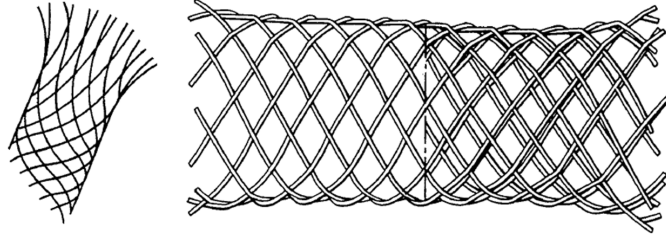


Figure 1.5: Wallstent<sup>®</sup> self-expanding prosthesis described in 1991 in the patent US5061275 [5]

### Comparison of the different structures

Spring stents expansion is driven by the elastic energy contained in the initial compressed structure. If the elastic energy is not sufficient to fully deploy the stent, the final diameter is lower than the diameter targeted, and it can sometimes lead to thrombosis [38]. On the other hand, if the elastic energy is too large, the vessel can be overdilated. Therefore this structure is less commonly used nowadays because of a lack of control during the deployment. Palmaz-type stents are currently the most usual structure employed for angioplasty. This choice is notably due to the malleability of such structures that can be deployed with a sufficient control, by dilating the vessel wall and the stent simultaneously [38]. Palmaz stents are also associated with less complications than Strecker stent or Wallstent according to a study on the treatment of biliary obstruction [39]. From canine experiments [40], it was observed that Strecker stents lead to higher neointimal growth compared to Wallstent and Palmaz stent, which provoke a larger reduction of the luminal diameter. Therefore Palmaz stent seems more adapted to limit the risks of stenosis. In the other hand, Palmaz stent leads to larger chronic trauma of the arteria wall due to its rigidity. Also, this study indicates that Palmaz stent is 1.5 times more resistant to external compression than a Wallstent, and about 7 times more resistant than a Strecker stent. If the stent has to undergo deformation by external pressure, Palmaz stent will deform plastically, while Wallstent and Strecker stent will deform elastically. That is why Palmaz stents must be implanted deep within the body to avoid any damage by external pressure on the human body [38]. For conditions which require large flexibility and elastic properties, Strecker stent and Wallstent are preferable. For other conditions, Palmaz stent is usually employed due to its higher formability and its limited induced restenosis. Thereof, Palmaz stent is the most employed stent structure due to the large past experience and to its suitable integration in most conventional



cases. The following metallurgical study will be illustrated in the case of the development of Palmaz stents due to its widespread use for angioplasty. As this study provides a general investigation on the metallurgy of L-605 alloy, it can be applied as well for the processing of wires in order to elaborate Wallstent or Strecker-type stents, but also for the elaboration of other biomedical implants [41], as well as for high-temperature [42] and aerospace applications [43].

#### **1.1.1.2 Specifications on metallic biomaterials for vascular implants**

##### **Norms and specifications for metallic biomaterials**

To be applicable for biomedical applications and fulfill the general norms, a metallic material must satisfy the following conditions [44]:

- Biocompatible and non-toxic for the organism
- Highly resistant to corrosion
- Hard and resistant to wear and fatigue
- Ductile to permit adjustments and avoid brittle comportment

To fulfill these requirements, ISO and ASTM norms are defining the specifications for biomedical application. The specifications on the chemical composition and mechanical properties of some usual alloys for surgical implants are listed in Table 1.1 [45]. For hard drawn conditions, the average specifications impose a yield stress (noted  $R_p$ ) above 1 GPa, an ultimate tensile stress ( $R_m$ ) above 1.2 GPa, and a maximal elongation ( $A$ ) above 5%. For annealed materials the average specified yield stress must be above 500 MPa, the ultimate tensile stress must be above 900 MPa, and the elongation at rupture must exceed 40%. As a consequence, biomaterials for stent applications must device must combine high strength and large ductility. The initial material constituting the retracted stent must satisfy the annealed material average specification:  $R_p > 500$  MPa,  $R_m > 900$  MPa and  $A > 40\%$ . After deployment of the stent, the material is deformed and must keep a maximal stress  $R_m > 1.2$  GPa and a ductility  $A > 5\%$ .

##### **Mechanical solicitations on stents during the deployment step**

During the balloon expansion, Palmaz-type stents undergo large plastic deformation. This deformation process of 316L stainless steel Palmaz stents was studied by Dumoulin et al [6] in 2000 (Figure 1.6a), and Etave et al. [46] in 2001. According to Etave et al. the expansion of a Palmaz-Schatz stent with struts size of 0.2 mm require a pressure about 2.1 atm. in the balloon to be expanded, and this pressure can slightly decrease during the expansion process .



ASTM and ISO	UNS	International description	Condition	R <sub>p</sub> (MPa)	R <sub>m</sub> (MPa)	A%
ASTM F.138 ISO 5832.1 ASTM F.2257	S.31673	Fe-18Cr-14Ni-2.5Mo	Hard drawn	760	935	5%
ASTM F.2229	S.29108	Fe-23Mn-21Cr-1Mo-1N	Annealed	340	670	> 40%
ASTM F562 ISO 5832.6	R.30035	Co-35Ni-20Cr-10Mo	Hard drawn	990	1400	4%
ASTM F90	R.30605	Co-20Cr-15W-10Ni-1.5Mn	Annealed	500	940	> 40%
ASTM F1314	S.20910	Fe-22Cr-12.5Ni-5Mn-2.5Mo	Annealed	> 483	> 965	> 40%
ASTM F1058 ISO 5832.7	R.30008	Co-19Cr-17Ni-14Fe-7Mo-1.5Mn	Annealed	448	827	> 40%
			Hard drawn	1300	1450	8%
			Annealed	450	950	> 40%

Table 1.1: Description of ISO and ASTM chemical composition and mechanical properties specifications for surgical implants (Minitubes specifications [45])

During the deformation process, stress concentrate at link nodes and can reach locally 400 MPa after an expansion of the stent from 1.4 mm to 3 mm. Intrinsic elastic recoil after expansion is within 5 to 7% range. The detailed finite-elements study of Dumoulin et al. on 316L Palmaz stent (as described in [38]) also indicates the apparition of stress and strain concentration areas at link nodes of the mesh structure (Figure 1.6). The maximal local Von Mises equivalent stress exceeded locally 500 MPa, and the equivalent plastic strain (PEEQ) was about 40% in these areas, as illustrated on the Figure 1.6b. As a consequence, metallic materials for stent elaboration must exhibit a sufficient ductility to allow large deformations exceeding 40% without fracture.

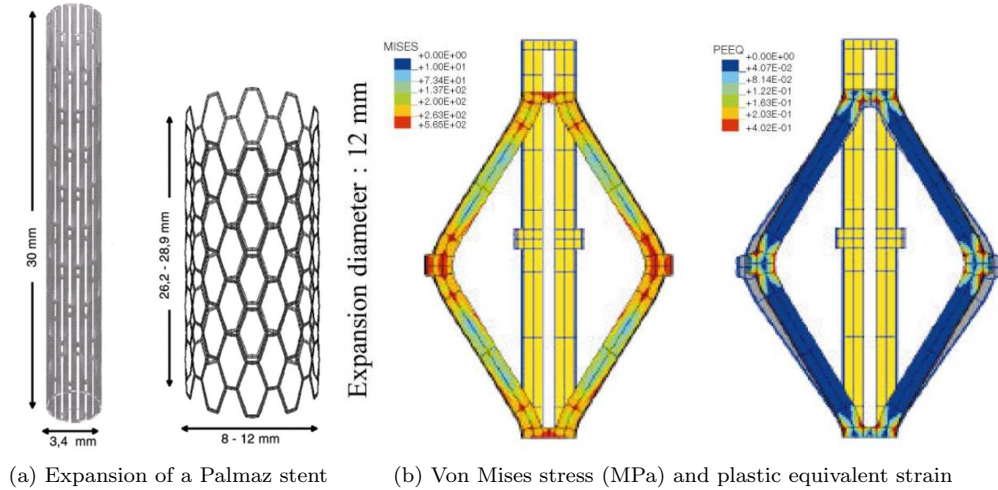


Figure 1.6: Finite elements analysis of a Palmaz stent deployment until 12mm diameter [6]



## Biocompatibility of metallic implants

Biocompatibility of the material is of course a fundamental factor in the development of medical devices. The ISO 10993 norm compels an exacting series of tests to evaluate the biocompatibility and the effect on the human body. The Table 1 [47] in the Appendix 1 (page 183) indicates the different tests included in this norm. Among these tests, the standards ISO 10993-3 to 10993-6 and 10993-15 are especially relevant in the context of the current study to estimate the biocompatibility. The ISO 10993-5 evaluates the in-vitro cytotoxicity of the material, and is a compulsory preliminary step to in-vivo tests. Cytotoxicity can be evaluated by estimating cells proliferation, DNA damages, metabolism and morphology of cells. The proliferation of fibroblast NIH 3T3 mouse cells on pure metals and some dental alloys was investigated by Hornez et al. [7]. The Figure 1.7a represents the proliferation of 3T3 cells on some pure metals. These results demonstrate the high cytotoxic effect of silver, copper and nickel, with a cell proliferation lower than 20 % after 3 days. For noble metals like gold and palladium, cell proliferation rises above 50% after 3 days and increases further after 6 days. Therefore noble metals exhibit a cytotoxicity significantly lower than usual metals. This study examined also the dissolution of pure metals. On the Figure 1.7b, the dissolution of some pure metals is represented after 3 days and 6 days in the culture medium. Copper has the highest dissolution rate, with a concentration above 390 ppm in the medium after 3 and 6 days. Silver has a significant dissolution rate as well, with 1.4 ppm and 2.8 ppm after 3 and 6 days respectively. These two metals were found to have high cytotoxic effects based on cell proliferation tests. Unsurprisingly, gold and palladium have very low dissolution rates, with less than 1 ppm after 6 days. Therefore cytotoxicity and dissolution rate are correlated: the alloy must have noble comportment to avoid metallic ions release in the organism. Therefore a good resistance to corrosion is fundamental for optimizing biocompatibility.



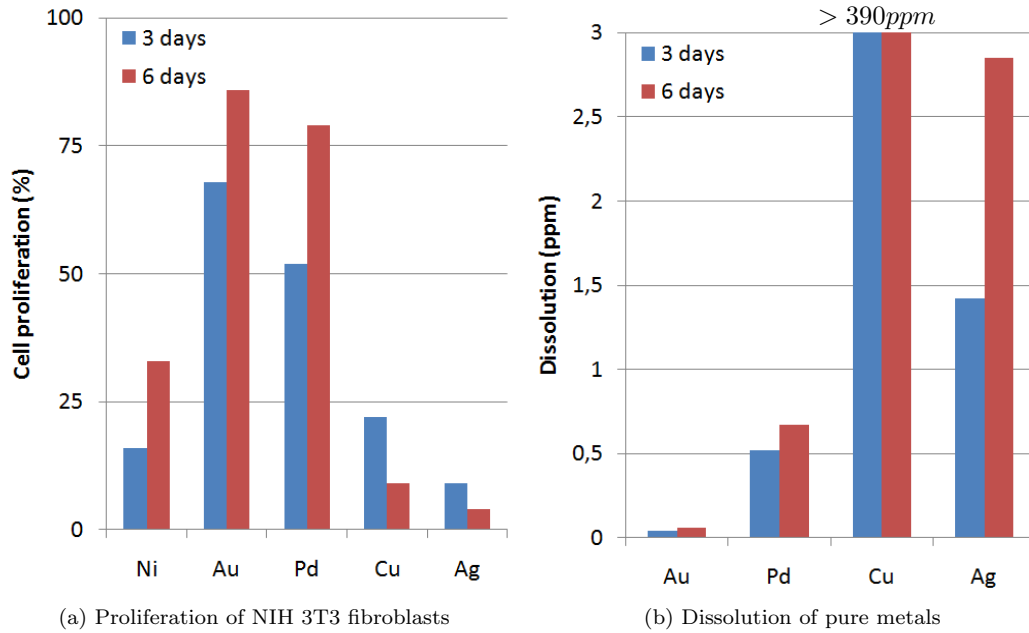


Figure 1.7: Cell proliferation and dissolution after 3 and 6 days on pure metals [7]

The mitochondrial activity of fibroblasts deposited on dental alloys was investigated by Al-Hiyasat et al. [8]. The cell activity of Balb/C 3T3 mouse fibroblasts on different alloys is illustrated on the Figure 1.8. In one hand, the copper-based alloy was exhibiting the highest cytotoxic effect, in agreement with the previous data from Hornez et al. The cytotoxicity is attributed to the capability of copper alloys to tarnish and corrode. In the other hand, alloys containing high amount of chromium and molybdenum exhibit limited cytotoxicity, with a cell activity above 75%. This superior biocompatibility is attributed to the development of an oxide protective layer enhanced by the high content of chromium and molybdenum. The Co-Cr-Mo alloy was presenting a similar cytotoxicity to the Ni-Cr alloys, and both alloys can develop a suitable passive oxide film decreasing the ions release and the cytotoxic effects.

Furthermore, the allergenic potential of metals is a major issue for biocompatibility. For instance, in Europe, 20% of young females and 4% of young males suffer from nickel allergy, and this trend is increasing [9]. The Figure 1.9 indicates the percentage of allergy for several metallic elements. Nickel, chromium and cobalt are responsible for 35% of these allergies; their effect on health is therefore significant. Thereof, allergy risks are limiting the use of metals such as nickel, chromium and cobalt for biomedical devices.



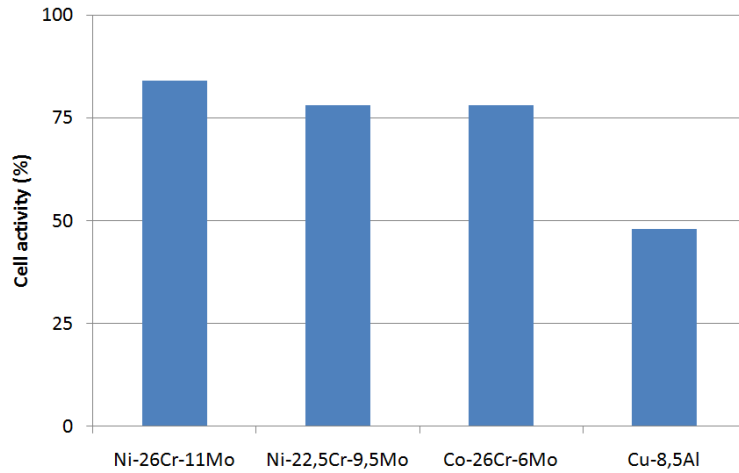


Figure 1.8: Percentage of mean cell activity of Balb/C 3T3 fibroblasts on dental alloys [8]

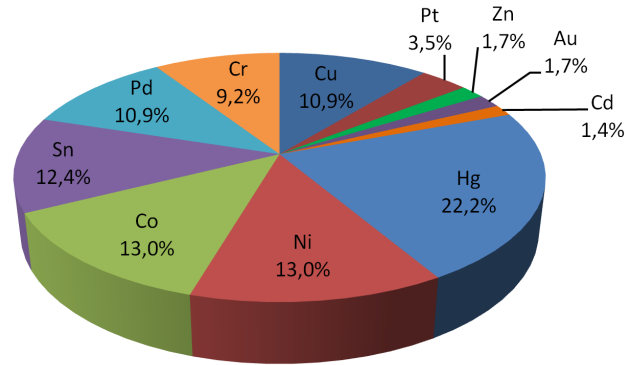


Figure 1.9: Percentage of allergy caused by metallic elements [9]

### 1.1.1.3 Selection of materials for stent applications

#### The Ashby maps

As a consequence of the specifications on mechanical properties (page 6), the material for elaborating stents must have high strength ( $R_p > 500$  MPa,  $R_m > 900$  MPa) and a large ductility ( $A > 40\%$ ). However, it is well known that most of the hard materials having high strength present a poor ductility, and conversely soft materials have large ductility. Therefore the issue of selecting an adequate material is not trivial and requires some compromises between hardness and ductility. An usual selection procedure consists in gathering mechanical properties of a large amount of available materials, and representing two relevant and critical properties on 2D maps, so called Ashby maps [48]. By this way it is possible to visualize these two properties for many materials, and selecting the optimal one fulfilling the specifications based on compromises.

The following selection process was applied in a pragmatic case. The whole materials datasheets available in 2011 from the special alloys manufacturer Aubert&Duval (Eramet group) were collected.



These datasheets set includes engineering steels, stainless steels, cobalt and nickel superalloys, aluminum and titanium alloys. For each material the yield stress, the ultimate tensile stress and the maximal deformation were noted down. The dataset used is fetched in the Annex 1 (Table 2, page 184). The maps representing the yield stress, the ultimate tensile stress and the maximal deformation are illustrated on Figure 1.10. The dashed lines indicate the average specifications for stents. On the Ultimate Tensile Stress-Deformation map (Figure 1.10a), we can conclude that only nickel and cobalt superalloys can fulfill the targeted mechanical requirements. Some special steels could also be considered to a lesser extend. Among all materials, only the L-605 (Co-20Cr-15W-10Ni) cobalt-based superalloy fulfil the requirements in terms of both strength and ductility, with a ultimate tensile stress of 1GPa and a deformation above 40%. Therefore L-605 is a good candidate for stent elaboration. In spite of its excellent strength, Co-28Cr-6Mo alloy usually employed for biomedical implants is not fulfilling the requirement due to a lack of ductility. Also of interest is the PER625 nickel superalloy (Ni-22Cr-9Mo-3.6Nb), which is the material with the highest ductility among all the materials considered. PER625 has a maximal deformation of 65 % and an ultimate tensile stress of 750MPa. Even if this material is not hard enough to pass the usual specifications, it could be used in some special cases for stents requiring an outstanding ductility.

The Figure 1.10b illustrates the Yield Stress-Deformation map. On this map, it can be confirmed that cobalt and nickel superalloys are the two main alloys groups satisfying the mechanical specifications. However no material among the initial dataset is totally satisfying the requirements: there is no points upper to the 40% deformation limit (horizontal dashed line) or higher than 500MPa yield stress. The cobalt based superalloy L-605 and the nickel-based superalloy PER2X (Ni-20Cr-2.5Ti-0.35Al) are the best candidates for combining a maximal ductility and a high yield stress.

Ductility is from far the most critical parameter: as it was shown in the previous section (page 7), during the expansion of the stent deformation can exceed 40%, and according to the specifications (page 1.1.1.2) the material must keep a maximal deformation of 5% after hard drawing. Therefore a maximal deformation about 45% would be just sufficient for stent applications. Considering this, the L-605 is the only material with sufficient strength and with a ductility of 45%, and should be preferred to PER2X due to its higher ductility.

### **Context of the current study**

From the previous results, it can be concluded that L-605 (Co-20Cr-15W-10Ni) is the optimal material for stent elaboration, as it constitutes the best optimum between strength and ductility among the materials considered. Moreover the ductility is sufficient to enable the proper deployment of the stent without rupture. Therefore L-605 superalloy was selected in this study for stent



manufacture. Yield stress is somewhat low compared to other cobalt-based superalloys such as Co-28Cr-6Mo, and satisfy barely specifications. It can be very interesting to seek a method to obtain much higher yield stress: if the yield stress is higher, then the stent will be less susceptible to undergo plastic deformation and damage by an external pressure on the human body and will be more resistant. A method to increase the yield stress consists in decreasing the grain size. Therefore the current study proposes to proceed to severe plastic deformation at high-temperature during the forging process of the stent to decrease the grain size. However it is well known that advanced grain refinement can decrease dramatically the ductility of the material ([49], [50]). In the current context, initial ductility of the base material is already the acceptable limit of 45% deformation. In spite of a global yield stress increase after the forging operation, an additional loss of ductility by grain refinement would be significantly depreciative for the targeted application. Recent study [51] suggests new promising tracks on the microstructure design: bimodal grain size distribution could be a solution to increase yield stress without affecting significantly the ductility. Therefore the current study proposes a thorough examination of the hot-working process conditions to obtain grain refinement with different grain size distributions, and investigates in a second time the effect of size distribution on mechanical properties.

### **1.1.2 Manufacture process of stents**

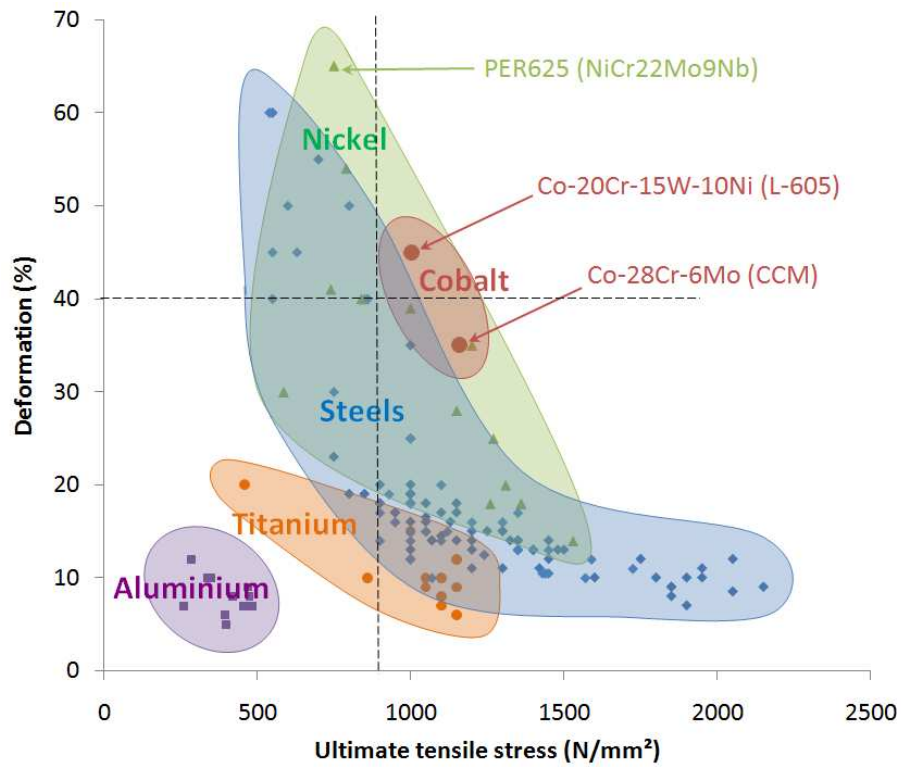
Palmaz-type stents are processed by laser cut or machining from metallic pipes. The initial pipe can be produced by drawing from a rod, or by welding of a thin metallic sheet. Strecker stents and Wallstents are produced by conventional knitting and weaving from metallic wires. The following part will treat the manufacture process of Palmaz-type stents only, which was the structure selected for the current study. The reader having interest in metallic wire based stents should report to patents JP 2010-279809 for weaving method, WO 2004021933 for knitting method, and US6514063 for wires welding manufacture technique.

#### **1.1.2.1 Manufacture of pipes for semi-finished products**

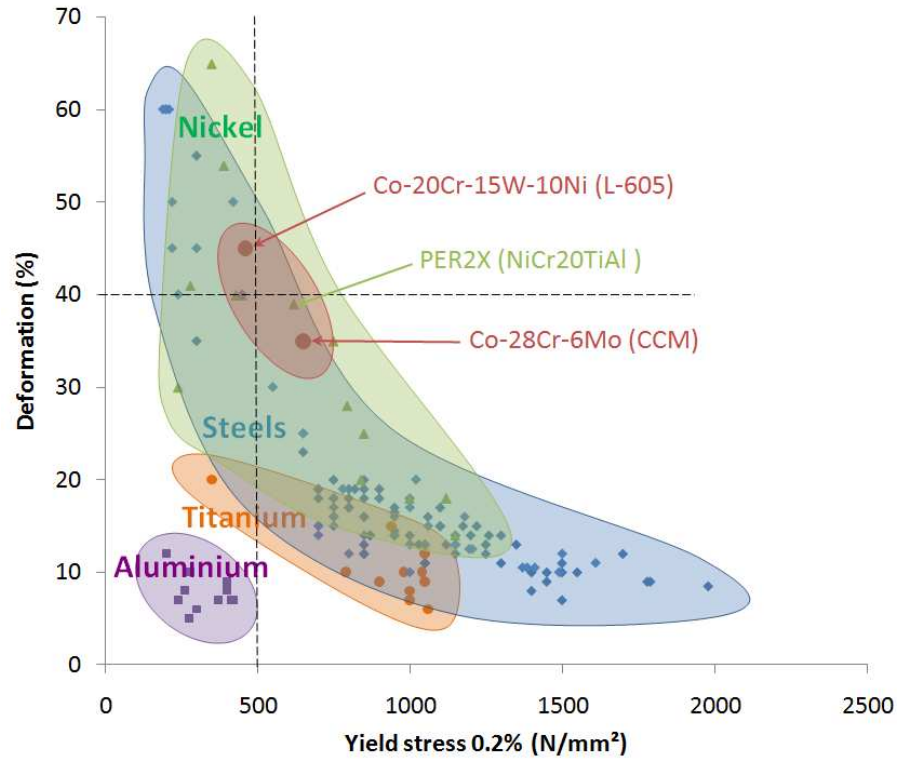
##### **Production of seamed tubes by roll forming**

Roll forming has been extensively used since long ago to produce pipes from strip products. A metallic sheet is formed by continuous roll-bending into a tubular shape (Figure 1.11a) [10]. The seam of the pipe is then welded by electrical resistance welding, butt welding or arc welding. This method is conventionally used for usual superalloys tubes (Haynes, Figure 1.11b). For large pipes, the tubular shape can be also obtained by bending of a strip into an helix shape, and welding of the helical seam. However, welded seam pipes does not exclude the possibility of creating some undetectable defects during the welding process. Therefore the welded seam method is usually





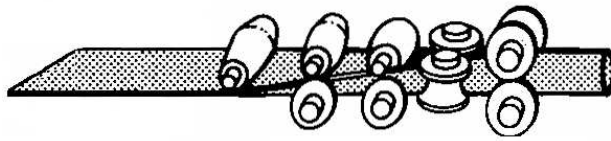
(a) Map of Ultimate tensile stress (MPa) - Deformation



(b) Map of Yield stress (MPa) - Deformation

Figure 1.10: Ashby maps indicating the ultimate tensile stress, the maximal deformation and the yield stress (0.2%) based on datasheets from Aubert&Duval (Eramet)





(a) Production of pipes by roll-forming [10]



(b) Pipes welding, Haynes Intl Inc.

Figure 1.11: Roll-forming and continuous welding of strips to produce pipes

not applied for the production of stents for safety reasons and to ensure the compliance to the specifications [13, 12]. For that matter, seamed pipes are not recommended by biomedical grade tubes manufacturers (e.g. Minitubes Grenoble) for stent applications.

### Seamless tubes manufacture

Seamless short tubes are produced by conventional extrusion. The simplest extrusion process consist in the extrusion of a hollow billet by a mandrelled ram (Figure 1.12a). The pipe shape is formed by the spacing between the chamber hole and the mandrel. This technique require a preliminary drilling step, which can be conducted by trepanning or boring of the initial billet. Some variants of this technique with a floating long mandrel are also conventionally applied (e.g. Ugine-Sejournet process, with glass lubricant). However, the long mandrel can sway and lead to an eccentric tube with an irregular thickness.

Hollow products can also be extruded from a solid billet by extrusion with a spider design as shown on Figure 1.12b. A plug is connected by large bridges to the reduction die to ensure the formation of the hollow shape [10]. The extruded material is pressed through port holes to reach the reservoir, then the tube is formed by extrusion between the die and the plug. The plug placing is more precise than the mandrel. Therefore the hollow shape is more accurately controlled, with a more even tube thickness.

### Other seamless pipes processes

Pipes can be produced also from solid rods by Mannesmann piercing, also called rotary rolling mill (Figure 1.13a). The rod is rotated between two rolls by a small inclination from the symmetry axis of the rod. The rod diameter is reduced by rolling between the mill rods. During the reduction process, a piercing mandrel penetrates into the rode and forms a tube. This process is suitable for thick tubes, and the maximal length of the tubes is limited by the length of the mandrel. Also the tube obtained is seamless, but with poor dimensional control. Therefore, successive rolling or



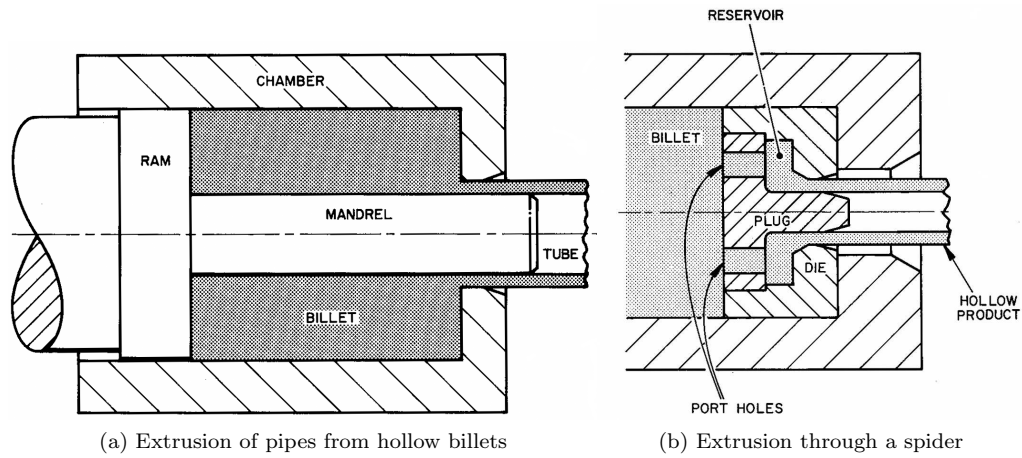


Figure 1.12: Extrusion process of hollow products [10]

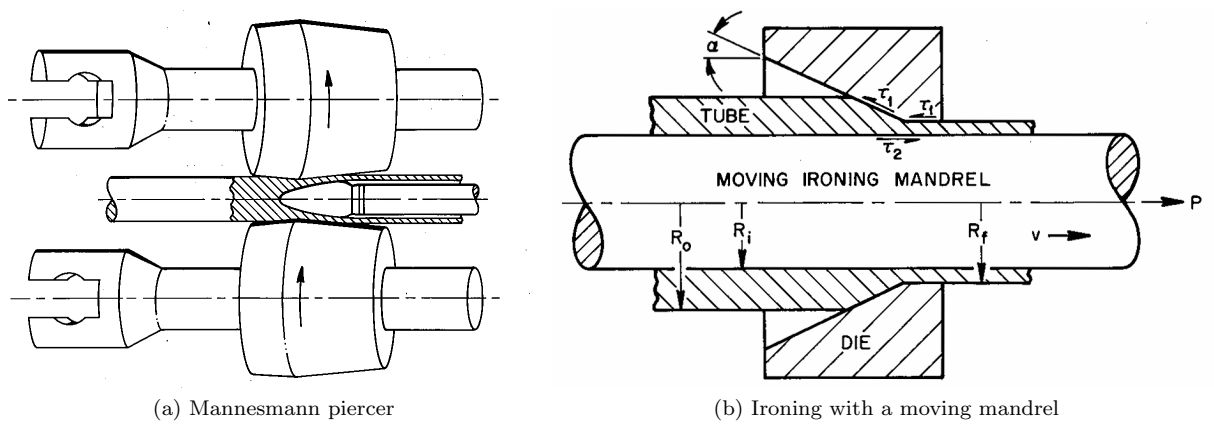


Figure 1.13: Rotary rolling mill and ironing process [10]

drawing steps are required to refine the geometry of the product. This method is much less common than the extrusion process.

Tubes can also be produced from the thickness reduction of a hollow billet by ironing process. The initial workpiece has a cup shape, and the ironing mandrel pushes the cup through a conical die (Figure 1.13b). Therefore the cup walls are squeezed between the mandrel and the die, leading to a refinement of the cup walls. This process allow us to manufacture very thin walls products that could not be obtained by extrusion or conventional drawing.

### Tube drawing

Tubes can be reduced in both diameter and wall thickness by drawing, also called tube sinking. The tube is pulled through a conical converging die to reduce its diameter. As in the ironing process,



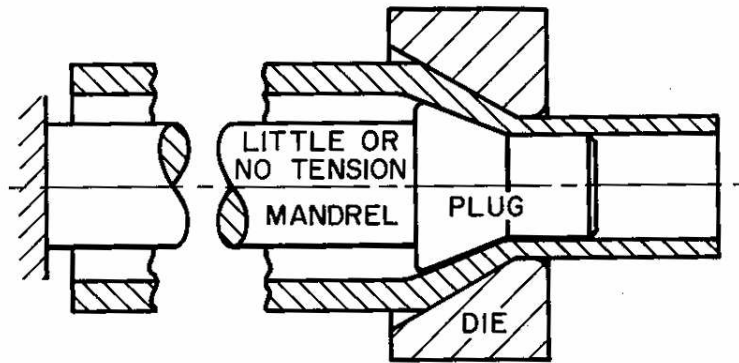


Figure 1.14: Drawing process of pipes with a plug [10]

a mandrel is inserted inside the pipe before drawing to ensure the control of the inner diameter of the final product and to provide a good inner surface finishing. The mandrel can move together at the same speed with the pipe, in a similar way with the ironing process. In this case the friction between the mandrel and the workpiece is minimized, but removing the mandrel from the final product can be a problem. The problem of removing the mandrel can be solved with a fixed mandrel, but the friction between the mandrel and the tube will be high and the mandrel will extend elastically. Using a plug in the top of the mandrel solves these problems, as illustrated on Figure 1.14. The plug is a conical extension of the mandrel squeezing the tube during its flow to keep the inner diameter constant [10]. With using a plug, the tension on the mandrel decreases dramatically, and friction occurs only on the borders of the plug. Moreover, the continuous production of pipes is enabled by using floating plugs. The floating plug is inserted in one extremity of the pipe and does not require to be connected to a mandrel as it is dragged to the die by friction. This technique is especially convenient for the drawing of long and coiled pipes.

#### 1.1.2.2 Finalization of the stent product

After manufacturing, pipes are cut to produce stents. Laser can be used to directly cut the metal by local melting of the pipe. Another method based on the photolithography techniques conventionally used for semiconducting materials consists in selective chemical etching of some areas of the tube. Both methods enable very complex cut paths and are suitable to product most Palmaz-type stents architectures with a very high flexibility. The cut pipes are finally polished mechanically and electropolished to remove burrs, smooth the sharp edges and erase the surface roughness.

#### Direct laser cut of stents

Direct cut of stents can be operated by a Q-switched pulsed Nd/YAG laser, as described in the patent US5780807A [11] (Figure 1.15). A high frequency Q-switching laser produces very short



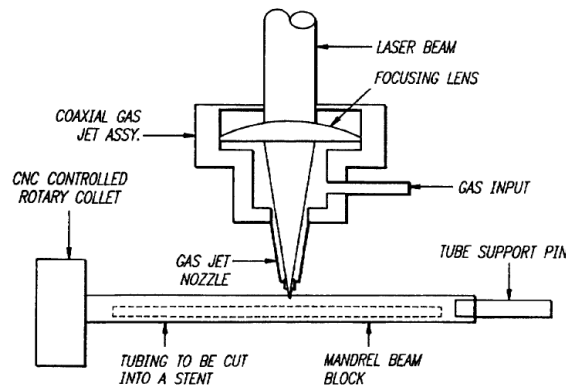


Figure 1.15: Laser cutting of a tube to produce a stent [11]

pulses ( $< 100ns$ ) of very high power peaks above 1 kW. The energy per peak is lower than 3 mJ, and minimizes the overheat to prevent excessive burn of the metal or thermal distortions. The frequency of the laser beam is doubled to decrease the final spot size and enhance the cut precision. A jet nozzle centered on the focus laser beam blows oxygen to assist the cut process. The cutting process occurs by combustion of the metal with oxygen in a similar way to the oxy-fuel cutting torchs. The opposite side of the stent is protected from unwanted laser cut by inserting inside the pipe a steel mandrel to stop the stray laser beam. Slag re-solidifies along the cut line and slimes the scraps produced during the cut process. Successive cleaning steps are necessary to remove the scrap parts and the solidified slag. Scraps are removed by cleaning in an ultrasonic bath, and the slag is etched by hydrochloric acid. This cutting method is fast and presents few process step. It produces a high-resolution narrow cut suitable for complex stent patterns. However the cutting process leads to a local heating of the stent, which have some consequences on the geometry and the microstructure.

### Photo-etching cutting of stents

Photo-etching process consist in the selective etching of metallic parts, and is similar to the photolithographic techniques employed for microelectronics. The initial pipe is coated with an etching-resistant photoresist layer. The stent pattern is transferred to the photoresist layer by selective light exposure. Exposed photoresist film areas can either degrade with light and leave the tube surface unprotected, or cure to constitute a protective film. The chemical etching engraves the stent pattern on the pipe until the unprotected areas are completely removed. This process has the main advantage to enable the cut of very fine patterns without involving thermal process, so it preserves the stent geometry and the tube microstructure. Photo-etching process can be carried out by the film contact imaging method. This very simple method uses negative film masks, as described on the patent US6726829B2 [12]. The initial tube is cleaned by electro-etching, and then



coated with photoresist resin. The tubes are then patterned by selective exposure of the photoresist resin to ultraviolet light. The system described on the Figure 1.16 consist in a negative film rolling on the tube. The light passing through the transparent portions of the negative crosslinks the photoresist. The tube is treated by a developing solution to remove the un-cured photoresist. The inner part of the tube is protected by injecting rubber in the hollow of the tube. Etching is carried out by soaking the coated tube in an etching solution, or by spraying the solution on the tube in rotation. Conventional etching solutions contain usually acids or iron perchloride depending on the pipe material. The etching step removes all the unprotected areas of the tube and generates directly the stent in its final shape. The final product is obtained after cleaning of the stent and electropolishing,

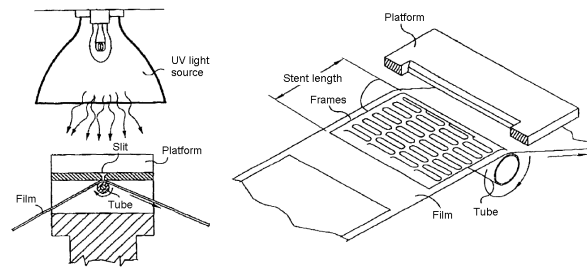


Figure 1.16: Film contact imaging method [12]

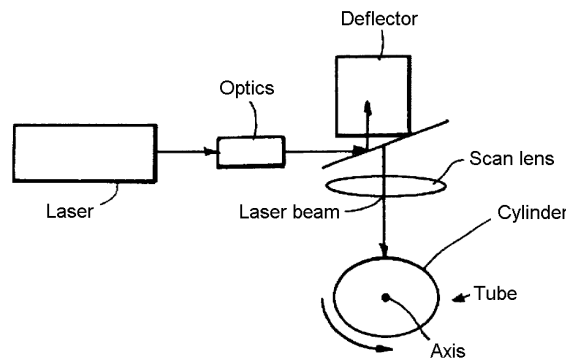


Figure 1.17: Laser scanning method [13]

Stents can also be produced from pipes by the laser scanning method as mentioned in the patent US5776161A [13] (Figure1.17). The tube is prepared and coated with photoresist as detailed previously. The main difference is that light exposure of the photoresist layer is not ensured anymore by a negative film, but by a laser scanning the stent surface. The laser can be a conventional continuous laser, and does not require high power like the laser cut presented on the previous paragraph. The wavelength of the laser must be selected carefully to generate curing or ablation of the photoresist coating. The next steps are similar to the negative film technique: the photoresist



is developed, and then etching is carried out to remove the uncoated areas. The main advantage of this method is to enable the direct transfer of a computer-designed stent pattern to the photoresist with skipping the elaboration step of a negative film. However this technique is more complex to set up and is relatively expensive, compared to the film contact imaging method [12].

## **Conclusion**

Manufacture of stents requires large deformation processes to produce seamless pipes and finally stents. During thermomechanical processing, microstructure is expected to change, affecting in the same time the mechanical properties. As a consequence, microstructure evolution and its consequences on mechanical properties must be thoroughly understood to obtain the desired final product combining sufficient strength and ductility. The following part will present some elements of the metallurgical characteristics of cobalt alloys, with advanced analysis on the relationship between the microstructure and mechanical properties.



## 1.2 Cobalt-based superalloys: microstructure and mechanical properties

One of the first alloys developed for gas turbine applications was the X-40 (Co-25Cr-8W-10Ni), invented in 1943 by R.H. Thielemann [52]. This alloy and its variants are still employed in aeronautics. Then technology of nickel alloys overtook cobalt, due to its outstanding strength and high-temperature resistance. However, we have now reached the limits of nickel alloys systems, and metallurgists turn back to cobalt alloys. Cobalt-base alloys are wear-resistant, corrosion resistant and heat-resistant alloys. The outstanding mechanical properties of cobalt alloys are due to solid-solution strengthening (with Cr, W, Mo), and the formation of metal carbides. The high corrosion-resistance is due to the addition of chromium in the alloy. The soft and tough alloys are used for high temperature applications such as gas-turbine and aeronautics; while harder alloys are used for their resistance to wear [14]. Several cobalt-base alloys containing Cr, W, Ni, Mo were developed for corrosion-resistance and high-temperature applications

### 1.2.1 Phase diagrams and typical microstructures of cobalt superalloys

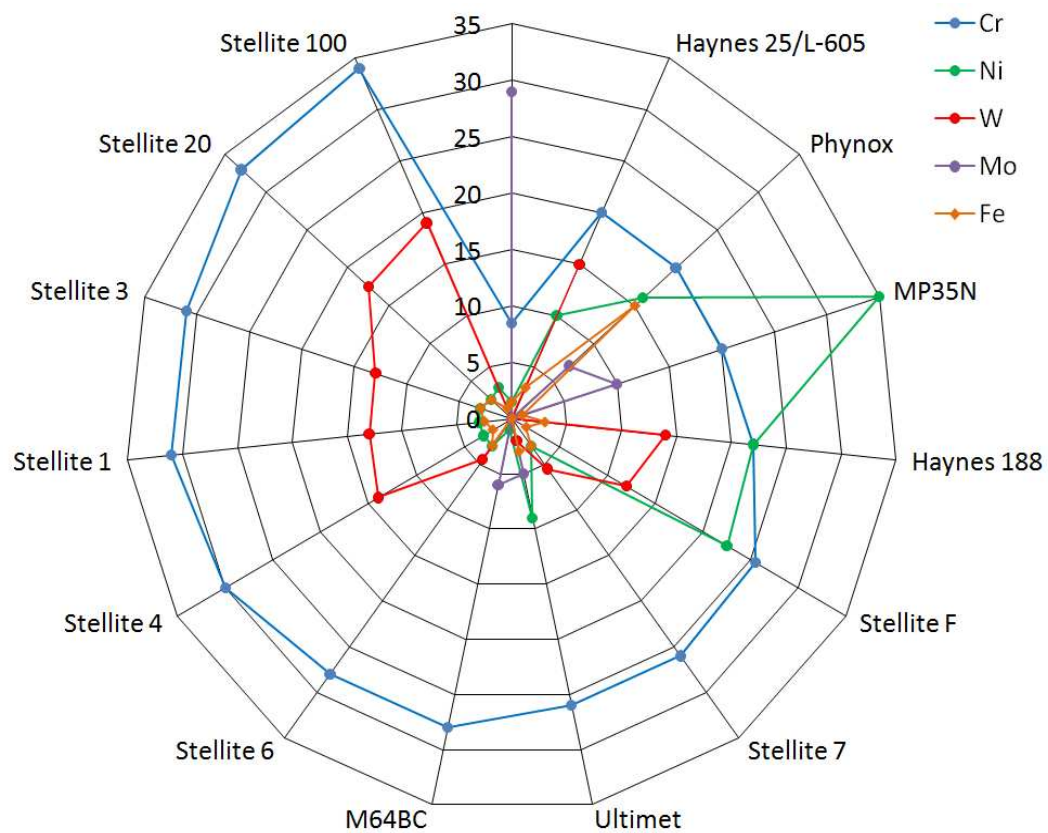
#### 1.2.1.1 Phase diagrams of usual cobalt superalloys

Figure 1.18 represents the composition of some common cobalt-based alloys based on datasheets available from different superalloys manufacturers. Of course this list is not exhaustive, and many variants of these composition are available. Most of cobalt alloys contain chromium within the range 10% (Tribaloy T-400) to 35% (Stellite 100 ) weight. Co-Cr alloys usually contain tungsten (e.g. Stellite 100, Haynes 188, Haynes 25) or molybdenum (e.g. Tribaloy T-400, MP35N, M64BC), but in a lower concentration. Nickel is sometimes included for improving the ductility, and can reach 35% weight for MP35N. The carbon content is illustrated on the Figure 1.18b for the previous alloys. Stellites contain usually several percent of carbon to develop carbides in the Co-Cr alloy matrix, conferring hardness and enhanced wear resistance. On the other hand, carbon concentration is minimized for alloys like Haynes 25 (L-605) or M64BC for which the occurrence of carbides is usually not desired. To understand the effect of the alloying elements on the properties of superalloys, the analysis of binary and ternary phase diagrams is necessary.

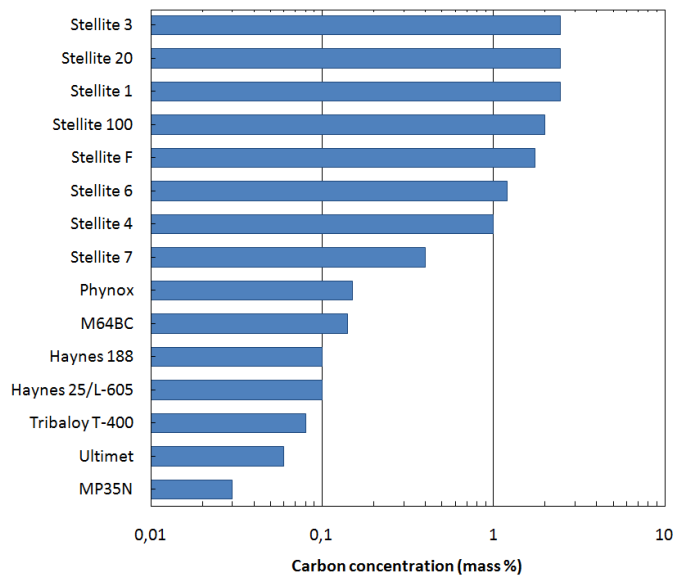
#### Co-C system

The Co-C binary phase diagram is illustrated on Figure 1.19 [14]. Liquid cobalt can dissolve about 3% weight of carbon at 1500°C. During the solidification process, the  $\gamma$ -cobalt phase can retain until 1% of the carbon in solid solution, the remaining carbon forms graphite during the eutectic transformation[53]. The metastables phases  $\text{Co}_2\text{C}$  and  $\text{Co}_3\text{C}$  can also form during the cooling process.





(a) Composition of cobalt alloys



(b) Carbon concentration

Figure 1.18: Composition of usual cobalt alloys based on datasheets from Deloro Stellite Inc., Haynes Intl Inc., Aubert&Duval (Eramet), Carpenter Tech. Corp. and Matthey SA



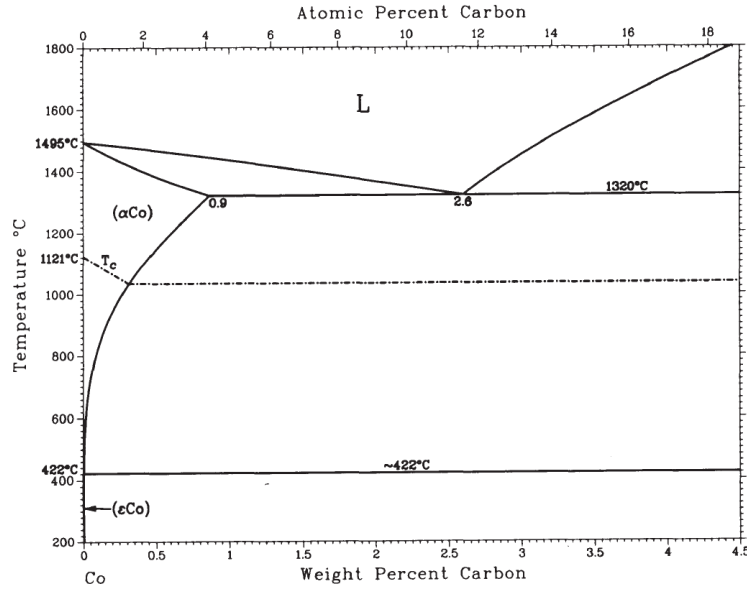


Figure 1.19: Binary phase diagram of Co-C system [14]

### Co-Cr system

The Co-Cr binary phase diagram is illustrated on Figure 1.20a. The maximal concentration of chromium in the  $\gamma$ -cobalt is about 38% for the eutectic temperature of 1400°C. The addition of chromium increases the temperature of the martensitic transformation from the FCC  $\gamma$ -cobalt to the HCP  $\epsilon$ -cobalt. Therefore chromium addition is promoting the formation of  $\epsilon$  martensite. The solubility of chromium remains stable until 960°C, and then drops until  $< 20\%$  below 800°C [53]. Cobalt-rich BCC chromium phase undergo a congruent transformation at 1280°C and 58% weight Cr to form the intermetallic Co-Cr  $\sigma$ -phase. The metastable intermetallic  $\text{Co}_3\text{Cr}$  can also form during the cooling [14].

### Co-Ni system

As illustrated on the phase diagram of the Figure 1.20b, nickel forms a solid-solution with  $\gamma$ -cobalt for temperature above 400°C. For lower temperature and nickel concentration below 30% weight, cobalt undergo martensitic transformation and coexists with a nickel-rich phase. Nickel reduces the transition temperature of the martensitic transformation. This transition temperature is below room temperature for nickel content above 30% weight, leading to a single phase  $\gamma$  cobalt alloy.



## Co-W system

The Co-W binary diagram is illustrated in Figure 1.20c. Cobalt forms an eutectic with tungsten at 1480°C for a concentration of 40% weight tungsten. Solubility of tungsten drops from 40% to 30% weight at 1050°C. Tungsten addition increases the transition temperature of the martensitic transformation. The solid solution is in equilibrium with the intermetallic phase  $\text{Co}_3\text{W}$  for temperatures lower than 1100°C.

## Co-Mo system

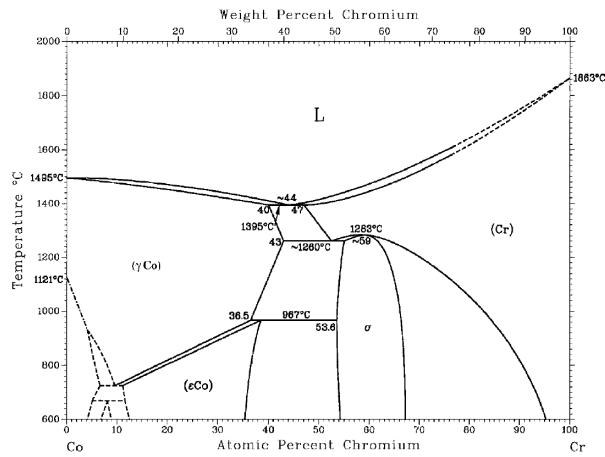
The Mo-Co phase diagram illustrated on Figure 1.20d presents some similitude with the Co-W diagram. Cobalt forms an eutectic with molybdenum at 1335°C for a concentration of 40% weight molybdenum. Just as the Co-W system, the addition of molybdenum increases the transition temperature of the martensitic transformation, from 417°C for pure cobalt to about 1000°C after addition of 15% weight molybdenum. The K intermetallic phase  $\text{Co}_3\text{Mo}$  is in equilibrium with the  $\epsilon$  solid solution below 1000°C.

Additional binary diagrams for the Cr-W, Cr-Mo and Ni-W are displayed in the Appendix 1 (page 185). Ternary diagrams of the systems Co-Cr-Mo, Co-Cr-W and Co-Ni-W were established by Gupta et al. [55, 54, 56], and the Co-Cr-Ni was established by Zhmurko et al. [57]. The ternary phase diagrams are illustrated in the Annex 1, Figure 2 (page 186).

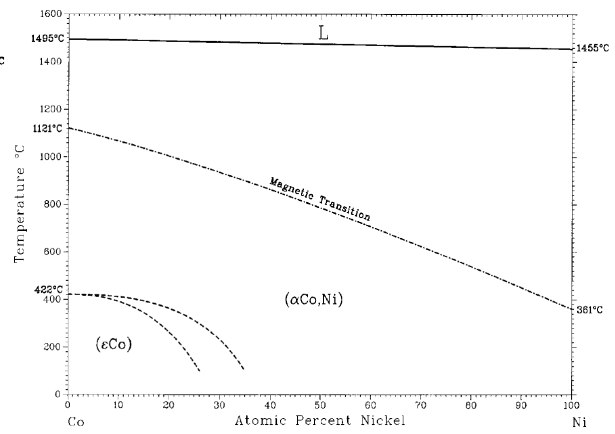
## Microstructure of some usual cobalt superalloys

Figure 1.21a shows the microstructure of the alloy MP35N (Co-35Ni-20Cr-10Mo) with a grain size of 38  $\mu\text{m}$ . The microstructure exhibit a large number of annealing twins, typical of low stacking-fault energy materials [58]. Figure 1.21b illustrates the microstructure of the alloy M64BC containing 0.16N (Co-28Cr-6Mo, so called CCM) after hot swaging. The grain size is about 80  $\mu\text{m}$ , and the material is a single-phase FCC alloy with many annealing twins. The addition of nitrogen prevents the formation of  $\epsilon$  martensite during the cooling process [59]. Figure 1.21c illustrates the microstructure of M64BC with 0.06% weight carbon by optical microscopy [60]. The sample was etched with 20 ml 37 vol.% HCl and 1 ml 30%  $\text{H}_2\text{O}_2$ . The microstructure includes interdendritic primary  $\text{M}_{23}\text{C}_6$  carbides. The formation of these precipitates depends on the initial carbon content in the alloy and of the thermal processing.

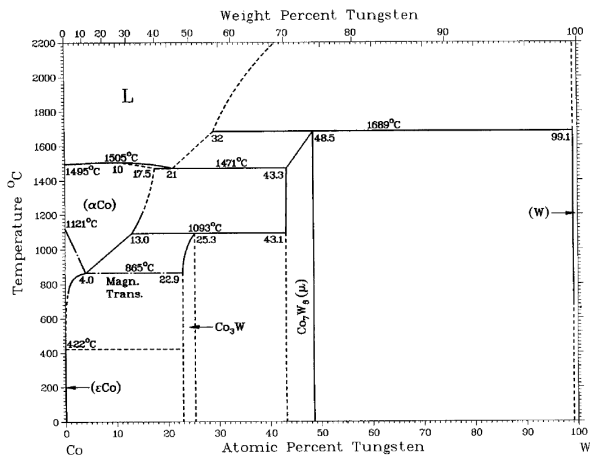




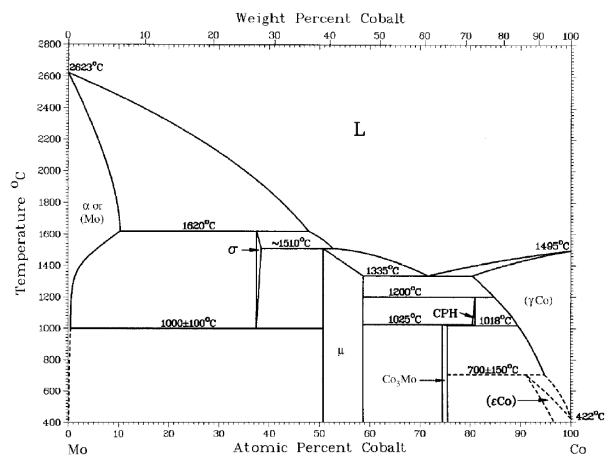
(a) Phase diagram of the Co-Cr system [54]



(b) Phase diagram of the Co-Ni system [55]

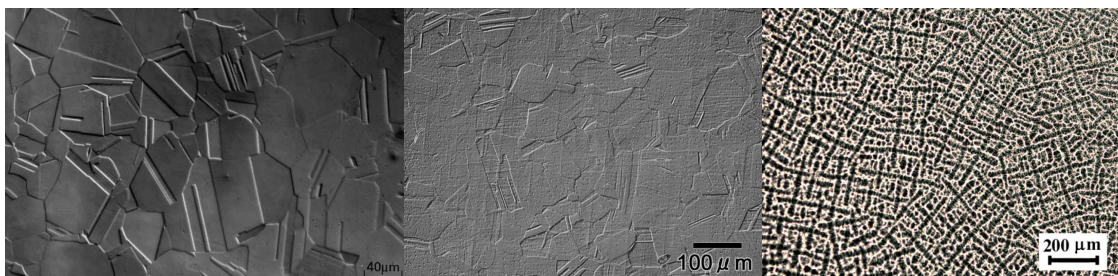


(c) Phase diagram of the Co-W system [56]



(d) Phase diagram of the Mo-Co system [54]

Figure 1.20: Phase diagrams of 1.20a Co-Cr, 1.20b Co-Ni, 1.20c Co-W and 1.20d Mo-Co systems



(a) Microstructure of MP35N [58]

(b) Microstructure of CCM [59]

(c) Microstructure of etched CCM [60]

Figure 1.21: Microstructure of MP35N and M64BC by optical microscopy



### 1.2.1.2 Stacking fault energy of cobalt alloys

Stacking faults are defined as the area lying between two or more Shockley partial dislocations. Partial dislocations are created by the dissociation of a perfect dislocation following the dislocation reaction (Equation 1.1):

$$\vec{b}_1 \rightarrow \vec{b}_2 + \vec{b}_3 + \dots + \vec{b}_n \quad (1.1)$$

where  $\vec{b}_1$  is the initial Burgers vector of the perfect dislocation and  $\vec{b}_2$  to  $\vec{b}_n$  correspond to the partial dislocations created. The stacking fault is a few atoms layer of misfit order with the surrounding matrix. Figure 1.22 [15] illustrates the stacking sequence of close packed [111] planes in the case of a FCC crystal. The normal stacking is a succession of planes A/B/C/A/B/C... The occurrence of a stacking fault in the stacking structure by two partial dislocations, represented in Figure 1.22b, lead to a local lack of the B plane between the two partial dislocations, forming an HCP structured layer with a two atomic planes thickness. Such a stacking fault is called intrinsic fault and constitutes the embryo for the nucleation of HCP martensite in FCC materials. The succession of two stacking faults is represented in Figure 1.22c: the two stacking faults create a local twin organization B/C/A/C/B with a two atomic planes thickness. This defect is called an extrinsic defect and is the nucleus for twinning on FCC metals [15]. The formation of a intrinsic stacking fault can be expressed following

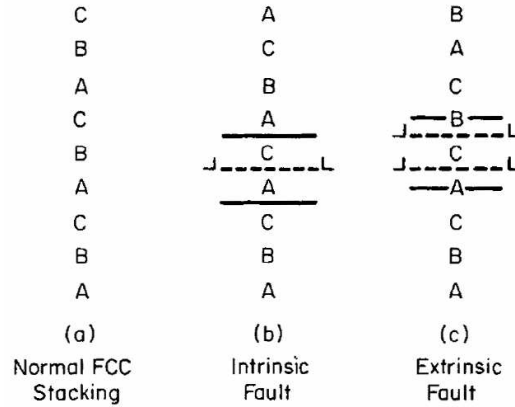


Figure 1.22: Stacking sequence of close packed planes in FCC stacking fault structures [15]

the classic nucleation theory. The formation of the stacking fault is driven by the chemical free energy difference  $\Delta G^{\text{FCC} \rightarrow \text{HCP}}$  between the FCC and the HCP phase, the strain energy  $\Delta E$  and the surface energy  $\sigma$  of the default. The strain energy is very low, about 0.1% of the total fault energy [15], and can be neglected. Therefore, the expression to calculate the stacking fault energy of a two atomic planes thick intrinsic fault is:

$$\gamma = 2\rho\Delta G + 2\sigma \quad (1.2)$$



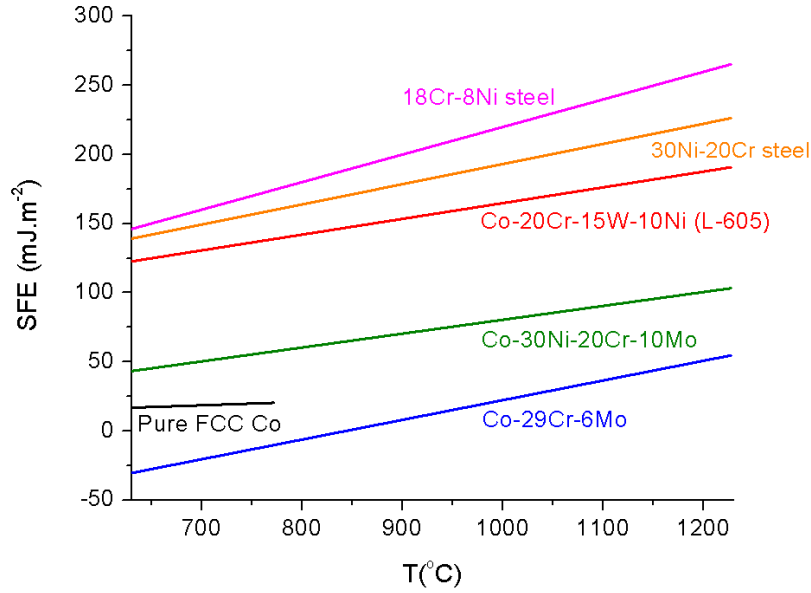


Figure 1.23: Dependence of the SFE of cobalt superalloys and steels with temperature calculated from thermodynamics modeling [16], and SFE of pure cobalt from experimental observations [17]

where  $\gamma$  is the stacking fault energy,  $\Delta G$  is the Gibbs free energy difference between the two phases,  $\sigma$  the interface energy and  $\rho$  the atomic density of 111 planes per mole. The surface energy  $\sigma$  is assumed to be about  $2\sigma=15\text{mJ.m}^{-2}$ , which is the value usually found for transition metals [61, 62, 63]. The atomic density  $\rho$  is expressed by the Equation 1.3:

$$\rho = \frac{4}{\sqrt{3}a^2N} \quad (1.3)$$

with  $a$  is the lattice parameter and  $N$  is the Avogadro constant.

The stacking fault energy (noted SFE) was estimated by Yamanaka, Chiba et al. [16] using the above equations. The Gibbs free energy of the martensitic transformation was estimated by thermodynamics simulations with the Thermocalc software (database Fe ver.6). The results are displayed on the Figure 1.23 for different cobalt alloys and steels. The stacking fault energy of pure cobalt was determined experimentally from the observation of dislocation nodes by Ericsson et al. [17], the data is reported on the Figure 1.23 (black line). It can be concluded that the stacking fault energy (SFE) of cobalt alloys is quite low compared to usual metals. SFE of Co-29Cr-6Mo is only about  $36\text{ mJ.m}^{-2}$  at  $1100^\circ\text{C}$ , while it is six times higher for stainless steels, with a SFE between 200 and  $250\text{ mJ.m}^{-2}$ .

For low stress dislocation tangles are predominant and stacking fault width is very low. When stress overcomes a critical level ( $> 600\text{MPa}$  for 316 steel), large stacking faults and large twin bands become predominant[63]. The forces applied on the partial dislocations determine the stacking fault width at the equilibrium. In a FCC metal, the perfect dislocations with a Burgers vector  $\frac{a}{2}[\bar{1}\bar{1}0]$



dissociates on the (111) plane into  $\frac{a}{6}[2\bar{1}\bar{1}]$  and  $\frac{a}{6}[1\bar{2}1]$  Shockley partial dislocations, as illustrated on the Figure 1.24a. The forces exerted on the two partial dislocations delineating the stacking fault are:

- The forces exerted by the external stress fields of the partial dislocations (Peach-Koehler)
- The interaction forces between these stress fields
- The attractive forces exerted by the stacking fault, pulling closer the partial dislocations
- Resistance forces impeding the movement of the dislocations

The equilibrium between the above forces is reached for a stacking fault width following the expression below [63]:

$$\frac{Gb_p^2}{\pi(2\gamma_{SF} - \tau b_p |\sin(\theta_2) - \sin(\theta_1)|)} \left( \cos(\theta_1)\cos(\theta_2) + \frac{\sin(\theta_1)\sin(\theta_2)}{1 - \nu} \right) \quad (1.4)$$

with  $G$  the shear modulus,  $b_p$  the Burgers vector modulus of the partial dislocations,  $\tau$  the shear stress,  $\theta_1$  and  $\theta_2$  the angles of the Burgers vectors of partial dislocations with the line vector of the complete dislocation (Figure 1.24a), and  $\nu$  the Poisson ratio [63, 16]. The calculation was carried out in the case of an initial complete dislocation in the Co-29Cr-6Mo alloy by Yamanaka et al. The result is reported on the Figure 1.24b. The stacking fault width is found to increase with the applied shear stress. After a critical value of stress, the stacking fault width diverges to very large length. The critical stress value increases with increasing temperature and decreasing stacking fault energy [16].

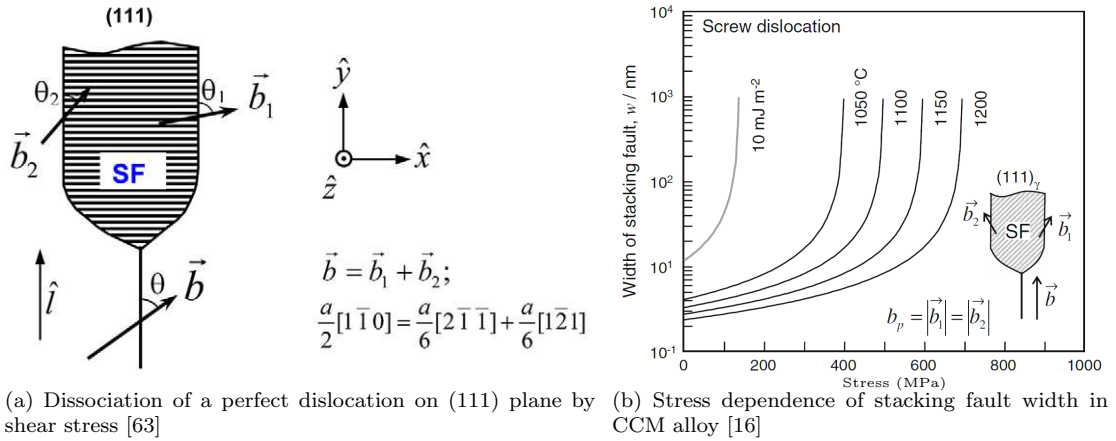


Figure 1.24: Calculation of the stacking fault width evolution with shear stress



### 1.2.1.3 Martensitic transformation

Pure cobalt metal undergo a martensitic transformation at 417°C: structure is HCP below this temperature, and FCC above. The transformation temperatures are: martensite start (MS) 388°C, austenite start (AS) 431°C and equilibrium temperature 417°C. This transformation is sluggish, and some metastable FCC phase can be preserved during the cooling process. The FCC phase presents better ductility and work-hardening strengthening capability than the HCP phase. Therefore cobalt alloys often contain elements stabilizing the FCC phase by lowering the martensitic transformation temperature, so the transformation becomes even more sluggish and do not occur [52]. The Figure 1.25 illustrates the effect of the addition of 1% of different alloying elements on the FCC→HCP transformation [64]. Also the solubility limit for the corresponding alloying elements in FCC cobalt is displayed on the ordinate. In one hand the following additional elements are favourable to FCC phase formation: Ni, Fe, C, Mn, Ti. In the other hand, addition elements such as Cr, Mo, W, Si tend to stabilize the HCP structure. Nickel is a very efficient element for stabilizing the FCC phase, and in spite of the addition of elements favorizing the HCP phase (Cr, W, Mo), the FCC phase can be generally retained. For instance, L-605 alloy is FCC ordered thanks to the addition of 10% nickel, and in spite of large fractions of Cr and W. The Co-Cr-Mo contains HCP promoting alloying elements, and develop more easily martensite during cooling. In the case of Co-Cr-Mo, the martensitic transformation of the metastable FCC phase can be also stimulated by plastic deformation: the phenomenon is so-called strain-induced martensitic transformation (SIMT). This phenomenon can occur during the deformation of cobalt superalloys, and play a role on the initiation of cracks in CCM [65].

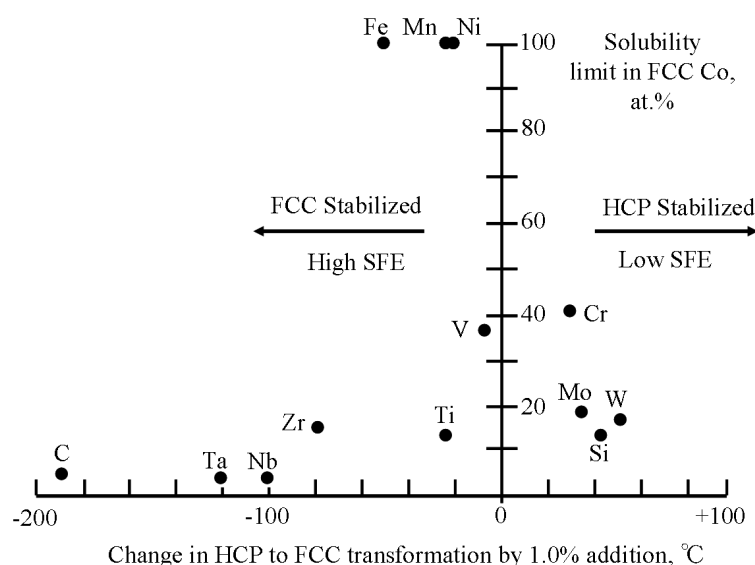


Figure 1.25: Effect of alloying elements on the FCC→HCP transformation temperature as a function of solubility in FCC cobalt



#### 1.2.1.4 Precipitation in cobalt alloys

##### Carbides

Carbides commonly forms in cobalt alloys during the cooling process or after aging treatment. The most common carbide formed is  $M_{23}C_6$ . This carbide forms very frequently in cobalt alloys with chromium concentration above 5%.  $M_{23}C_6$  is formed by the direct precipitation of carbon included in the alloy, but can also be formed by the degeneration of the MC carbides [52]. The  $M_{23}C_6$  carbides usually contain a high concentration of chromium, and have a cubic structure similar to the  $\sigma$  phase.  $M_{23}C_6$  can have beneficial effect on strength, but a large amount may affect also the ductility.  $M_6C$  is another carbide forming mainly in alloys with high Cr and C content, for conditions where  $M_{23}C_6$  is less expected. It is also usually met for a molybden or tungsten content above 6-8% weight.  $M_6C$  carbides can form from the decomposition of MC carbides and reaction with the surrounding matrix. Therefore,  $M_6C$  is often present at the vicinity of MC carbides. The MC carbides are formed mainly with Ta, Nb, Zr, Ti alloying elements, and has a very strong strengthening effect.  $M_3C_2$  and  $M_7C_3$  are less common carbides and form in alloys with low Cr and carbon content.

##### TCP and laves phases

Topologically close-packed (TCP) intermetallics phases are blocky or plate-like phases in cobalt alloys. These phases are nearly always detrimental to the mechanical properties. These compounds include the phases named  $\sigma$ ,  $\mu$ , R and  $\pi$ . When the alloying elements reach their solubility limit, the phase  $\sigma$  is usually formed.  $\sigma$  phase follows a body-centred-tetragonal structure, and has a very variable composition depending on the alloy. The  $\mu$  phase can also be formed, and follows a chemical formula of the type  $A_7B_6$ . The electron compound R and the semi-carbide  $\pi$  phase can also occasionally be met in cobalt alloys. Laves phases are size compounds with a composition  $AB_2$ , and has a negative effect on the mechanical properties similar to TCP phases. This phase is frequently met in the case of the L-605 alloy, and causes a severe loss of ductility for high-temperature applications [52].

#### 1.2.1.5 Effect of grain refinement on mechanical properties

Grain refinement can occur during the high-temperature forging process [66, 16]. Microstructure with small grain sizes can also be achieved by sintering process of fine powders [67]. Grain refinement usually strengthens the material by the creation of grain boundaries that refrain dislocations motion. Grain refinement is the main way to increase the strength of L-605 without affecting significantly the ductility. The increase of strength by grain refinement is mainly due to the increase of the yield



stress, expressed by the Hall-Petch relationship:

$$\sigma_y = \sigma_0 + \frac{k}{\sqrt{d}} \quad (1.5)$$

The mechanical properties of nanocrystalline pure cobalt were investigated by Karimpoor et al [68], and the tensile curves for different strain rates are displayed on the Figure 1.26. The grain sizes tested were 12nm and 4.8 $\mu$ m, leading to an average yield stress of respectively 970 MPa and 422 MPa. Therefore the k parameter of the Hall-Petch relationship is about  $k=0.063\text{MPa}\cdot\sqrt{m}$ . For nanocrystalline cobalt, the Hall-Petch relationship is reversed, and yield stress decreases with lowering grain size [69].

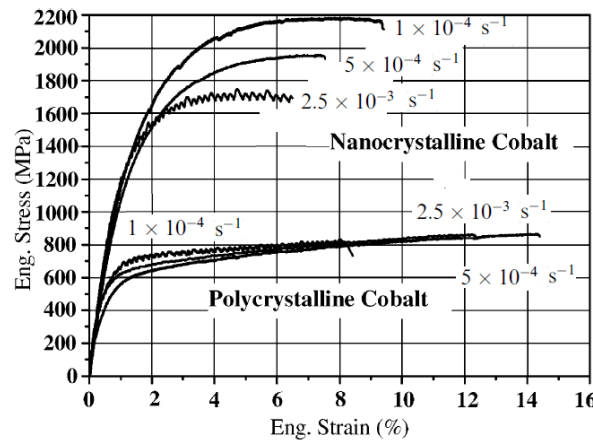


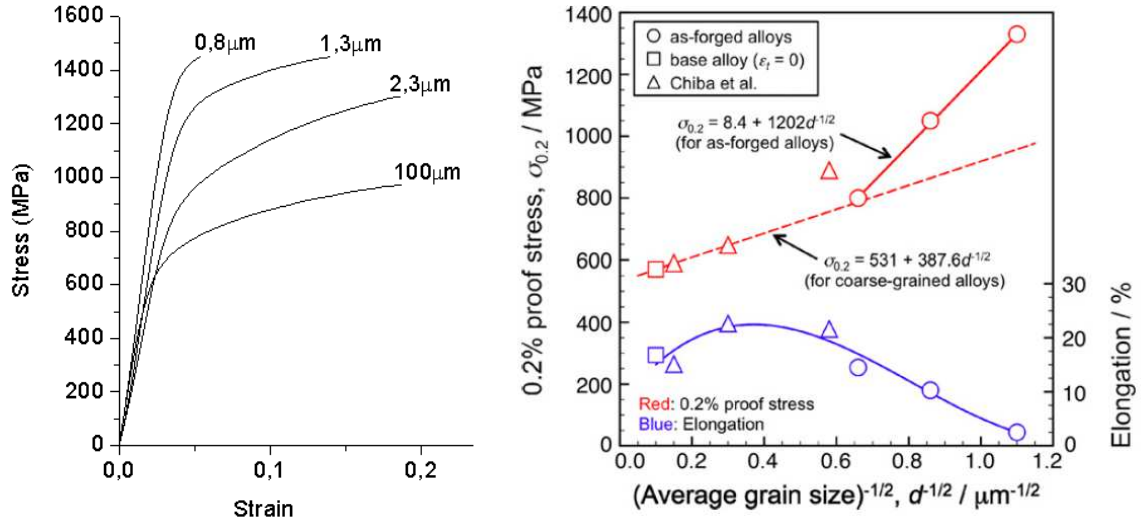
Figure 1.26: stressstrain curves for nanocrystalline cobalt (12nm) and microcrystalline cobalt (4.8 $\mu$ m)

The effect of grain refinement on the mechanical properties of the Co-29Cr-6Mo alloy after hot deformation has been investigated by Yamanaka et al [18], and is reported on the Figures 1.27a and 1.27b. The Hall-Petch relationship is verified for this alloy, as illustrated on the Figure 1.27b. For grain size above 4  $\mu$ m, the coefficient k is 0.39  $\text{MPa}\cdot\sqrt{m}$ , and increases to 1.2  $\text{MPa}\cdot\sqrt{m}$  for sub-micron grain sizes. The grain refinement from 100  $\mu$ m to 5  $\mu$ m leads to an increase of 40% of the maximal deformation. Further grain refinement is detrimental to the ductility: for a refinement until 0.82  $\mu$ m, the deformation is only 20% of its initial value for base metal. This loss of ductility in ultrafine grains materials is usually attributed to a decrease of the strain-hardening rate. However the situation is quite complex for Co-Cr-Mo alloy, and the presence of  $\epsilon$  martensite in this material might be a predominant factor for the evolution of ductility with grain size.

### 1.2.2 Properties of L-605 superalloy

L-605 is a non-magnetic superalloy combining excellent strength at both room and elevated temperature. Moreover it has a good resistance to corrosion and to high temperature oxidation. Therefore it





(a) Tensile curves of forged CCM with different grain size (b) Evolution of yield stress and elongation with grain size

Figure 1.27: Mechanical properties of Co-29Cr-6Mo after hot deformation process [18]

is commonly used in the aerospace industry and for gas turbine engines. Its outstanding mechanical properties and its corrosion resistance make it an attractive material for biomedical applications as well.

#### 1.2.2.1 Microstructure and mechanical properties

The microstructure of L-605 superalloy is constituted of a single FCC  $\gamma$  phase with alloying elements in solid solution. This superalloy forms very easily  $\Sigma 3$  annealing twins, especially in coarse microstructures. Some example of microstructure observations by optical microscopy (OM) are illustrated on the Figure 1.28. The annealed microstructure does not form HCP  $\epsilon$  martensite during the cooling process due to the presence of nickel stabilizing the FCC  $\gamma$  phase. However a small fraction of the material can undergo the martensitic transformation during the room-temperature plastic deformation. This process is so-called the stress induced martensitic transformation (SIMT), and was extensively studied in the case of cobalt alloys by Lee et al. [65]. Some laves phases and carbides can form during annealing treatments or cooling, and their formation conditions are listed thereafter (page 32). Commercially available material usually has a grain size between 50 and 100  $\mu\text{m}$ . It is usually constituted of the FCC phase only, without precipitated phases. The production process used in Carpenter is illustrated in Figure 1.29. The commercial homogeneous microstructure is obtained by plastic deformation at high temperature, followed by a solution treatment above 1200°C to erase precipitates and undesired phases, and finally a high-temperature deformation process to give the final shape to the product.



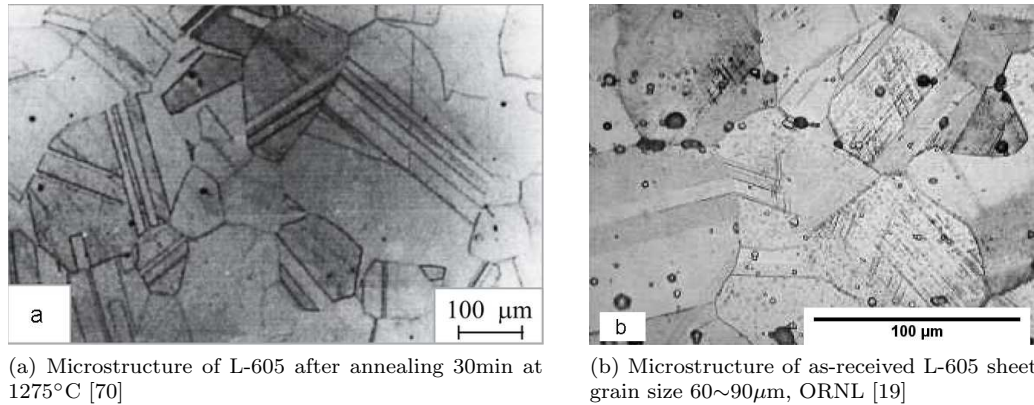


Figure 1.28: Microstructure of L-605 superalloy after annealing



Figure 1.29: Processing of long products made of L-605 alloy in Carpenter ©

The mechanical properties of L-605 alloy were investigated at room and high temperature by Shingledecker et al. (ORNL Laboratory). The tensile curve of the base alloy corresponding to the microstructure of Figure 1.28b is illustrated on Figure 1.30 [19] (black line). The ultimate tensile stress is about 1 GPa and the maximal deformation is up to 60%. For comparison, the tensile curve for the same material after annealing at 675°C during 6000h is illustrated on the same figure (red line). The annealing treatment leads to a significant increase of flow stress, while the maximal deformation plummets to 8%. This change on the mechanical properties is due to the occurrence of precipitation during the annealing treatment, and will be detailed on the next step. The evolution of Young modulus and shear modulus with temperature were determined by resonant ultrasound spectroscopy [19]. The Young modulus and shear modulus decrease linearly with temperature, while Poisson's ratio increase slightly from 0.2 at room temperature to 0.3 at high temperature (Figure 1.30b).

### 1.2.2.2 Precipitation behavior

The binary diagram L-605-C was simulated by Thermocalc software using the Ni7 database (2009). Phase diagram is illustrated on Figure 1.31. Laves phases are predicted to be formed during aging treatment below 700°C, and carbides formation is expected between 700°C and 1100°C. For temperature above 1100°C precipitates are dissolved, and the material becomes a single FCC phase.

Two main FCC carbides are present in Co-20Cr-15W-10Ni alloy: the first is  $M_6C$  and the second is  $M_{23}C_6$  [71, 72], where M is one or several of the metallic elements of the alloy. Hexagonal  $M_7C_3$



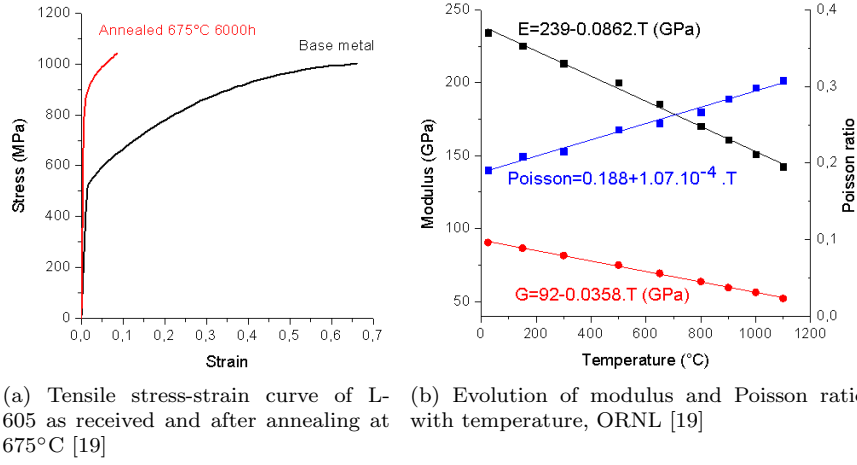


Figure 1.30: Mechanical properties of L-605 at room and high temperature

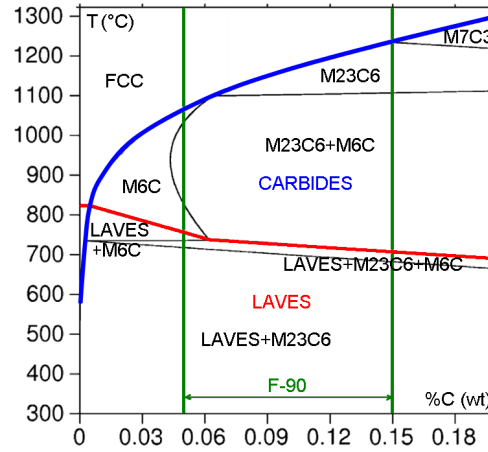


Figure 1.31: Phase diagram of L-605 alloy with variable carbon content (Thermocalc with database Ni7)

carbide can also be found in this alloy (Yukawa and Sato [71]).  $M_7C_3$  is a transitional phase appearing at the earlier stage of aging on grain boundaries, and disappearing for long ageing treatments.  $M_{23}C_6$  occurs in the early stage of aging, and succeeds to  $M_7C_3$ . It appears as spheroidal particles, first on grain boundaries and then within matrix for longer ageing treatment.  $M_{23}C_6$  is coplanar to the matrix: the  $\{111\}$  planes of this carbide are parallel to those of the matrix [71]. For long aging time, plate-like shaped  $M_6C$  succeeds to  $M_{23}C_6$  within grains. For temperatures upper to 1000°C,  $M_6C$  can precipitate directly within the matrix, without involving the formation of transitional  $M_{23}C_6$ .

The most common intermetallics compound is the  $Co_2W$  phase, with a hexagonal  $C_{14}$  Laves structure ( $a=0.473$  nm,  $c=0.770$  nm,  $c/a=1.63$ ) [42].  $Co_2W$  succeeds to  $M_6C$ , and form some platelets at grain boundaries. For long aging time they coagulate to large intergranular precipitates. This phase was detected by Wlodek [72] in grain boundaries, and was identified as the main em-



brittling process in L-605 alloy. Yukawa and Sato [71] confirmed the occurrence of  $\text{Co}_2\text{W}$ , and they also found three other  $\text{Co}_x\text{W}_y$  phases by TEM: a transitional  $\alpha\text{-Co}_3\text{W}$  with  $\text{L}_{12}$  fcc structure; which transforms to  $\beta\text{-Co}_3\text{W}$ , a  $\text{D0}_{19}$  hexagonal phase. A plate-like shaped  $\mu\text{-Co}_7\text{W}_6$  phase was also detected after prolonged ageing treatment. The phases  $\alpha$  and  $\beta\text{-Co}_3\text{W}$  are both coherent with the matrix, and  $\beta\text{-Co}_3\text{W}$  occurs preferentially on the  $\epsilon$ -phase (HCP) and on stacking faults.

Yukawa and Sato [71] investigated the formation of intermetallics and carbides at different temperatures and aging time, and summed up the results into a Time-Temperature-Precipitation (TTP) diagram. Additional experiments were conducted by Shingledecker et al., and the resulting TTP diagram is illustrated on Figure 1.32.

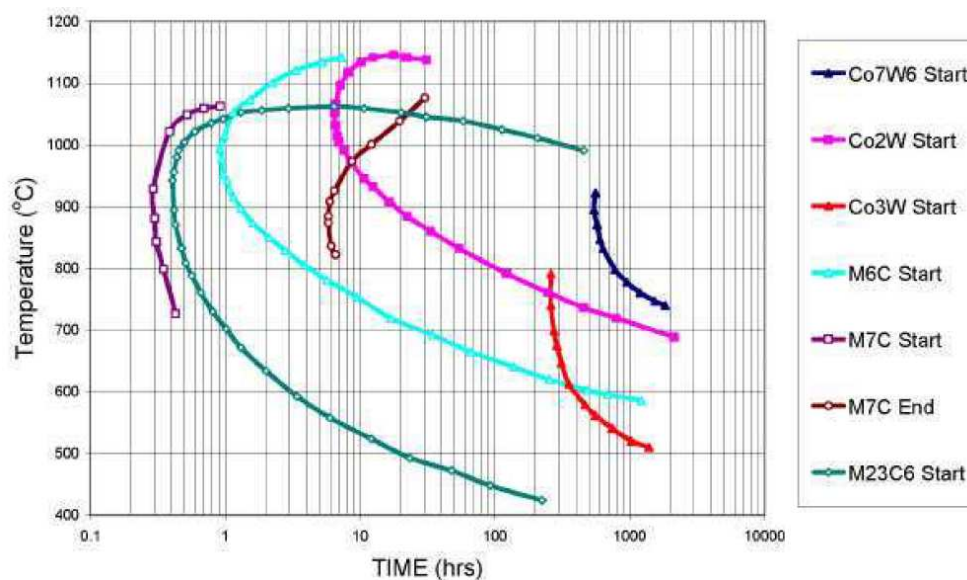


Figure 1.32: Time-Temperature-Precipitation diagram of L-605 from ORNL data (2007) [19]

The occurrence of precipitation at earlier and later stages of aging treatment is responsible of the age-hardening phenomenon in L-605 alloy. The maximum hardening occurs at nearly 900°C, and induces a significant loss of ductility. The tensile curve of the Figure 1.30a is a characteristic example of hardening and embrittlement by precipitation. After annealing 6000h at 675°C, carbide phases such as  $\text{M}_{23}\text{C}_6$  or  $\text{M}_6\text{C}$  and laves phases are formed. These precipitates contribute to the age-hardening and embrittle the material. To conclude, precipitates are easy to form in L-605 alloy and can lead to age-hardening which is of great interest industrially for the production of hard materials. The downside of precipitation is a dramatical loss of ductility, which can lead to the premature rupture of the material. Therefore the amount and the morphology of precipitates is a key point for obtaining the adapted mechanical properties.



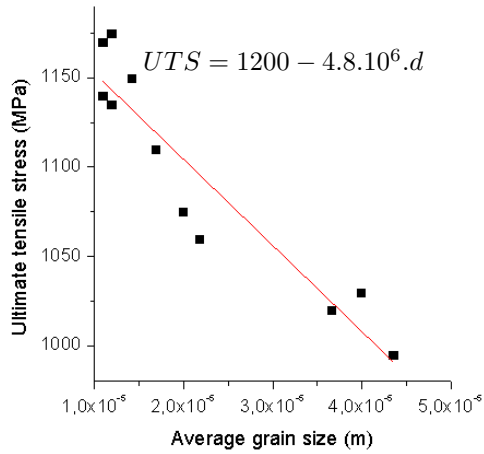
### 1.2.2.3 Effect of grain refinement on mechanical properties

The effect of grain size on the mechanical properties was investigated by Haynes International and by Gupta et al. [70]. The Haynes 25 datasheet includes a significant data set on the mechanical properties of recrystallized L-605 alloy with different grain sizes. Results are summarized on the Figure 1.33. Yield stress increases with the refinement of the microstructure, as expected by the Hall-Petch law (Figure 1.33c). The coefficient  $k$  of the Hall-Petch law is  $k=1 \text{ MPa}\sqrt{\text{m}}$ . Both Ultimate Tensile Stress (UTS) (Figure 1.33a) and Rockwell hardness (Figure 1.33d) increase with decreasing grain size. UTS increases of 15% when the grain size is divided by 4. The UTS is upper to the stents requirement of 900MPa (Cf. specifications page 6) for a grain size smaller than  $50\mu\text{m}$ . The grain refinement is detrimental to the elongation, as illustrated on the Figure 1.33b: elongation decreases of 30% with dividing the grain size by 4. The elongation is expected to decrease below the limit of 40% required for stents for a grain size smaller than  $10\mu\text{m}$ . As a consequence, the grain size should be within the range  $10\text{-}50\mu\text{m}$  to fulfill the mechanical properties requirements for stents application.

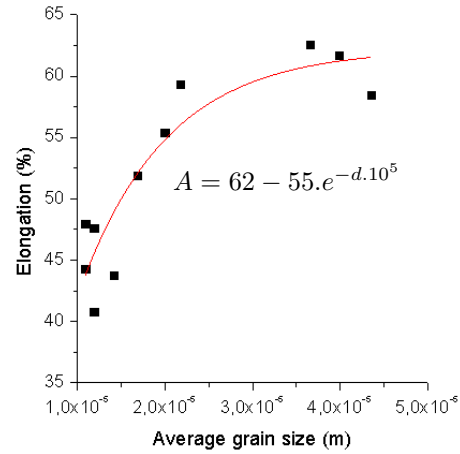
### Conclusion

L-605 superalloy is constituted of a single FCC phase with alloying elements in solid solution. Some intermetallics phases and carbides can precipitate during annealing treatment in the temperature range  $600\text{-}1100^\circ\text{C}$  after several hours. Precipitation is not expected during for less than 1 hour annealing for any temperature. Precipitation hardens and embrittles the material, therefore this phenomenon is detrimental on the targeted mechanical properties and should be avoided for stent application. As in usual metals, grain refinement in cobalt alloys leads to strengthening and reduces the ductility after a certain level, while coarsening improves ductility at the expense of tensile strength. In the case of L-605 alloy, grain size must be small enough to ensure sufficient strength, but should not be lower than  $10\mu\text{m}$  to keep sufficient ductility. The previous results were established in the case of a single mode grain size distribution. Tailoring the grain size distribution could lead to further improvement on mechanical properties, by combining small and large grains in a same microstructure. The grain size distribution can be controlled by the recrystallization process during hot deformation process. The following part will indicate the mechanisms of plasticity and recrystallization, and their effect on the grain size. From the study of recrystallization mechanisms, it is possible in a second step to determine the deformation conditions to achieve the desired grain size distribution.

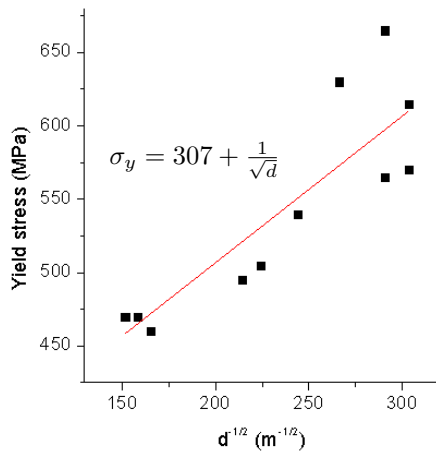




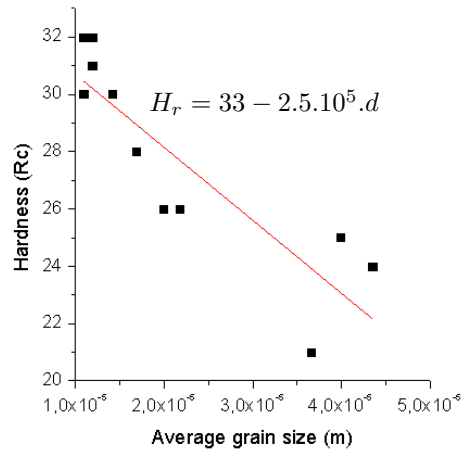
(a) Evolution of ultimate tensile stress (MPa) with grain size



(b) Evolution of elongation with grain size



(c) Evolution of yield stress (MPa) with grain size



(d) Evolution of Rockwell hardness with grain size

Figure 1.33: Dependence of mechanical properties of L-605 with grain size, data from Haynes 25 datasheet



## 1.3 Physics of high-temperature plasticity

Mechanical behavior of metals and alloys depends entirely on their metallurgical structure. The main structural elements affecting the mechanical properties are grain size and dislocation structure. Grain size can affect the yield stress through the Hall-Petch law previously mentioned (page 30). Dislocation structure necessarily changes during the plastic deformation, as dislocations motion is the origin of deformation. This change affects the mechanical behaviour of the material during its deformation and leads to strain-hardening. The relationship between the microscopic dislocation structure and the macroscopic mechanical behaviour will be detailed further in this section.

### 1.3.1 Mechanical behavior of metals at high temperature

The stress  $\sigma$  resulting of deformation is usually separated into an elastic part  $\sigma_y$  depending on grain size (Hall-Petch relationship) and a plastic part  $\sigma_p$ , also called flow stress, depending on the dislocation structure. The flow stress depends on the deformation temperature  $T$  and strain rate  $\dot{\epsilon}$ : for usual metals and alloys flow stress decreases with temperature and increases with strain-rate, in accordance with the visco-plastic materials behaviour. The equivalence of temperature and strain rate on the material mechanical behaviour is gathered into a single parameter, so-called the Zener-Hollomon parameter  $Z$ :

$$Z = \dot{\epsilon} \cdot \exp\left(\frac{Q}{RT}\right) \quad (1.6)$$

where  $Q$  is an apparent activation energy. The Zener-Hollomon parameter is linked up to the flow stress by the following empirical relationship [31]:

$$Z = c_1 \cdot \sinh(c_2 \cdot \sigma)^n \quad (1.7)$$

where  $c_1, c_2$  and  $n$  are constants. For low stress values, the equation 1.7 is reduced to a power law with  $Z$  parameter:

$$\sigma = c_3 \cdot \dot{\epsilon}^m \cdot \exp\left(\frac{Q_1}{RT}\right) \quad (1.8)$$

with  $c_3, Q_1$  and  $m$  are constants. This relationship is equivalent to a power law dependence of flow stress with strain rate and a dependence with temperature following an Arrhenius law.

### 1.3.2 Dynamic materials model and thermodynamics of plasticity

Dynamic Materials Model (DMM) is a thermodynamic approach based on energetic considerations. This model captures microstructural information from the evaluation of the energy dissipated or stored in the material [73]. The few assumptions concerning the metal at a microscopic make this model easy to handle. The final results draw up the average flow behaviour of the material at a macroscopic scale.



The DMM model considers the worked sample as an energy dissipator, receiving a mechanical energy which is totally dissipated in the form of heat and metallurgical processes. The total power received, noted P, is split into two parts J and G [20] (Figure 1.34):

$$P = \sigma \dot{\epsilon} = \int_0^{\dot{\epsilon}} \sigma d\dot{\epsilon} + \int_0^{\sigma} \dot{\epsilon} d\sigma = G + J \quad (1.9)$$

where G is the energy dissipated by plastic deformation, and J is the one and dissipated by metallurgical mechanisms. If flow stress evolves with strain rate following a power law (i.e. the equation 1.8 is holding), the strain rate sensitivity m is equal to the ratio between J and G:

$$m = \frac{d \ln \sigma}{d \ln \dot{\epsilon}} = \left( \frac{\partial J}{\partial G} \right)_{T, \epsilon} \quad (1.10)$$

By integration of J from the equations 1.10 and 1.8, one obtains the following expression for J:

$$J = \frac{\sigma \dot{\epsilon} m}{m + 1} \quad (1.11)$$

The maximal value of J is  $J_{max} = (\sigma \dot{\epsilon})/2$ , in this case m=1 and J=G=P/2. The minimal value is J=0 and occurs when m=0. During deformation process, power dissipation is placed between these two extremes. The evolution of J with plastic flow can be visualized by the ratio of J and  $J_{max}$ , also called the efficiency of dissipation  $\eta$  [20, 73, 74, 59]:

$$\eta = \frac{J}{J_{max}} = \frac{2m}{m + 1} \quad (1.12)$$

The efficiency of dissipation represents the ability of the sample to dissipate energy by dynamic metallurgical processes. These processes can be diverse: recovery, recrystallization, dissolution or growth of phases, etc.

Flow instability conditions can be delineated by a flow instability criterion proposed by Ziegler [75] and modified by Prasad et al. [21]. Flow instability is expected when the following instability parameter  $\xi$  becomes negative:

$$\xi = \frac{d \ln \left( \frac{m}{m+1} \right)}{d \ln (\dot{\epsilon})} + m \leq 0 \quad (1.13)$$

The study of deformation processing through *processing maps* [74] consists into the determination and the study of the evolution of  $\eta$  and  $\xi$  versus temperature and  $\dot{\epsilon}$ . These maps could indicate the stable flow conditions and the conditions for the occurrence of dynamic metallurgical processes. An example of processing maps is illustrated in the case of electrolytic tough pitch (ETP) pure copper on Figure 1.35 [76, 77]. The conditions for  $T > 600^\circ\text{C}$  and strain rate  $> 1\text{s}^{-1}$  corresponds to high efficiency of power dissipation, and therefore metallurgical transformations are expected for these conditions. The solid thick line on the left of the map indicates the change of  $\xi$  parameter sign to negative. As a consequence, conditions corresponding to  $T < 300^\circ\text{C}$  should lead to unstable flow. On the other hand, the grain size was found to evolve linearly with Zener-Hollomon parameter [77], which



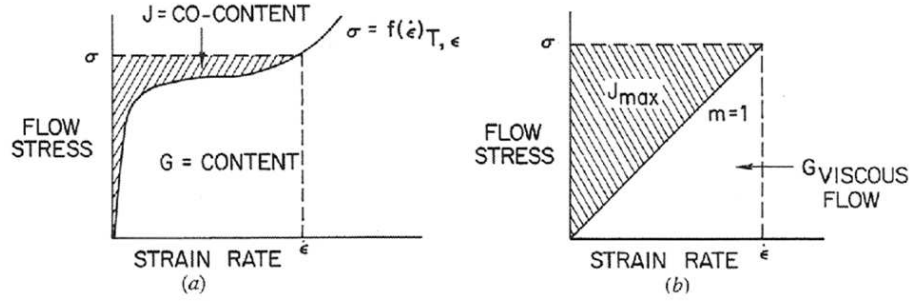


Figure 1.34: Schematic representation of the partition of total power  $P$  into two contributions  $J$  and  $G$  for: (a)  $m < 1$  and (b)  $m=1$  [20]

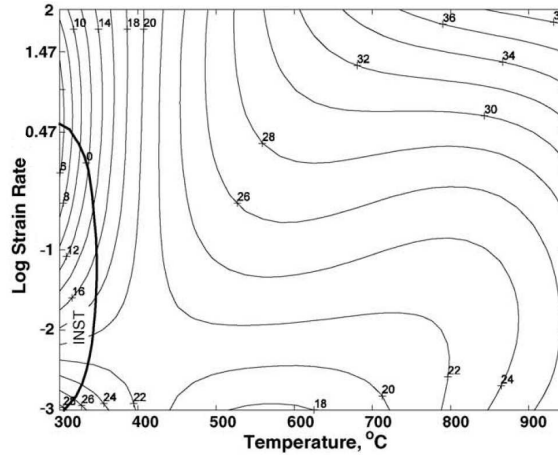


Figure 1.35: Processing map of ETP copper for strain=0.5[21]

indicates that larger grains are obtained for low strain rate and larger temperatures. The iso-value lines for grain size would be straight lines oriented from the bottom-left to the top-right on the map of Figure 1.35. Therefore there is no clear evidence of a relationship between grain size change and  $\eta$ . Moreover the predicted flow instability is usually not supported by experimental observations [21, 76, 77], so the nature of instabilities remains unclear. As a conclusion, processing maps should rather be considered as a macroscopic empirical approach of the deformation of a workpiece. Microstructural considerations deduced from thermodynamic modeling should be discussed carefully [78], and require to be validated by strong experimental evidences.

### 1.3.3 Physics of hardening and recovery mechanisms

Flow stress can be considered in a more physically-based way by considering its relationship with the microstructure and the dislocation structure. The plastic stress is representative of the dislocation density inside the material, and these two variables are linked by the Taylor equation [22, 79]:

$$\sigma = M\alpha\mu b\sqrt{\rho} \quad (1.14)$$



with  $M$  the Taylor factor about 3 for FCC materials with a random orientation [22],  $\alpha$  a constant between 0.1 and 1,  $\mu$  the shear modulus and  $b$  the magnitude of the Burgers vector. This relationship is applicable to cases where the stress is controlled by dislocations-dislocations interactions only, with little regard to their arrangement. During plastic deformation, some dislocations are created and contribute to the strain-hardening, and some dislocations are eliminated by dynamic recovery. The balance between the two contributions is expressed by the general Kocks-Mecking-Estrin equation [25, 22]:

$$\frac{d\rho}{d\epsilon} = k_1\sqrt{\rho} - k_2\rho \quad (1.15)$$

The term  $k_1$  represents the athermal storage of mobile dislocations moving along a mean free path  $\Lambda = \rho^{-1/2}$ . The term  $k_2$  is associated with the rate of dynamic recovery and is depending on temperature and strain rate. The Figure 1.36a illustrates the Taylor relation in the case of pure copper. Combining the equations 1.14 and 1.15 leads to the following evolution of flow stress with strain:

$$\theta = \frac{d\sigma}{d\epsilon} = \theta_0 \left(1 - \frac{\sigma}{\sigma_V}\right) \quad (1.16)$$

$$\text{with } \theta_0 = \frac{M\alpha\mu b k_1}{2}$$

$$\text{and } \sigma_V = \frac{M\alpha\mu b k_1}{k_2}$$

The equation 1.16 is so-called the Voce law [22, 80, 81], corresponding to a linear decrease of the hardening rate  $\theta$  with flow stress. The Figure 1.36b illustrates the approximation of stress-strain curves with the Voce law for pure copper. The normalized initial hardening rate  $\theta_0/\mu$  for  $\epsilon \rightarrow 0$  is supposed to be independent of temperature as it is a function of  $k_1$  only. The saturation stress  $\sigma_V$  is the stress extrapolated for large strain in the case where no softening is occurring, and depends with temperature and strain rate. The Voce equation can be integrated with strain, and the resulting flow stress follows a saturating exponential law:

$$\sigma = \sigma_V \left(1 - e^{\frac{-\epsilon \cdot \theta_0}{\sigma_V}}\right) \quad (1.17)$$

The athermal initial hardening rate  $\theta_0$  and the steady-state stress  $\sigma_V$  can be determined experimentally from the evolution of hardening rate with stress (Figure 1.37a). If the Voce law holds, then hardening rate is proportional to stress and its initial value for  $\sigma \rightarrow 0$  is  $\theta_0$ . The stress  $\sigma_V$  corresponds to the intersection point of the linear extrapolation of hardening rate with the x-axis. The Voce law provides a suitable fit for the initial part of the stress-strain curve (Figure 1.37b [24]). For large strain, some flow softening can occur due to the operation of some microstructure changeovers such as recrystallization or the formation of shear bands. In this case hardening rate drops with increasing strain, and the Voce law is not applicable anymore.



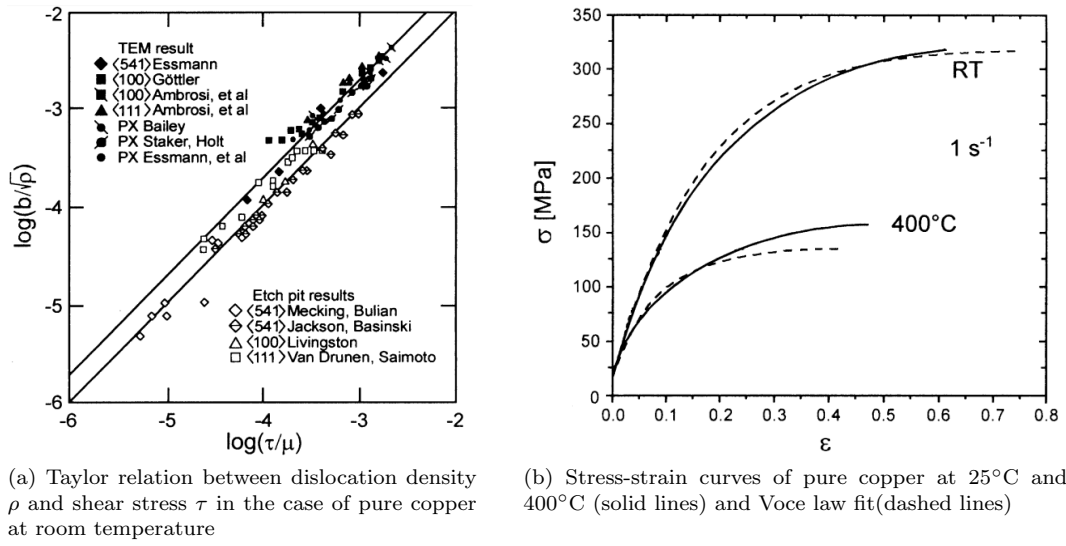


Figure 1.36: Dislocation density and flow stress of pure copper, data from Kocks and Mecking [22, 23]

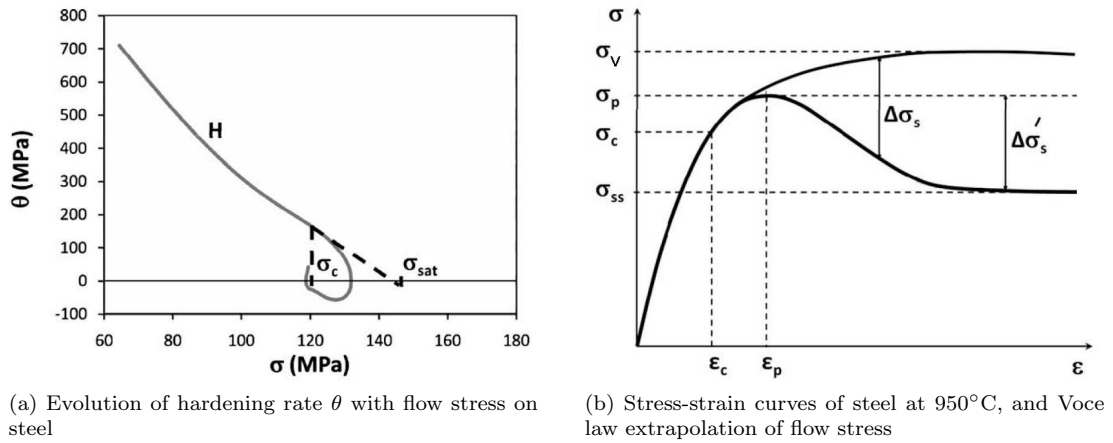


Figure 1.37: Evolution of hardening rate and flow stress of (0.03 C, 0.3 Mn) steel at 950°C strain rate  $1s^{-1}$  [24]

### 1.3.4 A single-parameter based description of work hardening

As indicated on the equations 1.7 and 1.6, flow stress evolves with strain rate following a power law, and with temperature following an Arrhenius law. Kocks and Mecking gathered the contribution of both temperature and strain rate in an adimensional parameter noted  $g$ :

$$g = \frac{kT}{\mu b^3} \cdot \ln\left(\frac{\dot{\epsilon}_0}{\dot{\epsilon}}\right) \quad (1.18)$$

with  $k$  the Boltzmann constant,  $\mu$  the shear modulus and  $\dot{\epsilon}_0$  a floating parameter. Flow stress normalized by shear modulus is found to follow a power law with  $g$  parameter.  $\log(\sigma/\mu)$  is found to be proportional to  $g$  (Figure 1.38), and  $\sqrt{\sigma/\mu}$  is proportional to  $\sqrt{g}$ . By adjusting the parameter



$\dot{\epsilon}_0$  to  $10^7 s^{-1}$ , flow stress can be gathered into a single master curve  $\log \sigma/\mu = f(g)$   $\sqrt{\sigma/\mu} = f(\sqrt{g})$  for a given material.

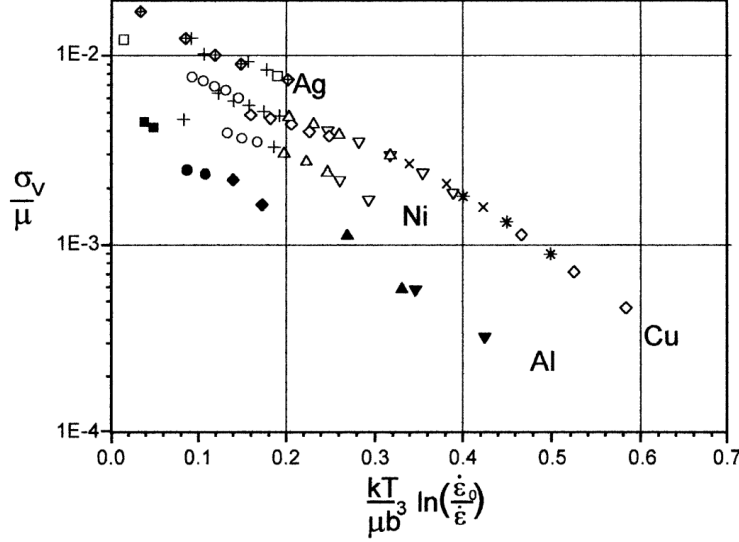


Figure 1.38: Evolution of normalized flow stress with g parameter for different materials [22]

The main feature of the Kocks-Mecking model is to gather all the experimental data into a single master curve representing the evolution of stress with deformation conditions. The g parameter provides a good flexibility for fitting the experimental data over a large range of conditions, and enable comparison between different materials. Therefore, the g parameter is an alternative to the Zener-Hollomon parameter, and is preferable for large data sets due to larger applicability range. The extrapolation of the master curve can provide an estimation of flow stress for any untested deformation conditions.

### 1.3.5 Effect of strain rate on the dislocation structure: the Cottrell-Stokes law

Strain rate dependence with temperature is usually expressed by a phenomenological model following the Arrhenius equation [23]:

$$\dot{\epsilon} = \dot{\epsilon}_0 \cdot \exp\left(-\frac{\Delta G}{RT}\right) \quad (1.19)$$

with  $\Delta G$  the activation energy and  $\dot{\epsilon}_0$  a constant. Kocks and Mecking [22] propose the following dependence of  $\Delta G$  with stress:

$$\Delta G = A \cdot \ln\left(\frac{\dot{\sigma}}{\sigma}\right) \quad (1.20)$$



with  $A$  a material constant and  $\hat{\sigma}$  the stress for a given reference structure of the material ('hardness parameter' [25]). Therefore the Arrhenius equation 1.19 can be re-written in a power law form:

$$s(\dot{\epsilon}, T) = \frac{\sigma}{\hat{\sigma}} = \left( \frac{\dot{\epsilon}}{\dot{\epsilon}_0} \right)^m \quad (1.21)$$

with  $m$  the isostructural strain rate sensitivity at constant dislocation density and constant temperature. The reference stress  $\hat{\sigma}$  is assumed to follow exactly the Taylor equation, however for different conditions (e.g. higher temperature or strain rate), the parameter  $s(\dot{\epsilon}, T)$  quantifies the discrepancy to this law.

The strain rate sensitivity parameter  $m$  can be added on the Taylor equation [25, 82]:

$$\sigma = M\alpha\mu b\sqrt{\rho} \cdot s(\dot{\epsilon}, T) = M\alpha\mu b\sqrt{\rho} \left( \frac{\dot{\epsilon}}{\dot{\epsilon}_0} \right)^m \quad (1.22)$$

with  $m$  the strain-rate sensitivity parameter, and  $\dot{\epsilon}_0$  a reference strain rate. The above dependence is equivalent to the well-known Cottrell-Stokes law [83, 84]: during an increment of strain-rate, if the dislocation structure is assumed to be unchanged, then the increment of stress is proportional to the flow stress:  $\Delta\sigma \propto \sigma$ . By considering the equation 1.22, one can identify the strain rate sensitivity  $m$  as the proportional coefficient between  $d\sigma/d\ln\dot{\epsilon}$  and  $\sigma$ . As a consequence, the Cottrell-Stokes law holds if  $m$  is a constant with deformation. Isostructural strain rate sensitivity is usually neglected, with a magnitude of 0.01 only [85]. The Figure 1.39 illustrates the flow stress change during a strain rate jump for pure copper. Based on the data of Estrin and Mecking [25], Cram, Hutchinson et al. [30] estimated the strain rate sensitivity of pure copper to  $m=0.02$  and the reference strain rate to  $\dot{\epsilon}_0 = 4.5 \cdot 10^{-7} s^{-1}$ .

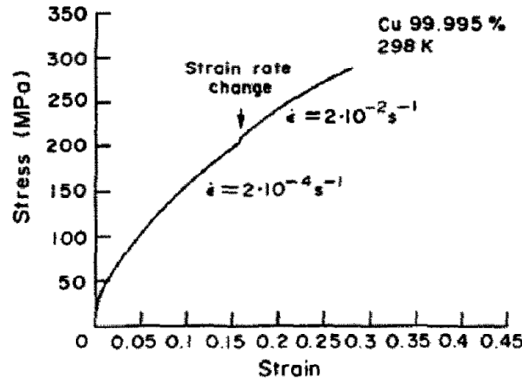


Figure 1.39: Strain rate jump on pure copper for determining  $m$  [25]

### 1.3.6 Plasticity of polycrystals

A challenging point in the study of the deformation behavior of metals is to achieve a simple but realistic description of polycrystalline plasticity. While the previous considerations provide average



information over the material, the local deformation and stress in each single grain is not well known. An early theory was developed in 1928 by Sachs et al., and assumes that all grains undergo the same stress. The Sachs theory, also called low bound theory, considers that each grain can deform independently of its neighbors, and does not ensure the equilibrium across the grain boundaries. This theory is not physically reliable: stress should be larger in harder grains than in softer ones.

A complementary theory is the one developed by Taylor in 1938, and is also called upper bound theory. In this case, all the grains are supposed to undergo the same strain increment. This theory is equivalent to considering a strain rate equal for each grain. However this theory does not ensure strain compatibility between grains, and is not physically realistic: soft grains are expected to deform more than harder ones.

Experimental reality is located somewhere between these two extreme bound theories. To attempt a compromise, iso-work assumption was developed by Bouaziz et al. [86], and applied to polycrystal modelling by Cram et al. [30]. Each grain is assumed to receive a same amount of work equal to the macroscopic work increment. Even if this main assumption is not physically-based, it has the effect to allow soft grains to deform more than hard grains. The isowork model is especially convenient for estimating the strain rate repartition in two-phases alloys. This model makes a suitable compromise between the upper and lower bound theories and provides results close to self-consistent modelling [86, 87].

Self-consistent models consider each grain as an inclusion in an homogeneous matrix, and the interaction between the grain and the matrix is calculated for each grain individually [88]. The method is physically reliable and gives a suitable estimation of the strain rate and stress deviation between the grain and the matrix. On the other hand, this method is quite complex and computationally demanding. Other possible models are the grain neighbour interaction model (LAMEL model [89]), and crystal plasticity finite element models [90].

### 1.3.7 Conclusions

Experimental stress-strain curves can be empirically fitted by the Voce law. The two fitting parameters required are the athermal initial hardening rate  $\theta_0$ , and the steady-state stress  $\sigma_V$  which is temperature and strain rate dependent. Besides a simple exponential fit, the Voce law enables the estimation of hardening and recovery parameters that rule the evolution of dislocation density. The evolution of  $\sigma_V$  with deformation condition can be sum up into a master curve  $\log(\sigma_V/\mu) = f(g)$ , where  $g$  is a single parameter gathering the effect of temperature and strain rate. From this curve, steady-state flow stress can be extrapolated for any deformation condition, and the stress-strain curves can be deduced [22]. Using the Taylor formula [79], or its equivalent modified by Estrin et al. [25], dislocation density evolution can be determined from flow stress. As a consequence, a thorough extraction of informations from experimental data using the Kocks-Mecking-Estrin model



and the Taylor formula enables the prediction of dislocation density evolution with strain for a large range of deformation conditions. The estimated dislocation density constitutes the fundamental basis for further physical modelling to understand microstructural changes during metals plasticity at high-temperature.



## 1.4 High-temperature microstructure evolution and recrystallization process

During thermomechanical processing of metals, the combined action of plastic deformation and temperature affects the whole microstructure through interlocked phenomenons. As mentioned on the previous section, the plastic deformation leads to a change on the dislocation structure by the joint operation of hardening and recovery. On the other hand, due to temperature effect, grain boundaries gain a sufficient mobility to generate grain growth. The energy balance between the grain boundaries surface energy and the stored energy inside grains by dislocation structure constitute the driving force for grain growth, and this driving force is changing with time. Therefore, predictive estimations of the microstructure evolution can be achieved by combining a thermodynamics approach for estimating the driving force evolution, and a kinetics approach dealing with the mobility and speed of grain boundaries. The current section provides the physical basis for understanding and predicting grain size evolution mechanisms during thermomechanical processes.

### 1.4.1 Grain boundary migration

Grain growth is the main phenomenon driving the grain size evolution during annealing treatments. In the case of recrystallization, it can operate jointly with nucleation of new grain so grain refinement can occur as well. During grain growth process, the kinetics law controlling the grain boundary speed is [31, 91]:

$$v = M.P \quad (1.23)$$

with  $v$  the speed of the grain boundary ( $m.s^{-1}$ ) and  $M$  the grain boundary mobility ( $m^4.J^{-1}.s^{-1}$ ).  $P$  is the driving force, and represents the energy change per volume unit of material swept by the grain boundary during its migration ( $J.m^{-3}$ ). The difference between the grain growth mechanisms listed below reside mainly on a different combination of the energy contributions to the driving force  $P$ .

#### 1.4.1.1 Boundary migration in a relaxed material

##### Burke-Turnbull model

In an annealed metal, dislocation density is low ( $\rho \simeq 10^9 m^{-2}$ ) and is quite homogeneous in the material, therefore its contribution to the driving force is negligible compared to boundaries surface energy contribution. As a consequence,  $P$  is assumed to be a function of the energy stored under the form of grain boundaries solely. An early grain growth model developed by Burke and Turnbull [92]



assumes the driving force equal to the Laplace pressure in grains. For spherical grains  $P$  is expressed as:

$$P = \frac{2\gamma}{R} \quad (1.24)$$

with  $\gamma$  the surface energy of grain boundaries and  $R$  the average grain radius. As a consequence the grain boundary speed is proportional to the Laplace pressure  $2\gamma/R$ , weighted by the boundary mobility  $M$  (equation 1.23). This consideration leads to the growth of all the grains, which does not respect the volume conservation. It is well known that during experimental observation, large grains grow and consume smaller grains [31]. It is physically consistent: small grains have larger Laplace pressure than large grains, therefore they are less stable and disappear. Therefore average grain size increases, while total grains number decreases preserving the volume constant.

### Hillert model

A more realistic model has been developed by Hillert et al [91, 93], and estimates the driving force  $P$  as the difference of curvature between the growing grain and surrounding grains:

$$v = M \cdot \gamma \left( \frac{1}{R_c} - \frac{1}{R} \right) \quad (1.25)$$

where  $R_c$  is a critical grain radius delineating the boundary above which grains grow, and below which grains decrease. This critical radius can be identified to the average radius of surrounding grains, and is changing with time. This model enable grains smaller than the average size to decrease, and therefore provides a better agreement with experiment than the previous one.

#### 1.4.1.2 Grain growth during the deformation process

During the hot working process or the annealing of deformed microstructures, some new grains are formed and grow in the material. This phenomenon is called recrystallization. During their migration, grain boundaries sweep out the dislocation structure, and leave behind them a nearly dislocation-free material [94]. The driving force for growth is the difference of dislocation density between the two sides of the migrating grain. As the dislocation density is very high during plastic deformation, the contribution of surface energy on the grain migration is usually neglected [31].

Early grain growth models in the case of recrystallization were developed by Sandstrom and Lagneborg [94, 96], and pursued by Roberts and Ahlblom [97]. These models assume the driving force  $P$  equal to the energy stored into the dislocation structure of the non-recrystallized material. The dislocation density on the side of the recrystallized grain is assumed to be null. Therefore the boundary speed is:

$$v = M\tau\rho = M \cdot \frac{1}{2} \cdot \mu b^2 \cdot \rho \quad (1.26)$$



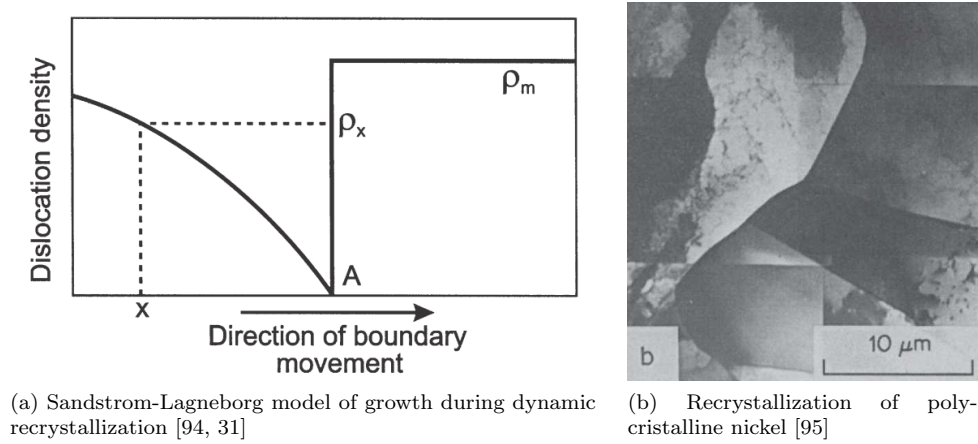


Figure 1.40: Dislocation density profile at the grain boundary interface

with  $M$  the mobility,  $\tau$  the dislocation line energy equal to  $0.5\mu b^2$ , and  $\rho$  the dislocation density in the non-recrystallized material. Figure 1.40b illustrates the MET imaging of a recrystallized grain after a deformation of  $\epsilon = 0.28$  at 1050K. The growing grain has a very low dislocation density compared to the deformed surrounding grains, validating the assumption that migrating boundaries clear off the dislocations. In the case of dynamic recrystallization, the dislocation structure rebuilds again due to the continuous deformation, as illustrated in Figure 1.40a. However, the model of Sandstrom-Lagneborg does not consider the effect of dynamic recovery. Indeed, the mobility of dislocations is by far faster than the mobility of grain boundaries [97]. Thus, the dislocation density profile in dynamically recrystallized grains described by Roberts-Ahlblom may vanish rapidly with time by dislocations rearrangements. Other dislocation profiles along the growing grain diameter were proposed by Sakai et al. [95]. However the exact profile is not quantitatively known. Many recent grain growth models make the assumption of a constant dislocation density in the dynamically-recrystallized grain [98, 99, 30, 100]. Therefore in the case of dynamic recrystallization, the grain boundary speed is:

$$v = M\tau(\bar{\rho} - \rho(t)) \quad (1.27)$$

with  $\bar{\rho}$  the average dislocation density in the material, and  $\rho(t)$  the dislocation density in the growing grain. The growing grain hardens in the case of dynamic recrystallization due to plastic deformation in process, and  $\rho(t)$  evolves with time following the equation 1.15 (page 40). As a conclusion, in the case of dynamic recrystallization, the hardening of the growing grain decreases the driving force and the migration speed [99]. For static recrystallization, dislocation in the growing grain is negligible, however the dislocation density stored in the material decreases by recovery, and the speed of migration decreases as well with time.



#### 1.4.1.3 General expression of grain growth

In the case of recrystallization in materials with low dislocation density, the equations 1.25 and 1.26 can be combined to provide a general equation of the migration speed. Bernard, Loge et al. [100] considered the driving force due to capillarity effects equal to the difference of Laplace pressures based on the Hillert model, and proposed the following growth equation:

$$v = M\tau(\bar{\rho} - \rho(t)) + 2M\gamma\left(\frac{1}{\bar{R}} - \frac{1}{R(t)}\right) \quad (1.28)$$

with  $\bar{R}$  the average grain radius in the material, and  $R(t)$  the radius of the growing grain changing with time. The following equation can be employed in numerical modelling for predicting the grain size evolution during hot working process.

#### 1.4.1.4 Effect of solute-drag and precipitation on grain boundary mobility

The grain boundary mobility is increasing with temperature, and is usually estimated as a fraction  $\beta$  of the Turnbull estimate [101]:

$$M_0 = \beta \frac{\delta \cdot D_{GB} \cdot V_m}{b^2 \cdot RT} \quad (1.29)$$

with  $M_0$  the intrinsic mobility of the boundary in the absence of solute elements,  $\beta$  the fraction parameter usually estimated between 0.1-0.5 [102],  $\delta$  the grain boundary thickness (usually taken as 1nm [103, 102]), and  $D_{GB}$  the self-diffusivity along the grain boundary.

The presence of an impurity atmosphere can decrease the mobility of boundaries due to segregation of alloying elements to the grain boundaries. This phenomenon called solute-drag effect involves the dragging of segregated impurities together with the boundary, hindering its migration [104]. The force exerted by all the impurities on the boundary is defined by Cahn [104] as:

$$P = -N_v \int_{-\inf}^{+\inf} (C(x) - C_0) \frac{dE}{dx} dx \quad (1.30)$$

with  $N_v = 4/a^3$  the number of atoms per unit volume,  $C(x)$  the concentration profile of impurities along the axis  $x$  perpendicular to the boundary,  $C_0$  the mean impurity concentration, and  $-dE/dx$  the force exerted by a single impurity atom. The above equation can be resolved by evaluation of the concentration profile  $C(x)$  and integration. Finding a global solution is complex, and the problem is usually partitioned into two cases: one for impurity concentration lower than a critical value  $C^*$  ('low branch'), and one for concentration above  $C^*$  ('high branch'). The expression for mobility becomes:

$$\text{if } C < C^* \Rightarrow M = \frac{M_0}{1 + M_0 \cdot \alpha \cdot C_0} \quad (1.31)$$

$$\text{if } C > C^* \Rightarrow M = M_0 - \frac{\alpha \cdot C_0 \cdot M^2}{\beta^2 \cdot v^2} \quad (1.32)$$



$$\text{where } \alpha = \frac{N_v \cdot (kT)^2}{E_0 \cdot D} \left( \sinh\left(\frac{E_0}{kT} - \frac{E_0}{kT}\right) \right) \text{ and } \beta^2 = \frac{\alpha kT \delta}{2N_v E_0^2 D} \quad (1.33)$$

with  $v$  the velocity,  $M$  the effective grain boundary mobility,  $M_0$  the intrinsic mobility in the absence of solute,  $E_0$  the binding energy of impurities to the boundary,  $D$  the diffusivity across the boundary, and  $\delta$  the grain boundary thickness. Figure 1.41a illustrates the evolution of the ratio driving force/mobility versus velocity. For pure metals, relationship is linear with a slope=1, corresponding to the curve (a). For higher concentration, driving force is increased at low speed due to solute-drag effect (curve (b)). For concentration high enough (curve (c)), the two regimes corresponding to the low and high Cahn branches become significant. The first regime corresponds to a constant solute drag effect leading to strong impediment of mobility. During the second regime, solute drag diminishes with increasing velocity: fast boundaries create only a little change in the solute concentration due to limited diffusivity, and therefore solute drag effect is reduced.

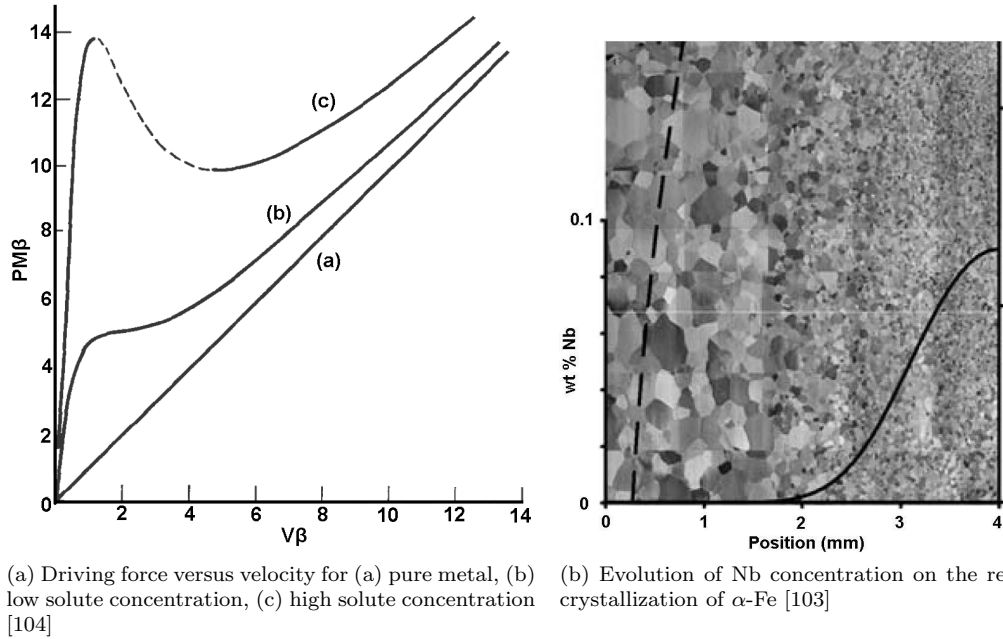


Figure 1.41: Effect of solute drag on the grain boundary motion and on grain refinement

The solute drag effect has been illustrated experimentally by Sinclair et al. in the case of pure  $\alpha$ -Fe with a concentration gradient of niobium [103]. After static recrystallization, a microstructure gradient correlated to the Nb concentration is visible in the diffusion couple, as shown on the Figure 1.41b. The grain size is about 0.2mm on the left side of the picture corresponding to Nb-free area, while the right side of the picture exhibits highly refined microstructure due to higher Nb concentration about 0.1%wt. As a conclusion, Nb impurity is found to decrease grain size after recrystallization by hindering boundaries mobility. This experimental result illustrates the applications of solute-drag effect for the production of ultrafine grain materials by recrystallization.



Another factor decreasing boundaries motion is the occurrence of precipitation at boundaries: this phenomenon is called Zener pinning [105]. Precipitates exert on the moving boundary a pinning force, noted  $F_z$ . For a planar boundary sweeping a material containing randomly distributed precipitates, pinning force is [102, 105]:

$$F_z = \phi \frac{V_f}{r} \quad (1.34)$$

with  $\phi$  a parameter depending on the precipitates geometry,  $V_f$  is the volume fraction of precipitates, and  $r$  is the mean precipitate radius. For spherical precipitates,  $\phi$  parameter is equal to  $3\gamma/2$ . Contrarily to solute-drag, Zener pinning does not affect the mobility, but it delays or stops the grain boundary migration. Therefore if the driving force is lower than pinning force, grain boundaries are halted. The effective driving force is the difference between driving force and pinning force  $F_z$ . The dependence of speed with driving force  $P$  is [102]:

$$v = M(P - \phi \frac{V_f}{r}) \quad (1.35)$$

The above equation is a first approximation which does not consider local relaxations of the boundary [31]. More complete models include these effects [106], however results do not differ significantly from the one obtained by the above equation.

#### 1.4.2 Modeling of discontinuous dynamic recrystallization

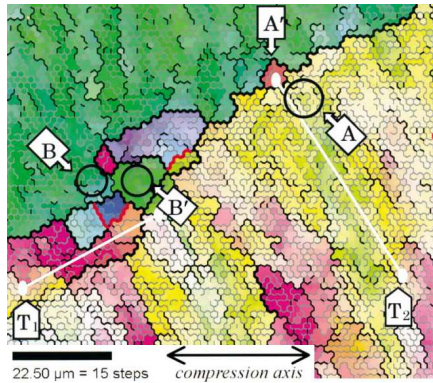
During the high-temperature deformation process, the energy from the plastic deformation is dissipated by heat, and a fraction is stored in the material into the form of dislocations. These dislocations can either eliminate each other by recovery or disappear by the generation of new grains. The second process is called dynamic recrystallization [31, 107]. *Discontinuous dynamic recrystallization* (DDRX) is a mechanism occurring during the hot-working of a wide range of metals with a low to intermediate stacking-fault energy [99, 30]. For metals with higher stacking-fault energy, *continuous dynamic recrystallization* (CDRX) is more likely to occur. Modeling of dynamic recrystallization is required to achieve a predictive determination of the deformation conditions on which dynamic recrystallization operates, and to understand the physical mechanisms at stake. Dynamic recrystallization models can allow the prediction of the average grain size [99, 108] and of the grain size distribution [30]. The following part will treat mostly of the discontinuous dynamic recrystallization mechanism that operates in low stacking-fault energy materials such as cobalt [109, 16], and will give some details on other mechanisms (continuous and geometric recrystallization).



#### 1.4.2.1 Nucleation mechanisms of recrystallization

During the hot working of low stacking-fault energy metals, the plastic deformation leads to a serration of the grain boundaries. For a sufficient deformation level, the serrations can lead to the creation of new grains by bulging from the pre-existing grain boundaries [110, 27]. Figure 1.42a illustrates a typical partially recrystallized microstructure in the case of pure copper [28]: the initial boundary bows, and the resulting protuberances evolve to form new grains as shown on the positions A and B. While nucleation by bulging process is usually considered to operate on plane boundaries [97], Miura et al. shown that nucleation of new grains occurs preferentially at triple junctions [111]. The triple junctions acting as nucleation sites can be either constituted of three or more high angle grain boundaries solely, or include also some twins among the intersecting boundaries. Figure 1.42b illustrates the formation of a new grain on a serrated boundary by a process involving a twin boundary (white line).

The nucleation process corresponding to the Figures 1.42 was described qualitatively by Sakai et al. [27, 26], and is represented on the Figure 1.43. The shear on grain boundaries lead to the formation of inhomogeneous local strain and to the formation of sub-boundaries. These plastic heterogeneities assist the closing of the budding nucleus. Twins can also form in the surrounding of serrations and accelerate the separation of new grains from the parent boundary [28].



(a) EBSD IPF map showing nucleation of DRX on 6N copper deformed at  $T = 573K$ ,  $\dot{\epsilon} = 0.16s^{-1}$ ,  $\epsilon = 1.3$  [28]



(b) Copper bicrystal deformed at  $T = 923K$ ,  $\dot{\epsilon} = 4.2.10^{-4}s^{-1}$ ,  $\epsilon = 0.15$  [112]

Figure 1.42: Nucleation of dynamic recrystallization at grain boundaries in pure copper

Critical nucleus size can be quantitatively captured through a thermodynamic approach. In the case of homogeneous nucleation, the change of the Gibbs energy during the recrystallization comports two terms. One is volumic and represents the energy difference due to the elimination of the dislocations by formation of the dislocation-free nucleus. The second term represents the energy increase by creation of additional grain boundary interface. The global Gibbs energy change



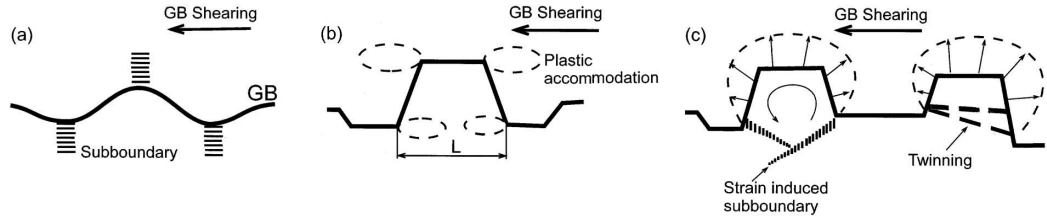


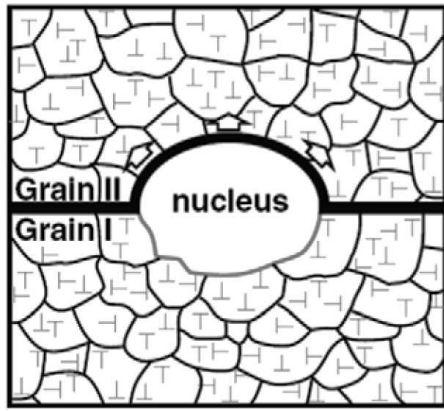
Figure 1.43: Schematic representation of nucleation mechanism [26, 27, 28]

is expressed by:

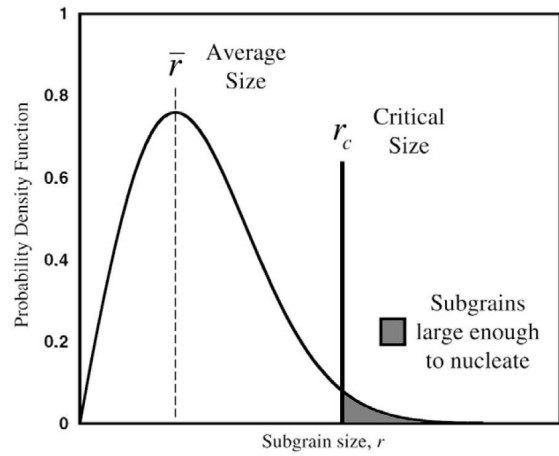
$$G = -\frac{2\pi r^3}{3}\mu b^2\bar{\rho} + 4r^2\gamma \quad (1.36)$$

with  $r$  the nucleus radius,  $\bar{\rho}$  the average dislocation density inside the parent grain,  $\gamma$  the grain boundary surface energy,  $b$  the Burgers vector, and  $\mu$  the shear modulus. The critical nucleus size noted  $r^*$  is reached when the Gibbs free energy change is maximal. The resulting expression of  $r^*$  is the equation, so-called the Bailey-Hirsch criterion [110]:

$$r^* = \frac{4\gamma}{\bar{\rho}\mu b^2} \quad (1.37)$$



(a) Nucleation mechanism by grain boundary bulging



(b) Subgrain size distribution, and fraction of subgrains able to nucleate

Figure 1.44: Bulging of a new grain from a pre-existing subgrain: mechanism diagram and subgrain size distribution[29, 30]

As a consequence, each subgrain lying on the grain boundary and larger than the critical size can potentially undergo bulging and forms a new grain, as illustrated on the Figure 1.44a. By assuming that the distribution of subgrains follows a Rayleigh distribution, the fraction of subgrains in a grain that are larger than the critical size is [29]:

$$F = \exp\left(\frac{-\pi r^{*2}}{4\bar{r}}\right) \quad (1.38)$$



with  $\bar{r}$  the average subgrain radius and  $r^*$  the critical radius. This fraction corresponds to the gray area on the Figure 1.44b and is obtained by integration over the subgrain size distribution. However, in addition of being larger than the critical size, subgrains must also be in contact with the boundary to enable bulging process. The number of subgrains lying on the boundary of one grain is  $N = 64R^2/\pi^2\bar{r}^2$  [30]. Finally, the number of subgrains able to nucleate from one grain is:

$$N_{\text{nuc}} = N.F = \frac{64R^2}{\pi^2\bar{r}^2} \exp\left(\frac{-\pi r^{*2}}{4\bar{r}}\right) \quad (1.39)$$

with  $R$  the mean grain radius. As a conclusion, the nucleus size can be determined by the Bailey-Hirsch criterion given in the equation 1.37, and the number of nucleus formed is obtained by the equation 1.39. These two equations combined can be used then for modeling the nucleation of dynamic recrystallization, without requiring the definition of critical conditions for the occurrence of nucleation [30]. The critical conditions and the functional form of nucleation rate can be directly determined from this approach without additional assumptions.

#### 1.4.2.2 Onset and transitory regime

The onset of recrystallization is usually defined by a critical value of strain, stress, work or dislocation density. It is usually observed that the recrystallization starts before the occurrence of the peak stress: for instance the critical strain is about the half of peak strain for pure cobalt according to Kapoor et al. [109]. Before the onset of recrystallization, flow stress follows the Voce law defined in the equation 1.16, and hardening rate  $\theta$  is proportional to flow stress. When recrystallization starts, this relation does not hold anymore, and  $\theta$  drops rapidly due to boundary migration induced softening (BMIS) [99]. The onset of recrystallization was defined by Poliak and al. as the inflexion point on the curve  $\theta = f(\sigma)$  (Figure 1.37a) [113]. The critical stress is obtained graphically when the derivation  $-\partial\theta/\partial\sigma$  is minimal. Practically, this point is determined graphically, as shown on Figure 1.46a.

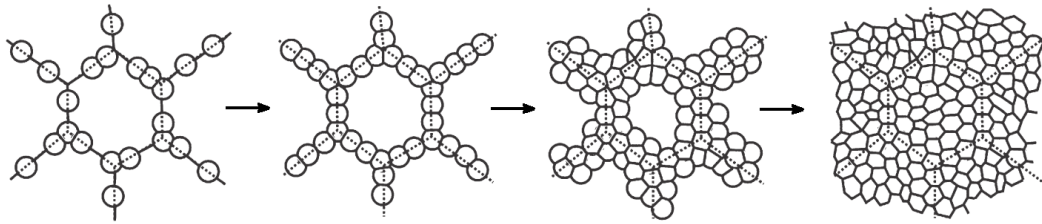


Figure 1.45: Formation of necklace microstructure during dynamic recrystallization [31]

Dynamic recrystallization starts at grain boundaries, and forms a necklace-type microstructure, as illustrated on the Figure 1.45. The fraction recrystallized increases with strain until the initial microstructure completely disappears. As illustrated on the Figure 1.46b, average grain size is constant during the initial stage of deformation, then it drops during the transient regime, and



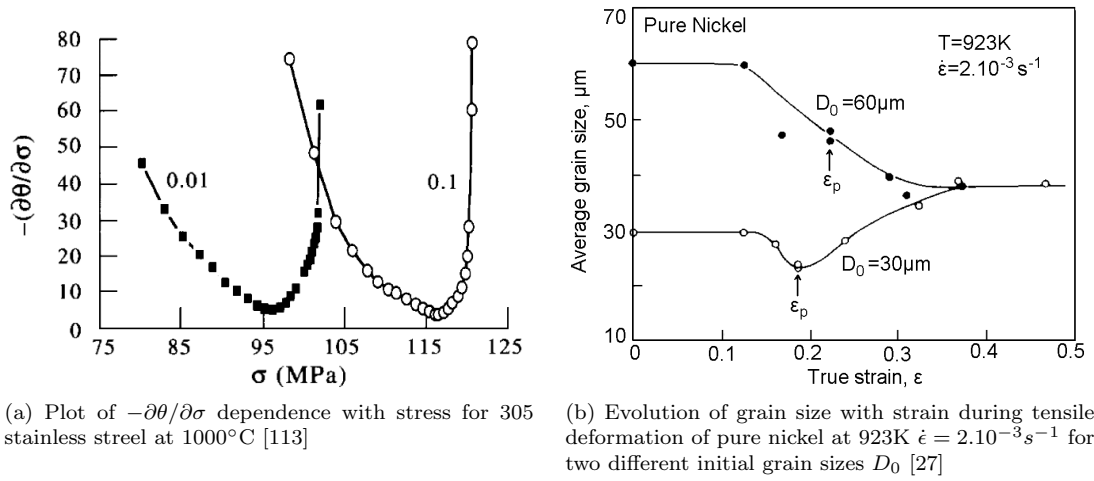


Figure 1.46: Onset of recrystallization and evolution of microstructure during the transient regime

stabilises to a constant value during the steady-state. During the transient regime, grain size passes first to a minimum due to nucleation of small grains at the onset, then the steady-state size is reached when the balance between grain growth and nucleation is established. As shown on the Figure 1.46b, changing the initial grain size  $D_0$  affects the transient regime, but the steady-state grain size remains constant and depends on deformation conditions only. In some cases initial grain size can be smaller than steady-state size (e.g.  $D_0 = 30 \mu\text{m}$  on the figure), therefore recrystallization globally leads to grain growth for such conditions. As a conclusion, it is of first importance industrially to understand properly the relationship between deformation conditions and steady-state microstructure in order to produce the targeted grain size by forging process.

### 1.4.2.3 Stationary regime

For large deformations (usually  $\epsilon > 0.5$  to 1 [107, 99]), the transient regime is followed by a steady-state regime during which all the average physical variables remain constant. Therefore flow stress, dislocation density and grain size are independent of the strain, and depends on the deformation conditions only. At steady-state the fraction recrystallized is about 1, however the recrystallization is still proceeding, with a constant nucleation rate [114]. The balance between strain-hardening and softening due to combined nucleation and grain growth forms a flow stress plateau on the stress-strain curve. The average values of state variables are constants at the macroscopic scale, but grain-scale variables are in permanent evolution [99]. Therefore steady-state is a dynamic regime far from equilibrium.

The steady-state grain size and flow stress both depend only on temperature and strain rate only. The evolution of stress with deformation was detailed in the section on plasticity through the Kocks-Mecking model (page 42) and the Zener-Hollomon parameter (equation 1.8 37). Grain size



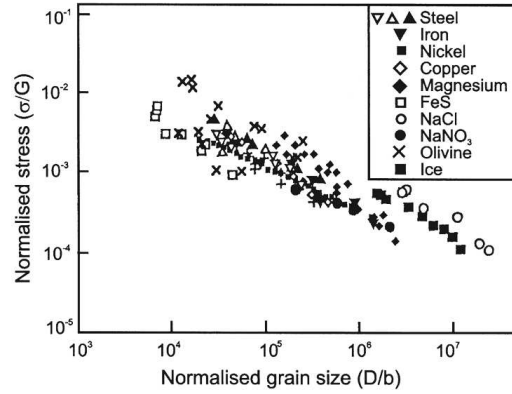


Figure 1.47: Relationship between dynamically recrystallized grain size and flow stress at steady-state [32]

evolution can be expressed as a function of Z parameter as well (e.g. on copper [76]). It is also convenient to express grain size as a function of steady-state flow stress: this relationship is called the Derby law [32]:

$$\frac{\sigma}{\mu} \left( \frac{D}{b} \right)^{2/3} = K \quad (1.40)$$

with D the steady-state grain size,  $\mu$  the shear modulus, b the Burgers vector and K a fitting parameter. The Derby law is represented on Figure 1.47 for a large range of metallic and mineral materials. To determine grain size for unknown deformation conditions, first flow stress must be extrapolated by Kocks-Mecking model, and in a second step the extrapolated grain size can be deduced from flow stress by the Derby law. To conclude, steady-state variables can be easily extrapolated due to their dependence with deformation conditions solely.

### 1.4.3 Other mechanisms of recrystallization

In large stacking fault energy metals, a different recrystallization process occurs, without involving nucleation and growth steps of new grains. Instead, grains are formed by a continuous transformation of subgrains into new grains. Dislocations accumulate to low angle grain boundaries (LAG) and increase their misorientation until it forms high angle grain boundaries (HAG) [31, 108]. This recrystallization process is called *continuous dynamic recrystallization* (CDRX). An example of partially recrystallized microstructure in aluminum alloy is illustrated on the Figure 1.48a: one can see typical CDRX microstructure composed of crystallites bounded partially by LAG and by HAG. A singular feature of CDRX microstructure is to exhibit a strong crystallographic texture at high strain, compared to DDRX microstructure.

Continuous recrystallization process leads to a single peak stress on the stress-strain curve, occurring for large strain ( $\epsilon > 1$ ). The peak is followed by significant but sluggish flow softening. Flow



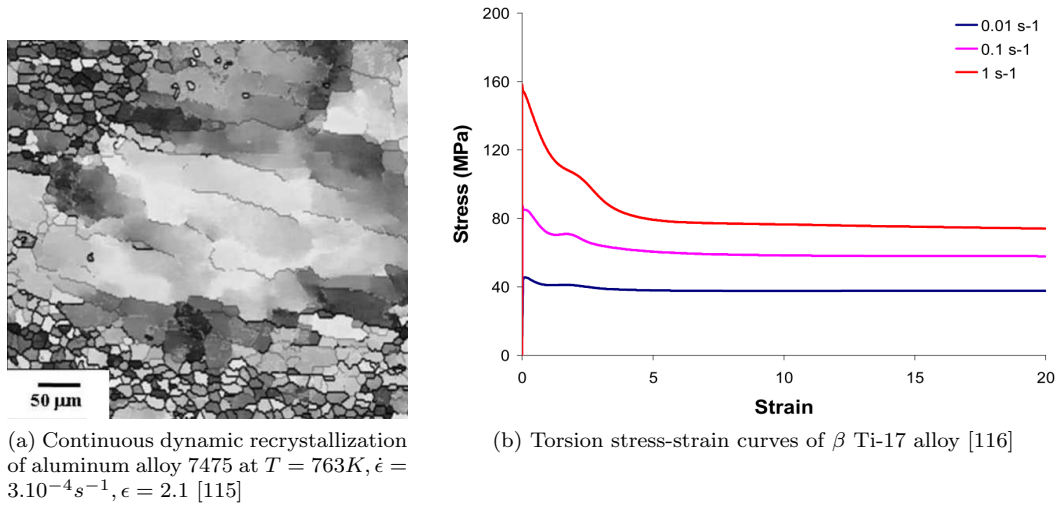


Figure 1.48: Continuous dynamic recrystallization of titanium and aluminum alloys

stress reach then a steady-state for very large deformation level ( $\epsilon \approx 30$ ) [108]. Typical stress-strain curves are represented in Figure 1.48b for  $\beta$  Ti-17 alloy [116]. During the flow softening step, crystallites size decrease strongly from  $\epsilon \approx 5$ , and then increases slowly until it reaches a constant value at the steady-state. Continuous is of great interest industrially as it can lead to significant grain refinement during the processing of high SFE alloys such as aluminum or titanium.

For very large deformations, a different mechanism related to continuous mechanism can occur jointly, and is called *geometric recrystallization* [31]. At large strain, grains are flattened and become pancake-shaped. Shear strain to grain boundaries leads to boundary serration (Figure 1.43), with a serration size of the same magnitude as subgrain size. The subgrain size and serrations size are independent of strain for large deformation. If the pancake-shaped grain thickness is lower than the serrations size, the interpenetration of serrations from the two sides of the grain can form new grains. This mechanism involves limited grain boundary migration, an texture of new grains is similar to the deformed texture.

## Conclusions

To conclude, two main categories of recrystallization can occur during hot working of metals. The first occurs in a discontinuous way from grain boundaries in low SFE metals, and lead to grain refinement for limited strain ( $\epsilon < 1$ ). The second operates in high SFE metals by continuous evolution of subgrains, and generate significant grain refinement for large strain ( $\epsilon \approx 30$ ). It is of first importance to understand the recrystallization mechanism at stake during hot working of a given material to select properly deformation conditions, as much by the  $(T, \dot{\epsilon})$  conditions as by the strain level in order to obtain the targeted microstructure.







## Chapter 2

# Materials and experimental procedure



## 2.1 Initial materials: microstructure and properties

### 2.1.1 Chemical composition

The list of materials used in the current study is detailed in the Table 2.1. The precipitation behaviour study (page 101) was carried out using the Ø15.87mm Carpenter material, containing 0.07% wt carbon. Samples for hot-working experiments (page 126) were prepared by cold-swaging of this rod and annealing. The grain growth and static recrystallization experiments (page 107) were carried out on the Ø35mm forged material from Kamaishi. Finally, hot-working experiments followed by water quench (Gleeble) were carried out from the Ø9.77mm from Carpenter.

Provenance	Diameter	Chemical composition (wt %)								
		Co	Cr	W	Ni	C	N	Fe	Si	Mn
Carpenter	15.87mm	bal.	20.18	15.11	9.93	0.07	0.034	2.01	0.01	1.51
Carpenter	9.77mm	bal.	20.11	15.05	9.78	0.07	0.026	1.87	0.04	1.61
Kamaishi	35mm	bal.	20	15	10	0.094	0.0024	2.03	0.29	1.46

Table 2.1: Chemical composition of L-605 samples

The elaboration process of samples produced by Carpenter is illustrated in Figure 1.29 (page 32): bars are forged, then annealed and finally hot-rolled. Material from Kamaishi was forged at a temperature between 1000°C and 1230°C with a reduction of 67%, then hot-rolled with a reduction of 57%, then annealed 45min at 1100°C and finally cold-swaged with a reduction of 4%.

### 2.1.2 Initial microstructure

Initial microstructure was observed by optical microscopy and SEM. Figure 2.1a illustrates the microstructure of L-605 (Carpenter Ø15.87mm) at magnification 50x by optical microscopy. The picture reveals the presence of many annealing twins inside grains. Figure 2.1b obtained by electron microscopy shows similar result: microstructure is constituted of coarse grains containing many twins.

Microstructure was also observed by EBSD to determine the nature of grain boundaries. Figure 2.2a represents the Inverse Pole Figure (IPF) map, giving the crystalline orientation on the scanned area. Twins can be localized by a change of crystalline orientation inside grains, corresponding to coloured stripes on the map. Figure 2.2b indicates the phases indexed by the diffraction diagram: red color corresponds to FCC  $\gamma$ -phase, and green color is the HCP  $\epsilon$ -phase. As one can see on this map, green color is absent, therefore the material is composed of FCC phase uniquely. Figure 2.2c illustrates the different types of boundaries in the microstructure. Most boundaries are high-angle grain boundaries (black lines,  $15^\circ \sim 90^\circ$ ) and twins (blue lines). Twins are identified as  $\Sigma 3$  annealing twins, with a boundary angle of  $60^\circ$ . Some low-angle boundaries can be sometimes detected (red



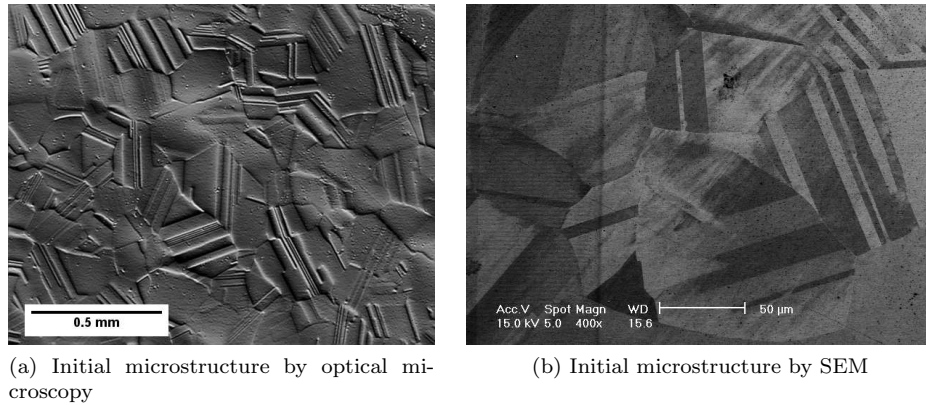


Figure 2.1: Initial microstructure of Ø15.87mm Carpenter L-605 alloy

lines,  $2^\circ \sim 15^\circ$ ). However they represent a very small fraction of boundaries, as the material is in an annealed state, and has not been deformed.

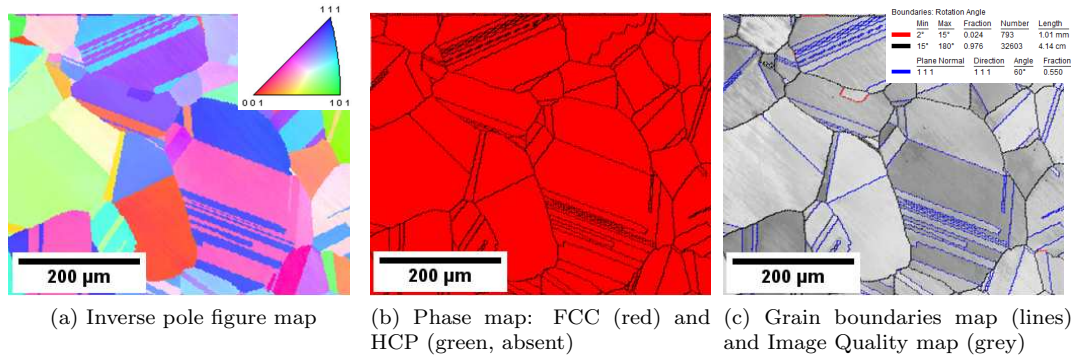


Figure 2.2: Initial microstructure of Ø15.87mm Carpenter L-605 alloy observed by EBSD

The phases fraction has been investigated by X-ray diffraction (XRD). Figure 2.3 shows the diffraction diagram of L-605: two main peaks are visible and correspond to the two orientations  $\langle 111 \rangle$  ( $43^\circ$ ) and  $\langle 200 \rangle$  ( $51^\circ$ ) of the FCC  $\gamma$ -phase. No other phase was detected by XRD, therefore the initial material is constituted of a single FCC phase, in agreement with the literature and EBSD (Cf. page 32).

The Figure 2.4 represents the grain size distribution of the different materials used in this study obtained by EBSD. Size distributions are found to follow a Log-normal law, and fits by this law are represented by plain lines. Material from Carpenter have a mean grain size of 53 and 118  $\mu\text{m}$  for Ø15.87mm and Ø9.77mm respectively. Carpenter Ø15.87mm material was cold swaged and annealed 10min at  $1200^\circ\text{C}$  and then 5min at  $1000^\circ\text{C}$ , resulting in a mean grain size of 87  $\mu\text{m}$  after processing. Kamaishi material has a very refined microstructure due to the forging process, with a mean grain size of 3.5  $\mu\text{m}$ . Average grain sizes were calculated over the total number of grains. On the other hand, distributions are represented by the area fraction. Therefore it is coherent to obtain



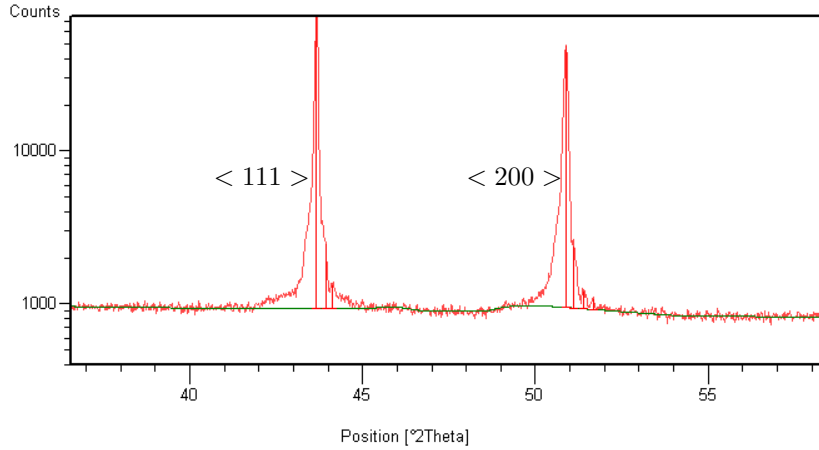


Figure 2.3: XRD diagram of L-605: Intensity (counts) as a function of  $2\theta$  angle

a mean grain size lower than the peak observed on the distribution of Figure 2.4: area fraction is a value giving higher weight to the larger grains, and its maximum is not supposed to coincide with the number average grain size.

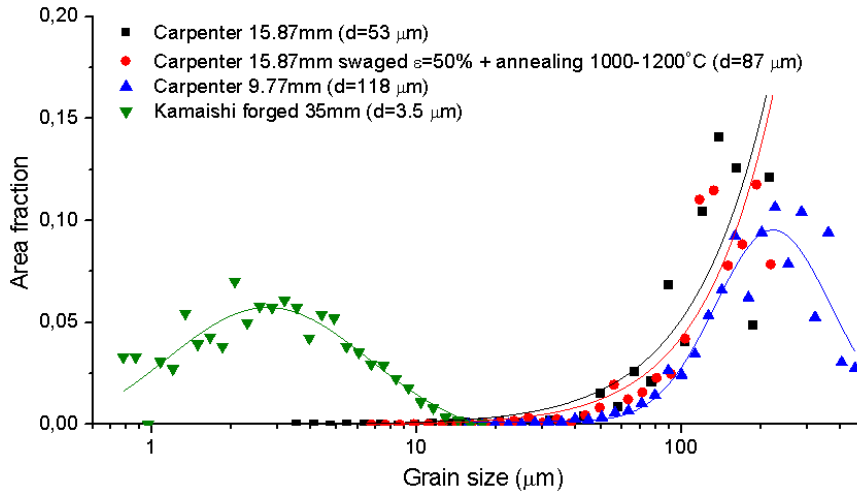


Figure 2.4: Initial grain size distribution of the different materials used for experiments

To conclude, the initial materials are constituted of a single FCC phase containing many  $\Sigma 3$  annealing twins. The presence of  $\epsilon$ -phase or precipitates was not detected by microscopy nor by XRD. Initial materials have a grain size distribution following a mono-modal Log-normal distribution with different mean sizes.

### 2.1.3 Mechanical properties

Mechanical properties of the initial materials are illustrated in Figure 2.5. Figure 2.5a represents the tensile stress-strain curve of L-605 as-received from Carpenter ( $\varnothing 15.87\text{mm}$ , average grain size  $d=53$



$\mu\text{m}$ ) and for the same material annealed 12h at  $1230^\circ\text{C}$ . Annealing treatment leads to an increase of 16 times on the grain size, with a final average grain size about  $800\mu\text{m}$ . Table 2.2 resumes the mechanical properties of initial and annealed material. Tensile test reveals a very important strength loss due to the annealing treatment: strength decreases by about 37%. The maximal strain remains unchanged, so there is no gain of ductility by coarsening the microstructure. We can conclude that a long annealing treatment is harmful for mechanical strength. Short annealing times ( $<1\text{h}$ ) at  $1200^\circ\text{C}$  do not engender significant grain growth, and should be preferred for solution treatment.

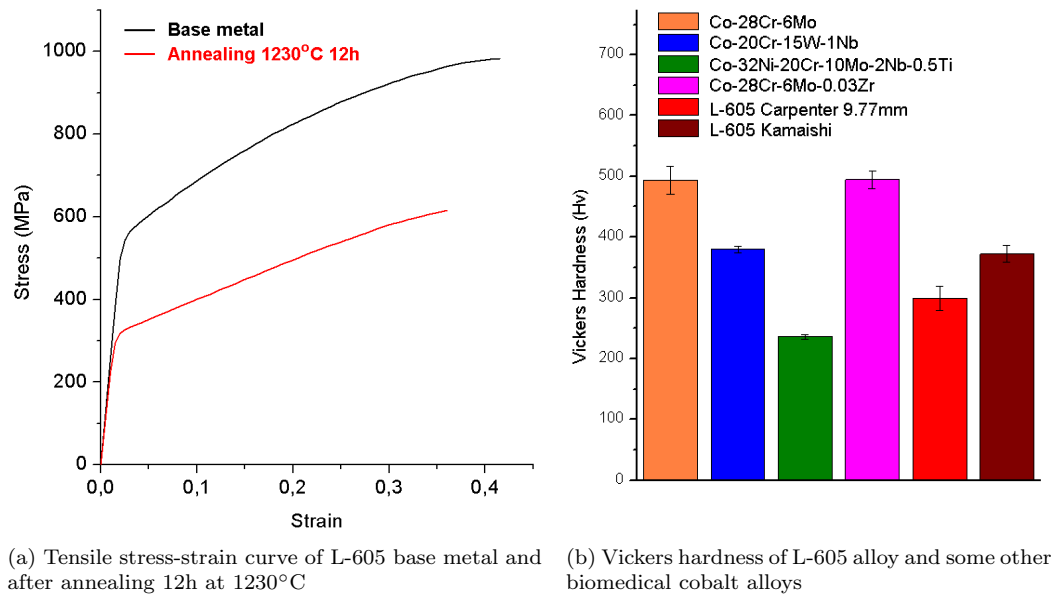


Figure 2.5: Mechanical properties of L-605 alloy

As illustrated in Figure 2.6a, elongation generates very large slip bands, and surface roughness become significant. On the annealed tensile test samples (Figure 2.6b), the localization of deformation is at the origin of rupture. The formation of very large slip bands is due to a bamboo-like structure: grain size is close to the sample width. Therefore macroscopic mechanical behaviour depends strongly on the orientation of each large grain in the sample, and deformation becomes very heterogeneous.

Material	Elongation( %)	Yield stress (MPa)	Ultimate tensile stress (MPa)
L-605 ( $d=53\mu\text{m}$ )	$41.7\pm 3.4$	535	$987\pm 24$
L-605 ( $d\approx 800\mu\text{m}$ )	$36.3\pm 3$	310	$620\pm 28$

Table 2.2: Tensile test mechanical properties of L-605 alloy

Vickers hardness was evaluated on the as received L-605 alloy and on some other biomedical cobalt alloys. The average hardness of L-605 is about  $300\pm 20\text{ Hv}$ , this value is higher than on the Haynes 25 datasheet ( $251\text{Hv}$  expected). This higher value might due to work hardening of the alloy



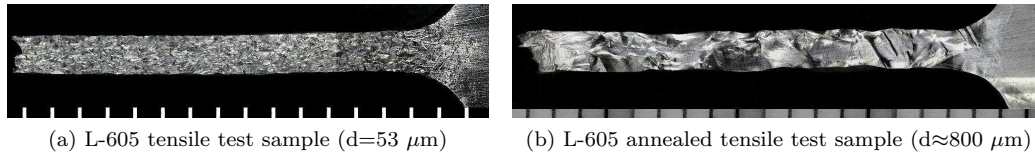


Figure 2.6: Tensile test samples surface after rupture (grading size=1 mm)

during the manufacture of the rod. The forged material from Kamaishi presents a higher hardness of  $372 \pm 14$  Hv, mainly attributed to the smaller grain size and to some residual stress from the hot-working process.

The cobalt alloys with the highest hardness are Co-28Cr-6Mo and Co-28Cr-6Mo-0.03Zr, with a hardness of  $494 \text{Hv} \pm 20$  Hv for both. Therefore the small addition of zirconium does not lead in a significant change of hardness. The alloy Co-20Cr-15W-1Nb was considered as a Ni-free alternative to L-605 to minimize the allergy risks. Hardness of this alloy is significantly higher, around  $379 \pm 5$  Hv. Also, in a previous study in Chiba laboratory (Sugihara et al.), this new alloy was shown to have a very limited ductility. This case illustrates very well the difficulty to fulfil the mechanical properties requirement without nickel addition. Finally Co-32Ni-20Cr-10Mo-2Nb-0.5Ti alloy shows a quite low hardness about  $236 \text{Hv} \pm 4$  Hv, in agreement with expectations for such a Ni-rich alloy. This alloy is a variant of SPRON alloy, well known for its high ductility, but also for its limited compatibility due to the high nickel concentration [117].

As a conclusion, initial L-605 material used in this study presents the suitable mechanical properties for stent applications: an ultimate tensile stress above 900MPa, and an elongation about 40%. Annealing treatment leads to a significant grain growth, and consequently strength drops below the limit of 900MPa, making this material somewhat weak for stents manufacture. On the other hand, forged L-605 from Kamaishi has a  $3.5 \mu\text{m}$  grain size, and presents a better hardness than the initial material, therefore strength is expected to be improved by decreasing grain size. As a conclusion, annealing treatment is detrimental to mechanical properties, whereas forging process seems to improve strength. The following study will investigate in detail the effect of annealing and hot-working on microstructure change, and its effect on mechanical properties.



## 2.2 High-temperature thermomechanical treatments and mechanical tests

### 2.2.1 High-temperature thermomechanical treatments

#### Thermecmaster-Z device

High-temperature behavior is studied by high temperature deformation of 25 cylinder-shaped samples at different temperatures and strain rates. Samples were prepared from the Ø15.87mm diameter rod from Carpenter. The desired diameter of samples is 8mm, so the initial rod must be processed to decrease the diameter. However the material is quite hard, making the machining process difficult. Moreover machining of the specimen would lead to a significant material loss. As a consequence, the rod was swaged at room temperature until 8.2mm, and then samples were machined to the final diameter of 8mm. The swaging process leads to a decrease of grain size (Figure 2.7a) and creates many crystalline defects in the material by plasticity, as illustrated on the KAM cartography in Figure 2.7c. Therefore an annealing treatment of 10min at 1200°C was performed to remove the crystalline defects and homogenize the microstructure by static recrystallization process. As shown on Figure 2.7d, annealing treatment erased all the crystalline misorientations, and multiplied the average grain size by 17, from 5 $\mu$ m to about 87 $\mu$ m (Figure 2.7b). Figure 2.4 illustrates the grain size distribution after annealing 10min at 1200°C followed by a temperature stabilization step of 5min at 1000°C.

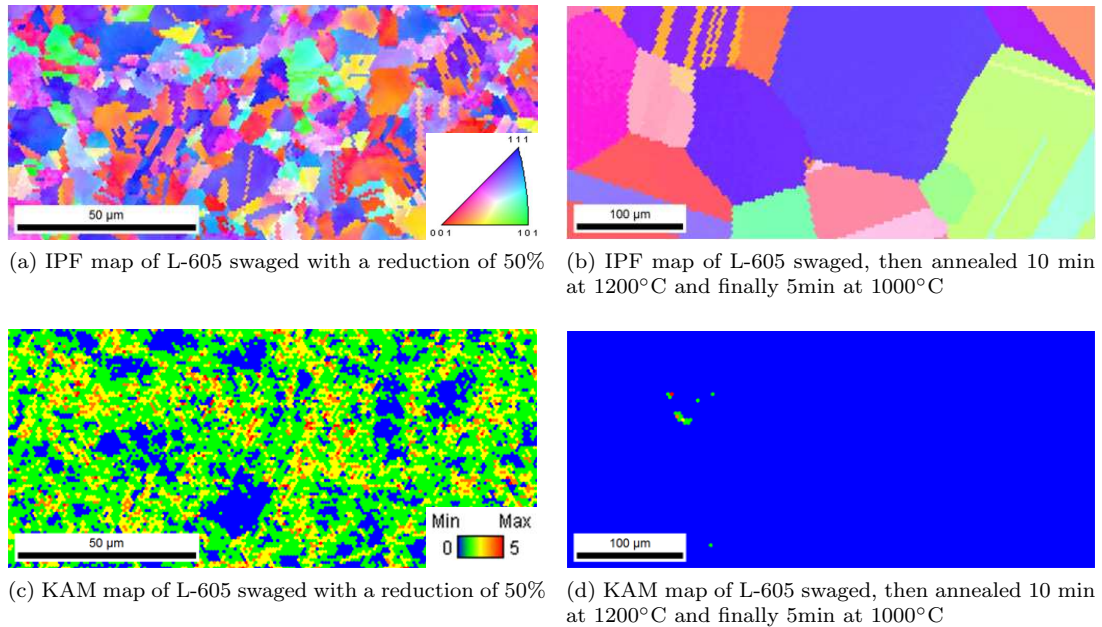


Figure 2.7: Microstructure change of L-605 swaged at  $\epsilon = 50\%$  by annealing treatment



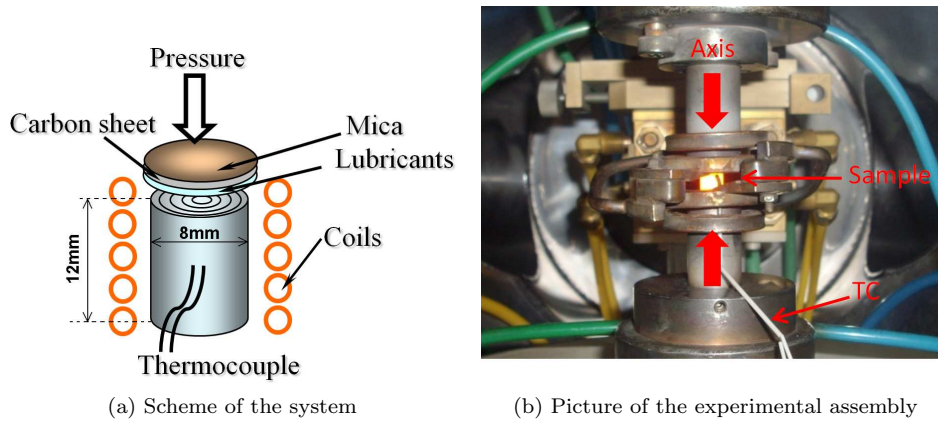


Figure 2.8: Thermecmaster-Z thermomechanical device

Samples have Rastegaev geometry (diameter 8mm x height 12mm), with 0.2mm depth grooves carved on the two edges to keep the lubricant. Figure 2.8a represents in a diagram the experimental device, and Figure 2.8b is a picture taken during the hot-working process. Carbon sheets are used as a lubricant to minimize friction with anvils. Moreover, mica foils are used to limit the heat loss by contact with the anvils. Due to these two layers, there was no problem of adhesion between the cobalt sample and the anvils made of  $\text{Si}_3\text{N}_4$ . Compression tests are carried out under vacuum on a hot-deformation simulator (Thermec-master Z device, Fuji Electronic Industrial Co. Ltd., Japan). Quick heating rate of  $5^\circ\text{C}\cdot\text{s}^{-1}$  is reached thanks to high-frequency induction heating. A solution treatment of 10min at  $1200^\circ\text{C}$  is applied in-situ in the Thermecmaster-Z device in order to homogenize microstructure and to dissolve potential precipitates. Then temperature is lowered to the desired value for carrying out the compression experiment, and temperature is hold 5min to stabilize the thermal gradient. Finally compression tests are carried out between  $1000^\circ\text{C}$  and  $1200^\circ\text{C}$  with a strain rate varying from  $0.001\text{s}^{-1}$  to  $10\text{s}^{-1}$ . Compression is uniaxial with a maximum engineering strain of 56%, corresponding to a maximal true strain  $\epsilon = 0.8$ . Sample is finally gas-quenched just after compression by a mixture of He and  $\text{N}_2$ , in order to preserve high-temperature microstructure. Strain is calculated from the measurement of displacement of the anvils. The final plastic strain after compression is checked by measurement of the sample geometry, and the error is found to be about  $\pm 5\%$ . Strain and stress were deduced from the force applied and the displacement of the ram based on the equations indicated in the Appendix 2 (page 187).

### Gleeble device

Another set of experiments was carried out on the Gleeble device, which differs from the previous device mainly by its heating system. First the heating is generated by conduction of a high current flow through the sample. By this way it is possible to proceed to very fast heat treatments. Moreover



the device was fit out with a hose to enable water-quench of the sample. Figure 2.9a is a scheme of the experimental assembly, and Figure 2.9b is a picture of the device with the water quench system. As illustrated in Figure 2.10b, water quench enable extremely fast cooling with a maximal speed of about  $-2000^{\circ}\text{C.s}^{-1}$ .

Lubrication was ensured by a carbon sheets and tantalum foils between the sample and anvils. Preliminary experiments showed that after hot-working process, the cobalt sample sticks to the anvils made of tungsten carbide. Tantalum foils were very efficient for preventing adhesion and to avoid to damage the anvils while removing the sample.

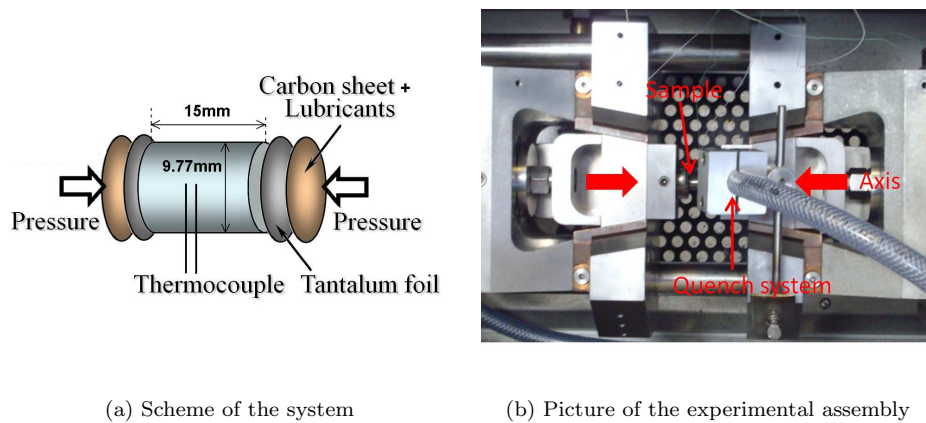


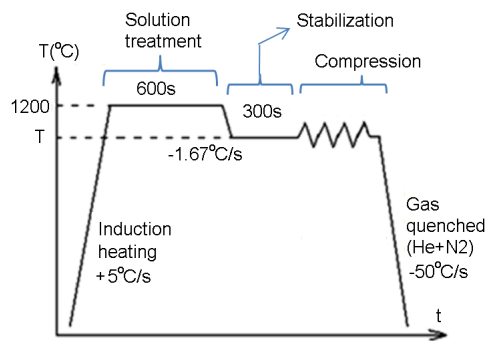
Figure 2.9: Gleeble thermomechanical device

Sample was made of L-605 with a diameter  $\varnothing 9.77\text{mm}$  from Carpenter. As the material has already a suitable diameter and is already in its annealed state, it was not necessary to carry out an homogenization treatment. The sample was simply heated with a speed of  $5^{\circ}\text{C.s}^{-1}$  and temperature was then hold for 1 min to obtain a stable thermal gradient. Then compression was carried out between  $1000^{\circ}\text{C}$  and  $1200^{\circ}\text{C}$  with a strain rate varying from  $0.001\text{s}^{-1}$  to  $10\text{s}^{-1}$ . Compression is uniaxial and is proceeded until an engineering strain of 64%, corresponding to a true strain  $\epsilon = 1$ . Sample is quenched by a high-pressure jet of water, and the experimental cooling curve is illustrated in Figure 2.10b.

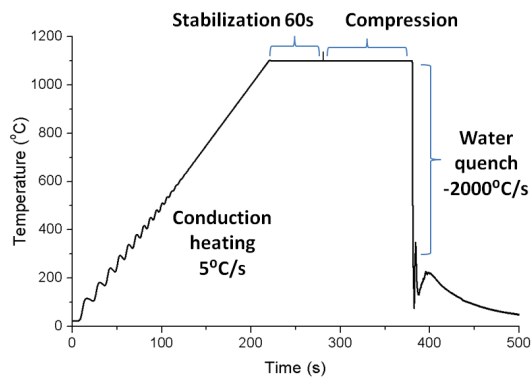
### Forging of $\varnothing 33\text{mm}$ large sample by 300T hydraulic press

Material with  $\varnothing 35\text{mm}$  diameter from Kamaishi was machined to produce cylinder-shaped samples with a diameter of  $\varnothing 33\text{mm}$  and a height of 52mm. Grooves with a depth of 0.5mm were carved on the two circular edges to keep the lubricant and to visualize the diameter change after compression. Samples were then annealed for 18 hours at  $1200^{\circ}\text{C}$  and then water quenched to obtain a single-phase homogeneous coarse microstructure. The mean grain size after annealing treatment was about  $200\mu\text{m}$  (Figure 2.12a), and the corresponding grain size distribution is illustrated in Figure 2.12b.





(a) Thermecmaster-Z thermomechanical treatment



(b) Gleeble thermomechanical treatment

Figure 2.10: Thermomechanical treatment applied for hot-working experiments

Before the hot working process, the sample was heated up 10min at 1280°C. The temperature was set at the maximum the muffle furnace can support, in order to obtain sufficient ductility and to balance the cooling during the compression. Sample was then taken with a clamp, and placed on the anvils of a hydraulic press. The hydraulic press system is described on the scheme of Figure 2.11a. The press does not include any heating system, and the deformation occurs while the sample cools down by heat conduction with the anvils. To minimize heat loss, 0.6mm thickness mica sheets were disposed between the two faces of the sample and the anvils. After 50 seconds of compression, the sample is still hot enough to enable deformation (Figure 2.11b). Also, carbon sheets were inserted between the contact surfaces to minimize friction with anvils. Compression was carried out with a constant displacement speed of the upper ram fixed at 0.33mm.s<sup>-1</sup> or 33mm.s<sup>-1</sup>, corresponding to an average strain rate of 0.01s<sup>-1</sup> or 1s<sup>-1</sup>. As the compression speed is constant, strain rate is not fixed and increases during the process. Temperature was measured with a thermocouple during the working process, and the cooling speed could be determined. Therefore the experimental conditions combine an increase of strain rate and a decrease of temperature. These complex conditions correspond to the situation met during industrial scale forging process. The resulting samples geometry and material properties after compression are illustrated on the section 3.1.7 (page 92). Sheets were then cut from the centre of the sample, and tensile test specimen were machined to test the resulting mechanical properties.

To conclude, most of the hot-working experiments are carried out with the Thermecmaster-Z device, followed by gas quench. Compression curves are presented in the section 3.1, and the resulting microstructure are illustrated in the section 4.4. For determining the effect of cooling speed on microstructure and to check reproducibility, some experiments were carried out in parallel on the Gleeble device, followed by water quench (Cf. page 139). In addition, some more complex treatments such as speed jump compression tests (page 91) or strain rate increment during compression were



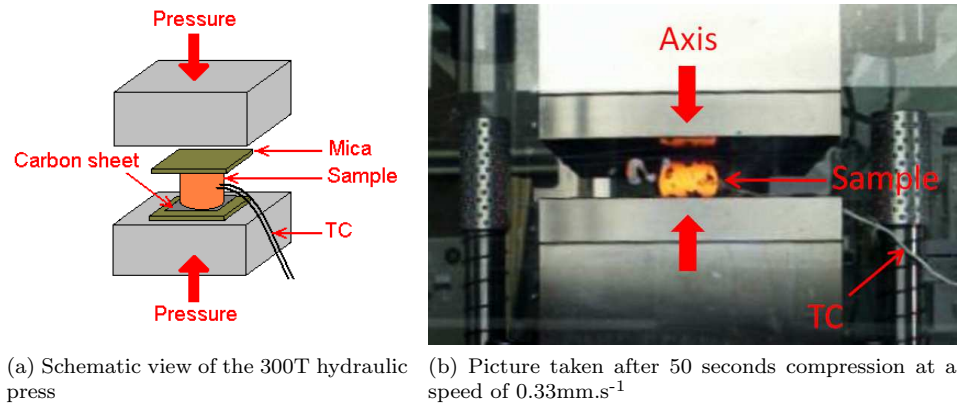


Figure 2.11: Thermomechanical treatment applied for hot-working experiments

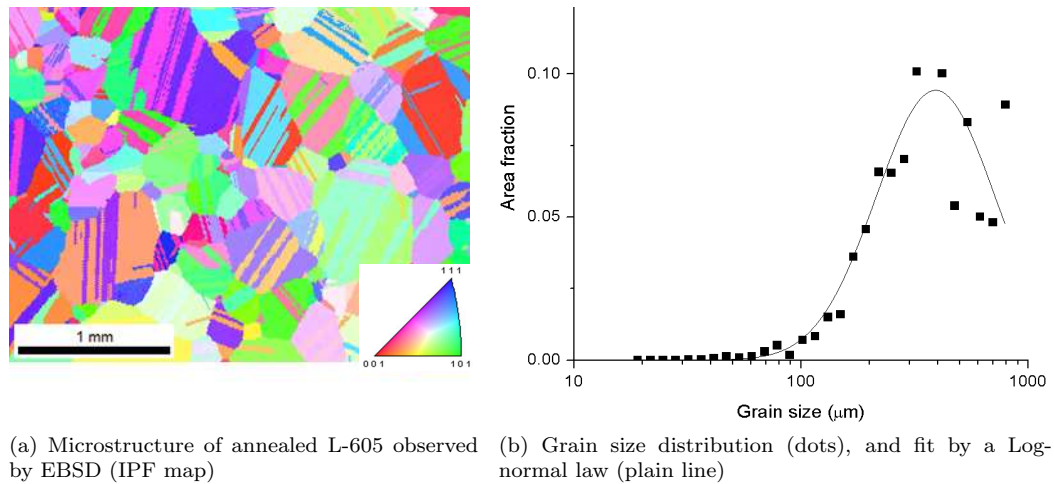


Figure 2.12: Microstructure of L-605 Ø35mm Kamaishi after annealing 18h at  $1200^{\circ}\text{C}$

carried out in the Gleeble device (page 196). Finally hot working experiments were carried out on large samples to reproduce the industrial conditions and to proceed then to tensile tests on the resulting forged material.

## 2.2.2 Tensile tests and Vickers hardness measurement at room temperature

### Tensile tests

Tensile tests were performed on initial materials (Figure 2.5a) and after hot-working process (page 92). Specimen were cut by Electrical Discharge Machining (EDM) from 1.5mm thickness plate samples, with the dimensions indicated in Figure 2.13a. Initial materials tested were Ø15.87mm Carpenter L-605 ( $d=53\text{ }\mu\text{m}$ ) and Kamaishi Ø35mm material ( $d=3.5\text{ }\mu\text{m}$ ). Tensile tests were also carried out on these initial materials after annealing. Samples were annealed in a muffle furnace under air



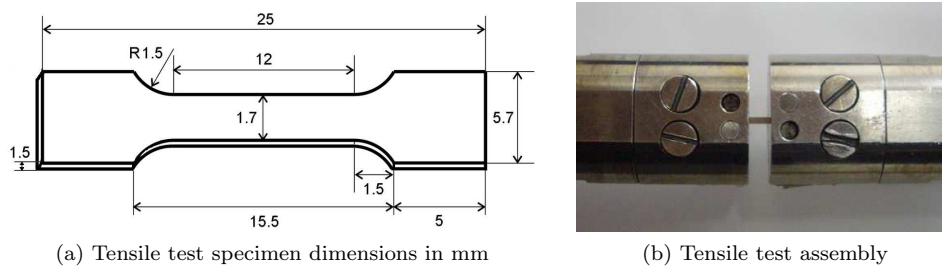


Figure 2.13: Tensile test sample dimensions and apparatus

atmosphere and then water-quenched. The specimen were then machined from the annealed material. Some large compressed samples were produced from Ø35 mm Kamaishi material. A sheet of 2mm thickness was cut from the centre of the deformed sample, then specimen were produced from this sheet.

Tensile test was carried out by displacement of the strut at a constant speed of 0.1mm/min. Displacement is measured by the position of the strut, therefore the total stiffness of the assembly is the combined stiffness of the specimen and the device. A treatment similar to the one indicated in the Appendix 2 (page 187) is applied for determining the strain and stress from force and displacement.

### Vickers hardness

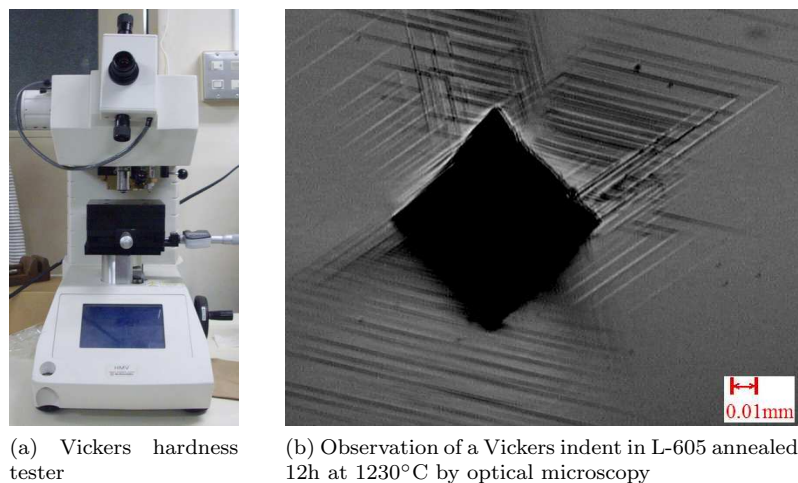


Figure 2.14: Vickers hardness test

Vickers hardness was measured on initial materials, and also after annealing treatments and hot-working process. Hardness test were carried out by applying a load of 9.807N during 10s, and then measuring the indent diagonals following the conventional procedure. For annealed samples, the surface was first abraded and then polished with finer emery paper to remove the surface layer



affected by oxidation. For hot compression samples, a sheet of about 1mm thickness was cut from the center of the specimen, and Vickers hardness was tested in the center of this sheet. Figure 2.14a illustrates the tester used for hardness measurements. Figure 2.14b shows a Vickers indent in annealed L-605 material. The indent creates many crystalline slips around the plastic deformed area.



## 2.3 Microstructure characterization

### 2.3.1 Microscopy observations

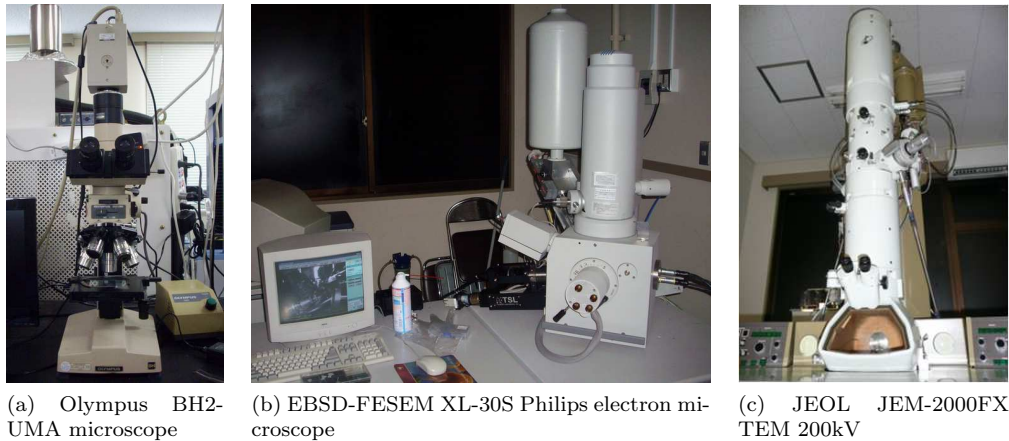


Figure 2.15: Optical and electron microscopes for microstructure characterization

Microstructure of the material after thermomechanical treatment was examined by optical and electron microscopy. The microscope devices are illustrated in Figure 2.15. Optical microscopy was employed when the homogeneity of microstructure must be characterized at low magnification. It is also very adapted for the observation of precipitates after annealing (section 4.1). Electron was employed to determine the grain size and to check the local chemical composition by EDX technique. SEM-EBSD is a very powerful technique providing the crystalline orientation, the grain size distribution and the nature of grain boundaries. It was extensively used to characterize the recrystallized microstructure in the section 4.4. Finally, TEM was employed to characterize the dislocation structure formed during hot deformation process and to observe the grain boundary interfaces.

#### Optical microscopy

Samples were cut by Electrical Discharge Machining (EDM) and abraded with grid paper with mesh from 300 to 2000 to remove scratches and make the surface to observe plane. The surface was then polished by  $1\mu\text{m}$  alumina suspension during a couple of minutes. The surface was finally polished with OP-S colloidal silica suspension with a particle size of  $0.04\mu\text{m}$  during 20 minutes. Optical microscopy was carried out on a Olympus BH2-UMA trinocular microscope. Pictures were taken with a Fujifilm HC-300Z digital camera. To observe properly the surface relief due to polishing and/or etching, a polarizer,  $\lambda$  plates and an analyzer were used.



## Electron microscopy: SEM and EBSD

Samples were prepared for electron microscopy following the procedure detailed previously. In addition of the conventional polishing step, electrolytic polishing is required to remove the top layer of the sample that may have been work-hardened during the sample preparation. Electro-polishing was carried out by applying a tension of 5V on the sample dipped in a solution of 10% sulfuric acid in methanol. However, this treatment was shown to create a surface roughness and some corrosion pits, even by lowering the potential applied or the etching time. A final polishing with an etching solution during 5 minutes was leading to a better improvement of surface quality and to remove a significant layer of material without any occurrence of pitting corrosion. The polishing etching solution was composed of OP-S colloidal silica, water and 30% vol hydrogen peroxide mixed in a ratio (6:3:1), with 0.7g of potassium hydroxide.

Sample was then cleaned in an ultrasonic bath of ethanol, and then in a bath of acetone to remove any dust or potential organic layer. The sample was finally observed with a FESEM XL-30S Philips field-emission scanning electron microscope, with an acceleration tension fixed at 20kV (intensity about 100mA). To observe the crystalline orientation, the microscope is set up with a camera coupled with an Electron Backscatter Diffraction system (TexSEM Laboratories, Inc., Provo, UT). Data were collected with the software TSL OIM Data Collection 5, and treated with the software TSL OIM Analysis 5 (EDAX TSL). The local chemical composition of annealed samples was determined by using an energy dispersive X-ray spectrometer (EDS) attached to the electron microscope.

## Transmission electron microscopy

Compression tests were carried out on the Thermecmaster-Z device with a reduction of 30% ( $\epsilon = 0.357$ ). TEM samples with a diameter of 2mm were cut by EDM close to the edge of the compression specimen. According to Finite Elements simulations carried out on Deform 3D software (Cf. section 4.4 page 124), the mean strain in the cut area is about  $\epsilon = 0.4 \pm 0.1$ . TEM sample were thin down until a thickness of 100  $\mu\text{m}$  by abrasion, and then polished by alumina and colloidal silica like conventional SEM samples. Samples were then polished in the central area with a Gatan 656 dimple grinder and diamond suspensions of 3 $\mu\text{m}$  and 1 $\mu\text{m}$  until the thickness in the central area of the groove reaches 10 $\mu\text{m}$ . Finally, the thin samples are subjected to ion beam milling using a Gatan 691 polishing system at 3kV. Samples substructure was observed in bright field with a JEOL JEM-2000FX TEM (Konno Laboratory, IMR) operating at 200kV, and diffraction patterns were taken with a camera length of 80cm.



### 2.3.2 X-ray diffraction

Phases in presence were investigated by XRD analysis using a Philips X'Pert Pro MPD diffractometer. The X-ray source was Cu-K $\alpha_1$  radiation (X-ray tube with V=45kV, A=40mA). Detection was achieved by an X'Celerator detector. Noise was reduced thanks to a Ni filter and a monochromator. Analyses were carried out by continuous absolute scanning in the angle range 20°-90° for general studies, and in the range 30°-50° for the study of precipitation. Step size was about  $2\theta=0.017^\circ$ , and step time was in the range 1000-2000 seconds in order to detect the small amount of precipitates. Data were treated with the PANalytical X'Pert Highscore software (PANalytical B.V.).

### 2.3.3 Measurement of Thermoelectric Power

Measurements of thermoelectric power were carried out on rectangular samples with 6cm length and 5mm width dimensions. To follow the precipitation kinetics (section 4.1), samples were cut from Ø15.87mm rod (grain size 53  $\mu\text{m}$ ) by EDM with a thickness of 0.65mm. Other specimen used for the study of recovery and grain growth were cut in 2mm sheets machined by EDM from the Ø35mm bar from Kamaishi (grain size 3.5 $\mu\text{m}$ ).

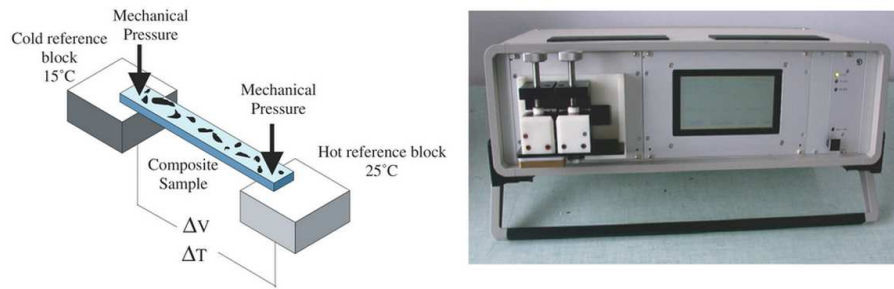


Figure 2.16: TEP measurement schema based on the Seebeck effect, and TEP measurement device [33]

The sample to test is placed between two blocks of pure copper with different temperatures, as illustrated in Figure 2.16: the cold reference block is set at 15°C and the hot reference block at 25°C. Mechanical pressure is applied between the sample and the copper blocks to ensure a good thermal and electric contact. Sample is left aside in the device for a couple of minutes to establish a thermal equilibrium. Due to the Seebeck effect [118], a potential difference between the two junctions sample/copper appears, and is proportional to the thermal gradient. This effect is the basic principle of temperature measurement by thermocouple. In the current experimental setting, the thermal gradient is known, therefore the thermoelectric power of the sample can be deduced from:

$$S_{\text{Sample}} - S_{\text{Reference}} = \frac{\Delta V}{\Delta T} \quad (2.1)$$



where  $S_{\text{Reference}}$  is the TEP of the pure copper blocks which is  $-0.01 \times 10^{-6} \text{ V} \cdot ^\circ\text{C}^{-1}$ . The resolution of the device is close to  $1 \text{ nV} \cdot ^\circ\text{C}^{-1}$ , and the maximal error range is below  $20 \text{ nV} \cdot ^\circ\text{C}^{-1}$  [33]. The measure of TEP is found to be very sensitive to the modifications of lattice structure in the material and to the amount of crystalline defects. For instance, TEP measurement was shown to be a good indicator of strain aging in steels [119]. It was also used to study the phases composition and repartition in a composite [33]. Even if the evolution of TEP with microstructure change is not yet completely understood from a theoretical approach, it constitutes a very sensitive indicator to follow the kinetics of microstructure change phenomenon.

To conclude, the combination of mechanical tests described in the previous section with a thorough investigation of microstructure change by microscopy, X-ray diffraction and TEP measurement provides all the information to characterize the microstructure evolution during hot working. Some correlations between the macroscopic mechanical behavior and the microstructure change can be established by comparing the data sets. The next section will detail further the mechanical response of L-605 during hot deformation, and the resulting mechanical properties after working. Then microstructure change will be illustrated and analyzed by the methods described in the current section, and the mechanisms of deformation and recrystallization will be resolved. Finally, experimental data is used as a basis to establish a physical description of plasticity and recrystallization of L-605 by analytical mean field modeling.







## Chapter 3

# High-temperature mechanical behavior of L-605 alloy



## 3.1 High-temperature compression tests

The mechanical behavior of L-605 was determined at high temperature by uniaxial compression tests, following the experimental conditions described in the previous section. In a first step, empirical models can be applied to estimate the flow stress dependence with forging conditions. Semi-empirical analysis by the Kocks-Mecking model provides the constitutive equations to calculate stress-strain curves for any deformation condition. Further analysis treatment of the data combined with speed jumps tests and relaxation tests provide an estimation of hardening and recovery contributions to dislocation density. These results are key-informations for proper understanding of the microstructural changes described in the next section. As an illustration, the deformation of large size samples is illustrated in the end of this part, showing the technical difficulties to form real-size products.

### 3.1.1 Uniaxial hot compression tests: experimental data

#### 3.1.1.1 Evolution of flow stress with forging conditions

The evolution of stress with plastic strain is illustrated in Figure 3.1. All the curves exhibit a peak stress followed by flow softening. Peak stress occurs later for higher strain rate and lower temperatures. For high temperatures and low strain rate flow softening occur relatively early in the deformation process, giving a very broad and smooth peak stress. Flow softening is mainly attributed to the occurrence of dynamic recrystallization during the compression. Growth of new grains eliminates dislocations and softens the material by boundary migration induced softening (BMIS, page 55).

The flow softening occurring after the peak stress leads to a steady-state regime for strain  $< 1$ , suggesting that the dynamic recrystallization mechanism is discontinuous [31, 99]. During the steady-state, hardening due to the creation of defects by plastic deformation is balanced by the elimination of defects due to dynamic recovery and to discontinuous dynamic recrystallization [96, 107]. The peak stress can be finally interpreted physically as the transition from a mechanical behaviour controlled mainly by hardening before the peak stress, to a behaviour controlled also by dynamic recovery and discontinuous dynamic recrystallization operating jointly at steady-state. Further discussion on compression curves require to separate the contribution of the three effects of hardening, recovery and recrystallization to obtain a quantitative analysis of each metallurgical phenomenon taking place during high temperature deformation process.

Some compression curves exhibit a second hardening stage at large deformation (e.g.  $T=1000^{\circ}\text{C}$   $\dot{\epsilon} = 0.1\text{s}^{-1}$ ). This hardening is usually attributed to the friction between the sample and anvils. A correction procedure was developed to compensate the effect of friction assuming the friction coefficient constant during the deformation [120]. This method provides good results to correct stress for large strain in the case of cobalt alloys [59]. However, in the current data set such a correction was shown to affect also significantly the initial hardening stage, even if friction is known



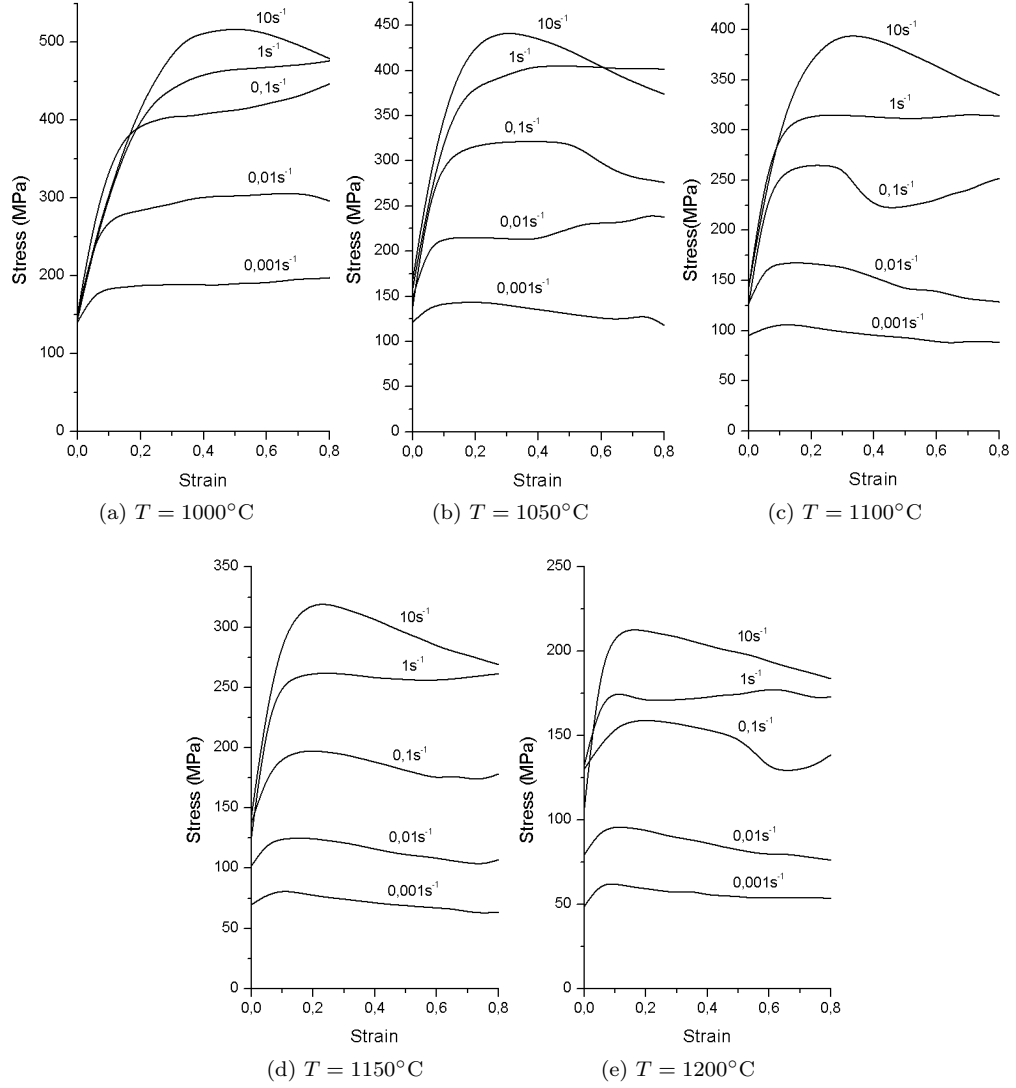


Figure 3.1: Stress - plastic strain curves of L-605 at high temperature

to be negligible at low strain. To allow accurate study of hardening behaviour, friction correction was not performed on the present data to preserve its entire physical informations content.

### 3.1.1.2 Empirical description of flow stress

Steady-state stress values are listed in the Table 3 of Appendix 2. The effect of temperature and strain rate on stress usually follows a power relationship with strain rate and an Arrhenius-type law with temperature (equation 1.8 page 37):

$$\sigma = A \cdot \dot{\epsilon}^m \cdot \exp\left(\frac{Q}{RT}\right) \quad (3.1)$$

with A an empirical constant, m the strain rate sensitivity, and Q the apparent activation energy for deformation. The dependence of steady-state stress  $\sigma_{ss}$  with strain rate is represented in Figure



3.2a: stress evolves with strain rate following a power law, and the average strain rate sensitivity is  $m=0.133$ . The proportionality parameter  $A$  was estimated to be equal to 0.124 from Figures 3.2a and 3.2b. The evolution of flow stress with temperature is described by an Arrhenius-type law with average activation energy for deformation  $Q=87\text{kJ.mol}^{-1}$ , and is illustrated on Figure 3.2b. Table 3.1 indicates the apparent activation energy  $Q$  for some other superalloys and pure metals. The apparent activation energy is very low compared to the activation energy for self-diffusion of pure cobalt ( $260\text{kJ.mol}^{-1}$  for FCC pure cobalt [121, 122]). This value is closer to the activation energy for grain boundary diffusion ( $117\text{kJ.mol}^{-1}$  for FCC pure cobalt [122]). However, it is difficult to determine a distinct metallurgical mechanism attached to this apparent activation energy, as the flow stress is the result of the operation of several conjugated phenomenon such as elastic deformation, hardening, recovery, and recrystallization.

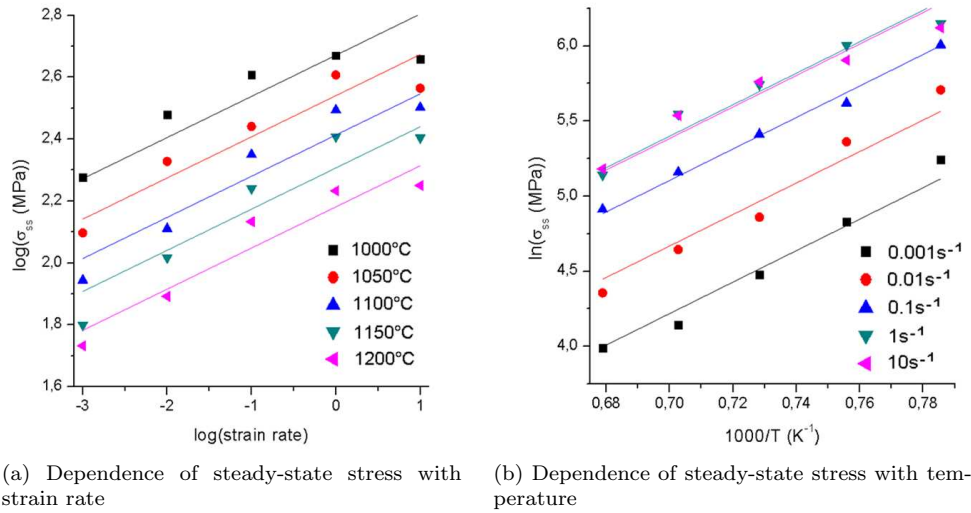


Figure 3.2: Evolution of steady-state flow stress with deformation conditions

Material	$Q$ (kJ.mol <sup>-1</sup> )	Reference
Co-20Cr-15W-10Ni (L-605)	87	-
Co-33Ni-20Cr-10Mo (SPRON)	300 ~ 1000	[117]
Co-29Cr-6Mo	562	[16]
Pure cobalt	254	[66]
Pure copper	100 ~ 200	[76]

Table 3.1: Apparent activation energy for other superalloys between 1000°C and 1200°C

Finally it can be seen that L-605 alloy exhibits a usual viscoplastic behavior, with a decrease of stress values when temperature increases. Moreover flow stress increases with the strain rate due to the positive strain rate sensitivity as usual on most metals [22]. Empirical equations based on power laws are convenient for illustrating stress evolution with deformation parameters at fixed



strain. However the description of the whole compression curve must be achieved by more complex phenomenological laws such as the Kocks-Mecking model. The following part details the data reduction process and provides the constitutive equations of L-605 alloy.

### 3.1.1.3 Kocks-Mecking model: determination of constitutive equations

Compression curves illustrated previously are derived with strain to obtain the hardening rate  $\theta = d\sigma/d\epsilon$ . The  $\theta - \sigma$  curves for  $T=1150^\circ\text{C}$  are illustrated in Figure 3.3. Evolution of  $\theta$  with stress is linear at low strain, as predicted by the Voce law (equation 1.16). The linear domain is followed by a sudden drop of hardening rate and stress due to the onset of recrystallization. Extrapolation of the linear domain at large strain provides an estimation of stress in the absence of recrystallization. Values of steady-state extrapolated stress  $\sigma_V$  are listed in the Table 4 of Appendix 2.

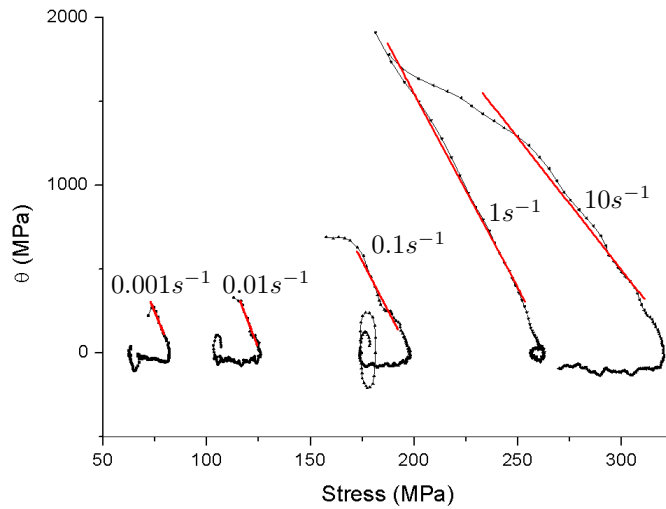


Figure 3.3: Linear decrease of hardening rate with stress following the Voce law at  $T=1150^\circ\text{C}$ : experimental curve (black) and linear fit (red)

The intersection of the linear extrapolation with x-abcissa corresponds to the extrapolated steady-state stress  $\sigma_V$ . This parameter is fundamental as it describes the equilibrium between hardening and dynamic recovery (equation 1.16). The extrapolated stress can be plotted as a function of  $g$  parameter (equation 1.18 page 41):

$$g = \frac{kT}{\mu b^3} \cdot \text{Ln}\left(\frac{\dot{\epsilon}_0}{\dot{\epsilon}}\right) \quad (3.2)$$

with  $\mu$  the shear modulus obtained from Figure 1.30b [19] and  $\dot{\epsilon}_0$  a parameter to fit in order to obtain a linear dependence of  $\log(\sigma_V/\mu)$  with  $g$  [22]. The optimal value of  $\dot{\epsilon}_0$  was found to be  $10^9\text{s}^{-1}$ : the experimental points of Figure 3.4 decrease linearly with  $g$ . This behaviour is in agreement with the results of Kocks and Mecking on pure copper and other FCC metals [22] (Figure 1.38). The linear fit with  $g$  and its equation are illustrated in Figure 3.4.



Steady-state effective stress  $\sigma_{ss}$  can be represented as a function of  $g$  as well. However the fit quality is poor because Kocks-Mecking model do not consider the occurrence of dynamic recrystallization and its effect on flow stress. Yield stress decreases with temperature and strain rate. Yield stress also can be fitted with  $g$  parameter, but  $\log(\sigma_y/\mu)$  does not follow a linear relationship with  $g$ . Indeed the physical phenomenon implicated in the variation of  $\sigma_y$  with temperature and strain rate are unknown (grain growth, dynamic strain aging), and may be a combination of several mechanisms. Therefore, yield stress cannot be interpreted through the Kocks-Mecking model. The nature of the fit  $\log(\sigma_y/\mu)=f(g)$  is purely empirical, and has no reason to follow a linear relationship. However it is convenient to gather yield stress data in a single plot with  $g$  parameter, and the fit  $\log(\sigma_y/\mu)=f(g)$  can be properly used to extrapolate yield stress for unknown conditions.

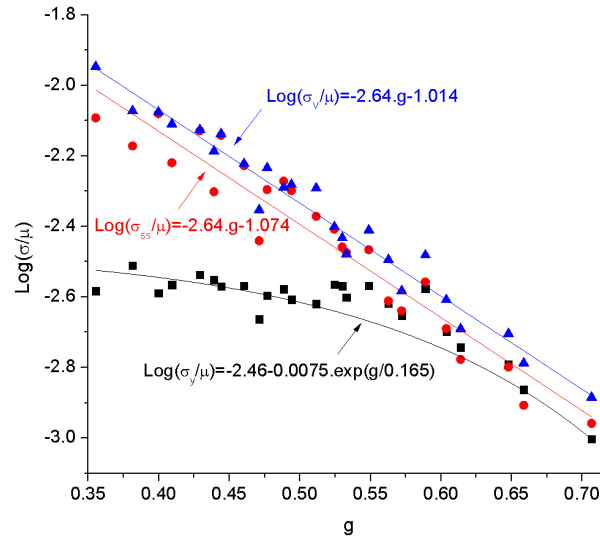


Figure 3.4: Evolution of steady-state extrapolated stress  $\sigma_V$ , steady-state flow stress  $\sigma_{SS}$  and yield stress  $\sigma_y$  with  $g$  parameter

The value of  $\theta$  when  $\sigma = \sigma_y$  is the initial hardening rate  $\theta_0$  for  $\epsilon \rightarrow 0$ , and is supposed to depend on temperature solely. The normalized hardening rate  $\theta_0/\mu$  is the second fundamental parameter to describe plasticity, and represents the hardening behaviour of the material (equivalent to  $k_1$  in equation 1.16). The average value of normalized hardening rate is found to be around 0.04, however  $\theta_0/\mu$  is not a constant and depends on both temperature and strain rate, as illustrated in Figure 3.5a. Normalized hardening rate varies with the  $g$  parameter following a gaussian equation, as illustrated in Figure 3.5b. Hardening rate increases by a factor 7 from 0.01 to 0.07 with increasing  $g$ , and then drops from 0.07 to about 0.03 for a  $g$  parameter above 0.5. This effect must be taken into account in order to reproduce properly the mechanical behaviour.

This phenomenon may be due to the occurrence of dynamic strain aging: solute elements interact with dislocations and affect the hardening rate. The segregation of elements at stacking faults in



cobalt superalloys was reported in the literature [117]. At low strain rate, dislocation speed is much lower than the solute elements diffusion speed. Therefore, segregation would not affect dislocations motion, and the hardening rate remain unchanged. With increasing strain rate, the dislocations speed increases, and dislocations may interact with solute elements for a critical value close to the elements diffusion speed. For higher strain rate, dislocations move fast enough to hinder the segregation, and recover some mobility.

For high temperature ( $T > 1150^\circ\text{C}$ ), normalized hardening rate is quite constant, with a value about 0.01. It can be assumed that due to the high diffusion speed of solute elements, segregation at dislocations does not occur, and normalized hardening rate remains unchanged. With decreasing the temperature, diffusion speed decreases, and therefore the critical strain rate at which dislocations interact with solute elements decrease. To conclude, the consideration of dynamic strain aging gives a fair interpretation of the initial hardening rate variations observed experimentally. However, this mechanism should be confirmed by an extensive investigation of the dislocation structure by transmission microscopy.

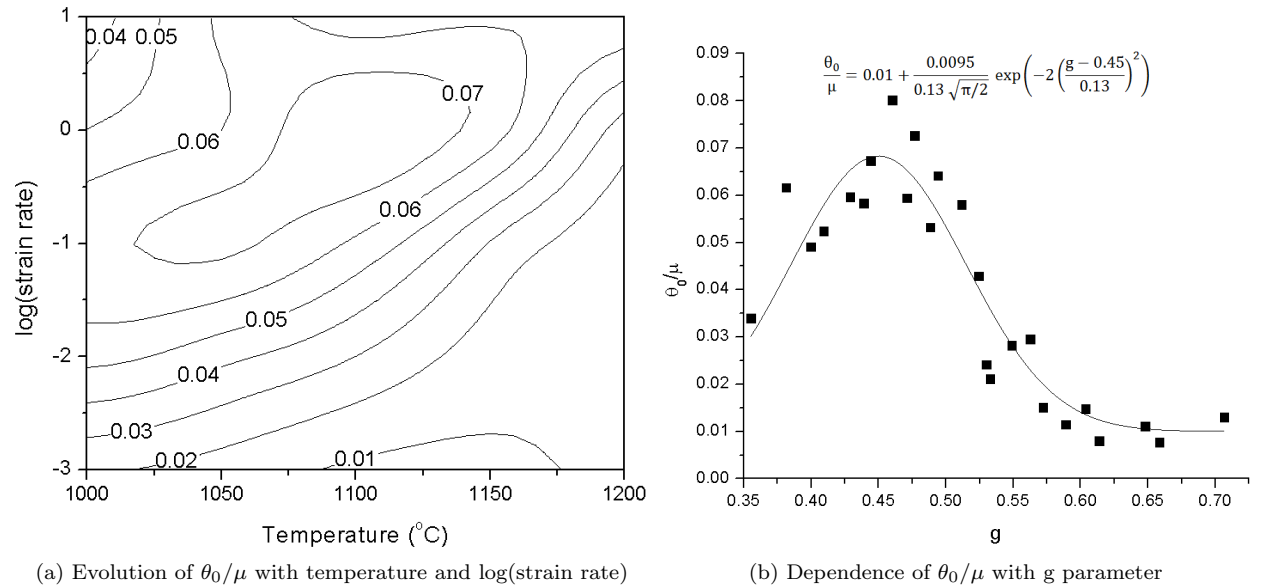


Figure 3.5: Evolution of normalized hardening rate  $\theta/\mu$  with deformation conditions

Figure 3.6 represents some experimental compression curves and the corresponding calculated curves from the equation 1.17. Calculation was made by using the parameters  $\sigma_y$ ,  $\sigma_V$  and  $\theta_0$  obtained from the analysis of experimental curves. The calculated curves are in good agreement with the experimental data.

To sum up, the mechanical behavior of L-605 material can be determined by the set of the three following equations giving the extrapolated steady-state stress, the yield stress and the normalized hardening rate:



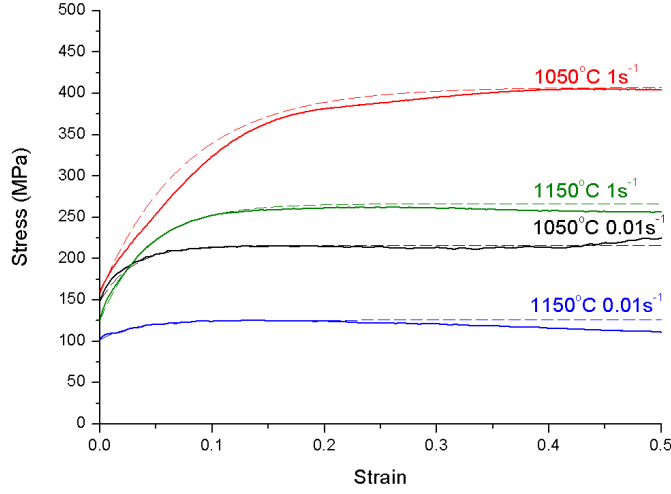


Figure 3.6: Comparison of experimental curves (solid) and Voce law fits (dashed)

$$\begin{cases} \text{Log}\left(\frac{\sigma_V}{\mu}\right) = -2.64.g - 1.014 \\ \text{Log}\left(\frac{\sigma_y}{\mu}\right) = -2.46 - 0.0075.\exp(g/0.165) \\ \theta_0/\mu = 0.01 + \frac{0.0095}{0.13\sqrt{\pi/2}} \cdot \exp\left(-2\left(\frac{g-0.45}{0.13}\right)^2\right) \end{cases} \quad (3.3)$$

To conclude, the Voce law combined with the Kocks-Mecking model enable to predict compression curves for a large scale of deformation conditions with a minimum of parameters. As expected in the Kocks-Mecking model,  $\sigma_V$  can be fitted with the  $g$  parameter, and the fit equation is the constitutive equation of the material. Yield stress is decreasing with temperature and increasing with strain rate, and an empirical fit with  $g$  parameter was proposed. Normalized hardening rate was shown to vary with  $g$  as well, which is an unusual behavior attributed to the effect of dynamic strain aging.

### 3.1.2 Estimation of dislocation density from flow stress

From the data collected by compression tests, it is possible to estimate the dislocation density from the flow stress using the Taylor relation (equation 1.14):

$$\sigma = M\alpha\mu b\sqrt{\rho} \quad (3.4)$$

with  $M \approx 3$  for FCC,  $b$  the magnitude of the Burgers vector and  $\alpha$  a constant.

For FCC metals, the magnitude of the Burgers vector is taken as the half inter-atomic distance in the direction [110]. Therefore  $b = a\sqrt{2}/2$ , with  $a$  the lattice parameter. The density of L-605 alloy is  $d = 9.2 \text{ g.cm}^{-3}$  at room temperature according to the L-605 datasheet (Carpenter Tech. Corp.). The atomic composition of L-605 is 59.45% Co- 24.5% Cr- 10.85% Ni- 5.2% W, so the mean molar mass



is  $M=63.7 \text{ g.mol}^{-1}$ . As a consequence, the lattice parameter and the Burgers vector magnitude are:

$$a = \left( \frac{4M}{d \cdot N_A} \right)^{1/3} = 3.58.10^{-8} \text{m} \quad (3.5)$$

$$b = \frac{a\sqrt{2}}{2} = 2.53 \text{\AA} \quad (3.6)$$

For comparison, the Burgers vector magnitude is  $2.50 \text{\AA}$  for pure cobalt [122], and  $2.54 \text{\AA}$  for pure copper [30].

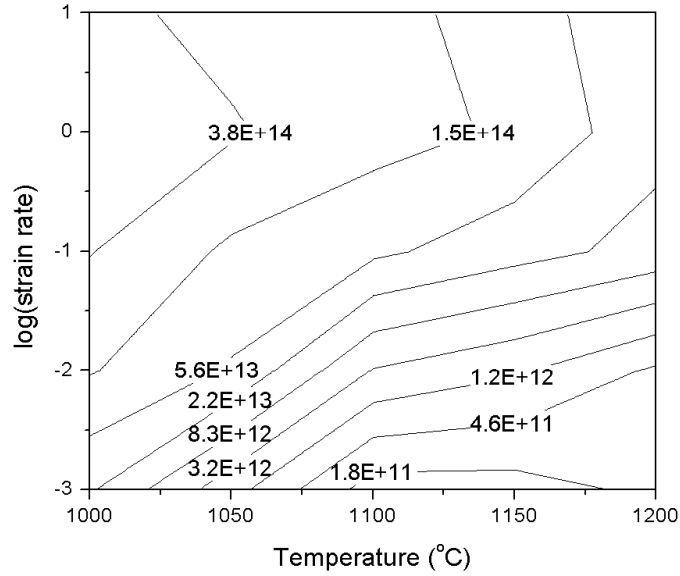


Figure 3.7: Map of the estimated dislocation density at the steady-state versus temperature and strain rate

Yield stress is obtained from the equation  $\sigma_y = f(g)$  in Figure 3.4 in order to remove the variations due to experimental measurement error. The steady-state stress is taken as the experimental stress at strain  $\epsilon = 0.8$  on the compression curves. Therefore the plastic stress is the difference between the steady-state stress and the yield stress, and can be injected in equation 3.4 to calculate the dislocation density at steady-state. Calculation was proceeded with setting the parameter  $\alpha$  to 0.3, which corresponds to the value used for copper in literature [30]. The estimated dislocation density at the steady-state is illustrated in Figure 3.7. Dislocation density decreases with temperature due to the increase of dynamic recovery. Dislocation density also increases with strain rate: because the dislocations move faster, interaction time between dislocations is lower and therefore dynamic recovery is hindered.

### 3.1.3 Effect of initial grain size

Compression tests were carried out on L-605 with different initial grain sizes. Stress-plastic strain curves are shown in Figure 3.8. Compression curves corresponding to grain size  $86 \mu\text{m}$  and  $118 \mu\text{m}$



are relatively similar, and illustrate the fair reproducibility of compression tests. Deviation from the mean trend is sometimes observed, like on Figure 3.8d, and can be attributed to a difference of friction coefficient. Tests carried out on grain size about 1mm shows similar mechanical behavior, but with larger difference compared to other curves. Mechanical test on such a coarse microstructure is not valid for studying the hardening behavior: the small amount of grains contained in the sample (only about 1200 grains per sample) leads to very anisotropic deformation due to statistic effects. Grain size  $3\mu\text{m}$  shows the maximal discrepancy with other curves: especially stress is abnormally low for low strain rate (Figures 3.8a and 3.8c). This result is quite unexpected as it is in contradiction with the Hall-Petch law which expects larger yield stress for finer grains. This fact can be explained by the occurrence of grain boundary sliding: this phenomenon is common for highly-refined microstructure at high temperature, and enable deformation with reduced grains plasticity. In addition, for low strain grain growth can occur jointly with the deformation and lower the yield stress during the compression process

Compression curves at  $1000^\circ\text{C}$   $\dot{\epsilon}=10\text{ s}^{-1}$  shows an increase of yield stress with decreasing grain size, in agreement with the Hall-Petch law, with a stress increment above 100MPa for a grain size reduction from about  $100\mu\text{m}$  to  $3\mu\text{m}$ . However such a trend is not confirmed for other temperatures and strain rates. The stress change due to grain refinement is usually within the error range, or hidden by other mechanisms such as grain boundary sliding. As a consequence the effect of grain size on the high-temperature mechanical properties can be safely neglected for the current experimental conditions, and the Hall-Petch law does not hold at such high temperatures.

### 3.1.4 Interrupted compression tests

Interrupted compression tests were carried out to characterize the mechanical properties of L-605 alloy during isotherm relaxation. Such a test is interesting because it helps to understand the kinetics of recovery and provide some relevant informations on dislocations motion. To achieve such experiment, a regular compression test is carried out, and at a defined strain (here  $\epsilon \approx 0.1$  and  $0.4$ ) the compression is paused during 10 s. The resulting compression curves are illustrated on Figure 3.9 for two temperatures and two strain rates. Stress is found to drop of about 50% of its initial value after 10 s relaxation. Table 3.2 lists the stress value and the stress drop during the relaxation step.

During relaxation process, the global strain remains constant, and stress decreases gradually with time [123, 124]. As a consequence, the total strain rate is null:

$$\dot{\epsilon} = \dot{\epsilon}_e + \dot{\epsilon}_p = 0 \iff \dot{\epsilon}_p = -\dot{\epsilon}_e = -\frac{\dot{\sigma}}{E_a} \quad (3.7)$$

with  $\dot{\epsilon}_e$  the elastic strain rate,  $\dot{\epsilon}_p$  the plastic strain rate and  $E_a$  the combined elastic constant of specimen and machine. In the current situation, the apparent elastic constant is estimated to 11.5



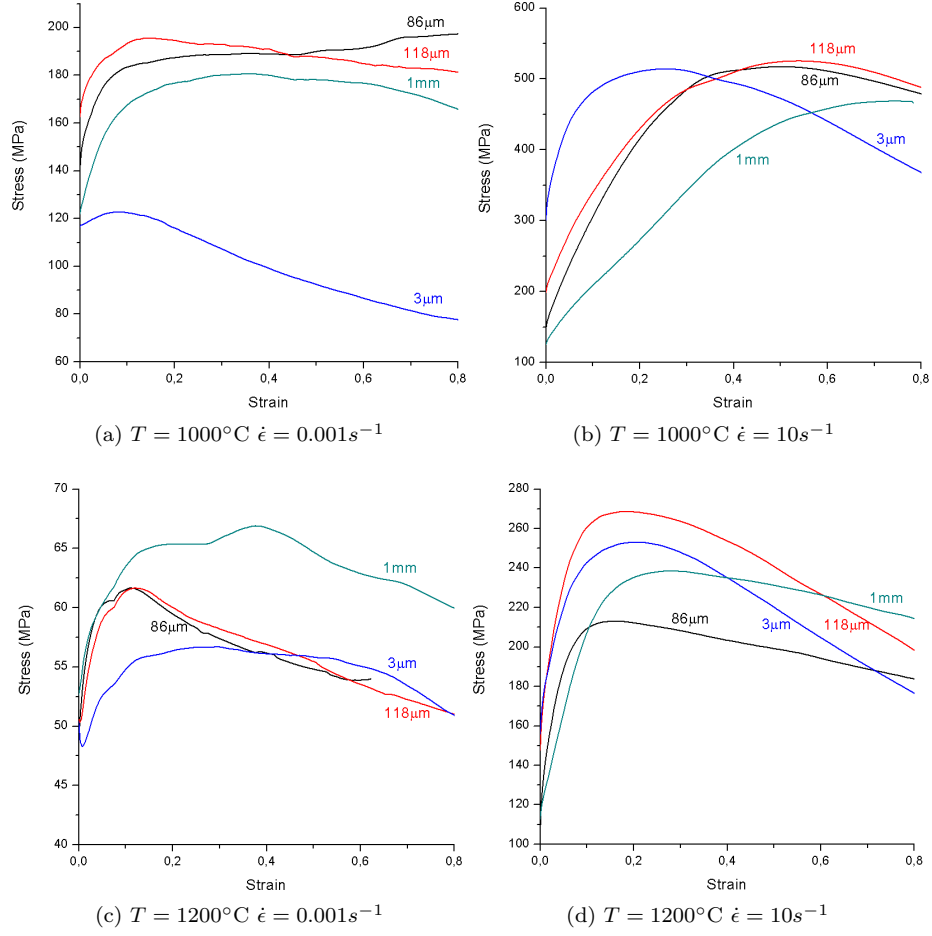


Figure 3.8: Stress - plastic strain curves of L-605 at high temperature

GPa by linear fit of stress-strain curves in the elastic domain. Plastic strain rate at  $t=10\text{s}$  is found to be 10 to 100 times lower than the initial strain rate imposed during the compression, and calculated values are listed in the Table 3.2. This estimation is especially interesting because it is linked to the dislocations speed and the dislocation recovery rate by the relation [125, 126]:

$$\dot{\epsilon}_p = \alpha b \bar{\rho} \bar{v} + \alpha b \bar{\rho} \dot{\Lambda} \quad (3.8)$$

with  $\alpha$  a geometric constant,  $b$  the magnitude of Burgers vector,  $\bar{\rho}$  the average dislocation density estimated by the Taylor formula (equation 1.14), and  $\Lambda$  the mean free path of dislocations. The structure is usually assumed to be constant due to the low increase of plastic strain during the relaxation process. Therefore one can neglect the term  $\dot{\rho}$  in a first order approximation. As a result, the dislocation speed can be roughly estimated by:



$$\alpha \cdot \bar{v} = \frac{\dot{\epsilon}_p}{b\bar{\rho}} = -\frac{\dot{\sigma}}{E_a \cdot b\bar{\rho}} \quad (3.9)$$

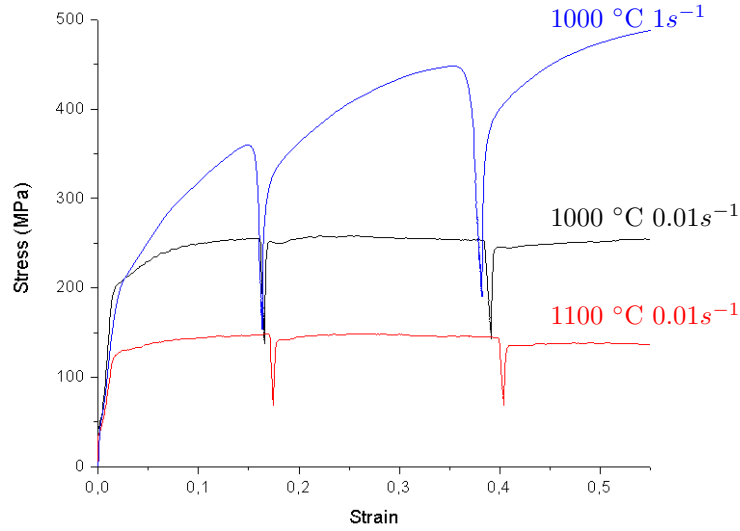


Figure 3.9: Relaxation of 10 seconds during compression deformation

Test	Strain	$\sigma_y$ (MPa)	$\sigma$ (MPa)	$\Delta\sigma$ (MPa)	$\rho(m^{-2})$	$\dot{\epsilon}(s^{-1})$	$\alpha \cdot \bar{v}(m \cdot s^{-1})$
1000°C 0.01s <sup>-1</sup>	0.16	190	255	116	$2.5 \times 10^{13}$	$10^{-3}$	$2 \times 10^{-7}$
1000°C 0.01s <sup>-1</sup>	0.38	190	254	110	$2.5 \times 10^{13}$	$10^{-3}$	$2 \times 10^{-7}$
1000°C 1s <sup>-1</sup>	0.15	190	359	206	$1.7 \times 10^{14}$	$2 \times 10^{-3}$	$4 \times 10^{-8}$
1000°C 1s <sup>-1</sup>	0.36	190	448	257	$4.1 \times 10^{14}$	$2 \times 10^{-3}$	$2 \times 10^{-8}$
1100°C 0.01s <sup>-1</sup>	0.17	115	148	80	$7.6 \times 10^{12}$	$7 \times 10^{-4}$	$4 \times 10^{-7}$
1100°C 0.01s <sup>-1</sup>	0.4	115	145	76	$6.3 \times 10^{12}$	$7 \times 10^{-4}$	$4 \times 10^{-7}$

Table 3.2: Flow stress drop during 10s relaxation tests

The calculated values of  $\bar{\rho}$  and  $\alpha \cdot \bar{v}$  are listed in the Table 3.2. Assuming the  $\alpha$  constant close to unity, the order of magnitude of dislocation speed is found to be between  $10^{-7}$  and  $10^{-8} m \cdot s^{-1}$ . In other words, dislocations travel 0.1 to 1 times their mean free path  $\Lambda = \bar{\rho}^{-1/2} \approx 10^{-7} m$  every second. Therefore a relaxation of 10s is likely to involve significant recombination of dislocation pairs, and the term  $\dot{\bar{\rho}}$  is probably effectively not negligible for relaxation longer than few seconds. It can be concluded that during the cooling step of compression experiments, the dislocation structure is expected to change significantly. Some experiments with different cooling speeds would be required to study the post-dynamic microstructure changes during the quench step (page 139).



### 3.1.5 Speed jump experiments

Speed jumps experiments were carried out from Ø9.77mm Carpenter L-605 material, with an initial mean grain size of 118  $\mu\text{m}$ . Experimental procedure is described in the section 2.2 page 67. As the experimental conditions and the initial material properties are slightly different (initial mean grain size 35% larger), the compression curves do not match exactly the data presented previously, and curves must be treated separately. The first part of this section provides the constitutive equations for the Ø9.77mm Carpenter material. Then in a second step, the parameters obtained from the Kocks-Mecking model are used to analyse the speed jump experiments and predict the flow stress change.

#### Treatment of the compression curves obtained with Gleeble device

Compression curves are illustrated in the Appendix 2 page 191 (Figure 7). The compression curves are derived with strain to obtain the hardening rate  $\theta$ , and hardening rate is plotted versus stress. Hardening rate decreases linearly with stress (Figure 3.10a), in agreement with the previous results (Figure 3.3). The fit of the linear part provides the steady-state stress  $\sigma_V$  and the normalized initial hardening rate  $\theta_0/\mu$ .

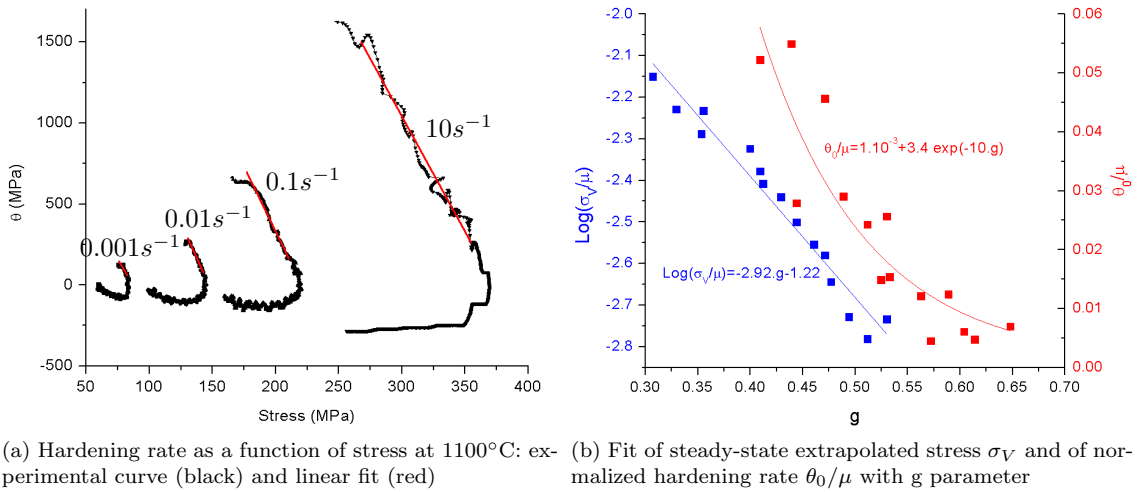


Figure 3.10: Determination of extrapolated steady-state stress and normalized hardening rate for Gleeble data

The two parameters  $\sigma_V$  and  $\theta_0/\mu$  depend on both temperature and strain rate, and can be gathered into a single plot versus the  $g$  parameter following the Kocks-Mecking method. The parameter  $\dot{\epsilon}$  optimal value was found to be about  $10^7 \text{s}^{-1}$ : for this value the experimental points of  $\text{Log}(\sigma_V/\mu)$  can be fairly approximated by a linear decay with  $g$  parameter. The normalized hardening rate is found to decrease with increasing  $g$  (i.e. increasing temperature and decreasing strain rate), in agreement with previous results. This variation is attributed to the dynamic strain aging effect:



initial hardening rate increase with increasing stress. Compression could not be performed at low temperature and high strain rate, due to the very high hardness of the sample, leading to a rupture of tungsten carbide anvils. Therefore no data is available to confirm the decrease of  $\theta_0/\mu$  for high values of  $g$  parameter. As a consequence, the variation of  $\theta_0/\mu$  with  $g$  was approximated by a simple exponential equation, indicated in Figure 3.10b.

### Speed jump experiments and Kocks-Mecking model

Speed jumps experiments are a conventional test to determine the isostructural strain rate sensitivity at constant dislocation density  $m = (\frac{\partial \ln \sigma}{\partial \ln \dot{\epsilon}})_{\rho, T}$  (Equation 1.22 page 43) [25]. During the speed jump test, dislocation density is assumed to be constant, and the strain rate increment is supposed to follow a sharp variation. In practice, dislocation density changes during the jump, and the strain rate increment is sluggish due to acceleration of the machine ram. Figure 3.11a illustrates the increment of strain rate during speed jumps carried out on the Gleeble device: strain rate increment proceeds in a time laps between about 0.1 to 0.4s. For instance, in a material with dislocation density about  $10^{12} m^{-2}$ , dislocations move with a speed  $v \approx \dot{\epsilon}/\rho b \approx 10^{-5}$  to  $10^{-4} m.s^{-1}$ , and have the time to travel about 4 to 40 times their mean free path  $\Lambda = \rho^{-1/2}$  during an acceleration of 0.1s. As a consequence, the conservation of the structure during the jump cannot be certified during the jump, and the equation 1.21 may not necessarily hold for the current experimental conditions. Finally, the stress increase should be predictable by the conventional Kocks-Mecking model solely, regardless of the Cottrell-Stokes law.

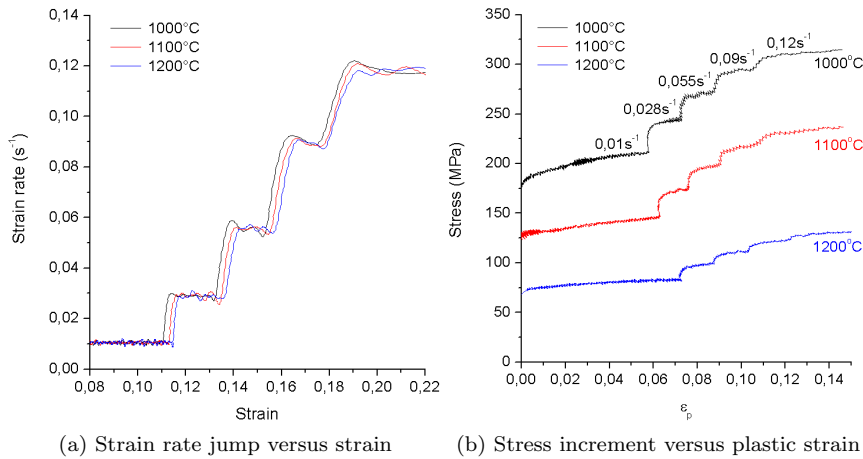


Figure 3.11: Strain rate jumps and induced stress jumps with changing temperature

Experimental strain rate is used to calculate the  $g$  parameter of the Kocks-Mecking model, with  $\dot{\epsilon} = 10^{-7} s^{-1}$  (Figure 3.10b). From  $g$  parameter, the value of the extrapolated stress  $\sigma_V$  and of nor-



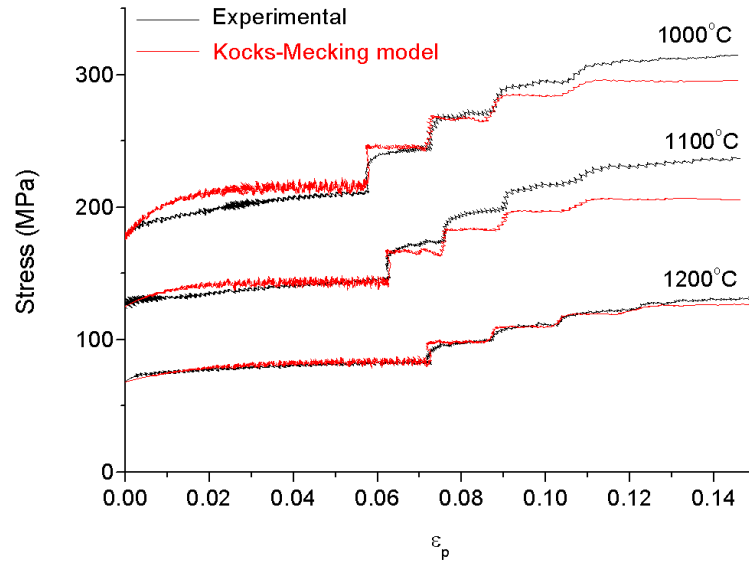


Figure 3.12: Stress jump calculated by Kocks-Mecking model

malized hardening rate  $\theta_0/\mu$  can be deduced using the equations of Figure 3.10b. Inserting these two calculated parameters into the equation 1.17 provides an estimation of flow stress evolution during jumps. Figure 3.12 represents the experimental stress-strain curves in black, and the calculated curves in red. Kocks-Mecking model is in good agreement with experiment and describes properly the stress jumps. Some discrepancy can be observed for large strains, for example on the curve  $T=1100^\circ\text{C}$ , due to the cumulative error at each jump. However the height of stress jumps is always of the same magnitude as the one observed experimentally. As a result, Kocks-Mecking model is considered to be sufficient for describing flow stress evolution, and is still applicable for predicting stress during fast strain rate change. This conclusion is very important, because the equations 3.3 of the Kocks-Mecking model will be reused for the modeling part (page 148). These equations would be still be valid in more complex deformation modes including strain rate jumps, like in industrial processes.

### 3.1.6 Vickers hardness after hot deformation

Vickers hardness was tested on the middle area of the samples after hot compression. Tests were carried out 5 times for each sample, with a load of 9.807N during 10s. The average hardness was determined, with an accuracy of  $\pm 2\%$ .

The average Vickers hardness is represented on Figure 3.13. The map has a bow shape, and maximal hardness is reached for intermediate strain rate and temperature lower than  $1100^\circ\text{C}$ . Base metal has usually a Vickers hardness in the range 200-300HV, but deformation at low temperature enable to harden the material above 400HV.



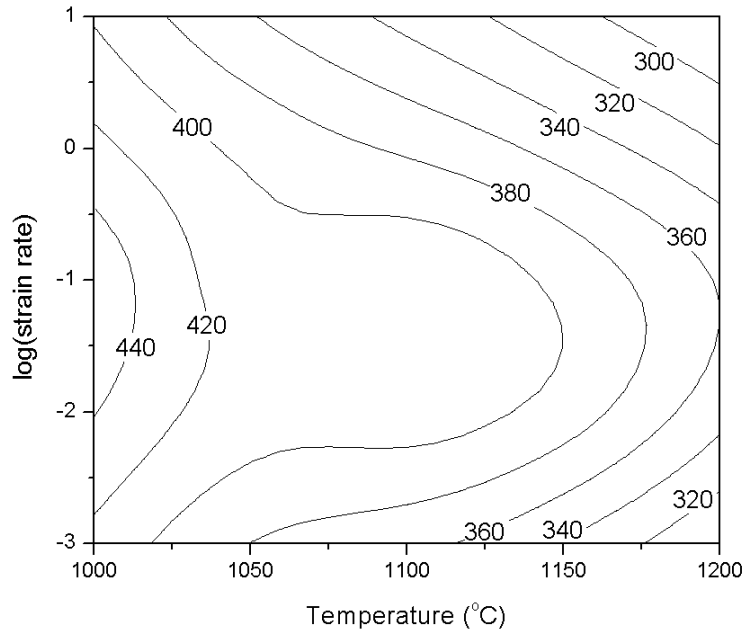


Figure 3.13: Vickers hardness of samples after hot compression at  $\epsilon = 0.8$  versus temperature and strain rate

There can be several explanations to such a hardening at low strain rate. The formation of small grains at low temperature could harden the material by grain refinement, and increase hardness. Also, at temperature close to  $1000^{\circ}\text{C}$ , precipitation is not excluded, and could harden the material as well. Finally, dynamic recrystallization usually softens the material at high temperature. Consequently, the conditions for high hardness may correspond to a low activity of dynamic recrystallization. The exact origin of hardening at low temperature will be fully understood in the next sections with the study of microstructure changes.

### 3.1.7 Forging of large samples under non-isotherm conditions: the industrial reality

Large samples of  $\varnothing 33\text{mm}$  diameter were forged with a 300T hydraulic press following the procedure described in Figure 2.11. The samples were warmed up 10min at  $1280^{\circ}\text{C}$ , and then the compression was carried out with a constant ram speed. Due to the cooling by heat conduction with the anvils, the sample cools down during the compression with a speed about  $-5^{\circ}\text{C.s}^{-1}$ . The compression was carried out until a strain of  $\epsilon = 1$  for a ram speed of  $0.33\text{mm.s}^{-1}$  ( $\dot{\epsilon} \sim 0.01\text{s}^{-1}$ ) and  $33\text{mm.s}^{-1}$  ( $\dot{\epsilon} \sim 1\text{s}^{-1}$ ). Figure 3.14 shows the sample after compression. For a compression at speed  $0.33\text{mm.s}^{-1}$ , the sample cools down until a temperature about  $550^{\circ}\text{C}$  during the compression, then it breaks before  $\epsilon = 1$  due to the loss of ductility. For a compression speed of  $33\text{mm.s}^{-1}$ , the sample cools down to about  $1000^{\circ}\text{C}$ , and the deformation occurs without fracture. As a result, the forgeability of L-605 at a strain rate  $\dot{\epsilon} < 1\text{s}^{-1}$  is quite poor due to technical reasons related with cooling. In hot deformation



devices like the Thermecmaster-Z or Gleeble, this difficulty did not appear because a heating system is set. However industrial forging is frequently operated on a simple hydraulic press without heating system, and the effect of cooling can severely narrow the suitable deformation conditions range.



Figure 3.14: Compression of 33mm diameter L-605 samples at  $T < 1280^{\circ}\text{C}$ : on the left compression at speed  $33\text{mm.s}^{-1}$   $\epsilon = 1$ , on the right compression at speed  $0.33\text{mm.s}^{-1}$  until rupture

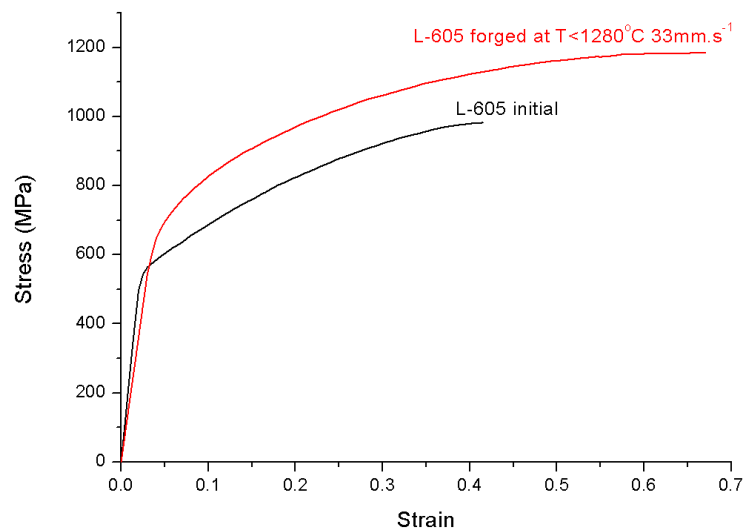


Figure 3.15: Tensile test stress-strain curves of L-605 initial (Carpenter  $\varnothing 15.87\text{mm}$ ) and of L-605 forged at  $T < 1280^{\circ}\text{C}$   $33\text{mm.s}^{-1}$

Tensile test samples were cut from the middle part of the forged sample deformed at speed  $33\text{mm.s}^{-1}$ . Three tensile tests were carried out, and the average stress-strain curve is illustrated on Figure 3.15. The ultimate tensile stress is  $1180 \pm 4\text{MPa}$ , and the maximal strain is  $0.67 \pm 0.015$ . For comparison, the stress-strain curve of L-605 initial material (Carpenter,  $\varnothing 15.87\text{mm}$  and grain size  $53\text{ }\mu\text{m}$ ) is illustrated on the same figure. The forging process leads to an ultimate tensile stress increase of 20% larger and a maximal elongation 60% larger than in the initial material. The yield stress is about  $630\text{MPa}$ , and is 18% larger than in the initial material. Therefore the increase of strength is mainly due to the increase of yield stress, and can be attributed to some grain refinement by recrystallization during the hot working process.



The increase of ductility with the hot working process is quite unusual. It would be expected that due to the hot working process, grain refinement occurs and lowers the maximal elongation. The increase of ductility may be attributed to the decrease of the strain localization during the tensile test. During tensile test on large grain size samples (Figure 3.15), the plasticity generates a significant surface roughness and leads to the rupture. For smaller grain size, this effect vanishes, and the elongation measured is larger due to a better homogeneity of the deformation. On the next section (page 112), tensile tests are carried out on annealed L-605 with a smaller grain size, and in this case the ductility decreases with decreasing the grain size, following the usual behaviour reported in literature (Figure 1.33b).

### 3.1.8 Conclusions

L-605 follows a usual viscoplastic deformation behavior at high temperature: stress increases with strain rate and decreases with temperature. Compression curves exhibit a peak stress followed by flow softening, and stabilizes to a steady-state stress value. This behavior is typical of the occurrence of dynamic recrystallization: at large strain the formation of new grains softens the material. Stress was shown to be weakly sensitive with grain size, and the Hall-Petch law does not hold at high temperature. Flow stress was properly described by the Kocks-Mecking model: even in complex experimental situations such as speed jump tests, the flow stress prediction is excellent. Fits of experimental data provide the normalized hardening rate  $\theta_0/\mu$  and the extrapolated steady-state stress  $\sigma_V$ . These two parameters are fundamental for describing the plasticity of L-605 alloy. Especially, the constitutive equation  $\sigma_V = f(g)$  indicates the ratio between recovery and hardening for any deformation condition. As a conclusion, Kocks-Mecking model is a very powerful tool to proceed to data reduction and to determine plasticity behaviour.



## 3.2 Analysis of flow stress and flow softening

During high temperature deformation, dynamic recovery and dynamic recrystallization can occur and affect both the microstructure and the final use properties. Such dynamic processes are conventionally comprehended by using Dynamic Materials Model (DMM) ([21], Cf page 39). This method is based on irreversible thermodynamics and is helpful for selecting optimal process conditions. It was used for cobalt superalloys [59] to determine stable flow process conditions. In addition to this method, a second approach based on the analysis of flow softening will be developed here. This technique was successfully applied on steels [24] and provides a fair estimation of recrystallized fraction during high temperature deformation.

### 3.2.1 Processing maps

The first method to determine optimal hot working process parameters is by using processing maps. The efficiency of power dissipation  $\eta$  (equation 1.12 [20]) and the instability parameter  $\xi$  (equation 1.13 [75, 21]) are plotted into 2D maps versus temperature and  $\log(\dot{\epsilon})$  for a corresponding strain level  $\epsilon=0.6$  [20, 59]. The power dissipation map and instability map are given in Figures 3.16. Dynamic recrystallization is usually considered to take place for an efficiency of dissipation in the range 30-50% [22]. From the power efficiency map (Figure 4a) it is expected to observe dynamic recrystallization for temperature above  $1000^{\circ}\text{C}$  and strain rate between  $0.001\text{s}^{-1}$  and  $0.1\text{s}^{-1}$ . On the other hand, power efficiency is very low for strain rate higher than  $1\text{s}^{-1}$ , therefore few "dynamic metallurgical processes" [20] are expected for such conditions, and thus dynamic recrystallization should not occur at high strain rate.

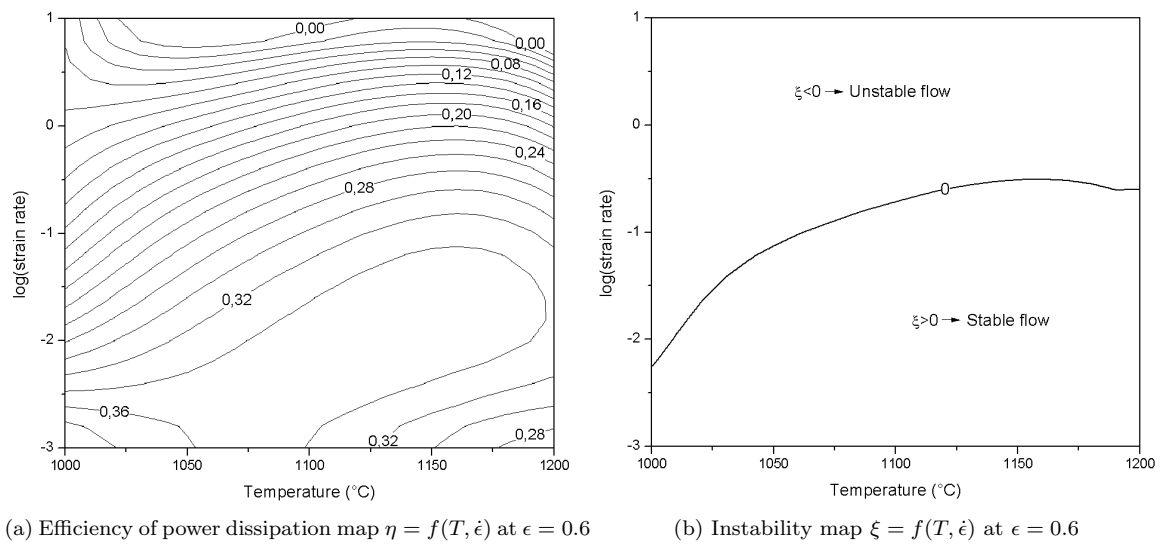


Figure 3.16: Processing maps of L-605 alloy in the range  $1000\text{-}1200^{\circ}\text{C}$   $0.001\text{-}10\text{s}^{-1}$



Unstable flow conditions are detected if the parameter  $\xi < 0$ . The instability map (Figure 4b) indicates unstable conditions for strain rate above  $0.1s^{-1}$ . The corresponding deformation conditions are then supposed to be unfavourable due to the occurrence of these instabilities. A first type of instabilities is adiabatic shear bands and flow localization [21], which can lead to a strongly heterogeneous microstructure detrimental for structural applications. Another type is cracks, of course to proscribe as well. Therefore, instability map is a representation of the deformation conditions for which there is a noteworthy risk to observe instabilities.

### 3.2.2 Softening maps: a new representation of flow stress contributions

The following approach is based on the separation of the contribution of hardening and dynamic recovery in one hand, and dynamic recrystallization in the other hand. Thereof we can evaluate the effect of dynamic recrystallization on mechanical behavior, and quantify the progress of dynamic recrystallization process.

During high-temperature deformation of FCC metals, flow stress usually follow the Voce law (equation 1.16): hardening rate  $\theta$  decreases linearly with flow stress. As it was demonstrated in the previous section, it is possible to extrapolate the curve  $\theta = f(\sigma)$  to determine the saturation stress  $\sigma_V$  (Figure 3.3). The extrapolated stress  $\sigma_V$  is the stress that would be observed experimentally if softening mechanisms such as recrystallization were not occurring. As a consequence, the fractional softening corresponding to the difference between this extrapolated stress and the experimental steady-state stress is representative of the activity of softening metallurgical processes. Fractional flow softening is defined as:

$$S = \frac{\Delta\sigma}{\sigma} = \frac{\sigma_V - \sigma_{ss}}{\sigma_V} \quad (3.10)$$

with  $S$  the fraction of flow softening, and  $\sigma_{ss}$  the experimental steady-state stress taken as the stress at  $\epsilon = 0.8$ . Figure 3.17 represents the flow softening evolution with temperature and strain rate. Three main domains can be identified on the softening map:

- For  $T > 1050^\circ\text{C}$   $\dot{\epsilon} < 0.1s^{-1}$ , flow softening is between 10 and 20%, therefore dynamic recrystallization is strongly expected to occur.
- For  $T > 1000^\circ\text{C}$   $\dot{\epsilon} > 1s^{-1}$ , flow softening increase with strain rate until 20%, and recrystallization may occur also for these conditions. However some other softening mechanisms could be responsible of flow softening at high strain rate (e.g. adiabatic heating, cracks or shear bands), and it cannot be excluded that several softening mechanisms occur jointly.
- For  $T < 1100^\circ\text{C}$   $0.1 < \dot{\epsilon} < 1s^{-1}$ , flow softening is lower than 10%, and recrystallization is not expected to occur.



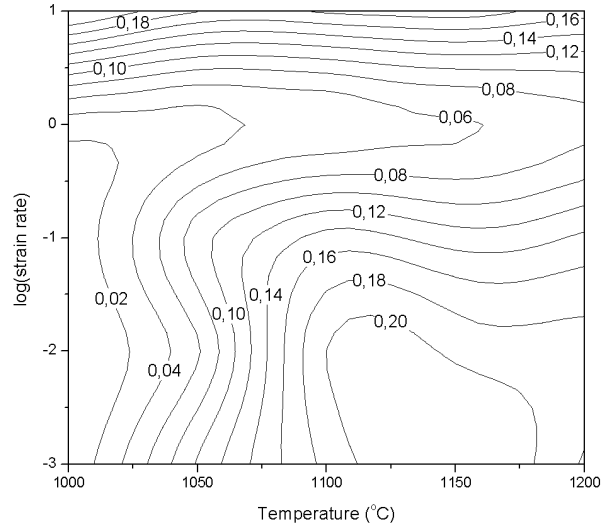


Figure 3.17: Softening map of L-605 alloy in the range 1000-1200°C 0.001-10s<sup>-1</sup>

Flow softening is a parameter making the link between macroscopic mechanical properties and microstructure changes. Extrapolation of steady-state stress  $\sigma_V$  and  $\sigma_{ss}$  could reasonably provide fair conjecture about the operation of recrystallization over the experimentally tested deformation conditions. Therefore the thorough study of flow softening provides sufficient prediction power to determine the deformation conditions on which dynamic recrystallization is taking place. Flow softening map provides some relevant information on the microstructure change with more physical comprehension than conventional processing maps. This method should be used jointly with processing maps to provide sufficient accuracy and predictability on the resulting microstructure after high-temperature deformation.

### 3.2.3 Conclusions

Deformation behavior was determined by applying the Dynamic Materials Model. Flow is stable at strain lower than  $\dot{\epsilon} < 0.1s^{-1}$ , and unstable at large strain rate. This mean some instabilities such as adiabatic shear bands or cracks are expected to be observed in the microstructure. Power efficiency is high at low strain rate ( $< 0.1s^{-1}$ ), and decrease with strain rate until 0 at  $10s^{-1}$ . As a consequence, "dynamic metallurgical processes" [20] such as dynamic recrystallization are expected at low strain rate, but should not occur at high strain rate. A more physical method was developed based on the analysis of Kocks-Mecking: fractional flow softening was calculated at large strain and plotted into a 2D map, similarly to processing map. This parameter is considered as an indicator of the recrystallization process. Both methods are based on macroscopic properties, and the relation with microscopic scale processes must be investigated to evaluate the agreement between mechanical behaviour and microstructure evolution.







## Chapter 4

# High-temperature microstructure evolution of L-605 alloy



## 4.1 Precipitation behavior of L-605 alloy

The current study investigates microstructure evolution during thermomechanical processes. It was shown previously that cobalt superalloys (page 29) and especially L-605 alloy (page 34) can form precipitates such as carbides or laves phases for annealing treatments below 1200°C. The formation of these phases affect strongly the final mechanical properties [70, 19], and can affect the recrystallization mechanism during high temperature deformation [31]. Therefore it is of first importance to verify if precipitation is expected to occur or not during conventional hot forming conditions.

### 4.1.1 Observation of precipitation by microscopy

Literature predicts the precipitation of phases such as  $M_6C$ ,  $M_{23}C_6$ ,  $M_7C_3$ , and  $Co_2W$  during aging treatment for temperatures between 600°C and 1200°C [71]. Ageing treatments were carried out on L-605 to verify these assertions. The selected initial material for this study was 15.87mm diameter bar purchased from Carpenter (Table 2.1). Annealing treatments were carried out in an IR Image Furnace with Ar inert atmosphere, and then the samples were water-quenched. For annealing time over 5h for temperature range between 1000°C and 1200°C, samples were sealed in vacuum silica capsules, and annealed in a muffle furnace.

Precipitation was visible by optical microscopy and SEM only for temperatures between 900°C and 1000°C. In this range of temperature, precipitation can occur very quickly, and is localized at grain boundaries (Figure 4.1). Only 30 minutes are enough to develop a network of precipitates all along the grain boundaries. Precipitates have a globular shape, and coalesce for annealing time above 1 hour.

For aging treatments longer than 5h, a second precipitation step occurs at twin boundaries. Precipitates localized at twins have a platelet shape oriented in the direction of the twin plane (Figure 4.2b). After 15h at 1000°C, this second precipitation type is considerable, and affects most of the twin boundaries. In this case, a third precipitation step sometimes occurs: globular precipitates occur inside grains. Nevertheless, this precipitation type occurs rarely, and can be neglected.

### 4.1.2 Detection of precipitation by X-ray diffraction

Occurrence of precipitation was evaluated by XRD analysis for different aging times and temperatures. Advanced precipitation of  $M_6C$  phase was observed after 15h at 1000°C, as indicated on the XRD diagram of Figure 4.4. The  $< 333 >$  peak of  $M_6C$  is the stronger one, and was selected for the identification of  $M_6C$  in samples. Precipitation occurrence was associated to this peak. These results were confirmed by direct observation of precipitates by optical microscopy and SEM.

It can be concluded  $M_6C$  phase precipitates at 1000°C, but this phase is not formed at temperature lower than 800°C or higher than 1100°C for aging treatment shorter than several hours. Other



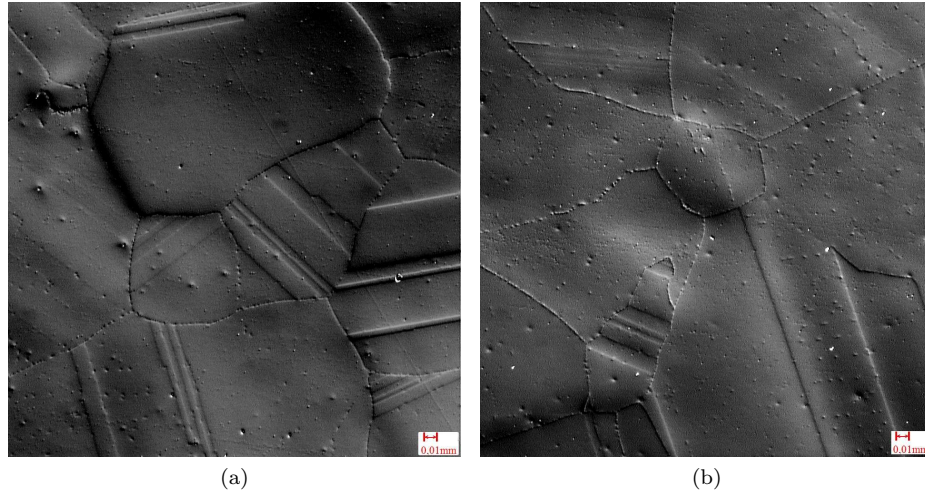


Figure 4.1: Microstructure of L-605 after 5h aging treatment at 1000°C, by optical microscopy

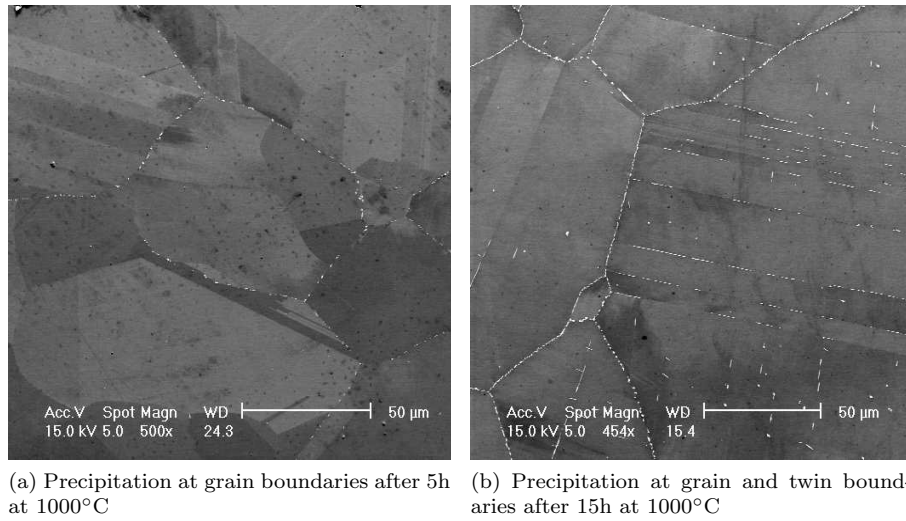


Figure 4.2: SEM observation of microstructure after aging at 1000°C

Time (h)	Temperature (°C)						
	600	800	900	1000	1100	1200	
0				vvw			<i>n=negligible</i> <i>vvw=very very weak</i> <i>vw=very weak</i> <i>w=weak</i> <i>m=medium</i> <i>s=strong</i>
0.08				vvw			
0.5		vw	vw	vw			
1				vw			
5				vw	vw		
15				m			

Table 4.1: Occurrence of  $M_6C < 333 >$  diffraction peak for different aging times and temperatures. The precipitation becomes really discernible by XRD for holding time above 5h



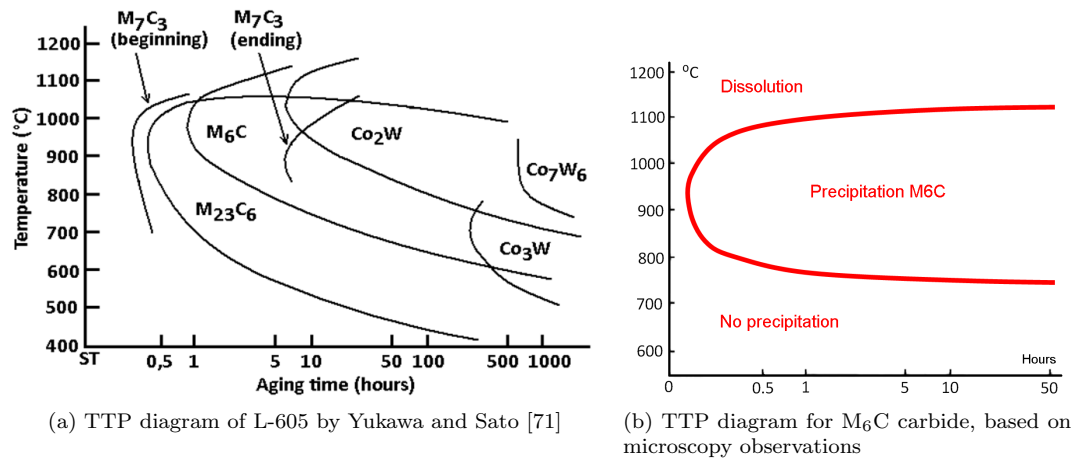


Figure 4.3: TTP diagram for carbides in L-605 alloy

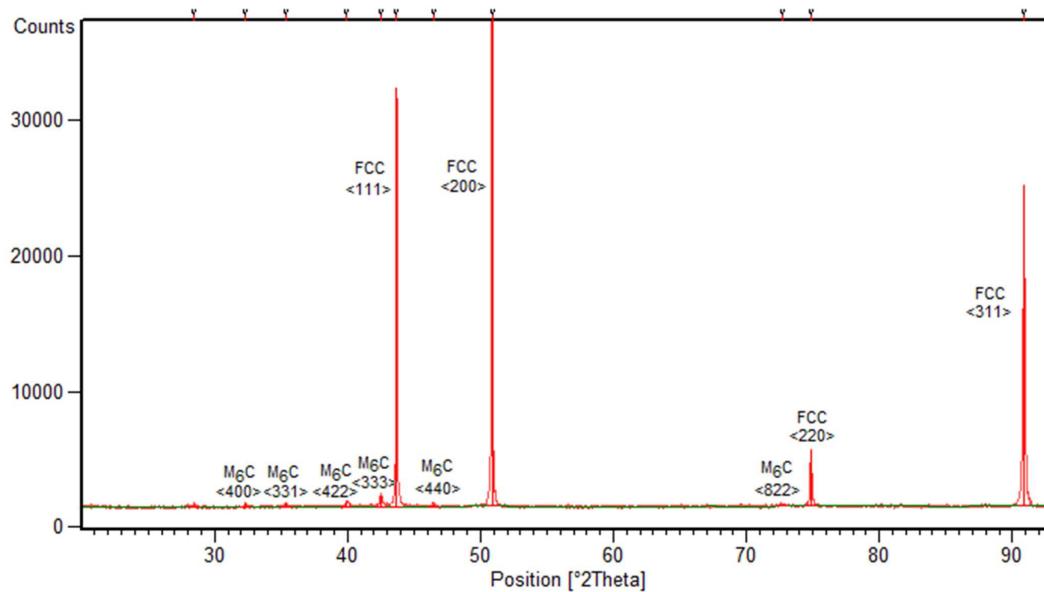


Figure 4.4: XRD diagram of L-605 aged 15h at 1000°C: only  $M_6C$  carbide is formed in FCC matrix

phases mentioned in the literature such as  $M_{23}C_6$ ,  $M_7C_3$ , and  $Co_2W$  were not detected by XRD, nor by microscopy. This might be due to their very small size and to a high degree of coherency for short aging treatments, or maybe due to a very low volume fraction of precipitates. Especially  $M_{23}C_6$  is a fcc-structured carbide and may be difficult to detect. It may require much larger aging time than expected to precipitate these phases with a fraction high enough to be detected by XRD method or visible by microscopy.



### 4.1.3 Chemical composition of carbides

The chemical analysis of  $M_6C$  carbides by EPMA and EDX revealed they contain principally tungsten and chromium. They can sometimes contain some cobalt, and traces of nickel. We can write the chemical composition of  $M_6C$  by the following way:  $Co_wCr_xW_yNi_zC$ , with  $w+x+y+z=6$ . The measured values of  $w$ ,  $x$ ,  $y$ ,  $z$  are indicated in the Table 4.2. The average composition is  $CoCr_2W_3C$ , but composition of  $M_6C$ -type carbides can vary from  $CoCr_3W_2C$  to  $W_6C$ .

Carbides formed at grain boundaries, twin boundaries or inside grains have similar chemical composition. These carbides correspond to the same tungsten-rich  $M_6C$  phase. However, we can notice that precipitates at grain boundary contain slightly more tungsten and less chromium than their counterpart.

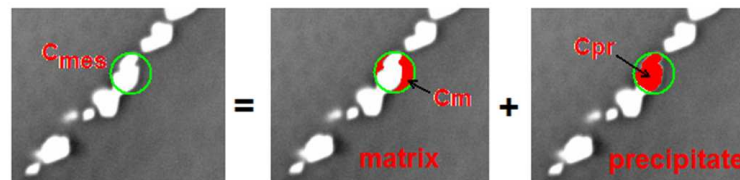


Figure 4.5: Decomposition of the area analyzed by EPMA or EDX in 2 phases

Coefficient	Technique	Grain boundary	Twin boundary	Inside grains
w	EPMA	0	0	0
	EDX	1	1	1.5
x	EPMA	2.1	2.6	0 - 3.3
	EDX	1.6	1.8	2.5
y	EPMA	3.9	3.4	2.7 - 6
	EDX	3.2	3.2	1.7
z	EPMA	0	0	0
	EDX	0.2	0.1	0.3

Table 4.2: Coefficients of  $M_6C$ -type  $Co_wCr_xW_yNi_zC$  carbide by EMPA and EDX measurements in a L-605 sample aged 15h at  $1000^\circ C$

### 4.1.4 Study of precipitation kinetics by thermoelectric power measurement

The kinetics of precipitation can be investigated by measuring the evolution of thermoelectric power (TEP) ([33] Figure 2.16 page 74). TEP is a good indicator of microstructure changes and was shown to be a suitable tool to follow the kinetics of precipitation in low-carbon steels [119]. Experimental procedure for measuring TEP is described in the section 2.3.3 page 74. Annealing treatment were carried out in the Gleeble machine for annealing time from 1s to 500s. Longer annealing treatments until 10 hours were carried out in a muffle furnace with argon sweep to minimize the oxidation of the sample. Successive TEP measurements and annealing steps were carried out on the same sample. In



the case of Gleeble annealing, experiments were carried out on two samples to ensure experimental reproducibility, and the TEP measured is taken as the average value for the two specimen. For each sample, TEP is measured successively 10 times, and the mean value is taken as the effective measured value, while error is quantified by the standard deviation.

Figure 4.6 illustrates the evolution of TEP with time. For the two cases of short and long treatment, the same trend is observed. For very short aging time lower than few seconds the thermoelectric power drops of -30 to -50nV/°C. This fast decrease can be attributed for example to some recovery processes or some surface change. From this point, TEP grows exponentially due to some microstructural changes such as precipitation or recovery. As the initial material is not work-hardened, recovery process is not especially expected for long aging treatment. Moreover grain growth is sluggish at this temperature and grain size can be fairly assumed constant. As a consequence, precipitation is the main microstructural change happening at 1000°C, and TEP increase can be directly attributed to precipitation progression. It can be concluded that according to TEP variations, precipitation starts very early for time above 10s. As a consequence, at 1000°C precipitation is faster than expected by TTP diagrams (Figure 1.32), and forms some particles that were not observable by optical microscopy nor detectable by X-ray diffraction.

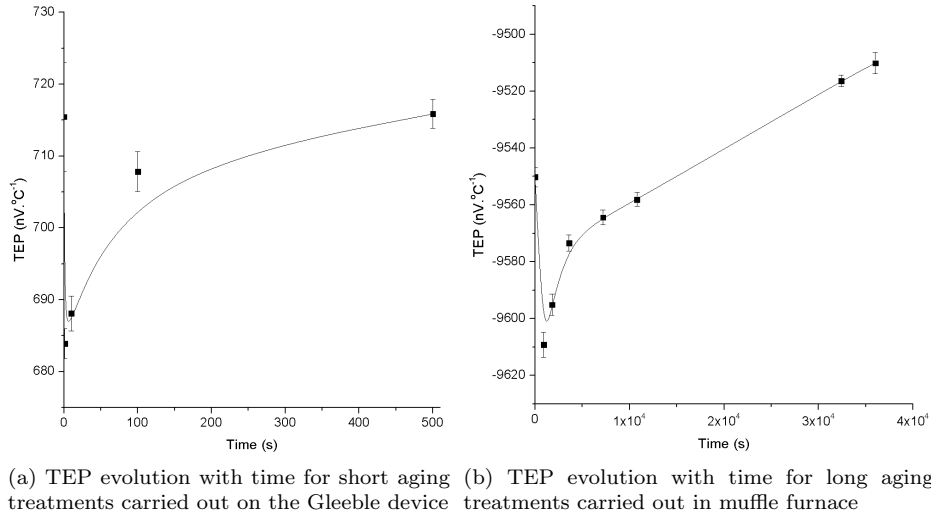


Figure 4.6: Evolution of thermoelectric power (TEP) with aging time

The normalized variation of thermoelectric power is evaluated by the equation:

$$\frac{\Delta S}{S} = \frac{S(t) - S_0}{|S_0|} \quad (4.1)$$

with  $S(t)$  the measured thermoelectric power at time  $t$  and  $S_0$  the absolute initial TEP value in the material as received. The variation of TEP provides information on the kinetics of precipitation, and is assumed to evolve jointly with the precipitates fraction. Figure 4.7 shows the evolution of



normalized TEP variation with time. The TEP variation is found to be linear with  $\log(\text{time})$ , in agreement with the results of Lavaire et. al for steels [119]. It can be seen on Figure 4.7a that no steady-state is reached for aging time above 10 hours, and that precipitation can pursue further. For longer aging time, some different types of carbides and intermetallics can be formed according to TTP diagram (Figure 1.32). However such aging conditions are not met during hot working process, and are outside the scope of this study.

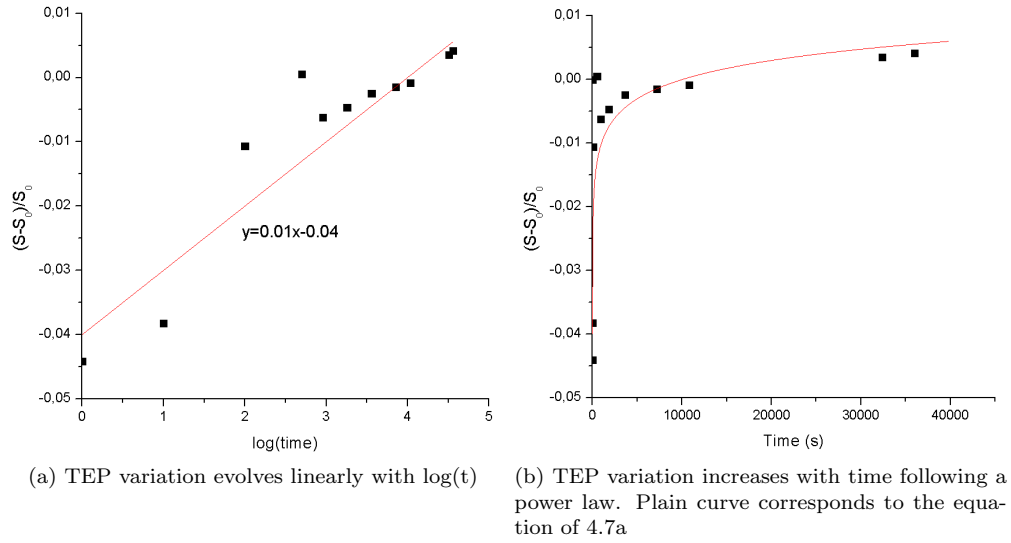


Figure 4.7: Evolution of TEP normalized variation with time

As a conclusion, thermoelectric power is a relevant indicator of precipitation behavior, and can reveal the kinetics of the precipitation process. In the current case, it was shown that precipitation occurs earlier than expected. Conventional characterization tools (XRD, microscopy) were not able to predict the onset of precipitation, and simply indicate the time at which particles become detectable. On the other hand, TEP provides the precipitation kinetics and enable to determine with better accuracy the minimal time for which precipitation can be considered to be active. The variation of TEP curve provides a qualitative comprehension of the kinetics law of precipitation, and enable some predictive speculation on the precipitation fraction.

#### 4.1.5 Conclusion

Hot working process of L-605 takes several minutes to complete. During this time, precipitation may occur at  $1000^\circ\text{C}$  according to the TEP measurements. Microscopy observations after aging treatment 30min at  $1000^\circ\text{C}$  confirm the formation of a network of  $\text{M}_6\text{C}$  carbides at grain boundaries. XRD detects the presence of  $\text{M}_6\text{C}$  carbides after few minutes aging at  $1000^\circ\text{C}$ . Therefore it can be concluded that there are strong possibilities to form precipitates for temperature around  $1000^\circ\text{C}$ .



However for temperature higher than 1100°C or lower than 800°C, precipitation is sluggish and is not expected during the hot deformation process.



## 4.2 Grain growth after annealing

Microstructure evolution during hot working results from the combined effects of temperature and plastic deformation. High temperatures promote the migration of grain boundaries and consequently the grain growth. Plastic deformation plays a more complex role in microstructure change: firstly by providing some driving force for grain growth, and secondly by generating new grains from the substructure formed by plasticity. We will try now to dissociate the effects of temperature and plasticity to understand and quantify each of them. Temperature effect is captured in the current section by grain growth experiment. Static recrystallization is investigated in the next section, and combines the joint effect of temperature and plastic deformation.

### 4.2.1 Evolution of grain size during annealing treatment

Annealing treatments were carried out on L-605 as-forged with an initial grain size of  $3.5\mu\text{m}$  (material from Kamaishi, Table 2.1). Annealing was carried out in a muffle furnace under air atmosphere for temperature between  $1000^\circ\text{C}$  and  $1200^\circ\text{C}$  during 16min to 18h. After annealing, sample were observed by EBSD to determine the grain size distribution. Table 4.3 illustrates the resulting microstructure before and after annealing treatment.

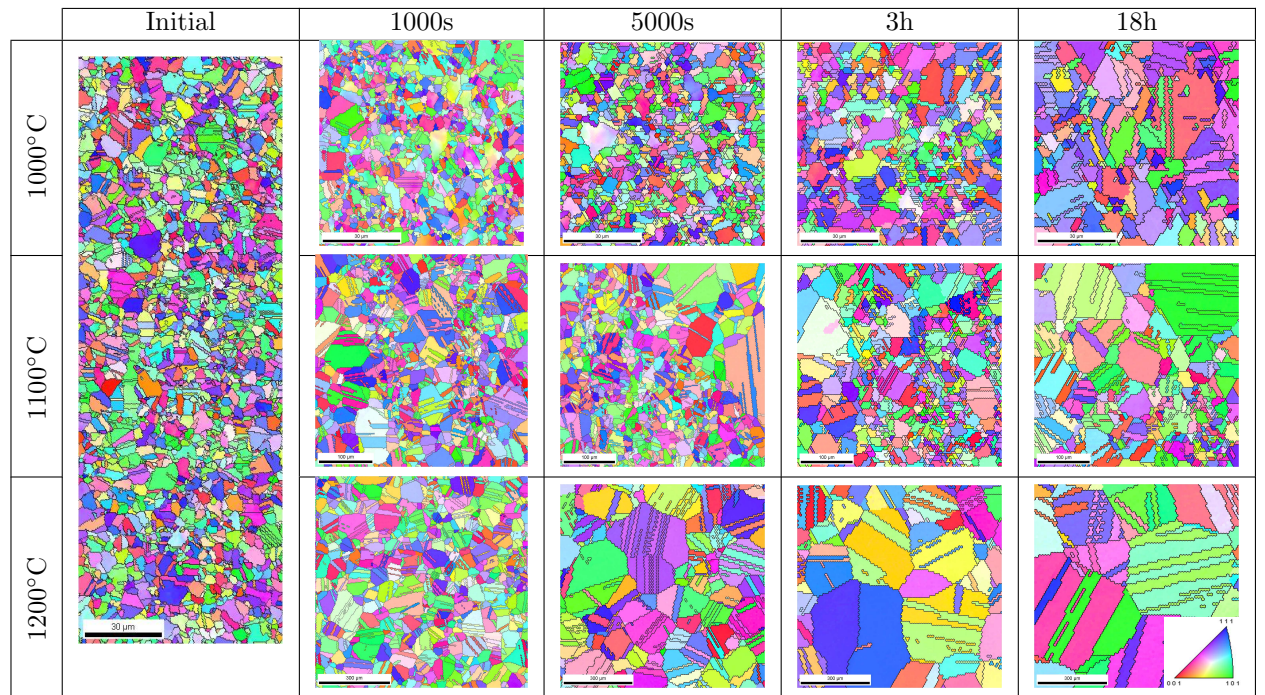


Table 4.3: IPF map of L-605 after annealing treatment

Grain growth is especially significant for annealing above  $1100^\circ\text{C}$  ( $>0.78 T_f$ ) for several hours: grain size exceeds  $100\mu\text{m}$  after 3 hours at  $1100^\circ\text{C}$ . Grain size follows a log-normal distribution, as illustrated in Figure 4.8a in the case of annealing at  $1000^\circ\text{C}$ . With increasing the annealing time, the



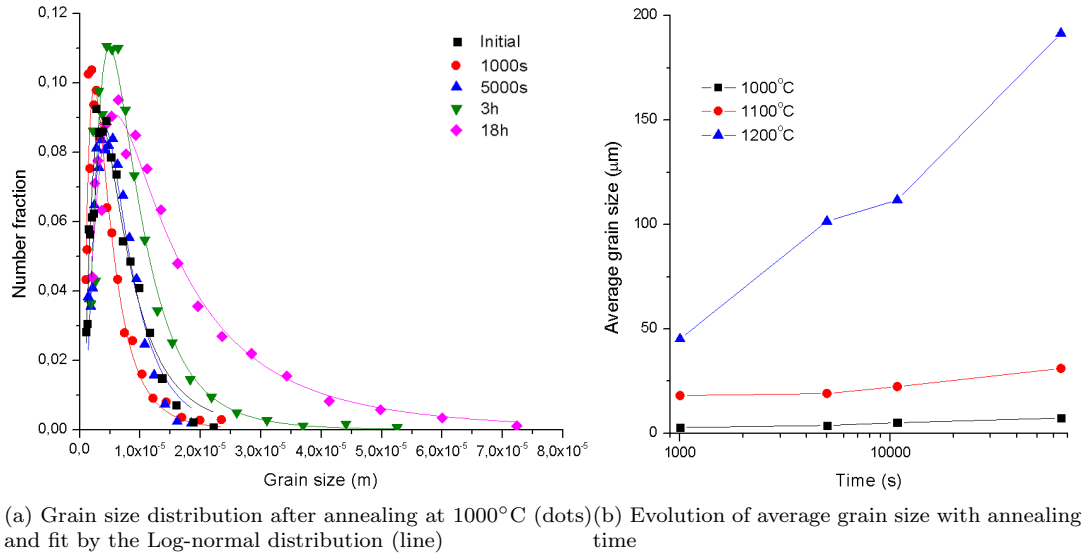
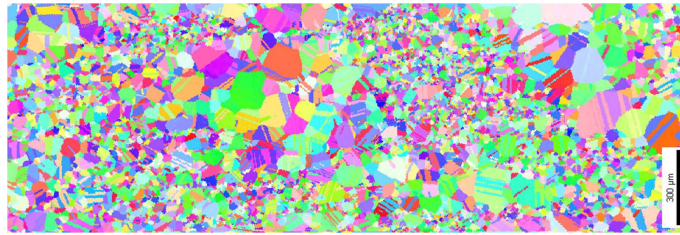
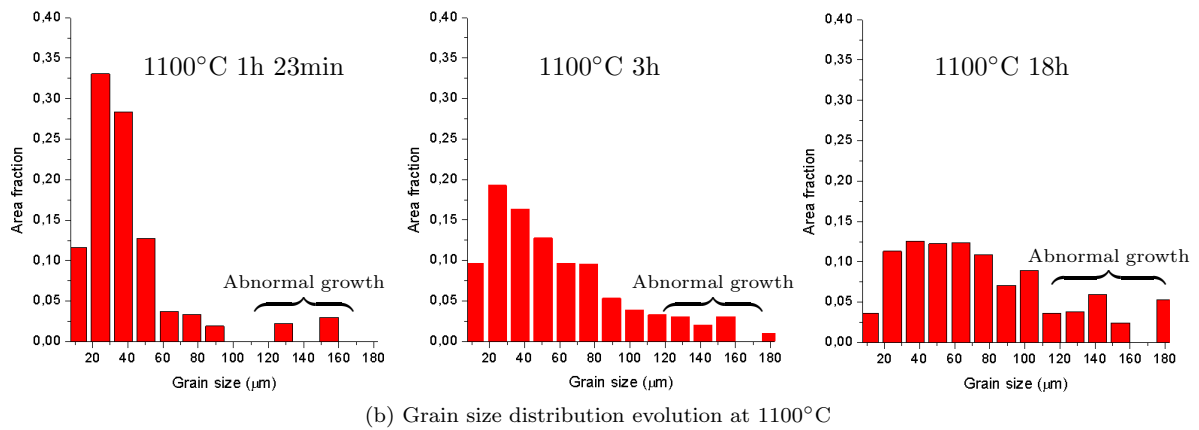


Figure 4.8: Grain growth of L-605: grain size distribution and average grain size evolution with time



(a) IPF map after annealing 3h at 1100°C



(b) Grain size distribution evolution at 1100°C

Figure 4.9: IPF map of microstructure after annealing 3h at 1100°C, and grain size distribution

peak height of the distribution drops and its deviation increases. Figure 4.8b illustrates the evolution of average grain size measured by EBSD with annealing time and temperature. At 1200°C, the time necessary to double the initial grain size is estimated to be about 3 minutes only, by extrapolation of the average size curve. Therefore grain growth is a very fast process at  $T > 0.7T_f$ , and annealing



treatment would lead to dramatic coarsening.

Figure 4.9 shows the resulting microstructure after annealing 3h at 1100°C. On the middle of the picture, some clusters constituted of very large grains compared to the mean size are visible. The presence of these clusters is a nice illustration of the occurrence of abnormal grain growth during the annealing process. Figure 4.9 shows also the evolution of grain size distribution. The resulting bimodal distribution is composed of two modes: one centered at 30μm corresponding to normal grain growth, and one above 100μm corresponding to abnormal growth mechanism. This second mode is especially visible for short holding time. For annealing treatment above 18h, the size distribution sprawls, and the bimodal distribution progressively vanishes. As a conclusion, short annealing treatment can be an attractive method to develop bimodal grain size distribution by using the abnormal growth phenomenon.

#### 4.2.2 Modeling of grain growth process

Grain growth process is driven by the decrease of grain boundaries surface energy stored in the material. Figure 4.10 shows the grain boundaries cartography of L-605 with increasing annealing time at 1000°C. The amount of grain boundaries decrease progressively, while the average grain size increases and the total number of grains decreases. This phenomenon implicates the growth of some grains at the expense of other ones.

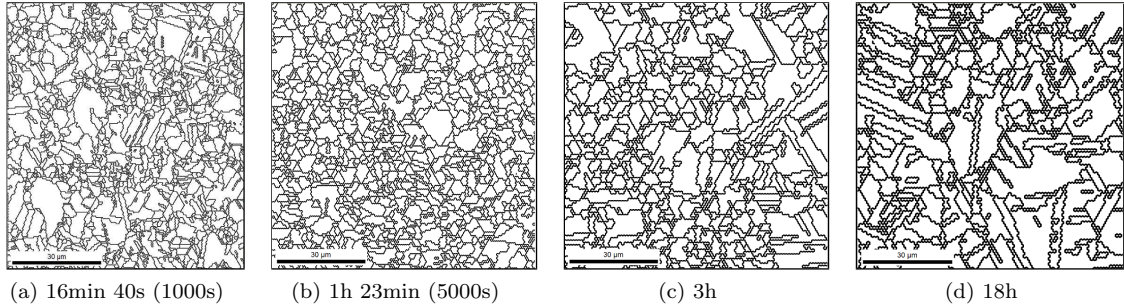


Figure 4.10: Grain boundary map for increasing annealing time at 1000°C

In a first approximation, the growth speed of a single grain can be assumed to be proportional to the difference of stored surface energy between the grain and its surrounding neighbors (Hillert-type model [91], equation 1.25 page 47):

$$v = M \cdot \gamma \left( \frac{1}{R_c} - \frac{1}{R} \right) \quad (4.2)$$

with M the mobility,  $R_c$  the critical grain size identified as the mean grain size in a first approximation, and R the radius of the growing grain. For applying the equation above, the grain boundary surface energy of L-605 alloy must be determined. Table 4.4 indicates the boundaries surface energy for each of the elements constituting the L-605 alloy. For each pure element, grain boundary



surface energy is within the range 0.6 to 1 J.m<sup>-2</sup>. Therefore the average grain boundary energy of L-605 superalloy was set to 0.7 J.m<sup>-2</sup>, corresponding to the mean energy weighted by the atomic fractions of each constituent. In spite of the importance of the  $\gamma$  parameter for determining grain size evolution, such an approximation is quite reasonable. First we should keep in mind that it is quite difficult to get experimentally an estimation of  $\gamma$  with an accuracy better than  $\pm 0.1$  J.m<sup>-2</sup>. As we know that  $\gamma$  is anyway likely to be comprised between 0.6 and 1 J.m<sup>-2</sup>, any attempt to determine  $\gamma$  experimentally would not necessarily improve significantly the accuracy. Moreover, any error on  $\gamma$  value is reported anyway on the value of the mobility M which is also unknown, and the global effect of error on the growth behaviour is null.

Element	$\gamma$ (J.mol <sup>-1</sup> )	Reference
Co	0.65	[127]
Cr	0.7	[128]
W	0.9 - 1	[129, 128]
Ni	0.6 - 0.7	[130]
L-605	<b>0.7</b>	<i>Estimation</i>

Table 4.4: Grain boundary surface energy of the different components of L-605 alloy

Temperature	M (m <sup>4</sup> .J. <sup>-1</sup> .s <sup>-1</sup> )
1000°C	3.10 <sup>-15</sup>
1100°C	8.10 <sup>-14</sup>
1200°C	3.10 <sup>-12</sup>

Table 4.5: Grain boundary mobility during grain growth process

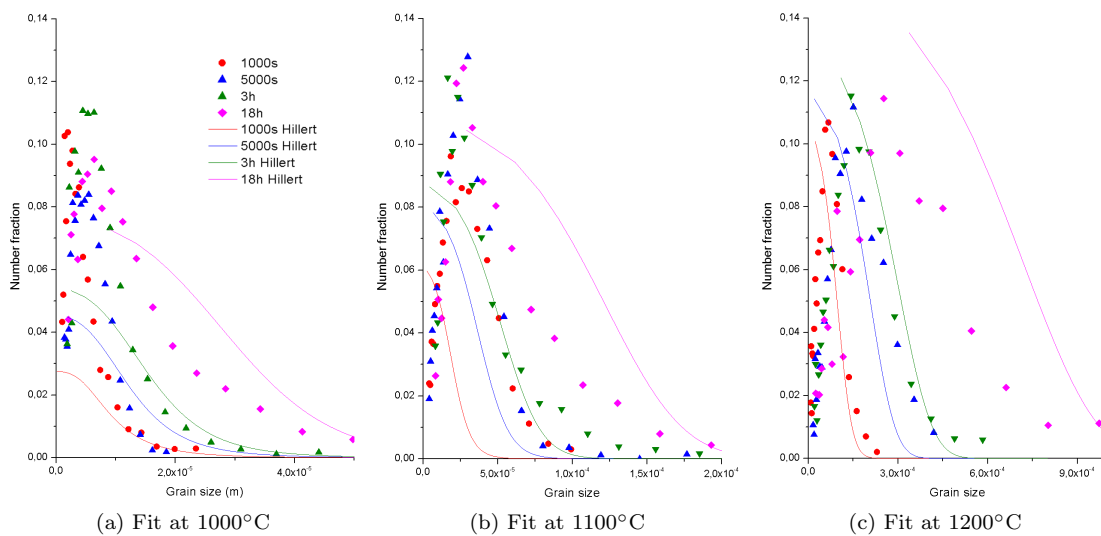


Figure 4.11: Fit of grain size distribution by the Hillert model



Mobility is taken as a floating parameter adjusted to fit the experimental distribution. The Table 4.5 lists the values of mobility selected to obtain the best agreement between model and experiment. Mobility increases with temperature, in agreement with literature (Turnbull estimate [101], equation 1.29). However the values of mobility determined in the current case should be considered carefully. Any error on the driving force or on  $\gamma$  would lead to significant change in the mobility value. Thus, the mobility determined here should be simply considered as a fitting parameter that may include some additional effects not considered by the Turnbull estimation.

Figure 4.11 represents the grain size distribution in number fraction measured by EBSD (dots), and the distribution calculated from the equation 1.25 (plain lines). The calculated distribution is in good agreement with the experiment for low temperature and short annealing time. For long holding time at high temperature (e.g. 1200°C 18h) discrepancy is significant, and it is not possible to adjust the mobility to have good fit both for short and long annealing time. This means that either mobility is changing with time, or more likely that the driving force estimated is not exact. This discrepancy illustrates the limits of the Hillert model to predict the grain size distribution. Moreover, none of the calculated distributions manage to reproduce exactly the Log-normal distribution, which is also a limitation of the Hillert model frequently reported in the literature [131]. As a conclusion, the model applied here is suitable to estimate the mean grain size and the trend of grain size distribution, but should not be taken too seriously considering the approximations employed. For further accuracy, more complex models were developed and have shown better predictability especially in the case of abnormal grain growth [132, 133].

### 4.2.3 Evolution of mechanical properties with grain size

Tensile tests are carried out on the initial forged material from Kamaishi (grain size 3.5  $\mu\text{m}$ ), and after annealing treatment 16min and 3h at 1100°C. The tensile tests were performed three times, and the average stress-strain curves are illustrated in Figure 4.12. The ultimate tensile stress, the elongation and the yield stress are reported on the Table 4.6. The increase of grain size comes with an increase of ductility and a loss of strength, in agreement with literature (Figure 1.33).

The annealing treatment of 16min leads to an increase of 23% of the maximal elongation, and a loss of 8% of the strength. For stent application, an ultimate tensile stress above 1GPa is enough, therefore the slight loss of strength after a short annealing treatment is not a matter. However the gain of ductility can be quite interesting to avoid any risks of rupture after expansion. To conclude, the annealing treatment after hot working process can be an interesting step to fit the mechanical properties to the targeted application. For stent application, the decrease of yield stress by annealing can lead to an easier set up of the stent during the expansion step.



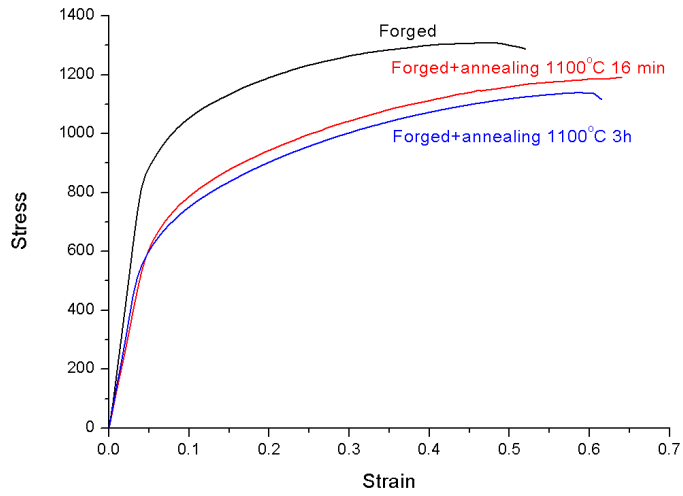


Figure 4.12: Tensile test stress-strain curves of L-605 before annealing (grain size  $3.5 \mu\text{m}$ ), and after annealing 16min and 3 hours at  $1100^\circ\text{C}$

Material	Average grain size	Yield stress (MPa)	Ultimate tensile stress (MPa)	Maximal elongation
L-605 forged	$3.5 \mu\text{m}$	310	$1287 \pm 28$	$0.519 \pm 0.016$
L-605 forged +annealing 16min $1100^\circ\text{C}$	$18.1 \mu\text{m}$	590	$1186 \pm 9$	$0.639 \pm 0.014$
L-605 forged +annealing 3h $1100^\circ\text{C}$	$22.4 \mu\text{m}$	515	$1137 \pm 15$	$0.615 \pm 0.024$

Table 4.6: Mechanical properties of L-605 forged before and after annealing treatment

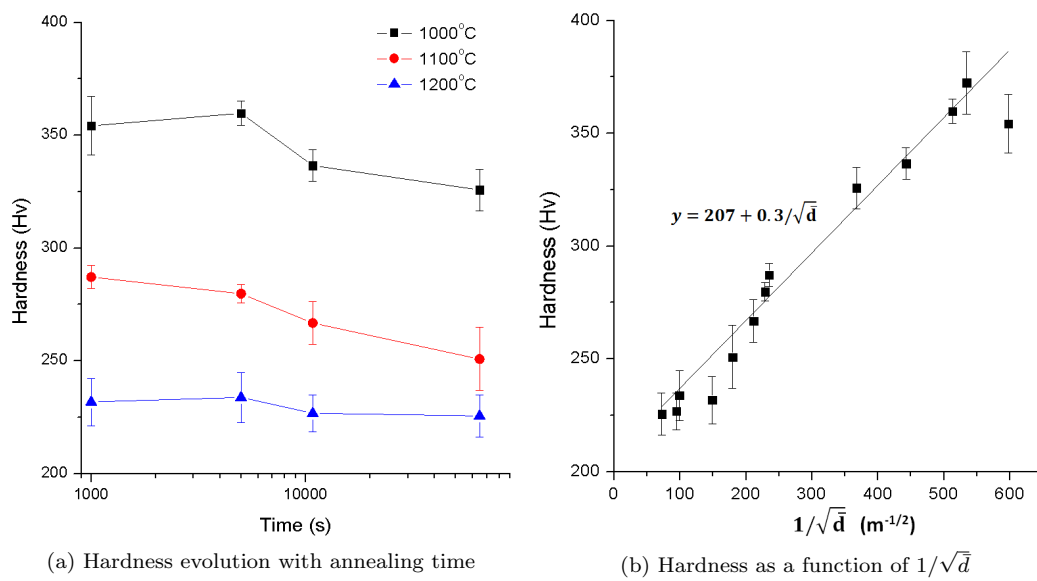


Figure 4.13: Evolution of Vickers hardness during grain growth



Vickers hardness was measured before and after annealing treatment. The initial Vickers hardness of L-605 material with  $3.5\text{ }\mu\text{m}$  grain size is  $372 \pm 14\text{ Hv}$ . Figure 4.13a illustrates the hardness change with time. The hardness decreases of 5% at  $1000^\circ\text{C}$ , 23% at  $1100^\circ\text{C}$  and 38% at  $1200^\circ\text{C}$  after annealing 1000s (16min 40s). The subsequent softening for longer annealing is only in the range 2-12%. Therefore hardness loss occurs mainly during short annealing time, then hardness remain relatively constant.

As illustrated in Figure 4.13b, hardness is increasing with decreasing grain size. A linear relationship is noted between hardness and average grain size to the power  $-1/2$ . Therefore hardness change meets up with the Hall-Petch relationship, with a proportionality coefficient  $k=0.3\text{ Hv.m}^{-1/2}$ . The initial hardness as grain size approaches  $+\infty$  is  $Hv_0=207\text{Hv}$  and corresponds to the hardness of a single crystal. Thereof, the increase of hardness can be mainly attributed by an increase of yield stress due to grain refinement. To conclude, the refinement is an interesting way to increase the strength of L-605 alloy, and lead to an increase of its hardness. Annealing treatment tends to decrease hardness by coarsening the microstructure, and is detrimental to the global strength of the material.

#### 4.2.4 Conclusion

Grain growth kinetics is very fast for temperature above  $1100^\circ\text{C}$  ( $>0.78\text{ }T_f$ ), and produces a coarse microstructure after several minutes annealing only at  $1200^\circ\text{C}$ . Therefore annealing treatment is strongly altering the initial ultrafine microstructure. If any solution treatment is required during the process of L-605 superalloy (e.g. to eliminate precipitates), it must be carried out before the forging process, so there is no degradation of the microstructure produced. Grain growth can imply severe complication in the metal processing. For instance, if any precipitate detrimental for mechanical properties were formed during hot working, one would be forced to choose between conducting a solution treatment after hot-working and loosing some strength by increasing grain size, or keeping the as-forged ultrafine microstructure including weakening phases.

On the other hand, grain growth can occur following an abnormal growth mechanism and produce an interesting bimodal grain size distribution. Such a distribution is very attractive for some applications requiring a compromise between strength and ductility: small grains usually promote strength and large grains help to preserve sufficient ductility. Thus, grain growth can be also a powerful tool for microstructure design.

After hot working, microstructure takes a couple of minutes to seriously evolve by annealing. Usually, a workpiece cools down in few seconds by gas quench or water quench. As a conclusion, a microstructure as forged like the one employed here is not very likely to undergo significant grain growth during the cooling process, and quench speed is not too much critical. Gas quench can be estimated to be fast enough for preserving small grains, and is probably sufficient in an industrial



point of view. However post-dynamic evolution of microstructure during cooling cannot be completely excluded, and some experiments with water quench are required to check the influence of cooling speed on grain size.

Grain growth can be properly modeled in a very simple way by considering the grain boundary surface energy as the main driving force for boundaries migration. However in the case of hot working, dislocation density is very high and becomes the predominant term of the driving force. As a consequence, the kinetics of grain growth in a work-hardened metal may be significantly different. What is the effect of plastic deformation on grain coarsening process? Could we observe simple grain growth of pre-existing grains, or would we rather create new grains by recrystallization? The next section investigates the differences on the growth mechanism in the case of a deformed sample.



## 4.3 Static recrystallization

This section examines the effect of temperature on the microstructure evolution of a work-hardened sample. The resulting phenomenon is not anymore grain growth only, but static recrystallization can occur jointly. The kinetics of recrystallization and the grain size evolution are determined, and recrystallization mechanisms are surmised based on microscopy observations. The detailed mechanisms of recrystallization in L-605 alloy will be detailed further in the next sections on the case of dynamic recrystallization. The grain growth model used successfully in the previous section is shown to be inadequate for studying recrystallization. The current section points out the necessity to understand completely the nucleation and growth process, and the necessity to develop some tools to determine them.

### 4.3.1 Evolution of grain size during fast-annealing treatment after cold-rolling

Annealing treatment were carried out on L-605 alloy after plastic deformation. Samples were prepared from  $3\mu\text{m}$  grain size forged material identical to the one employed on the previous section (Kamaishi, Table 2.1). Figure 4.14 illustrates the steps of the sample preparation. Sheets of 1.65mm thickness were cutted from a billet, and then cold rolled with a reduction of 23% until a thickness of 1.27mm, corresponding to a true strain  $\epsilon = 0.25$ . Cold-rolling was proceeded in 5 steps, with a deformation of  $\epsilon = 0.05$  for each step. Rectangular samples of 30x5mm were cutted in the sheets, with the long axis oriented in the cold-rolling direction. These samples were annealed during a very short time in the Gleeble machine, with a heating speed about 1 second, and a holding time between 1 and 100 seconds. Therefore the effective holding time for 1s annealing treatment may rather be about 2 seconds with considering the heating and cooling steps. Sample were gas quenched by air blowing on the sample, with a cooling speed of  $-300^\circ\text{C}/\text{s}$ . Figure 4.15 represents the evolution of temperature in the middle of the sample (black curve, regulating thermocouple), and at a distance of 1/3 from the centre (red curve). The thermal gradient is about  $80^\circ\text{C}$ , that is  $5.3^\circ\text{C}/\text{mm}$ . As we observe the microstructure in the close proximity of the thermocouple in the centre of the sample, thermal gradient can be safely neglected.

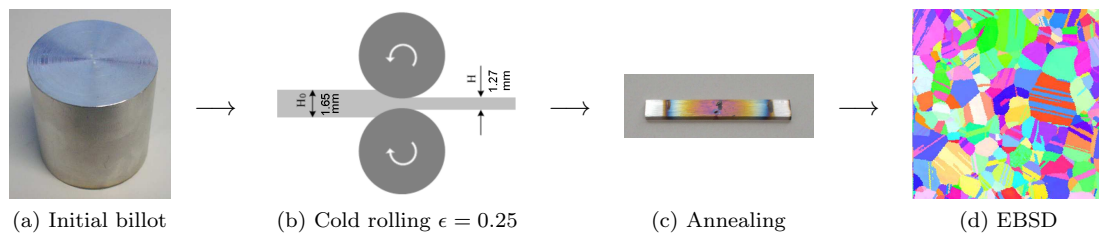


Figure 4.14: Sample preparation and procedure for static recrystallization experiment



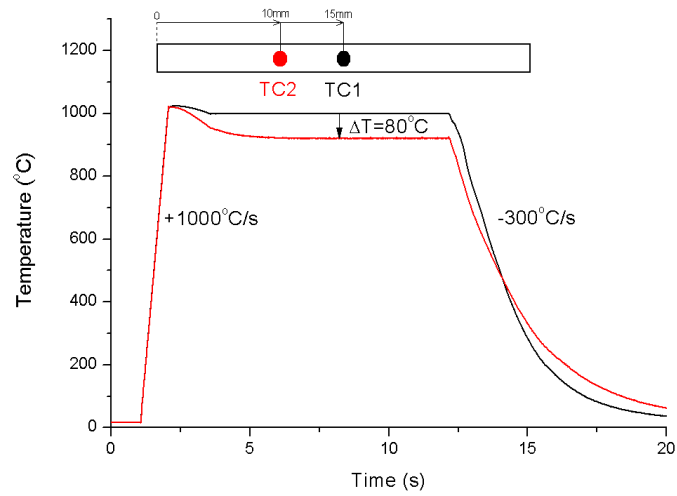


Figure 4.15: Temperature evolution measured in two different points during annealing 10s at  $1000^{\circ}\text{C}/\text{s}$

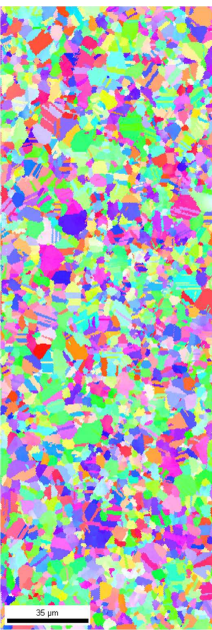



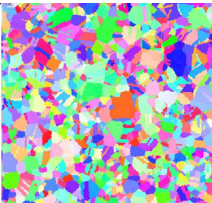
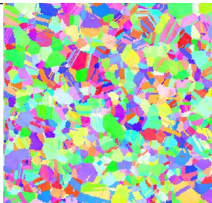



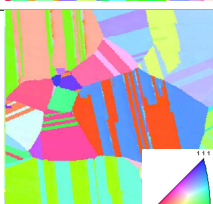
	Initial		1s	10s	100s
1000°C		Cold Rolling 23%			
1100°C					
1200°C					

Table 4.7: IPF map of cold rolled CR23 % L-605 after annealing treatment

The Table 4.7 illustrates the resulting microstructure after short annealing treatment. The grain size decreases by 45% from  $3.5\mu\text{m}$  to  $1.9\mu\text{m}$  during a short annealing about 1s at  $1000^{\circ}\text{C}$ . For longer holding time, grain size increases again until 75% of its initial value for 100s annealing. This increase is due to grain growth following recrystallization. As a consequence, static recrystallization is an extremely brief phenomenon taking a fraction of seconds to start and a couple of seconds to complete.



For  $T=1100^{\circ}\text{C}$ , grain size drops of 6% of its initial value only after 1s annealing, due to a higher activity of grain growth going with recrystallization. For  $T=1200^{\circ}\text{C}$ , no grain refinement is noticed, and grain size doubles after 1s annealing only. This means that despite the briefness of the annealing, recrystallization is already completed, and give way to simple grain growth. For  $T>1100^{\circ}\text{C}$  ( $T>0.78T_f$ ), recrystallization is likely to start during the heating step, and complete in a fraction of seconds. Therefore any attempt to estimate the kinetics of nucleation at such high temperature is pointless considering the transience of recrystallization onset.

At  $1200^{\circ}\text{C}$ , grain size reaches  $9\mu\text{m}$  after 10s and  $23\mu\text{m}$  after 100s holding time. Therefore the initial microstructure is totally erased after several seconds to 1 minute. To conclude, ultrafine highly deformed microstructure is very unstable for  $T>1100^{\circ}\text{C}$  and evolve in few seconds. As noticed here, the kinetics of a deformed material is much faster than in the same material without plastic deformation. This fact is due to the contribution of dislocation density to the driving force for growth. It is usually admitted that in the case of recrystallization, dislocation density difference between grains is the only driving force, and that capillary effects can be safely neglected [31]. Then once recrystallization is achieved, new grains swept most of the dislocation structure, and the driving force is lead by the capillary forces again. This steps corresponds to the usual grain growth mechanism, often so-called "secondary recrystallization".

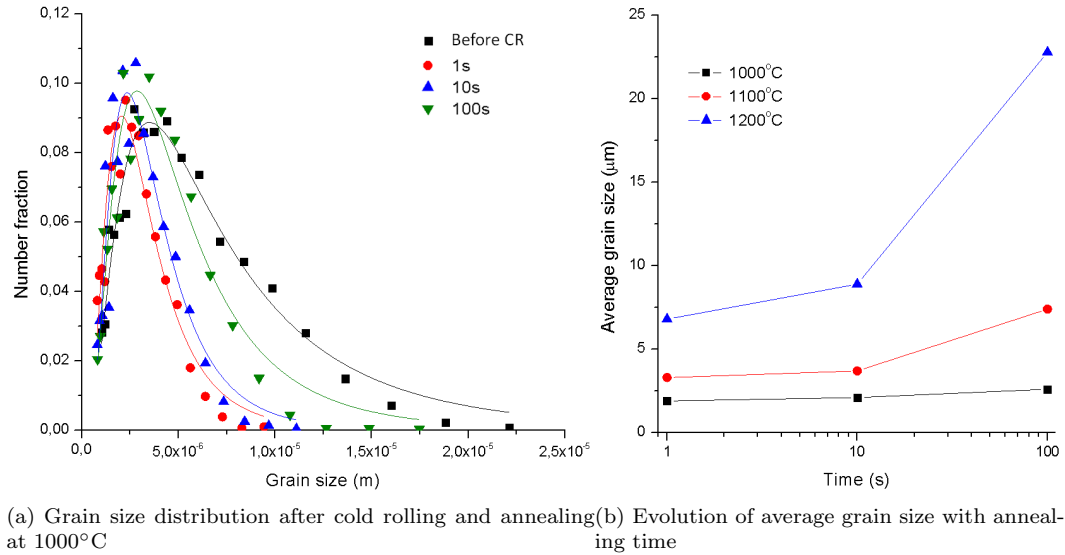


Figure 4.16: Static recrystallization of L-605: grain size distribution and average grain size evolution with time

As in the case of normal grain growth, recrystallization forms a microstructure with a Log-normal grain size distribution (Figure 4.16a). However, unlike grain growth, recrystallization leads to a decrease of both the average size and the standard deviation, and narrows the distribution. After a



sufficiently long holding time (time > 10s at 1000°C), distribution gets broader again and mean size increases due to grain growth. Figure 4.16 represents the increase of average grain size with annealing time. For high temperature and long holding time, mean grain size follows a similar evolution to the case of grain growth illustrated in Figure 4.8. Thus, for long annealing time the grain coarsening may be treated as a regular normal growth process as described in the previous section.

To conclude, annealing of highly deformed L-605 alloy leads to static recrystallization and grain refinement. This phenomenon is very brief and takes several seconds at 1000°C, to several fractions of second above 1100°C. Then normal grain growth pursues further the coarsening of the microstructure. The kinetics of grain coarsening is by far faster than in the case of a relaxed material, because dislocation density is the main driving force for growth.

### 4.3.2 Evolution of Vickers hardness during static recrystallization

Vickers hardness was measured on the cold rolled initial material, and after annealing treatment. Cold rolled material has a Vickers hardness of  $490 \pm 5$  Hv, therefore 30% higher than the initial non-deformed material. Figure 4.17a illustrates the hardness change with time. Hardness drops of 20% at 1000°C, 29% at 1100°C and 37% at 1200°C. The subsequent softening is within the range 5-13%, meaning that most of the softening process has already taken place after only a couple of seconds annealing. Softening mechanisms include jointly the effects of recovery, recrystallization and grain growth.

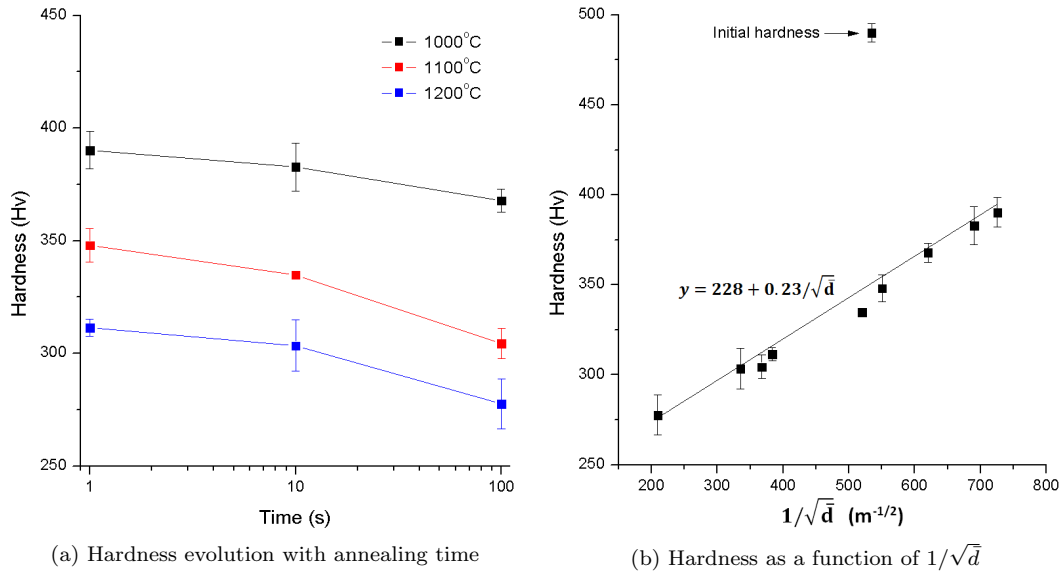


Figure 4.17: Evolution of Vickers hardness during static recrystallization

Figure 4.17b illustrates the dependence of hardness with grain size. Likewise the grain growth experiments described previously, hardness follows the Hall-Petch law. Therefore the increase of



hardness is also due to an increase of the yield stress by a conventional grain boundary strengthening effect. Proportionality coefficient is  $k=0.23 \text{ Hv.m}^{-1/2}$ , and hardness of the single crystal material is  $Hv_0=226\text{Hv}$ . These coefficients are very close to the ones obtained during grain growth, meaning the strengthening effect is of the same nature. Interestingly, the initial point corresponded to the cold rolled material does not follow the Hall-Petch law, due to the hardening due to cold deformation. Because other points follow pretty well this relation, it means that the effect of initial hardening has vanished after 1 second annealing, illustrating the extreme briefness of the recovery process. As a conclusion, grain boundary strengthening by grain refinement is significant and can be obtained by static recrystallization. Cold working leads also to an increase of hardness, but this effect disappears very quickly by annealing.

### 4.3.3 Is grain growth model applicable to static recrystallization?

The grain growth model developed in the previous section (equation 4.2 page 109) was applied to the case of static recrystallization, using the Hillert model (equation 1.25). Results are illustrated in Figure 4.18: dots correspond to the distribution measured by EBSD observation, and plain lines are obtained from the grain growth model. The Table 4.8 lists the values of mobilities required to fit the experimental distributions.

Temperature	M ( $\text{m}^4.\text{J}^{-1}.\text{s}^{-1}$ )
1000°C	$1.10^{-18}$
1100°C	$1.10^{-16}$
1200°C	$7.10^{-15}$

Table 4.8: Grain boundary mobility estimation during static recrystallization

As expected, the model totally fails to predict the distribution at 1000°C, because calculation does not includes the nucleation responsible of grain refinement. Therefore, the fitted mobility about  $10^{-18}\text{m}^4.\text{J}^{-1}.\text{s}^{-1}$  is extremely low and has no physical meaning, excepted to prove that normal grain growth is definitely not the predominant mechanism. For temperature above 1100°C, equation 1.25 gives a much more reasonable fit of the distribution, and can be fairly well employed for predicting grain size evolution. This agreement proves that for several seconds at  $T>1100^\circ\text{C}$  the coarsening mechanism is mostly normal growth and not anymore static recrystallization. However the mobility is still abnormally low compared to values of the Table 4.5, and the growth law gives simply an empirical fit of the "secondary recrystallization". Moreover the driving force for growth is the difference of dislocation density for short time (recrystallization), and the sum of dislocation and grain boundaries surface energy contributions for long holding time. As a result, the driving force is not properly estimated by Hillert model, so the mobility is found to be abnormally low.



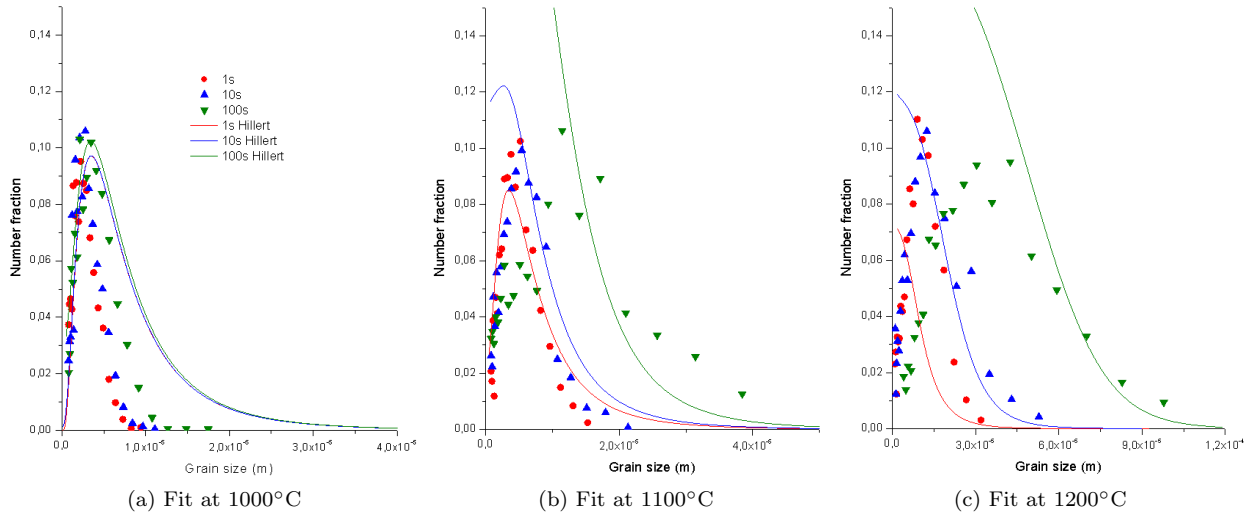


Figure 4.18: Fit of grain size distribution by the Hillert model

As a conclusion, the study of recrystallization requires two essential elements: a nucleation criterion with an equation of nucleation frequency in one hand, and a grain growth law accounting for the effectively predominant driving forces on the other hand. Therefore, the nucleation mechanism and the grain boundaries motion must be quantitatively determined from experimental data with minimizing the assumptions and keeping sufficient simplicity. A direct application of grain growth law is too simplistic to predict microstructure evolution of deformed metals. For sufficient predictability power, a complete model of recrystallization must be set up to estimate grain size distribution evolution.

#### 4.3.4 Conclusion

Static recrystallization was observed during the annealing of cold rolled 23% L-605 alloy. This phenomenon is very brief and results into the high instability of deformed ultrafine microstructure at high temperature. This observation illustrates the possibility that a microstructure with a similar strain level could undergo quick evolution during the cooling step after hot working. If dislocation density stored is high enough, the risk to affect the high-temperature formed microstructure gets very high. However the sample employed in this section is strongly work-hardened, and such conditions are not likely to be met during hot working due to the high activity of recovery. Warm and cold deformation can generate sufficient dislocation density to enable recrystallization, however temperature would not be high enough to allow the growth of new grains. Therefore in most common situations, static recrystallization is not expected during hot deformation of L-605 superalloy. But for some specific cases (e.g. sufficient temperature and very high strain rate), the occurrence of static recrystallization has to be considered.



Grain growth model is not adapted to predict microstructure evolution during recrystallization. Nucleation has to be considered jointly with growth to describe properly grain size change. The nucleus size, nucleation sites, nucleation frequency must be determined and linked up to the deformation conditions. On the other hand, grain boundary mobility must be determined more accurately by a complete estimation of driving forces at stake. From such considerations, the effect of time and temperature on the grain size evolution could be fairly estimated. The next section presents a detailed study of the dynamic recrystallization occurring during hot working: in this case the combined effect of plasticity and temperature can be directly observed through microstructure change and comprehended physically. The observation of nucleation mechanism provides all the informations for the establishment of a suitable nucleation criterion, while grain size dependence with temperature and strain rate provides essential informations on the grain boundaries motion. The extraction of these informations will be carried out by a combination of conventional approaches and innovative methods to obtain the sufficient elements to manage a complete comprehension of recrystallization.



## 4.4 Dynamic recrystallization

The following section examines the microstructure evolution during the hot working process. The situation met on the experimental tests detailed below corresponds to a very large number of processes applied in industry such as forging, hot rolling, extrusion, etc. If hot working is a very common process, it is also one of the most complex to understand physically in metallurgy science. The combination of temperature effect and plasticity leads to a non-trivial and hardly predictable evolution of dislocations structure and microstructure, and thus of the resulting mechanical properties. Grain size can either increase because of high temperature, or shrink with the occurrence of recrystallization. As a consequence, it is delicate to surmise the microstructure changes until the conditions for recrystallization occurrence are not determined experimentally. Also, the mechanisms of nucleation and grain boundaries migration involved during dynamic recrystallization must be properly understood physically to enable significant predictions on microstructure change during hot working.

This section details first the evolution of microstructure after hot working for different deformation conditions (temperature, strain rate). Microstructure features such as mean grain size, recrystallized fraction and crystalline defects are found to be linked together and point out the favorable conditions for recrystallization. Microstructure observations are compared with previous results on plasticity, and the validity of predictions on the occurrence of recrystallization is checked (page 97). From microstructural observations on partially deformed samples, the recrystallization mechanisms and nucleation sites are determined. Finally dislocation structure was observed and compared with usual observations on other cobalt alloys. The current information constitutes a fundamental basis for the modeling work carried out in the next section.

### 4.4.1 Plasticity gradient in compression tests

Hot compression tests are carried out on cylindrical samples of 12x8mm as described in the section 2.2 (page 65). The friction between the sample and anvils leads to a strongly heterogeneous repartition of strain and stress in the sample. Non-uniform plasticity leads to a gradient of microstructure (detailed at page 133). Therefore the position at which microstructure is observed must be carefully selected. The position where the local strain is equal to the macroscopic strain is especially interesting, because at this place the scale transition micro-macro is trivial, and the considerations on macroscopic mechanical behaviour determined in section 3.1 still hold. This position must be calculated by estimating the friction coefficient in a first step, and then by simulating the strain field in the sample by finite elements method.

After compression, samples have a barrel shape due to friction (Figure 4.24), with a height about 5.3mm, a minimal diameter of 9mm, and a maximal diameter of 13.3mm. Friction coefficient can be determined from the sample geometry based on finite elements calculations [120]. The Tresca



friction coefficient, noted  $m$ , is calculated based on the following equation:

$$m = \frac{3\sqrt{3}.R.b}{12h - 2b.h} \text{ with } b = 4.\frac{\Delta R}{R}.\frac{h}{\Delta h} \quad (4.3)$$

with  $R$  the theoretical final radius,  $h$  the final height of the sample,  $\Delta R$  the difference between minimal and maximal radius, and  $\Delta h$  the difference of height due to compression. For the geometry obtained here, theoretical radius is 6.2mm, and we obtain a barrelling factor  $b=1$ . From equation 4.3, the friction coefficient  $m$  is estimated about 0.6.

In a second step, this value is used to calculate the distribution of stress and strain in the sample volume by finite elements method using DeForm 3D simulation software. The compression curves obtained experimentally in Figure 3.1 are injected into the calculation to define the deformation behaviour of the material. Temperature is assumed to be constant in the sample in a first order approximation. It is common however to consider the opposite assumption, called adiabatic condition, by neglecting the heat transfer between the sample and the anvils. If the experimental reality is probably somewhere between these two limit simplifications, it is however thought that considering a homogeneous temperature is a fair approximation. As the sample is directly in contact with anvils, heat transfer is far from being negligible, and heat generated from mechanical deformation is rapidly dissipated. Sample self-heating measured experimentally was reaching a maximum of  $+20^\circ\text{C}$  at  $1000^\circ\text{C}$   $10\text{s}^{-1}$ . Considering adiabatic conditions would lead to a calculated self-heating of the sample above  $+100^\circ\text{C}$ , which is largely overestimated. Therefore homogeneous temperature assumption is a much more accurate and safer hypothesis than adiabatic conditions.

The strain and stress fields calculated are illustrated in Figure 4.19. At the edges of the sample, strain is only about 60% of its nominal value, while stress reaches 85% of its nominal value. In the core of the sample, strain concentration leads to a maximal local strain twice larger and a stress 9% higher than nominal values. As a conclusion, strain gradient is very strong in the sample, while stress gradient is much less significant and can be neglected in a first approximation. Figure 4.20 represents the strain profile along the radial axis. Strain gradient drops linearly with radius, and is weakly dependent on temperature and strain rate. The variation of strain is estimated by the linear equation:

$$\epsilon(r) = 1.67 - 175.r \implies \frac{\epsilon(r)}{\bar{\epsilon}} = 2.1 - 219.r \quad (4.4)$$

with  $\bar{\epsilon}$  the nominal strain and  $r$  the radius starting from 0 at the centre of the sample. The strain concentration  $\epsilon(r)/\bar{\epsilon}$  is equal to 1 for a position of 5mm from the centre of the sample. The microstructure observation presented thereafter were carried out at this position, so the strain is known and is equal to the macroscopic strain.



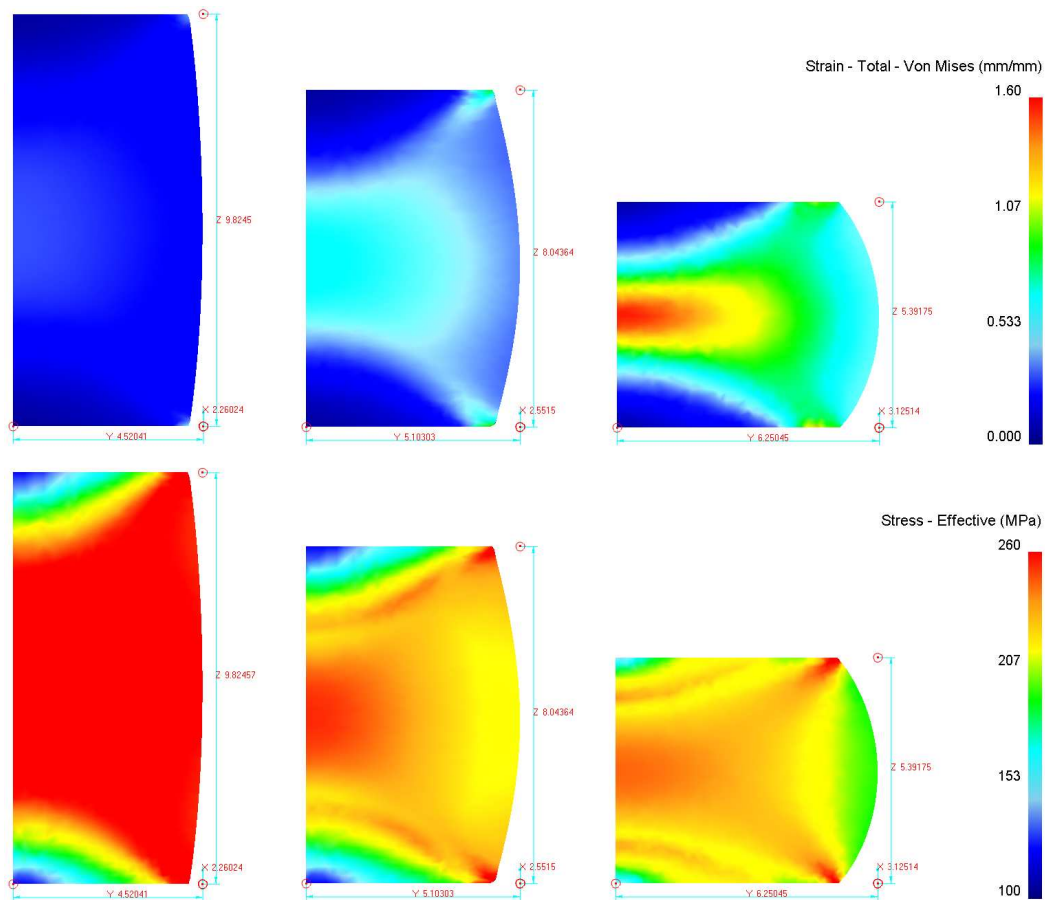


Figure 4.19: Calculation of Von-Mises strain and effective stress by finite elements method during deformation at  $1100^{\circ}\text{C}$   $0.1\text{s}^{-1}$

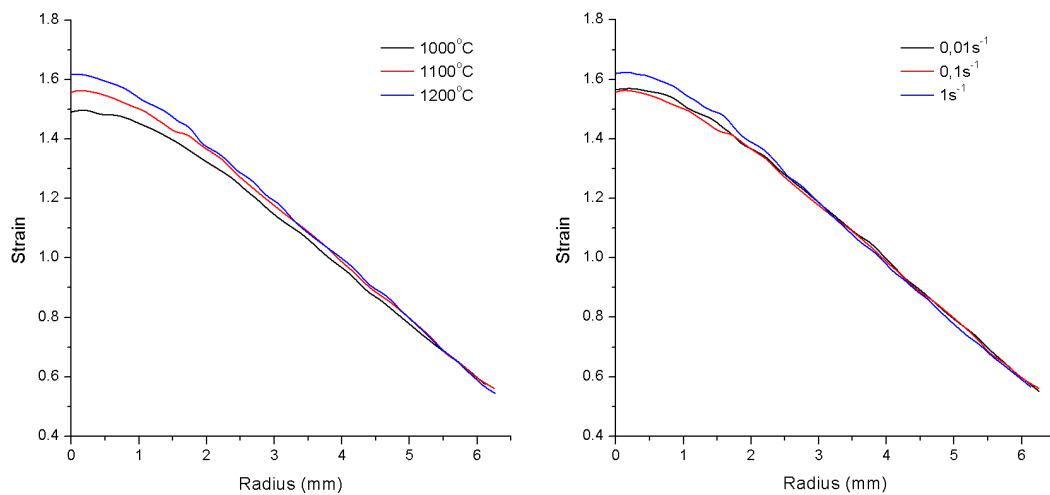


Figure 4.20: Strain profile along the radial axis of the sample: the core corresponds to the left (higher strain), and the edge to the right of the plot (lower strain)



#### 4.4.2 Microstructure evolution by hot deformation

Microstructure was observed by EBSD on the position previously determined by scanning an area of  $92 \times 270 \mu\text{m}$  with a step size of  $0.45 \mu\text{m}$ . The Inverse Pole Figure (IPF) maps are illustrated on the Table 4.9 (page 145), and shows the grains with their crystalline orientation. The Table 4.10 (page 146) illustrates the Kernel Average Misorientation (KAM) parameter maps. This parameter corresponds to the mean crystalline disorientation ( $^\circ$ ) between a scanned point and its 6 closest neighbours (hexagonal scanning grid). KAM parameter is a good indicator of the amount of crystalline defects created by plasticity and stored inside grains.

For any experimental condition the occurrence of dynamic recrystallization was observed. The recrystallization process leads to the formation of two types of microstructures:

- High temperature deformation generates significant recrystallization for  $T > 1100^\circ\text{C}$  and for low strain rate ( $\dot{\epsilon} < 0.01\text{s}^{-1}$ ) or high strain rate ( $\dot{\epsilon} = 10\text{s}^{-1}$ ). For these conditions, recrystallization is nearly complete and leads to a homogeneous equiaxial microstructure with a single mode grain size. Grain refinement is noticeable, and the grain size drops from the initial grain size of  $100 \mu\text{m}$  to an average size about  $10 \mu\text{m}$ .
- At intermediate strain rate ( $\dot{\epsilon} = 0.1 \sim 1\text{s}^{-1}$ ) and low temperature ( $T < 1150^\circ\text{C}$ ), recrystallization is partial and leads to a very heterogeneous microstructure. Recrystallized grains are very small (lower than  $1 \mu\text{m}$ ) and recrystallized fraction is low. Grain refinement is localized at the initial grain boundaries only, leading to a bimodal distribution of grain size.

The average size of dynamic recrystallized grains is represented versus temperature and log (strain rate) in Figure 4.21a. The surface fraction of recrystallized material is represented on Figure 4.21b. For temperature higher than  $1100^\circ\text{C}$  and strain rate lower than  $0.01\text{s}^{-1}$ , recrystallized grain size can reach  $10 \mu\text{m}$ , and the recrystallized fraction is about 100%. Similar behavior occurs for temperature higher than  $1100^\circ\text{C}$  and strain rate above  $1\text{s}^{-1}$ , with a recrystallized grain size around  $5 \mu\text{m}$ . The deformation regime at low temperature ( $< 1100^\circ\text{C}$ ) and strain rate in the range  $0.01\text{s}^{-1} \sim 1\text{s}^{-1}$  exhibit limited recrystallization with a recrystallized fraction between 10 and 30%. Recrystallized microstructure is very fine for this conditions range, with an average grain size about  $1 \mu\text{m}$ . The two maps on Figures 4.21a and 4.21b highlight a strong correlation between dynamically recrystallized grain size and recrystallized fraction: large grain size correspond to large fraction, and reciprocally. Grain size is larger for higher temperature and for lower strain rate because grain growth is very active in this case. As a conclusion, growth of recrystallized grains induces an increase of recrystallized fraction.

Crystalline misorientation can be quantified by the Kernel Average Misorientation parameter (KAM). The global average misorientation was then evaluated by taking the average over the whole scanned



area (273x92m). This mean KAM parameter is represented versus deformation parameters on Figure 4.21c. It can be seen on this map that misorientation parameter follows inverse evolution with grain size and recrystallized fraction: when misorientation parameter is high, recrystallized fraction is low and grain size is low. This correlation is due to the erasing of misorientations by the growth of new recrystallized grains leading to the elimination of misorientation. During the development of a new grain, the moving grain boundaries sweep the material and erase the dislocations structure, leading to a decrease of KAM parameter. Therefore, KAM misorientation parameter is directly an indicator of the operation of recrystallization process, in the same way as recrystallized fraction.

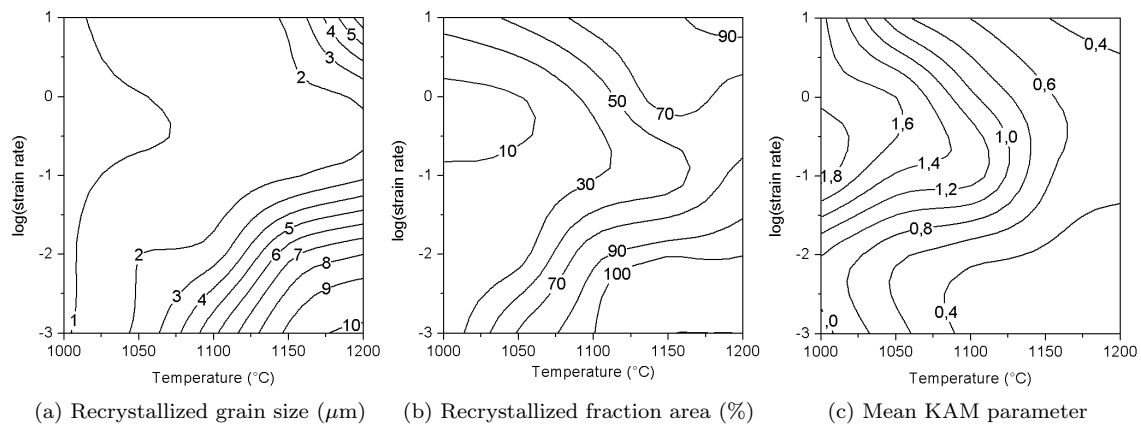


Figure 4.21: Maps of recrystallized grain size and fraction evolution with temperature and strain rate

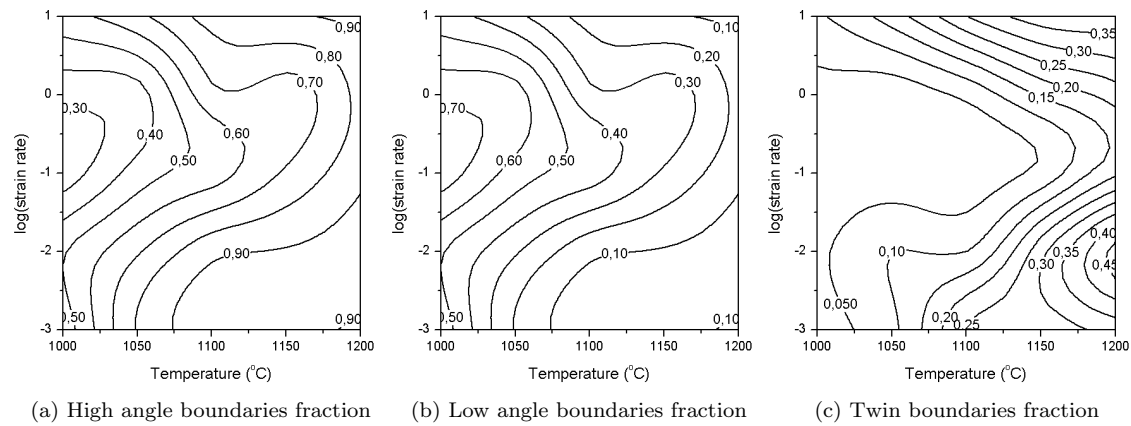


Figure 4.22: Maps of boundaries fractions after deformation at  $\epsilon=0.8$

Figure 4.22 indicates the nature of grain boundaries after hot deformation. Maps 4.22a and 4.22b are complementary, and illustrate the fractions of high-angle boundaries (noted HAG,  $15^\circ$ - $90^\circ$ ) and low angle boundaries (LAG,  $2^\circ$ - $15^\circ$ ). The threshold for the definition of low angle boundaries was set



to  $2^\circ$ . Misorientations with a lower angle do not reveal the limit between the different crystallites, and illustrate simply the storage of dislocations inside grains. The map 4.22c represents the fraction of  $\Sigma 3$  annealing twins ( $60^\circ$ ) over the other types of boundaries.

For high temperature ( $T > 1100^\circ\text{C}$ ) and low strain rate ( $\dot{\epsilon} < 0.01\text{s}^{-1}$ ) or high strain rate ( $\dot{\epsilon} > 10\text{s}^{-1}$ ), HAG fraction is above 80%, while LAG fraction is lower than 20%. The rapid grain growth eliminates the substructure by boundary migration, therefore the KAM parameter (Figure 4.21c) and LAG fraction (Figure 4.22b) are quite low for these conditions. At high temperature, twin fraction is quite high and reach 30 to 40% at  $1200^\circ\text{C}$ . Annealing twins are usually formed in recrystallized microstructure through grain growth [134] or grain boundary dissociation [135] processes. As the grain boundary migration process is very fast at high temperature, it is natural to observe a relatively high twin fraction.

On the other hand, deformation conditions at low temperature ( $T < 1100^\circ\text{C}$ ) and intermediate strain rate ( $\dot{\epsilon} = 0.1 - 1\text{s}^{-1}$ ) generates a microstructure with a large fraction of LAG boundaries and with nearly no annealing twins. The lack of annealing twins can be attributed to the limited activity of recrystallization, and to the transformation of some twin boundaries into HAG boundaries due to the plastic deformation.

To conclude, the nature of grain boundaries is strongly correlated to the activity of recrystallization. The occurrence of grain boundary migration eliminates LAG boundaries and generate a high twins fraction. On the other hand, heavily deformed microstructure with limited recrystallization is characterized by a large fraction of LAG boundaries and an absence of annealing twins.

#### 4.4.3 Microstructural interpretation of processing maps

Power efficiency processing map is predicting favorable conditions for the occurrence of dissipative metallurgical phenomenon at temperature above  $1050^\circ\text{C}$  and strain rate lower than  $0.1\text{s}^{-1}$  (Cf Figure 3.16 page 95 and Figure 4.23a). For this deformation conditions range, dynamic recrystallization was clearly identified (Table 4.9), and can be linked up to the high value of power efficiency parameter. On the other hand, power efficiency parameter is very low for high strain rate and can reach a negative value for strain rate about  $10\text{s}^{-1}$ , which should correspond to an absence of any dissipative metallurgical phenomenon and to the occurrence of some potential instabilities. Actually, the examination of microstructure reveals advanced recrystallization process for high strain rate (Table 4.9 for  $\dot{\epsilon} > 1\text{s}^{-1}$ ), which is in disagreement with power efficiency map. Such disagreement is observed for all the temperature range  $1000^\circ\text{C} \sim 1200^\circ\text{C}$   $10\text{s}^{-1}$ : dynamic recrystallization is observed, and no specific difference with the recrystallized microstructure obtained at low strain rate deformation was noted. Therefore dynamic recrystallization can operate even if no dynamic metallurgical processes are expected to occur according to power efficiency map.



Instability map is predicting flow instabilities for strain rate higher than  $0.1\text{s}^{-1}$  (Figure 3.16), indicating unfavourable deformation conditions. Such prediction of instabilities is not supported by microstructure observations presented above. Neither shear bands nor cracks were observed, and the deformation conditions for high strain rate are safe in terms of instabilities, contrary to the predictions of the instability map. As a consequence, the negative instability parameter is not a necessary and sufficient criterion for the occurrence of flow instabilities in the case considered here. For temperature lower than  $1100^{\circ}\text{C}$  and strain rate between  $0.1\text{s}^{-1}$  and  $1\text{s}^{-1}$ , many crystalline misorientations, slip bands and low angle grain boundaries can be noticed. This area of deformation conditions has been considered sometimes as unstable due to the occurrence of these defects and to the absence of dynamic recrystallization [59]. However it seems more rational to consider that defects such as slip bands are generated by regular plastic deformation without involvement of any specific unstable deformation mechanism. As recrystallization is not effective for these deformation conditions, it is quite natural to observe a high concentration of crystalline defects. The material do not manage to evacuate energy from the plastic deformation through dynamic recrystallization, therefore other dissipation mechanisms can occur instead.

From the following analysis of processing maps, it can be concluded that the application of Dynamic Materials Model have limitations [78] that should be considered very carefully. Power efficiency map gives simply a coarse outline of the dynamic metallurgical processes for a given area of deformation conditions, while instability map gives an estimation of deformation conditions that could include a potential risk of plastic instabilities. However processing maps cannot serve as a proof to determine rigorously the mechanisms involved during deformation. The prediction power of processing maps is limited in the case considered here, and estimations are correct for a narrow range of experimental conditions only. Extrapolation of processing maps over the experimental conditions range is hardly reliable. Moreover it provides incomplete information on the underlying metallurgical phenomenon and on the resulting microstructure.

Figure 4.23b represents the softening map obtained in the section 3.2. Softening parameter was calculated from the equation 3.10 (page 96), and represents the fractional flow softening observed at large strain. At strain rate lower than  $0.01\text{s}^{-1}$  or higher than  $1\text{s}^{-1}$  softening parameter (Figure 4.23b) and recrystallized fraction (Figure 4.23c) reach together high values, while for strain rate about  $1\text{s}^{-1}$  both softening and recrystallized fraction are very low. Thus a very good correlation is observed between softening and recrystallized fraction. As a consequence, the dynamic recrystallization can be identified as the main softening mechanism during the deformation of L-605 alloy. Therefore, softening parameter is a good indicator of the operation of dynamic recrystallization.

The study of flow softening from compression curves provides a softening parameter resulting from the macroscopic mechanical properties of the material and representative of the microstructural



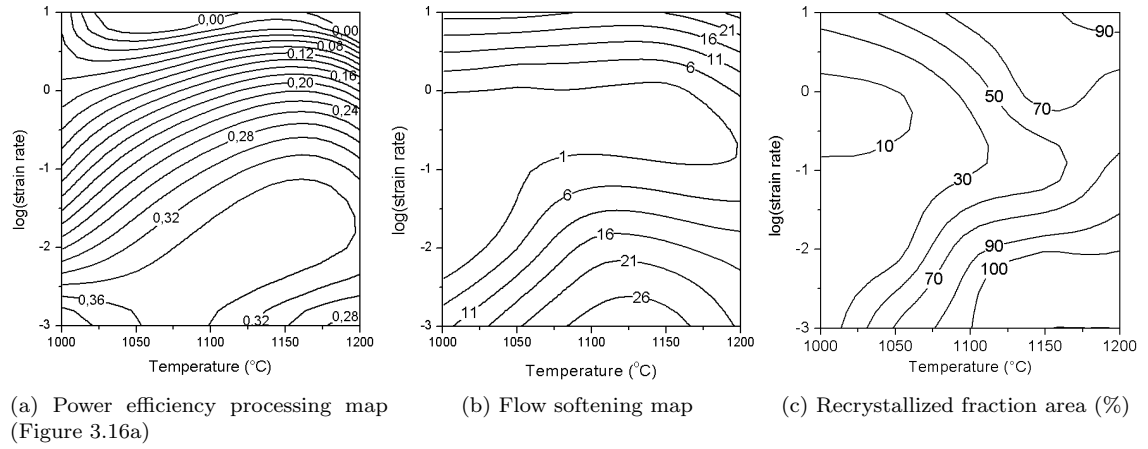


Figure 4.23: Comparison of power efficiency map and softening map with the recrystallized fraction

changes like dynamic recrystallization. This procedure could be applied to the study of other microstructural changes leading to flow softening, such as adiabatic shear bands or cracks. This method was shown to be suitable to describe dynamic recrystallization in the whole experimental condition range. Moreover, an extrapolation of steady-state stress  $\sigma_V$  and  $\sigma_{ss}$  could reasonably provide fair conjecture about the operation of the dynamic recrystallization over the experimentally tested deformation conditions. Therefore the thorough study of flow softening provides sufficient prediction power to determine the deformation conditions on which dynamic recrystallization is taking place. This method provides some relevant information on the microstructural change with a better reliability and with more physical comprehension than conventional processing maps.

To conclude, processing maps are in agreement with experimental result for  $T > 1050^\circ\text{C}$  and  $\dot{\epsilon} < 0.1\text{s}^{-1}$  only: in this range flow is stable and high power efficiency is corresponding to dynamic recrystallization process. For other forging conditions processing maps are inconsistent with experimental result. Therefore processing maps shows limited prediction ability to determine the operation conditions of dynamic metallurgical mechanisms. The study of flow softening provided a softening parameter resulting from compression curves, and describing properly the operation of dynamic recrystallization for any experimental condition. This method should be used jointly with processing maps to provide sufficient accuracy and predictability on the resulting microstructure after high-temperature deformation.

#### 4.4.4 Observation of dynamic recrystallization mechanism on partially compressed samples

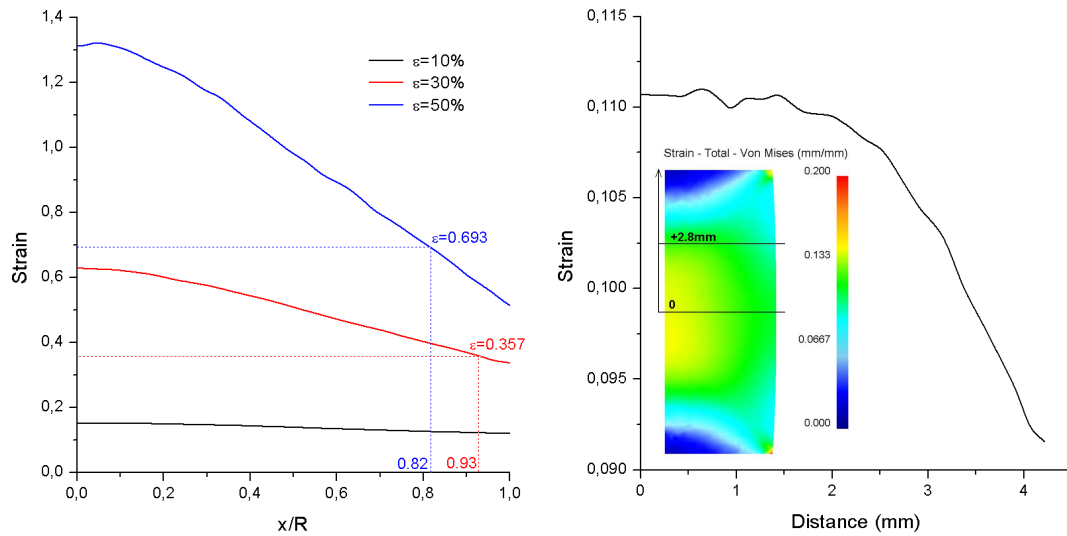
Observation of the microstructure at different strain levels gives further information on the dynamic recrystallization mechanisms: recrystallized grains can be observed at different stages of their life, and nucleation sites can be determined. Compression is carried out until a reduction of  $\epsilon = 10\%$ ,  $30\%$



and 50% (true strains  $\epsilon = 0.10$ ,  $\epsilon = 0.36$  and  $\epsilon = 0.69$ ) (Figure 4.24). The local position corresponding to a true strain  $\epsilon = 0.36$  and  $\epsilon = 0.69$  are located at 0.82 and 0.93 times the sample radius according to Figure 4.25a, based on Finite Elements calculations. The local strain along the radial axis for a reduction of  $\epsilon = 10\%$  is found to be always above 0.105 due to the strain concentration. Therefore, the strain profile was plotted along the radial axis shifted up of +2.8mm from the centre of the sample. According to Figure 4.25b, along this axis a strain of  $\epsilon = 0.105$  is met at 2.9mm from the longitudinal axis. On Figures 4.26, 4.27 and 4.28, microstructure observed at the locations calculated for the three compression levels achieved are illustrated.



Figure 4.24: Partial compression at strain  $\epsilon = 0.11$ ,  $\epsilon = 0.36$  and  $\epsilon = 0.69$



(a) Strain gradient along the radial axis as a function of relative position

(b) Strain gradient along the radial axis shifted of +2.8mm from the centre for 10% reduction

Figure 4.25: Calculation of strain gradient by Finite Elements Method, and determination of the area to observe by EBSD

The condition  $T=1000^{\circ}\text{C}$   $\dot{\epsilon} = 1\text{s}^{-1}$  leads to the creation of many low angle boundaries with deformation (Figure 4.26). The high concentration of defects in initial grains is due to the lack of dynamic recovery at low temperature. Recrystallization is visible at grain boundaries by the formation of very small grains ( $<1 \mu\text{m}$ ), corresponding to a final recrystallization fraction of 10% of the area. It can be concluded that for this deformation condition, the creation of defects is



enough to generate nucleation of new grains by bulging of initial grain boundaries, but the low temperature is not favourable to the growth of new grains. Therefore the size of new grains is small, and recrystallized area is very low. These observations point up that for process conditions between  $0.1\text{s}^{-1}$  and  $1\text{s}^{-1}$  and for temperatures lower than  $1100^\circ\text{C}$  the recrystallization is proceeding mainly by nucleation from grain boundaries, with a limited grain growth of new grains.

The condition  $T=1100^\circ\text{C}$   $\dot{\epsilon}=0.001\text{s}^{-1}$  leads to significant dynamic recrystallization, with a final recrystallization fraction of 90% of the area after compression at  $\approx 50\%$ . Recrystallization occurs at grain boundaries, and significant grain growth allow to the new grains to develop properly and to spread in the initial grains (Figure 4.26). The final grain size is the size of recrystallized grains, and initial microstructure is totally erased. As both dynamic recovery and dynamic recrystallization are very active due to high temperature and low strain rate, few low angle grain boundaries are visible in the microstructure during compression. Therefore substructure is hardly visible for this condition as it is eliminated by recovery and recrystallization.

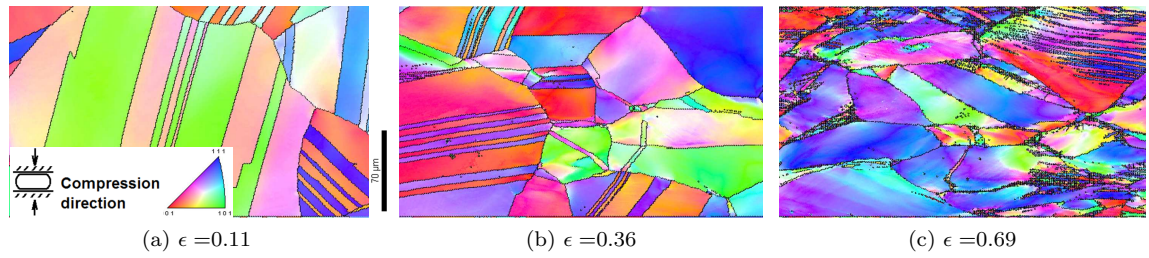


Figure 4.26: IPF maps of microstructure after partial compression at  $1000^\circ\text{C}$   $1\text{s}^{-1}$

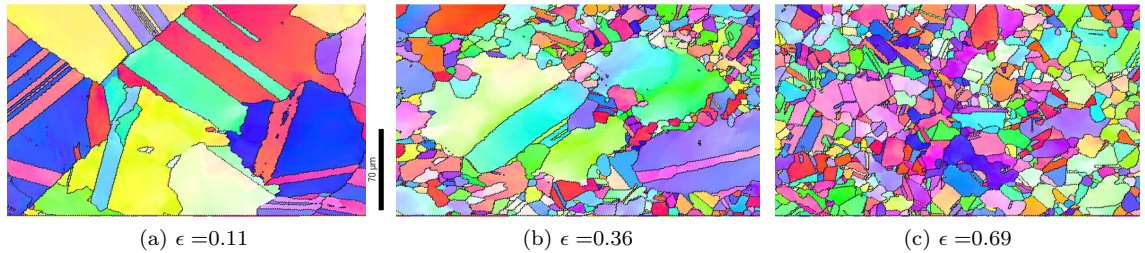


Figure 4.27: IPF maps of microstructure after partial compression at  $1100^\circ\text{C}$   $0.001\text{s}^{-1}$

The condition  $T=1200^\circ\text{C}$   $\dot{\epsilon}=10\text{s}^{-1}$  gives very similar results as for  $1100^\circ\text{C}$   $0.001\text{s}^{-1}$ . Recrystallization proceeds from grain boundaries, and lead to a high recrystallization fraction of 70% of the area for  $\approx 50\%$ . Due to high temperature and in spite of the high strain rate, few defects are visible due to the activity of recovery and recrystallization. For this condition annealing twins rotate from their initial angle of  $60^\circ$  to become high angle grain boundaries with an angle about  $55^\circ$ . After rotation, nucleus bulge from the annealing twins (Figure 4.28). This mechanism leads to the formation of recrystallized bands on annealing twins. On Figure 7c for a deformation level of  $\approx 50\%$ , the



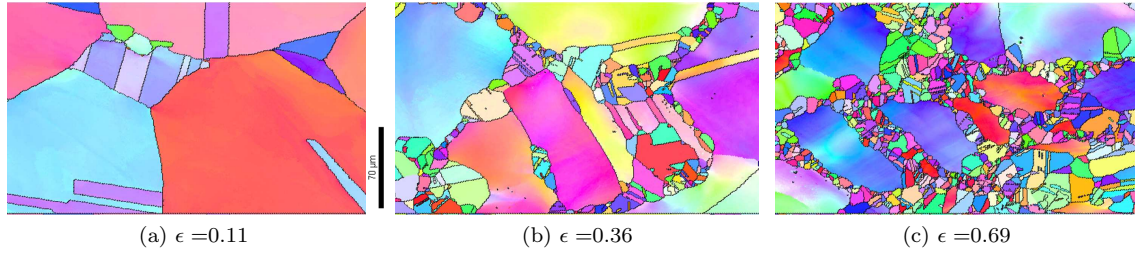


Figure 4.28: IPF maps of microstructure after partial compression at 1200°C 10s<sup>-1</sup>

non-recrystallized grains observed have the same crystalline orientation, and thus belong to a same initial grain that was fragmented by recrystallization in bands. The disposition and spacing of these bands is similar to the one of annealing twins, and suggest that twins were initially present on this place. The evolution of annealing twins into grain boundaries and its bulging can be observed for the condition 1100°C 0.001s<sup>-1</sup> as well (Figure 4.27). However for 1100°C 0.001s<sup>-1</sup> this mechanism is not frequent, while for 1200°C 10s<sup>-1</sup> it seems very usual.

The fraction of annealing twins ( $\Sigma 3$  grain boundaries) was evaluated from EBSD data after compression at  $\epsilon = 0.8$  and is detailed in the Table 4.11. The high twin fraction at 1200°C 10s<sup>-1</sup> explain the high frequency of nucleation mechanism by bulging from twins, while this mechanism is rarer for 1100°C 0.001s<sup>-1</sup> and not observed for 1000°C 1s<sup>-1</sup> due to the lack of twins available for nucleation.

Deformation condition	HAG fraction (15-90°)	$\Sigma 3$ twin fraction (60°)
1000°C 1s <sup>-1</sup>	0.89	0.11
1100°C 0.001s <sup>-1</sup>	0.72	0.28
1200°C 10s <sup>-1</sup>	0.58	0.42

Table 4.11: High angle boundaries and twin boundaries fraction after deformation at  $\epsilon = 0.8$

During the bulging mechanism from annealing twin, a high angle grain boundary is developing from a plane twin boundary, as illustrated in Figure 4.29a. The nucleus formed has a lens shape, as we can see in Figure 4.29b which is a detailed view of Figure 4.28b for  $\epsilon = 30\%$ . The angle  $\beta$  measured is about 40° between the two boundaries of the nucleus of Figure 4.29b. The surface energies can be approximated in a first order by a projection in the plane of  $\gamma_1$  as the twin boundary is near a cusp position [136]:

$$\gamma_1 + \gamma_2 \cdot \cos(\alpha) + \gamma_3 \cdot \cos(\xi) = 0 \quad (4.5)$$

If the grain boundaries energies are equal, the nucleus boundaries should form an angle  $\beta = 120^\circ$ . Surface energy of high angle grain boundary is about 0.65J.m<sup>-2</sup> and twin surface energy is 0.0127J.m<sup>-2</sup> for pure cobalt [127]. Therefore, direct bulging from an annealing twin without preliminary rotation



is energetically unfavourable to the system, as it replaces a low-energy interface by a higher one. In the present case, the value of  $\beta$  is three times below this critical value, indicating that the energy of the nucleus boundaries is lower than the initial twin boundary. We can conclude that twins acquire a high surface energy by rotation from  $60^\circ$  to about  $55^\circ$  (Figure 4.29b). This high surface energy constitutes the driving force for the nucleation of grains with lower surface energy. Therefore the rotation of annealing twins is essential in the nucleation process as it provides the driving force.

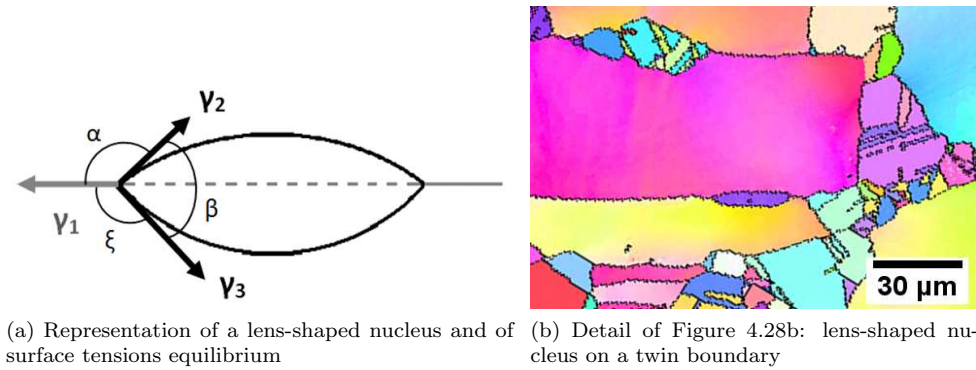


Figure 4.29: Formation of lens-shaped nucleus on annealing twins: surface tension equilibrium and boundaries angles

#### 4.4.5 Microstructure gradient inside compression samples

##### Microstructure at low magnification

As mentioned previously (Cf. page 123), compression of cylindrical samples leads to a severe heterogeneity of deformation. Due to the recrystallization process, grain size usually decreases with strain, resulting in a strong gradient of microstructure. This section proposes to investigate the variation of microstructure with strain field. From this approach, the variation of grain size with strain can be estimated from a single EBSD observation at very low magnification. Thereof, the effect of deformation conditions on the grain refinement kinetics can be understood for a large range of processing conditions.

Figure 4.30 illustrates the microstructure gradient observed in a sample deformed at  $1100^\circ\text{C}$   $0.01\text{s}^{-1}$   $\epsilon=0.8$ . This picture was generated by assembling 33 images taken at magnification 50x by optical microscopy using the AutoStitch software (M. Brown, UBC). The upper part of the sample corresponds to the top surface of the sample in contact with anvils, and exhibits larger grain size. The middle part of the sample presents a relatively homogeneous microstructure, with no cracks or shear bands visible. One can recognize in the middle area some large grains flattened due to the compression. The microstructure surrounding these grains is weakly perceptible, and corresponds to refined microstructure by recrystallization.



The same observations can be obtained by EBSD at low magnification. Figure 4.31 shows the microstructure near the edge of the sample regarding the radial axis, for a deformation of  $\epsilon = 0.8$  at  $1200^{\circ}\text{C}$   $10\text{s}^{-1}$ . Large flattened grains are surrounded by recrystallized grains, forming a necklace structure. For this deformation condition, the recrystallization occurs frequently at twin boundaries and forms recrystallized bands splitting the initial grains, as mentioned previously. The KAM map illustrated on the Figure 4.31b shows that non-recrystallized grains contains many misorientations, while recrystallized grains contain nearly no misorientations, in agreement with the results presented previously. Similar cartographies taken close to the peripheral edge of the samples are displayed on the Appendix 2 page 192 (Figures 8 and 9).

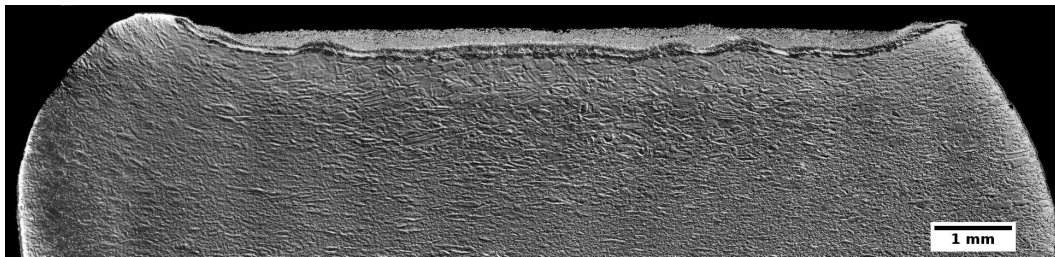


Figure 4.30: Mosaic of 33 pictures taken by optical microscopy at 50x after compression at  $1100^{\circ}\text{C}$   $0.01\text{s}^{-1}$   $\epsilon=0.8$ . Width of the picture=13.3mm

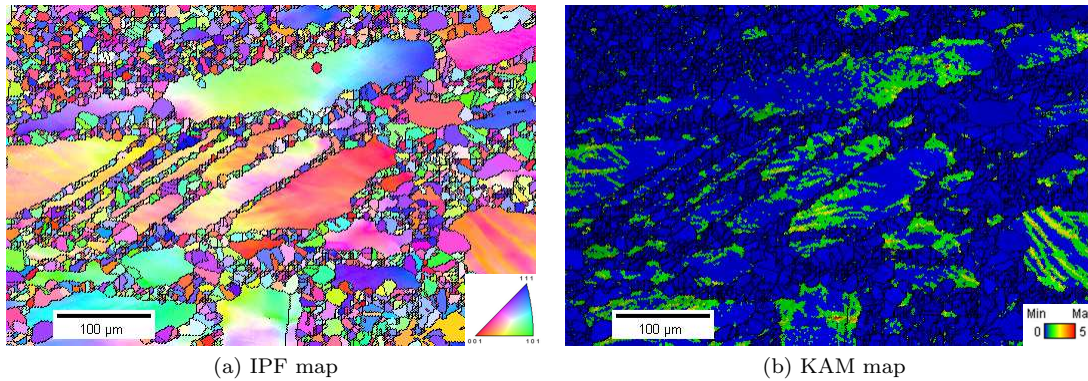


Figure 4.31: Microstructure after deformation at  $1200^{\circ}\text{C}$   $10\text{s}^{-1}$  observed at low magnification (250x) near the sample edge

### Microstructure gradient along the longitudinal axis

EBSD cartographies were established at 30x magnification along the longitudinal axis of the sample. IPF and KAM cartographies are illustrated in the case of the deformation at  $1200^{\circ}\text{C}$   $10\text{s}^{-1}$  on Figures 4.35 and 4.36. Cartographies for other deformation conditions are illustrated in the Appendix 2 page 194:  $1000^{\circ}\text{C}$   $0.1\text{s}^{-1}$  (Figure 10),  $1100^{\circ}\text{C}$   $0.01\text{s}^{-1}$  (Figure 13),  $1100^{\circ}\text{C}$   $0.1\text{s}^{-1}$  (Figures 11 and 14),  $1200^{\circ}\text{C}$   $0.1\text{s}$  (Figures 12 and 15). These cartographies were then cropped into 7 to 8 squares



pieces of 400x400  $\mu\text{m}$ , and each piece was analysed separately. The average grain size, the average KAM value, and the average fraction of the different boundaries were determined for each area. These mean values were attributed to the middle point of each area. Thereof, the evolution of these microstructure parameters can be plotted as a function of the position on the longitudinal axis. Finite elements calculations were carried out for the corresponding conditions (e.g. Figure 4.19). The strain evolution along the longitudinal axis was determined, and is illustrated on the Figure 4.32a for 8x12mm samples until  $\epsilon = 0.8$  (Thermecmaster-Z), and in Figure 4.32b for 9.77x15mm samples until  $\epsilon = 0.8$  (Gleeble). The strain gradient is weakly dependent on deformation conditions, and can be approximated by a Gaussian equation:

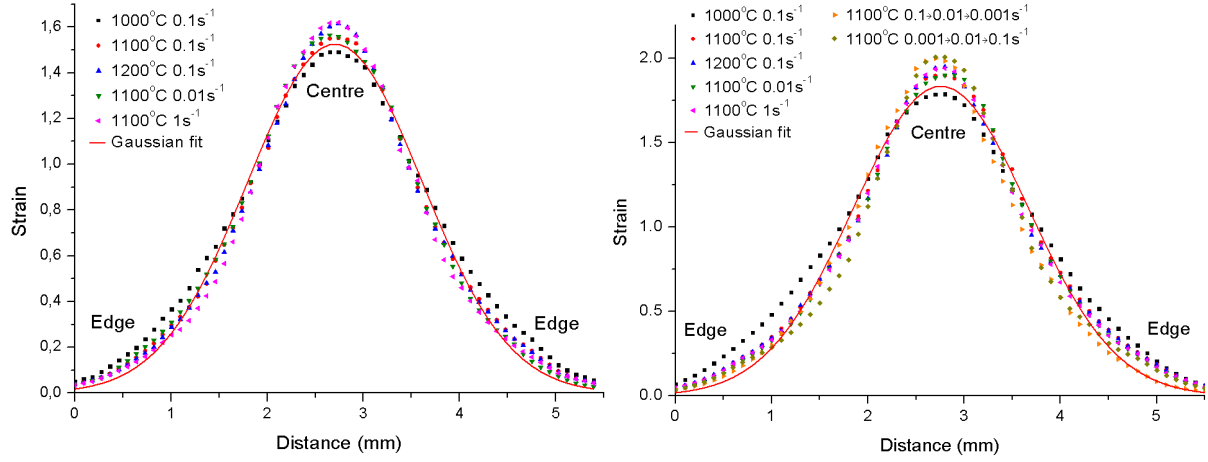
$$\epsilon = \frac{3.462}{1.810 \cdot \sqrt{\Pi/2}} \cdot \exp\left(-2\left(\frac{x-2.703}{1.810}\right)^2\right) \quad (\text{Thermecmaster} - \text{Z}) \quad (4.6)$$

$$\epsilon = \frac{4.181}{1.817 \cdot \sqrt{\Pi/2}} \cdot \exp\left(-2\left(\frac{x-2.758}{1.817}\right)^2\right) \quad (\text{Gleeble}) \quad (4.7)$$

From these equations, the local strain corresponding to the different positions of the large EBSD cartographies can be calculated, and microstructure properties can be plotted as a function of strain. Figure 4.33 shows the evolution of mean grain size and KAM parameter with strain for different deformation conditions. For all conditions, grain size decrease significantly until  $\epsilon = 0.5$ , then the grain size stabilizes. For  $\epsilon > 1$ , recrystallization reaches the steady-state, and grain size is constant. The grain refinement is found to be stronger for intermediate temperature and intermediate strain rate. Indeed, deformation at low temperature induces a very low recrystallized fraction, and the mean grain size remains despite the formation of very small recrystallized grains. At high temperature, grain growth leads to the formation of large grains and the average grain size is higher. Therefore, at intermediate temperature an apparent minimum of mean grain size is detected due to the formation of a significant amount of small grains. For  $T=1200^\circ\text{C}$ , the increase of strain rate leads to an increase of grain size, in agreement with previous observations (Table 4.9). Higher strain rate provide a higher driving force for recrystallization, so larger grains are observed at high strain rate.

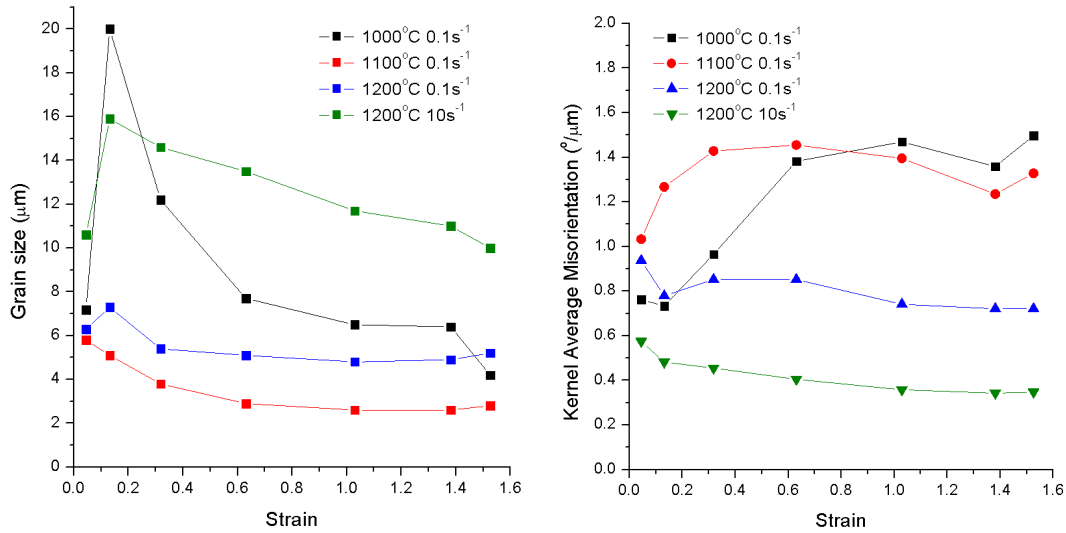
Figure 4.33b illustrates the gradient of average KAM parameter as a function of local strain. For temperature below  $1100^\circ\text{C}$ , KAM value increase with strain until  $\epsilon > 0.6$ , then stagnate at higher strain. This shows the hardening of the material with deformation: 'geometrically necessary' dislocations accumulate and increase progressively the crystalline misorientations. For strain above 1, KAM slightly decrease due to recrystallization consuming the stored dislocations. On the other hand, at  $T=1200^\circ\text{C}$  the mean KAM value is quite constant with strain. The general trend is a soft decrease with strain, due to the recrystallization process. At higher strain rate, KAM value is lower due to a stronger activity of recrystallization.





(a) Strain profile of Thermecmaster 8x12mm samples at  $\epsilon = 0.8$  (b) Strain profile of Gleeble 9.77x15mm samples at  $\epsilon = 1$

Figure 4.32: Strain gradient profile along the longitudinal axis calculated by Finite Elements Method



(a) Evolution of grain size with strain from the edge to the centre (b) Evolution of mean KAM parameter with strain from the edge to the centre

Figure 4.33: Grain size and KAM parameter as a function of strain along the longitudinal axis of the sample, after gas quench at  $-50^{\circ}\text{C.s}^{-1}$

Figure 4.34 illustrates the grain and twin boundaries fraction evolution with strain. For  $T=1000^{\circ}\text{C}$ , the amount of Low-Angle Grain boundaries (LAG) is increasing with strain, while High-Angle Grain boundaries (HAG) decrease with strain. For this temperature, the sluggish recrystallization process does not generate significant increase of HAG by formation of new grains. The accumulated misorientations illustrated in Figure 4.33b lead to an increase of LAG fraction in Figure 4.34a. The twin fraction remains below 1%: grain boundary migration process is very slow and generates a



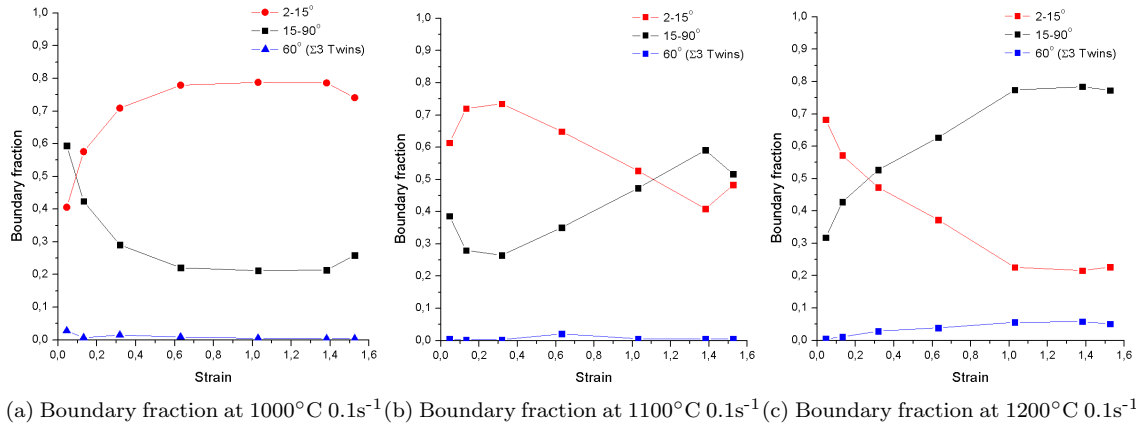


Figure 4.34: Evolution of grain and twin boundaries fractions with strain gradient for temperature between 1000 and 1200°C and strain rate 0.1s<sup>-1</sup>

very limited amount of twins by grain growth or grain boundary dissociation [134, 135]. Moreover, twins formed during the deformation process may transform into HAG due to the plastic deformation. For T=1200°C, HAG fraction increases due to the operation of recrystallization. LAG fraction decreases, because the substructure formed at the initial stage of deformation is progressively consumed by recrystallization through the nucleation process, or cleared off by boundary migration. Twin fraction increase with strain until 5% due to the recrystallization and the subsequent growth of new grains. The temperature T=1100°C is an interesting intermediate case: for strain below 0.5 recrystallization is limited and boundaries fraction evolution is similar to T=1000°C. Then for larger strain, recrystallization is sufficient to lower the fraction of LAG and increase HAG fraction by nucleating new grains. To conclude, recrystallization leads to a progressive disappearance of substructure and to the joint formation of grain and twin boundaries.

### Effect of cooling speed on the microstructural gradient

Hot working at high temperature and high strain rate usually leads to post-dynamic microstructure evolution: due to the high stored energy and to the high mobility of boundaries, meta-dynamic recrystallization and static recrystallization can occur during the cooling step. In the case of meta-dynamic recrystallization, the nucleus are formed during the dynamic regime, but do not have sufficient time at high strain rate to grow completely. Therefore these nucleus grow during cooling, and an increase of grain size with strain rate is observed. Static recrystallization mechanism occurs when neither nucleation nor growth have the time to occur during the dynamic regime, and therefore occur during the cooling step. This case differs from the previous one by the formation of nucleus during the cooling step.

It was observed previously that for strain rate above 0.1s<sup>-1</sup>, mean grain size is increasing with strain



rate for any temperature between 1000 and 1200°C (Figures 4.21a and 4.33a). Therefore the increase of dynamic recrystallization at high strain rate is quite unexpected. The recrystallization process at high deformation speed may be indeed the combined result of dynamic and meta-dynamic or static recrystallization operating jointly. This section investigates the effect of cooling speed on the microstructure gradient to quantify the occurrence of post-dynamic mechanisms.

Compression tests were carried out at  $T=1200^{\circ}\text{C}$   $\dot{\epsilon}=10\text{s}^{-1}$  on Thermecmaster-Z device until  $\epsilon=0.8$ , followed by gas quench with a cooling speed of  $-50^{\circ}\text{C.s}^{-1}$ . Hot-working at the same temperature and strain rate was also carried out on the Gleeble device, and then water quenched, with a maximal cooling speed of  $-2000^{\circ}\text{C.s}^{-1}$ . The microstructure gradient along the longitudinal axis was observed by EBSD with the same procedure as mentioned previously. The resulting microstructure are illustrated in Figures 4.35 and 4.36. Additional microstructure gradients are illustrated in the Annex 2 (page 194) after gas quench (Figures 10, 11 and 12) and after water quench (Figure 13, 14 and 15).

Both Figures 4.35a and 4.36a exhibit a significant grain refinement in the centre of the sample, corresponding to high values of strain. Grain size is slightly larger in Figure 4.35a corresponding to gas quench, due to some grain growth occurring during the cooling process. Figures 4.35b and 4.36b represent the KAM maps after gas quench and water quench respectively. Both the two maps indicate the existence of some crystalline misorientations in the intermediate region of the sample. However map 4.35b exhibits a lower amount of misorientations, probably due to some recovery process and to the occurrence of meta-dynamic recrystallization. The persistence of some crystalline defects after gas quench proves that the post-dynamic recrystallization is 'meta-dynamic' and not static: otherwise the totality of crystalline defects would be erased by boundary migration.

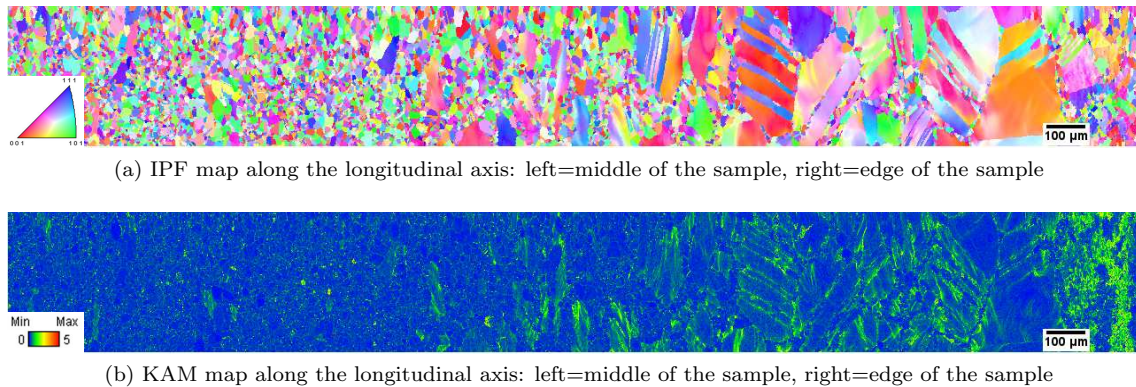


Figure 4.35: Microstructure after deformation at  $1200^{\circ}\text{C}$   $10\text{s}^{-1}$  with Thermecmaster-Z device, followed by  $-50^{\circ}\text{C.s}^{-1}$  gas quench

The microstructure gradient can be comprehended quantitatively by combination with Finite Elements calculations. The strain gradient was calculated as indicated in the previous section, and is illustrated in Figure 4.32b. Strain evolution along the longitudinal axis can be fitted by a Gaussian



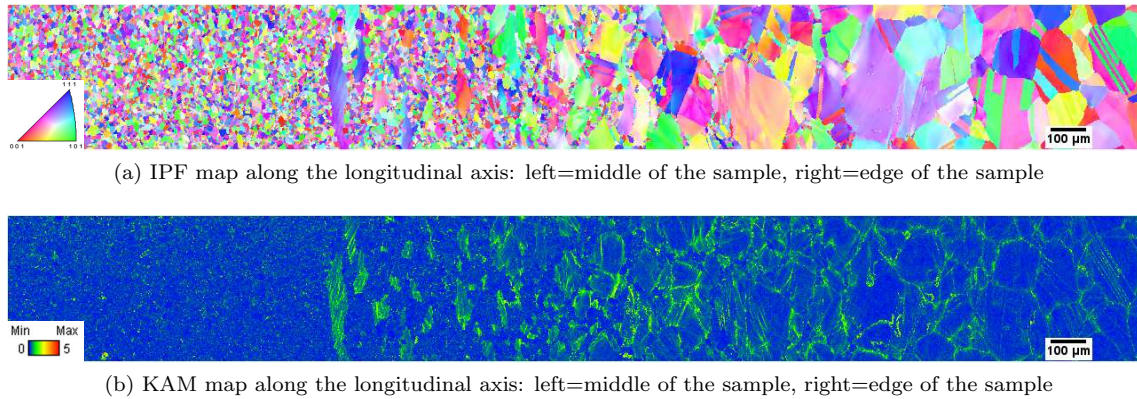


Figure 4.36: Microstructure after deformation at  $1200^{\circ}\text{C } 10\text{s}^{-1}$  with Gleeble device, followed by  $-2000^{\circ}\text{C.s}^{-1}$  water quench

curve, with the equation 4.7. From this equation, the evolution of the different microstructure parameters with strain can be determined. Figure 4.37a represents the evolution of grain size with strain for gas quench and water quench. For  $1100^{\circ}\text{C } 0.1\text{s}^{-1}$  and  $1200^{\circ}\text{C } 0.1\text{s}^{-1}$ , surprisingly the mean grain size is larger in the core of the sample for water quench than for gas quench. This can be attributed to the difference of thermal gradient between the Thermecmaster-Z and the Gleeble devices. The temperature in the centre of the sample might be different, leading to a change of mean grain size. For  $1200^{\circ}\text{C } 10\text{s}^{-1}$ , grain size is very similar in the core of the sample for the two cooling speeds. This shows that post-dynamic recrystallization is very limited and leads to a negligible change on the mean microstructure properties.

At  $\dot{\epsilon} = 0.1$ , KAM parameter is found to be lower for water-quenched sample than for gas-quenched sample. This confirms that the temperature in the centre of the samples may depend on the device used for hot working. For instance, a higher increase of temperature due to adiabatic heating during the deformation in the case of Gleeble experiments could explain the larger grain size and the lower KAM parameter due to a more active recrystallization and recovery. For  $\dot{\epsilon} = 10$ , the KAM value of the central area is very close for the two cooling speeds, and no additional recovery due to cooling process can be identified in this area.

Figure 4.38 illustrates the grain boundary map after deformation at  $1200^{\circ}\text{C } 10\text{s}^{-1}$  for the two different cooling speeds. Large grains can be observed on Figure 4.38a ( $-50^{\circ}\text{C.s}^{-1}$ ). These large grains are absent of the microstructure in Figure 4.38b after cooling at  $-2000^{\circ}\text{C.s}^{-1}$ . The grain size distribution for the two cartographies is represented in Figure 4.38c. For a grain size between 0 and  $30\mu\text{m}$ , grain size distribution is identical for the two samples, showing there is no influence of cooling speed on the dynamic recrystallized size. For grain size above  $30\mu\text{m}$ , a second mode exist in the gas-quenched sample only. This would mean large grains are formed during the cooling process, so meta-dynamic recrystallization effectively occurs.



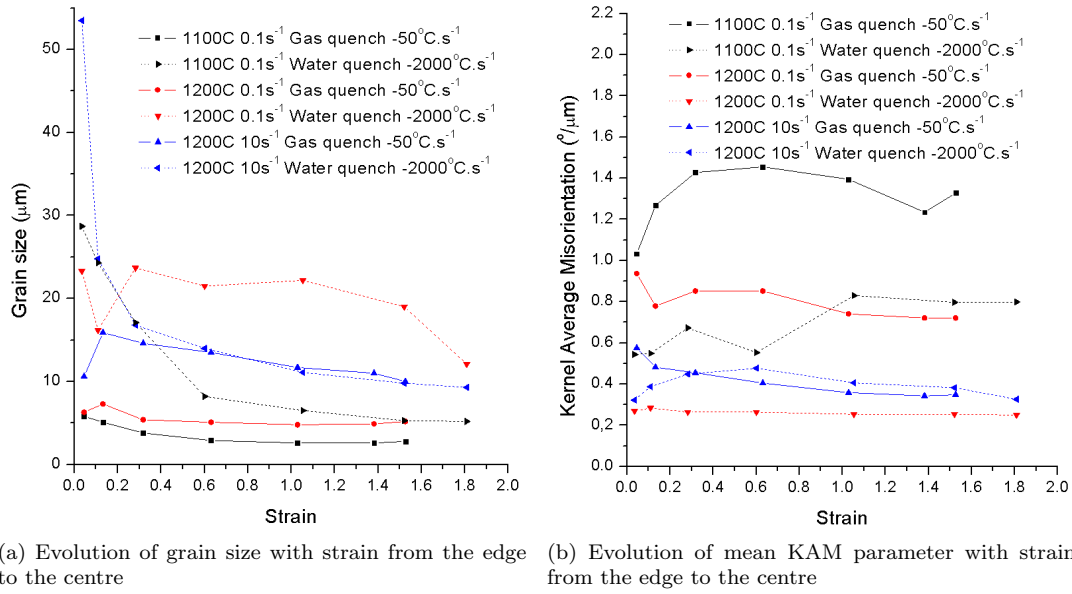


Figure 4.37: Comparison of grain size and KAM gradients after gas quench at  $-50^{\circ}\text{C.s}^{-1}$  (Thermecmaster) or water quench at  $-2000^{\circ}\text{C.s}^{-1}$  (Gleeble)

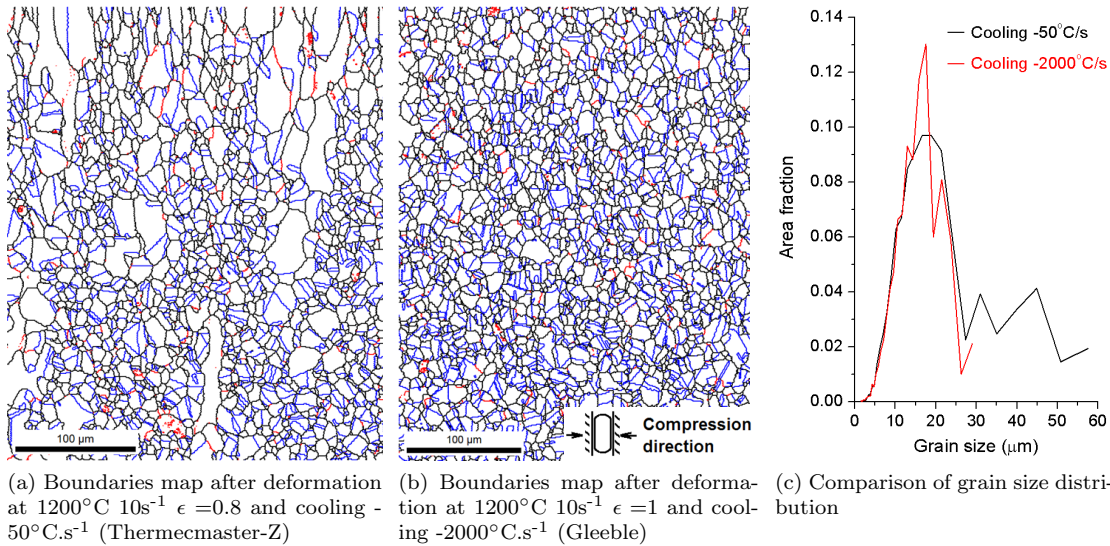


Figure 4.38: Grain boundaries map in the center of the sample after deformation at 1200°C 10s<sup>-1</sup>: HAG (black lines), LAG (red lines) and twins (blue lines), and corresponding grain size distribution

To conclude, the observation of microstructure gradient reveals the formation of some large grains for the gas-quenched sample, that do not exist in the water-quenched sample. Therefore, meta-dynamic recrystallization occurs during the cooling process. A slight increase of the KAM parameter can be seen at 10s<sup>-1</sup> and is attributed to the recovery process occurring during the cooling step. Substructure is still present after cooling, therefore the nature of post-dynamic recrystallization is meta-dynamic and not static. The post-dynamic microstructure changes remain very limited and does not affect



significantly the mean microstructure parameters such as the mean grain size or the mean KAM value.

#### 4.4.6 Observation of deformed substructure by transmission electron microscopy

The dislocation structure was observed after deformation at  $1000^{\circ}\text{C}$   $1\text{s}^{-1}$  and  $1100^{\circ}\text{C}$   $0.001\text{s}^{-1}$  for a reduction of 30% ( $\epsilon = 0.36$ ). The Figure 4.39 shows that deformation at  $1000^{\circ}\text{C}$  leads to the formation of a complex dislocation structure exhibiting some dark bands. These bands can be identified as stacking faults. Therefore the formation of stacking faults occurs as expected on the section 1.2.1.2 (page 25), due to the relatively low stacking fault energy of L-605 alloy. Also some dark contrast can be observed, and may correspond to some perfect dislocations. Figure 4.39b shows some stripes corresponding to some stacking faults, with dark contrast on its left vicinity. It is likely that the dislocation substructure is composed of some stacking faults and some perfect dislocations, and that these two types of defects interact each other. However further investigation on the substructure is required to confirm this interpretation.

Figure 4.40 shows the substructure in the recrystallized material at a grain boundary. The presence of a grain boundary in Figure 4.40a is confirmed by the presence of two diffraction diagrams corresponding to the orientations of each grain. Figure 4.40a shows a difference of contrast between the two sides of the boundary, suggesting that the two adjacent grains may have a different dislocation density. However only a small fraction of dislocations is visible on this picture, and the exact dislocation gradient is unknown. Figure 4.40b shows the structure of another grain boundary, with some well formed stacking faults on the right grain. No clear gradient of visible dislocations density was noticed in recrystallized grains.

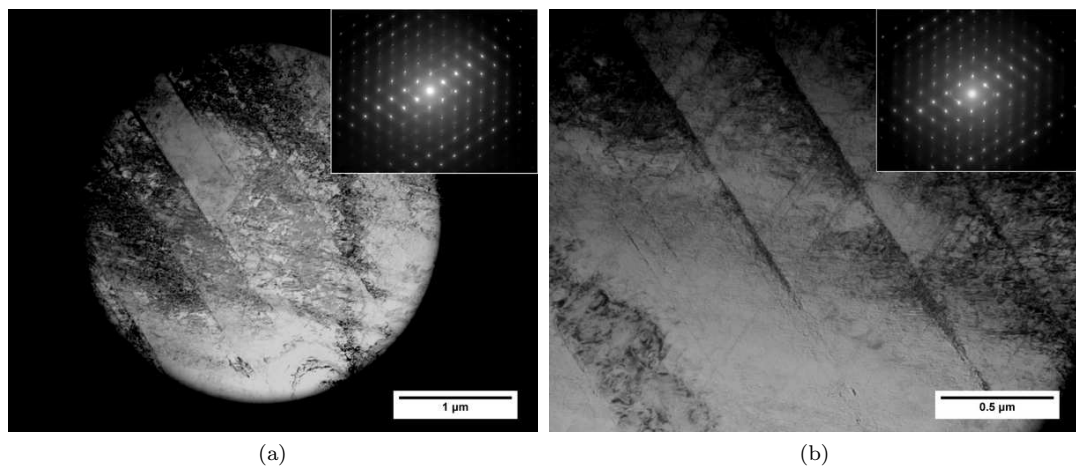


Figure 4.39: Observation by TEM after deformation at  $1000^{\circ}\text{C}$   $1\text{s}^{-1}$   $\epsilon = 0.36$



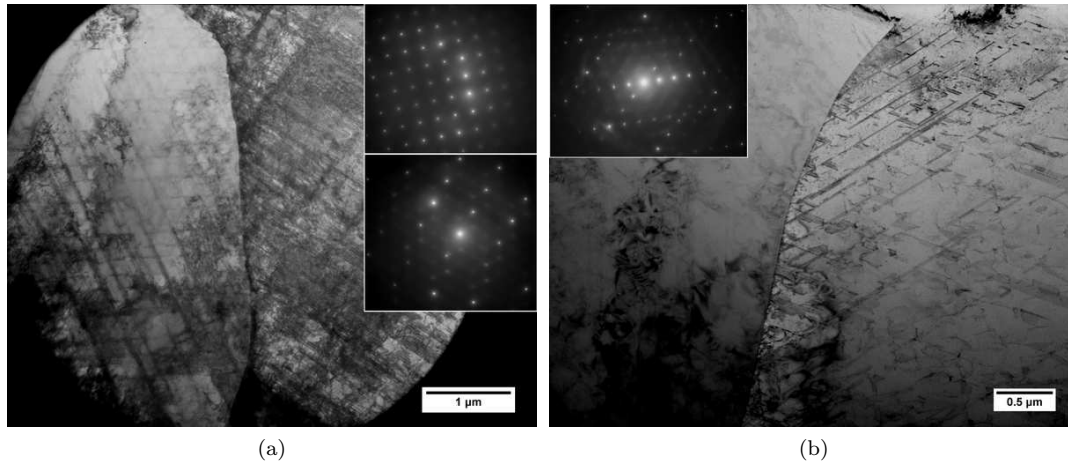


Figure 4.40: Observation by TEM after deformation at  $1100^{\circ}\text{C}$   $0.001\text{s}^{-1}$   $\epsilon = 0.36$

Figure 4.41 illustrates the substructure observed by TEM after hot deformation in other cobalt alloys. Figure 4.41a [16] shows the substructure of Co-Cr-Mo alloy deformed at  $1150^{\circ}\text{C}$   $1\text{s}^{-1}$   $\epsilon = 0.2$ : one can easily recognize very large stacking faults with a width above 100nm. The large amount of stacking faults is increasing the local misorientations inside grain during deformation, and lead to a significant amount of low-angle boundaries. This accumulation of crystalline defects leads to grain subdivision following a 'continuous' recrystallization mechanism by nucleation on low-angle boundaries [16]. This is quite surprising, as the continuous mechanism is generally met in high stacking-fault energy materials where recovery is very active, and do not involve clear nucleation and growth steps (Cf. page 56). In other words, the case of Co-Cr-Mo may illustrate a transition from a discontinuous to a 'continuous-like' mechanism involving unusual nucleation sites while lowering enough stacking-fault energy due to the profusion of very large stacking-faults.

Figure 4.41b shows the substructure of hot-deformed Co-Ni-Cr-Mo (SPRON) alloy [117]. Substructure seems to be nearly free of dislocations, and this fact was interpreted by the occurrence of recovery and static recrystallization during the cooling process. Moreover, one can notice the absence of stacking faults in agreement with the relatively high stacking-fault energy. The recrystallization mechanism for this material was identified to be discontinuous type.

To conclude, the substructure of L-605 alloy seems to be between the cases of Co-Cr-Mo and Co-Ni-Cr-Mo alloys. Some Shockley partial dislocations are frequently met like in Co-Cr-Mo alloy, but stacking-faults width is quite small. Substructure may contain also some non-dissociated dislocations, like in higher stacking-fault energy materials such as Co-Ni-Cr-Mo. The recrystallization mechanisms mentioned above involve conventional nucleation by bulging from grain boundaries following a discontinuous mechanism. Therefore, despite the presence of many stacking-faults, the recrystallization process in L-605 is closer to the one of Co-Ni-Cr-Mo, and the grains subdivision mechanism observed in Co-Cr-Mo is relatively absent in L-605 alloy.



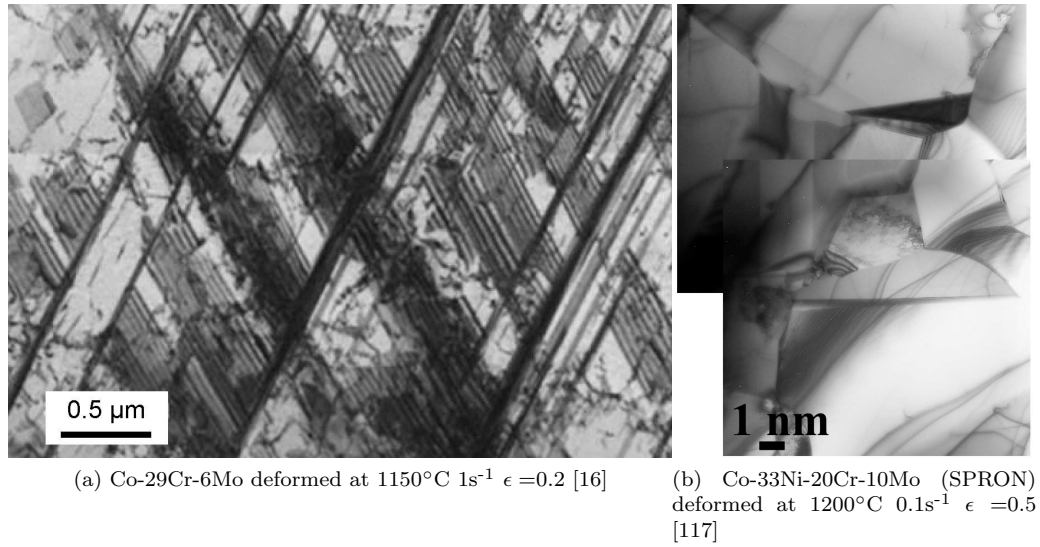


Figure 4.41: TEM observation of substructure in Co-Cr-Mo (CCM) and Co-Ni-Cr-Mo (SPRON) alloys

#### 4.4.7 Conclusions

The occurrence of dynamic recrystallization was observed for all the deformation conditions tested. For temperature higher than 1100°C and strain rate lower than 0.1s<sup>-1</sup> or higher than 1s<sup>-1</sup>, dynamic recrystallization leads to an homogeneous equiaxial microstructure with a grain size about 10  $\mu\text{m}$ . Deformation at temperature lower than 1100°C and strain rate in the range 0.1-1s<sup>-1</sup> results in an heterogeneous microstructure with grain size lower than 1  $\mu\text{m}$ . Dynamic recrystallization operates following a discontinuous mechanism by bulging from grain boundaries. A second nucleation mechanism involving annealing twins was highlighted at temperature higher than 1100°C. In a first step,  $\Sigma 3$  annealing twins rotate from 60° to 55°, and then in a second step bulging can operate. The recrystallized fraction was shown to evolve inversely with dynamic recrystallized grain size and misorientation parameter.

The observation of microstructure gradient along the sample central axis and the combination with Finite Elements simulations provided the kinetics of grain refinement during the hot working process. The comparison of microstructure after different cooling speeds suggests that meta-dynamic recrystallization happens for high strain rate condition ( $\dot{\epsilon} \geq 10\text{s}^{-1}$ ), and static recrystallization does not occur. However the material fraction affected by post-dynamic evolution is quite low, and the mean grain size remains unchanged.

The recrystallization behavior of L-605 superalloy seems quite unusual compared to other materials: the grain size and the recrystallized fraction do not follow a regular evolution with decreasing temperature and increasing strain rate, but presents a minimum for intermediate strain rate (Figure



4.21). This behavior could be explained by the occurrence of adiabatic heating and meta-dynamic recrystallization at high strain rate. In that case, the recrystallization for  $\dot{\epsilon} < 0.1\text{s}^{-1}$  would follow an usual behavior, and the sudden increase of grain size at high strain rate would be atypical and attributed to some other effects. However the temperature raise by adiabatic heating is lower than  $20^{\circ}\text{C}$ , and is not sufficient to explain the increase of grain size at high strain rate. Also, post-dynamic process do not affect significantly the grain size and cannot explain by itself the recrystallization at high strain rate.

The next section proposes a quantitative analysis of recrystallization through analytical modeling to try to reproduce the experimental data presented in this section. If the model does not predicts a minimum of recrystallized grain size at intermediate strain rate, then it would mean that some other mechanisms are operating. Otherwise, it would prove that recrystallization would follow a conventional mechanism. In either case, modeling would provide very important information on the recrystallization process, and at least a partial predictive description of microstructure change.



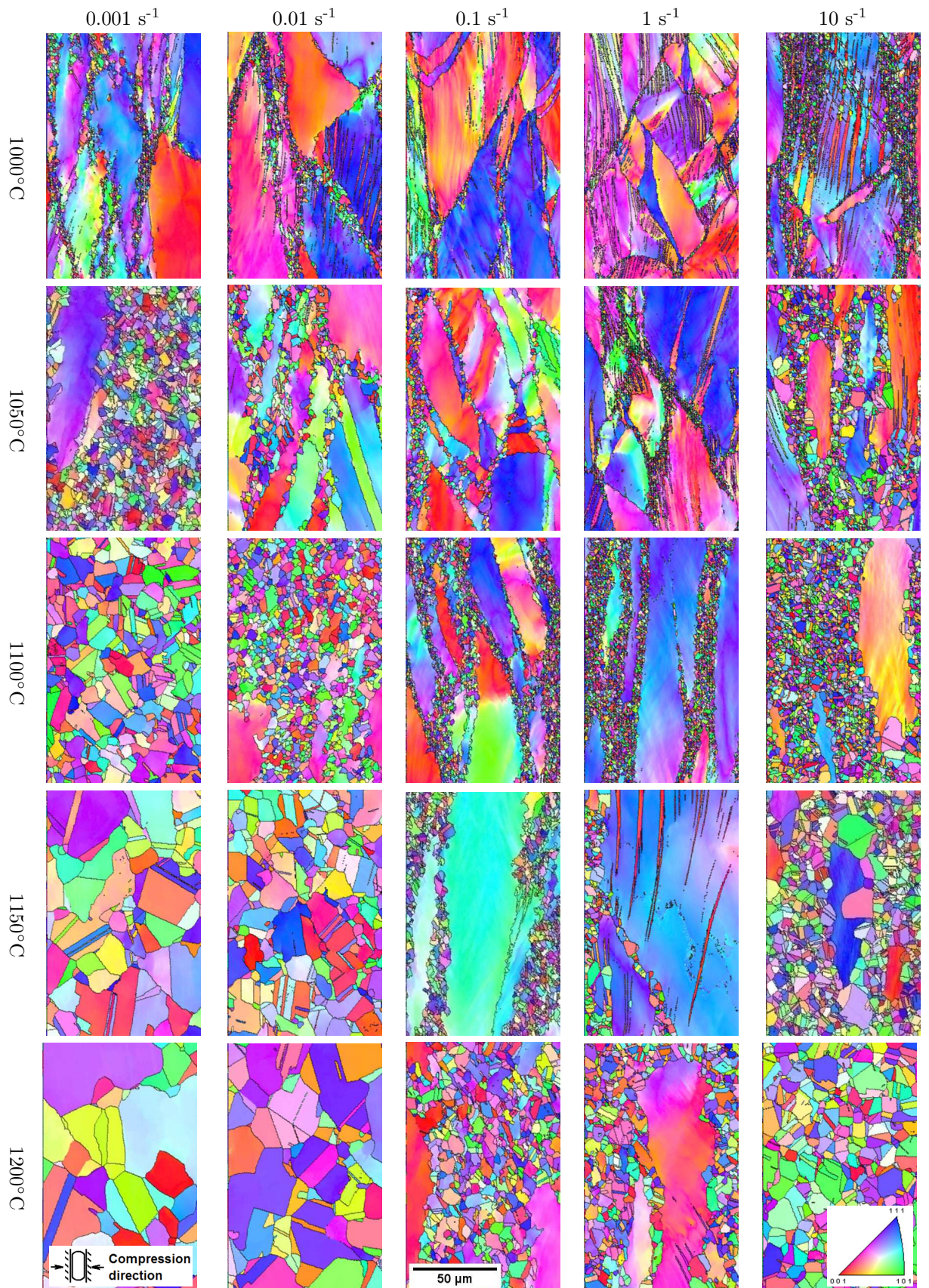


Table 4.9: IPF map of L-605 after deformation at  $\epsilon = 0.8$



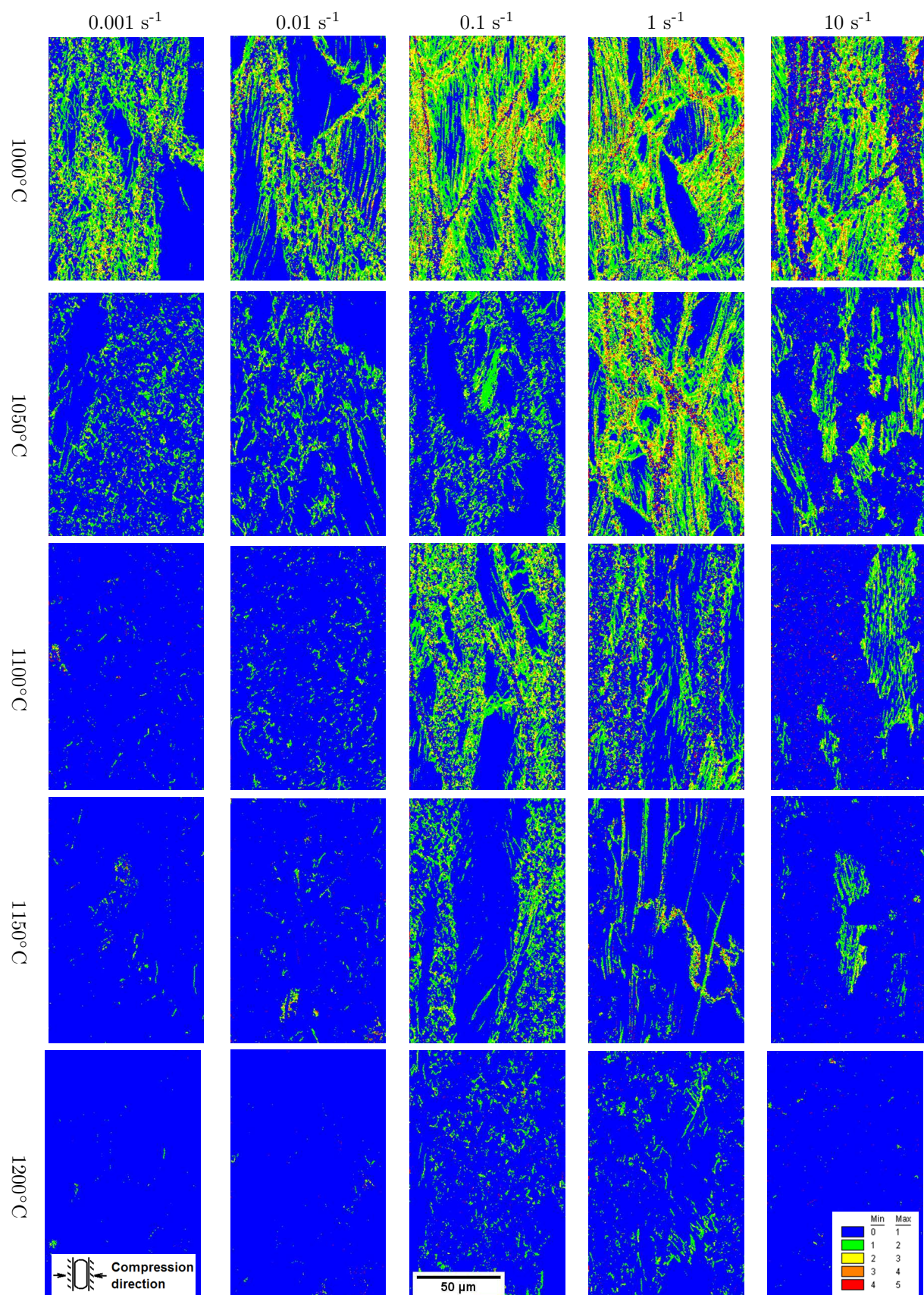


Table 4.10: KAM map of L-605 after deformation at  $\epsilon = 0.8$



## Chapter 5

# Modeling of discontinuous dynamic recrystallization



## 5.1 Determination of grain boundary mobility at steady-state

The following part proposes an advanced study of dynamic recrystallization by analytical modeling. A model of recrystallization must include a suitable description of plasticity, nucleation and grain growth. The deformation behavior of L-605 was extensively investigated in the section 3.1, and the constitutive equations 3.3 combined with the Taylor equation 3.4 can provide an estimation of dislocation density (Figure 3.7). Grain growth and nucleation have been described qualitatively on the section 4.4. However we have nearly no quantitative information on the grain boundary mobility, the nucleation criterion and the nucleation frequency. Therefore, the current section proposes to determine the grain boundary mobility based on the analysis of experimental data at the steady-state. The next section provides a method to extract from the previous results the nucleation frequency, and to revise the nucleation criterion to a new generalized expression. At this point, all the ingredients for the formulation of a complete model are gathered. Finally, the last section presents a class model of the recrystallization in L-605 alloy based on the previously calculated parameters, and compares the calculated microstructure with experimental data.

### 5.1.1 Determination of the steady-state flow stress and microstructure

The main difficult point in modeling recrystallization is the large number of interactions between state variables. For instance, both temperature and dislocation density contribute to the grain growth. However the dislocation density changes with temperature due to the increase of recovery, and also due to boundary migration induced softening. Because of these cross-interactions, the determination of the growth of a grain in a recrystallized microstructure is strongly non-linear. Moreover, the question of nucleation raises: what is the dependence of nucleation frequency with the dislocation density, or with temperature? In addition, a change of nucleation frequency leads to softening by recrystallization, therefore to a decrease of dislocation density, which can affect the nucleation itself, and affect the grain growth in the same time. These are few examples of the interactions and feedback effects taking place during the recrystallization process. From this consideration, one can deduce the necessity to disentangle these interactions and to separate the effect of each phenomenon on the microstructure change.

Steady-state is a very favorable situation for separating the contributions of plasticity, growth and nucleation. Indeed, macroscopic state variables remain constant at the steady-state: the average grain size, stress, dislocation density remain constant with strain [107, 99]. However, at the microscopic scale, none of these variables are constants: dislocation density and grain size change continually at the grain scale. Using the mean field formalism, a grain can be considered as an inclusion in an homogeneous matrix with state variables equal to the mean variables of the surrounding grains. At the steady-state, such an approach becomes very simple: the mean state variables of the matrix (grain size, dislocation density) are taken equal to the macroscopic experimental values



measured in the section 4.4. Therefore the growth of a grain can be directly calculated numerically using the equation 1.27, regardless of the evolution of state variables in the surrounding grains.

Last but not least, the nucleation frequency and the number of grains are constants at steady-state. Therefore each disappearing grain is replaced by a single grain. The nucleation contributes only to preserve a constant grain size, by replacing the disappearing grains. As a result, the resulting average grain size can be directly attributed to the grain boundary migration, with few concern to the nucleation.

	1000°C	1050°C	1100°C	1150°C	1200°C
$10s^{-1}$	-	-	318	254	178
$1s^{-1}$	-	-	-	256	-
$0.1s^{-1}$	-	-	-	-	136
$0.01s^{-1}$	-	-	129	104	78
$0.001s^{-1}$	-	125	88	63	54

Table 5.1: Stress at steady-state (MPa)

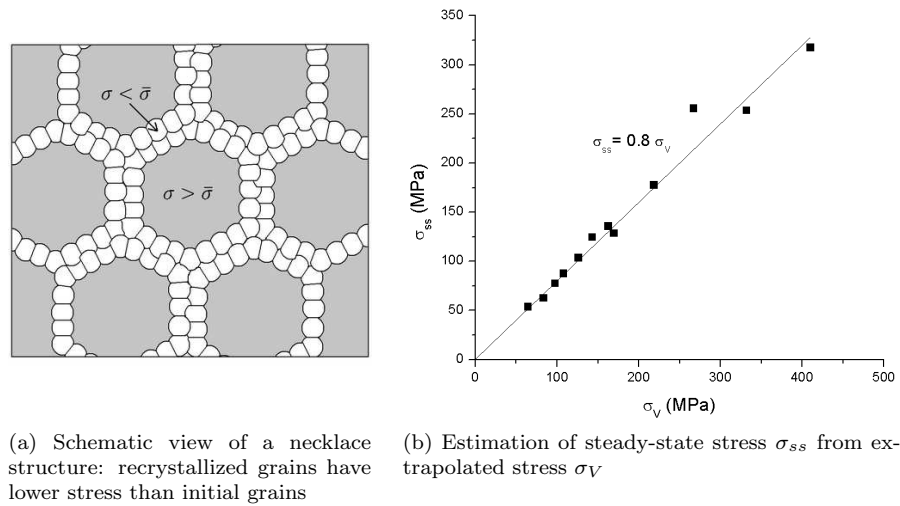


Figure 5.1: Grain boundary mobility of L-605 alloy calculated from experimental data

To achieve a mean field model of recrystallization at the steady-state, the state values of the material at a macroscopic scale must be determined. However, as illustrated in Figures 4.21a and 4.21a, the steady-state was experimentally reached for  $\epsilon < 1$  for a small number of conditions only. The Table 5.1 indicates the experimental stress at  $\epsilon = 0.8$  for conditions with more than 70% of the material recrystallized. For other conditions, most of the material has not proceeded to recrystallization (Figure 5.1a), and the apparent steady-state stress is overestimated. However, for any condition, the extrapolated stress  $\sigma_V$  is known, as it requires only the beginning of the compression curve to be determined. Steady state stress  $\sigma_{ss}$  is found to follow a linear evolution with extrapolated stress  $\sigma_V$ , as shown in Figure 5.1b. Therefore we can estimate the steady-state stress in the



recrystallized material by  $\sigma_{ss} \approx 0.8\sigma_V$ . Finally, the average dislocation density of the homogeneous matrix can be deduced by application of the Taylor equation.

The average grain size is obtained by EBSD, and is illustrated in the previous section (Figure 4.21a). This grain size was determined by analysing the recrystallized microstructure only, and does not accounts for large grains remaining from the initial microstructure. Also, the average grain size is obtained from a 2D metallographic cut of the material, therefore the grain size can be underestimated. The random intersection surface of a plane and a sphere is about  $\pi/4$  times the maximal disc area. If grains are assumed to be spherical, then the average grain size can be converted into a 3D size by multiplying with a factor  $4/\pi$ . The 3D size is then used in the next steps of the model to obtain the grain boundary mobility and some other material parameters. The next section gives the details of the procedure to extract these informations from experimental data.

### 5.1.2 Principle of the determination of boundary mobility

#### Fundamental equations

Based on the experimental data gathered, it is possible to calculate the size evolution of a single grain during its whole lifetime. The nucleus size is assumed to be negligible compared to the mean grain size, and the initial value of the grain size is fixed to 0. From that point, the grain growths with a speed proportional to the difference of dislocation density at the grain boundary interface (equation 1.27):

$$v = M\tau(\bar{\rho} - \rho(t)) \quad (5.1)$$

In the same time, the stress in the growing grain increases. Flow stress is calculated based on the constitutive equations 3.3 (page 84): from the  $g$  parameter we can deduce  $\sigma_V$ ,  $\sigma_y$  and  $\theta_0/\mu$ , and then predict the plastic stress  $\sigma_p$  for a given grain by using the Voce law (equations 1.16 and 1.17):

$$\sigma_p = \sigma - \sigma_y = (\sigma_V - \sigma_y) \left( 1 - e^{\frac{-\dot{\epsilon} \cdot t \cdot \theta_0}{\sigma_V - \sigma_y}} \right) \quad (5.2)$$

with  $\dot{\epsilon}$  the strain rate,  $t$  the time and  $\sigma_V$  the extrapolated steady-state stress calculated from  $g$  parameter. The dislocation density is estimated from the flow stress by the Taylor equation, reminded here (equation 1.14):

$$\sigma_p = M_T \cdot \alpha \mu b \sqrt{\bar{\rho}}$$

with  $M_T$  the Taylor factor taken equal to 3 for FCC metals,  $b$  the magnitude of the Burgers vector, and  $\alpha$  a parameter estimated about 0.3 (Table 5.2). The model must also take into account the heterogeneity of deformation between grains. Freshly formed grains are relatively dislocation-free and are very soft compared to older grains. Most plasticity models consider a same increment of



strain for all grains, in the framework of the Taylor assumption (Cf. page 43). However softer grains would be deformed more easily than other grains, and a simple way to account for this effect is to use the isowork assumption [86]. Each grain receive the same amount of work equal to  $\bar{\sigma} \cdot \bar{d}\epsilon$ , with  $\bar{\sigma}$  the macroscopic stress and  $\bar{d}\epsilon$  the macroscopic strain increment. Softer grains have a lower intrinsic stress than harder ones, so they undergo a larger strain increment. At the steady-state, the macroscopic stress  $\bar{\sigma}$  is equal to  $\sigma_{ss}$ , and the isowork assumption can be reformulated as a function of strain rate:

$$\dot{\epsilon}_i = \bar{\epsilon} \cdot \frac{\sigma_{ss}}{\sigma_i} \quad (5.3)$$

with  $\dot{\epsilon}_i$  the strain rate and  $\sigma_i$  the stress in the grain i, and  $\sigma_{ss}$  the macroscopic stress at steady-state. The g parameter is recalculated with  $\dot{\epsilon}_i$  for the grain i, and the value of  $\sigma_V$  is re-estimated for the grain considered. The change of local strain rate on the hardening rate is negligible and can be safely neglected.

Dislocation density is calculated from flow stress using the Taylor equation (equation 3.4), and its change affects the boundary migration speed through the equation 5.1. The boundary migration induced softening (BMIS [99]) is included in the model by redistributing the dislocation density in the new volume of the grain for each calculation step. If the growth speed is positive, the grain volume increases during the growth step, however the dislocations number remains the same. Therefore the new dislocation density at the step t+1 is calculated by:

$$\rho_{t+1} = \rho_t \cdot \frac{v_t}{v_{t+1}} \quad (5.4)$$

with  $v_t$  the grain volume and  $\rho_t$  the dislocation density at the step t. Finally the stress is recalculated from the new dislocation density  $\rho_{t+1}$  using the Taylor equation.

Therefore, the set of equations listed here describe the plasticity and the boundary migration, with taking into consideration the heterogeneity of deformation by the isowork assumption, and the boundary softening by the equation 5.4, within a quite simple formalism and with physically reasonable assumptions.

## Parameters

This simple model requires a reduced number of parameters compared to conventional analytical models. Parameters for L-605 alloy are listed in the Table 5.2. These parameters were determined for pure cobalt and pure copper from the literature, and by analysis of the data in [109, 76]. These parameters are used in the next section for the calculation of mobility in cobalt and copper, and the details of the data treatment are indicated in the Appendix 3 pages 199 and 205.



Parameter	L-605 superalloy	Pure cobalt	Pure copper
Burgers vector $  b  $	2.53Å (equation 3.6)	2.50Å [122]	2.54Å [30]
Shear modulus $\mu$ (GPa)	$92.1 - 0.03582.T(^{\circ}C)$ [19]	$91.3 - 0.05253.T(^{\circ}C)$ [122]	$35.8 - 0.01303.T(^{\circ}C)$ [29, 30]
$\theta_0/\mu$	Variable with g parameter (equation 3.3)	0.05 (From the analysis of data in [109] (Cf. page 205))	0.04 (From the analysis of data in [76] (Cf. page 199))
Dislocation junction strength $\alpha$	0.3 (Estimation)	0.3 (Estimation)	0.3 [30]
Strain rate reference $\dot{\epsilon}_0$	$10^9 \text{s}^{-1}$ (Determined page 81)	$10^3 \text{s}^{-1}$ (Determined page 205)	$10^6 \text{s}^{-1}$ (Determined page 199)
Grain boundary energy $\gamma$	$0.7 \text{J.m}^{-2}$ (Estimation, Table 4.4)	$0.65 \text{J.m}^{-2}$ [127]	$0.625 \text{J.m}^{-2}$ [29, 30]
Molar volume $V_m$	$6.92.10^{-6} \text{ m}^3.\text{mol}^{-1}$	$6.62.10^{-6} \text{ m}^3.\text{mol}^{-1}$	$7.11.10^{-6} \text{ m}^3.\text{mol}^{-1}$

Table 5.2: Parameters used for the model simulations

### Optimization process to determine the mobility

The grain grows until its dislocation density  $\rho_i$  becomes equal to the average value  $\bar{\rho}$  in the matrix. At this point, the grain boundary migration speed is null according to the equation 5.1. Beyond that point, the grain considered becomes harder than the matrix, and starts its shrinkage step. Having some grains with a dislocation density larger than the mean value is not a surprising fact: the material is composed of fresh soft grains and older hard grains, and it is therefore natural to have fractions of grains below and above the mean value. Equation 5.1 illustrates a competition between grains: older grains shrink and are progressively replaced by fresh growing grains, leaving the volume and the number of grains constant at steady-state.

Figures 5.2a and 5.4 illustrate the size evolution of a single grain in the recrystallized material. The curve has a bell shape, and reach a maximum at  $\rho_i = \bar{\rho}$ . Then the size decreases until 0, corresponding to the disappearance of the grain. Figure 5.2a shows the change of grain size curve with changing the boundary mobility: no shape change is noted, and the ending point of the curve is the same. The curves are simply shifted along the y-axis with changing mobility. Indeed, the ending point depends mostly on the hardening behaviour of the material: hardening is responsible of the variations on the driving force and for the shrinkage step. Therefore changing the mobility has negligible effect on the shape of the curve, nor on the ending point.

From the grain size curves  $d_i(t)$ , the mean grain size in number can be calculated by the equation:

$$\bar{d}_n = \frac{\sum n_i \cdot d_i}{\sum n_i} = \frac{1}{t_f} \int_0^{t_f} d(t) dt \quad (5.5)$$

with  $n_i$  the number of grains with the size  $d_i$ , and  $t_f$  the lifetime of a grain. The average can be reduced to an integral over the lifetime (equation 5.5), because each grain is assumed to follow the same path, with simply a time delay between each grain. Therefore the evolution of a single grain is



representative of the evolution of the system (ergodic assumption [99]), and the average values can be calculated over the lifetime of a single grain.

As the  $d(t)$  curve shape remains unchanged with mobility, the variation of the average grain size with mobility is reduced to a trivial linear relation, with a coefficient to be determined. From that point, it is very easy to adjust the mobility to have an average grain size matching the recrystallized grain size  $\bar{d}$  observed by EBSD (Cf. Figure 4.21a). This adjustment is carried out automatically using the Optimization Toolbox of Matlab<sup>®</sup>. The error parameter  $e = |\bar{d}_n - \bar{d}|$  is calculated, and mobility is adjusted to minimize this error parameter. The complete optimization procedure is represented in a diagram in Figure 5.3.

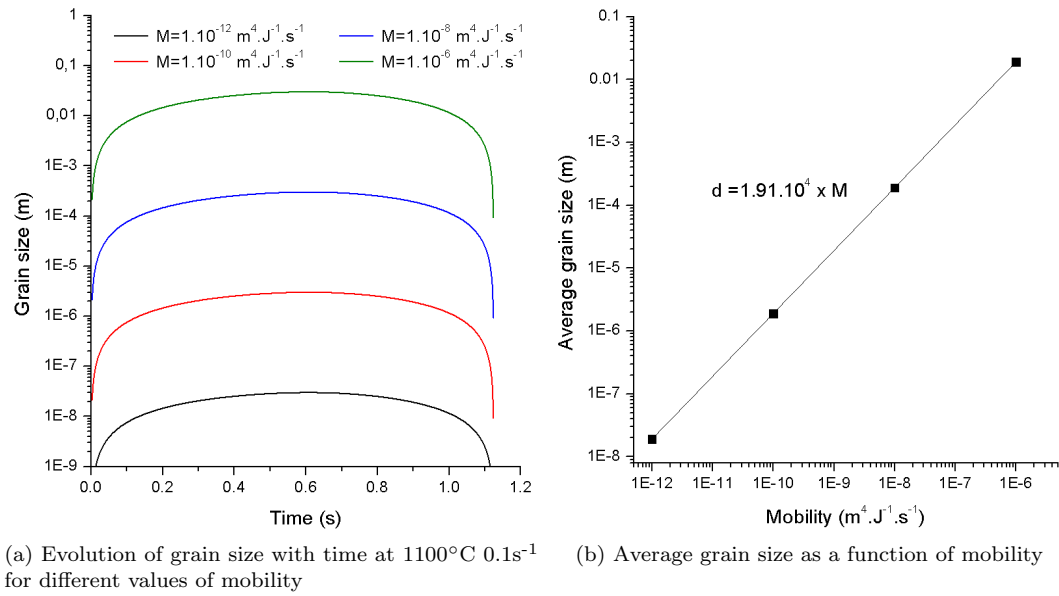


Figure 5.2: Grain size change with mobility at 1100°C 0.1s<sup>-1</sup>

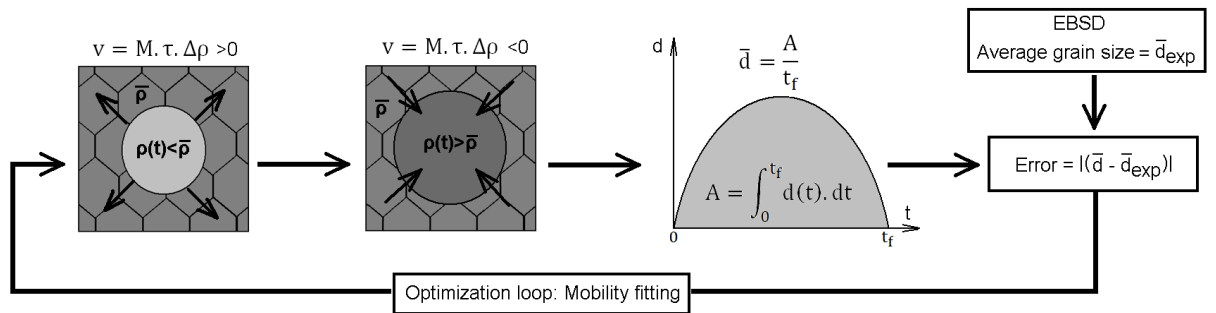


Figure 5.3: Schematic view of the modeling procedure to determine the mobility by fitting experimental grain size

The mobility is determined by optimization for each of the conditions tested experimentally in the section 4.4. Figure 5.4 illustrates the grain size curves as a function of time obtained after



optimization process for a strain rate  $\dot{\epsilon} = 0.1\text{s}^{-1}$ . The Table 5.3 provides the resulting optimized mobilities used for calculating the size curves. The mobility is found to increase with temperature, in agreement with Turnbull predictions [101]. The mobility will be analysed in further details on the next section. The grain size curves  $d(t)$  have a bell shape, with an ending point occurring at larger time for lower temperature. This is in agreement with the growth law used in the equation 5.1: at lower temperature, the grain takes a longer time to reach the mean dislocation density value that is higher than for high temperatures. Therefore the shrinkage step occurs later for lower temperature, leading to a longer lifetime  $t_f$ . Also, the curve reaches larger values at higher temperature, because the mean grain size is higher at high temperature due to higher mobility. Therefore, the grain size curves are a nice illustration of the competition between time, temperature and plasticity on the mean grain size.

Temperature ( $^{\circ}\text{C}$ )	Mobility ( $\text{m}^4.\text{J}^{-1}.\text{s}^{-1}$ )
1000	$5.10^{-12}$
1050	$2.10^{-11}$
1100	$9.10^{-11}$
1150	$4.10^{-10}$
1200	$4.10^{-9}$

Table 5.3: Grain boundary mobility at  $\dot{\epsilon} = 0.1\text{s}^{-1}$  obtained by optimization process

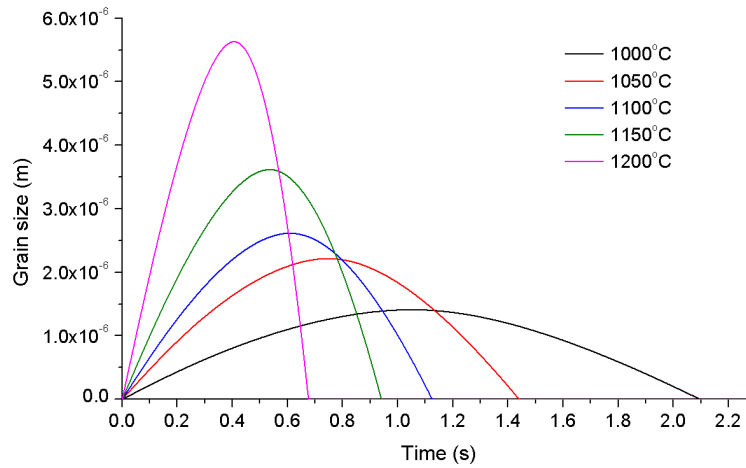


Figure 5.4: Evolution of grain size with time for different temperatures at strain rate  $\dot{\epsilon} = 0.1\text{s}^{-1}$

As a result, the mobility could be deduced for the L-605 alloy in the experimental conditions range, based on the treatment of experimental data by modeling. The variation of mobility with temperature must be checked to validate the values obtained by optimization process. In addition, the comparison with the same procedure applied to some pure metals could provide relevant information on the alloying elements effect on the boundaries motion.



### 5.1.3 Grain boundary mobility of L-605 and of some pure metals

The grain boundary mobility of L-605 was determined by the optimization method indicated previously, and the results are gathered in the Figure 5.5a. Mobility increases with temperature, as expected by Turnbull et al. [101] (equation 1.29), and reminded here:

$$M_0 = \beta \frac{\delta \cdot D_{GB} \cdot V_m}{b^2 \cdot RT} \quad (5.6)$$

with  $M_0$  the Turnbull mobility,  $D_{GB}$  the self-diffusivity along the grain boundaries,  $\delta$  the grain boundary thickness taken equal to 1nm, and  $\beta$  the fraction parameter usually estimated between 0.1-0.5 [102].

A weak dependence with strain rate is noted, but is negligible compared to the temperature dependence. For comparison, the mobility maps of pure cobalt and pure copper are illustrated in Figures 22a and 27 (Pure copper page 202, and pure cobalt page 206) of the Appendix 3. In the case of pure copper, a very strong increase of mobility with strain rate is noted (Figure 23a), and is attributed to the adiabatic heating mainly, and maybe to some post-dynamic microstructure evolution. The same phenomenon is observed for pure cobalt (Figure 28a), however in a lesser extend.

These comparisons support the assumption that L-605 deformed with the Thermecmaster-Z device may not undergo a significant adiabatic heating during the compression, nor any significant post-dynamic microstructure change during the cooling step. Otherwise some abnormal increase in the mobility would be observed, in the same way as pure copper or cobalt. The mobility was fitted by the Turnbull estimation (Equation 1.29), with taking the following parameters:  $\beta = 1$ ,  $D_{GB} = 1.10^{12} \text{m}^2 \cdot \text{s}^{-1}$  and  $Q = 600 \text{kJ} \cdot \text{mol}^{-1}$ . The Turnbull estimation fit for pure copper and pure cobalt are also indicated on the same figure for comparison. The fits for copper and cobalt were obtained from low strain rate data only in order to cut off the effect of adiabatic heat and meta-dynamic recrystallization (Cf. Appendix 3). Therefore it is normal to have a linear fit in agreement with the low mobility values only. The discrepancy with this fit illustrates well qualitatively the occurrence of adiabatic heat at high strain rate, especially in the case of pure copper.

The Turnbull estimation parameters for L-605, cobalt and copper are summarized in the Table 5.4. The activation energy for the self-diffusivity of pure cobalt and pure copper is quite reasonable and close to the values reported in the literature ( $Q = 107 \text{kJ} \cdot \text{mol}^{-1}$  for pure copper (Landolt-Börnstein database), and  $Q = 117 \sim 260 \text{kJ} \cdot \text{mol}^{-1}$  for pure cobalt [121, 122]). However the activation energy found for L-605 alloy is extremely high, due to the strong decay of mobility with  $1000/T$  in Figure 5.6. It can be deduced that Turnbull estimation can be used as a simple empirical fit for L-605 alloy, but the resulting fitting parameters have not the suitable physical meaning. The mobility in L-605 superalloy is not only driven by the atomic diffusion through the boundary interface, but also by some other phenomenon, making the Turnbull formula inadequate for understanding the mobility variations.



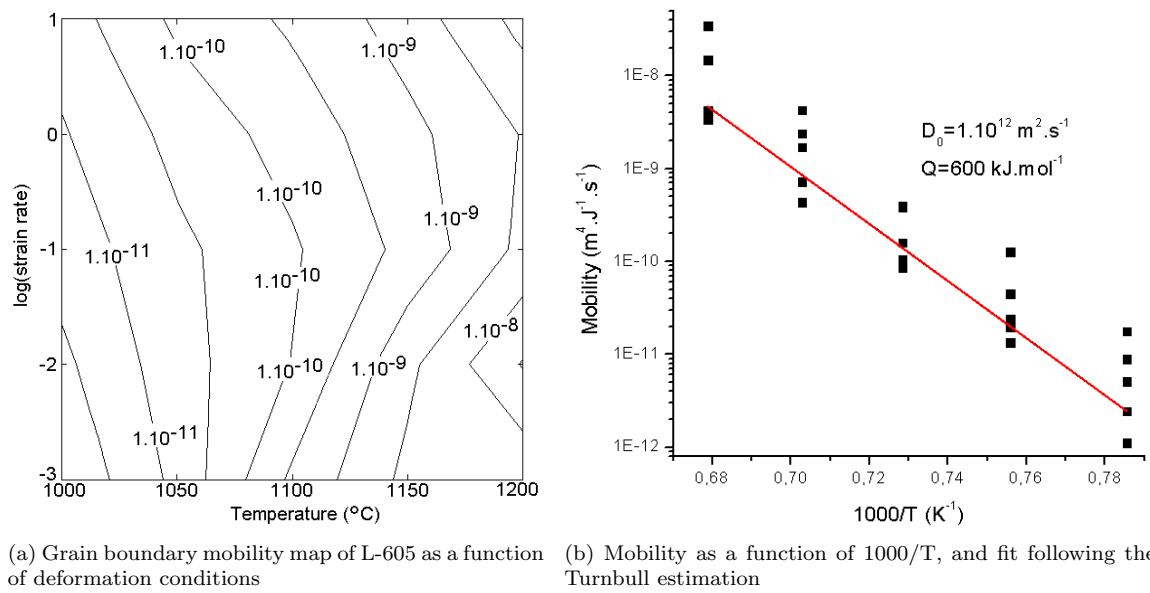


Figure 5.5: Grain boundary mobility of L-605 alloy calculated from experimental data

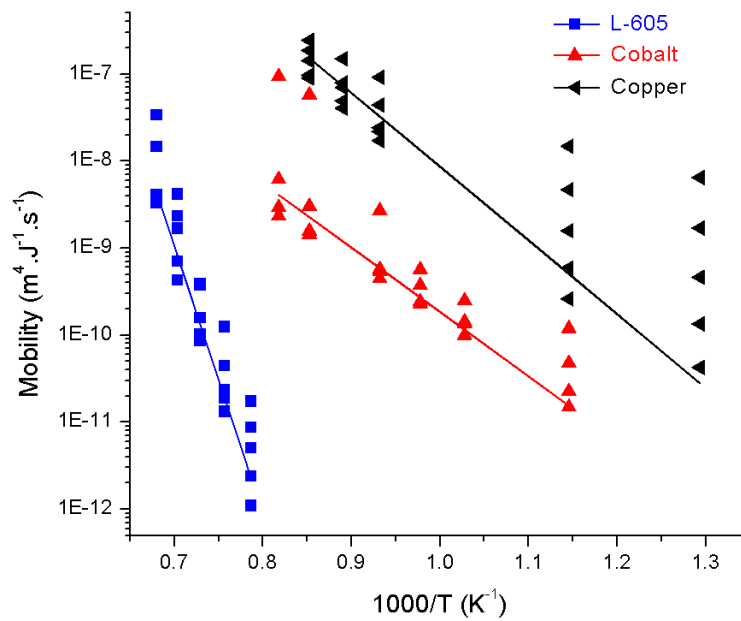


Figure 5.6: Evolution of mobility in L-605 superalloy, pure cobalt and pure copper as a function of  $1000/T$ , and Turnbull estimation

Material	$D_{GB}$ ( $m^2.s^{-1}$ )	$Q$ ( $kJ.mol^{-1}$ )
L-605	$1.10^{12}$	600
ETP copper	0.5	170
Cobalt	$1.10^{-3}$	150

Table 5.4: Grain boundary mobility at  $\dot{\epsilon} = 0.1s^{-1}$  obtained by optimization process



The lower mobility of L-605 and its fast variation compared to pure cobalt can be attributed to the effect of solute elements. L-605 contains an atomic fraction of solute elements about 40%, therefore it is not surprising to observe an interaction between solute elements and boundary interfaces. The solute elements may segregate to the grain boundaries and hinder their migration, following the solute-drag effect described by Cahn [104] (Cf. page 49). For low migration speed, mobility follows the low branch of Cahn, given by the equation 5.7 [104, 102]:

$$M = \frac{M_0}{1 + M_0 \cdot \alpha \cdot X} \quad \text{with} \quad \alpha = \frac{\delta(RT)^2}{V_m \cdot E_b \cdot D_{trans}} \left( \sinh\left(\frac{E_b}{RT}\right) - \frac{E_b}{RT} \right) \quad (5.7)$$

with  $D_{trans}$  the diffusivity of solute elements across the boundary,  $E_b$  the binding energy of solutes to the boundary,  $\delta$  the grain boundary thickness ( $\approx 1\text{nm}$ ),  $V_m$  the molar volume,  $X$  the atomic concentration of solute elements, and  $M_0$  the mobility in the absence of solute elements. In the case of L-605 the trans-diffusivity  $D_{trans}$  is unknown, however we can attempt to use the self-diffusivity obtained from the calculated mobility using the Turnbull relation. The  $\alpha$  factor can be deduced from the mobilities of L-605 and of pure cobalt by:

$$\alpha = \frac{M_{Co} - M_{L-605}}{X \cdot M_{Co} \cdot M_{L-605}} \quad (5.8)$$

with  $X$  the atomic concentration of solute elements taken to 0.4,  $M_{Co}$  the mobility in pure cobalt and  $M_{L-605}$  the mobility in L-605.

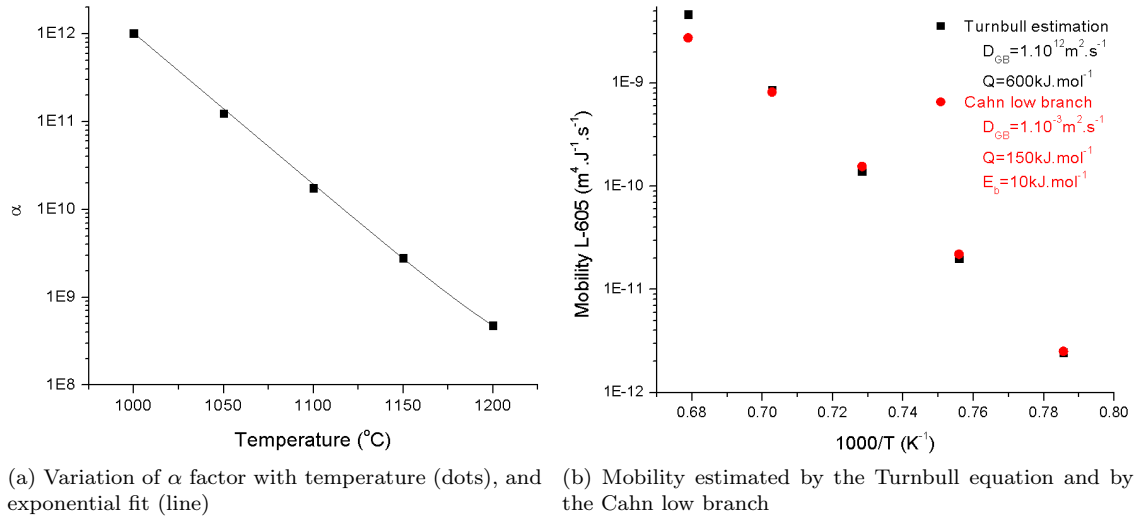


Figure 5.7: Determination of the  $\alpha$  factor, and comparison between the Turnbull estimation and the Cahn low branch

The variation of  $\alpha$  with temperature is illustrated in Figure 5.7a, and is decreasing exponentially with temperature. From this value of  $\alpha$ , the binding energy  $E_b$  can be fitted in order to match the calculated values and the equation 5.7. The optimal value is found to be  $E_b = 10 kJ \cdot mol^{-1}$ . This



value is close to the value of  $28.9\text{kJ}\cdot\text{mol}^{-1}$  used for Nb solute in  $\alpha$ -iron [103]. From this value and by using the parameters  $D_{\text{GB}}$  and  $Q$  of pure cobalt to calculate  $M_0$ , we obtain a very good agreement between the Turnbull estimation and the mobility calculated by the Equation 5.7, as illustrated in Figure 5.7b.

To conclude, the mobility of L-605 is found to be about one to three orders of magnitude lower than the mobility in pure metals. Mobility of L-605 can be empirically described by the Turnbull equation 5.6, but the parameters obtained are abnormally high. Therefore, this law is inadequate to explain the physical mechanisms leading to a relatively low mobility in L-605 superalloy. The consideration of the solute-drag effect was found to provide a good interpretation of the mobility variations. By applying the Cahn low branch equation 5.7, the binding energy of solute elements was estimated at about  $10\text{kJ}\cdot\text{mol}^{-1}$ , and the equation gives a fair agreement with the L-605 mobility determined by the Turnbull estimation.

Both the Turnbull and Cahn equations lead to the same estimation, and both can be used to calculate the mobility. Cahn equation contains a better comprehension of the phenomenon at stake, but is also more complex to handle. As a consequence, for the sake of simplicity the next steps will be operated by using the Turnbull estimation and the parameters of the Table 5.4.



## 5.2 Determination of nucleation criterion and nucleation frequency

The current section proposes to investigate the nucleation step during dynamic recrystallization, based on the results obtained in the previous section. Indeed, as the evolution of a grain at steady-state has been completely determined, it is now quite easy to deduce the nucleation criterion and the nucleation frequency. In a first step, the conventional nucleation criterion and its variants are revised, and a new generalized form of criterion is proposed. In a second time, few words will be said on the cycle of recrystallization to illustrate the complete recrystallization process from the nucleation of a grain to its disappearance. Finally, a new semi-empirical formula is proposed to estimate the nucleation frequency at steady-state as a function of the material parameters and the dislocation density. This relation is assumed to hold not only for the steady-state but also during the transient step, allowing the modeling of recrystallization for any deformation condition.

### 5.2.1 Nucleation criterion

In the case of discontinuous dynamic recrystallization, the nucleation event occurs when a subgrain becomes large enough to become a grain and grow. The nucleation criterion represents the critical size beyond which the growth of the subgrain is a stable process, and marks the limit between subgrains and grains. Therefore the nature of the nucleation criterion is inherently thermodynamic. The critical size of nucleated grains is usually expressed by the Bailey-Hirsch criterion [110]. The change of the Gibbs energy during the nucleation comports two terms. One is volumic and represents the energy difference due to the elimination of the dislocations by formation of the dislocation-free nucleus. The second term represents the energy increase by creation of additional grain boundary interface. In the classical Bailey-Hirsch approach, the nucleus size is assumed to be much smaller than the initial grain size so that the change in free energy associated with the removal of some grain boundary energy via the nucleation process can be safely neglected (Figure 5.8a). The global Gibbs energy change is expressed by:

$$\Delta G = -\frac{4}{3}\pi r^3 \cdot \frac{1}{2}\bar{\rho}\mu b^2 + 4\pi r^2\gamma \quad (5.9)$$

with  $r$  the radius of the grain under formation,  $\bar{\rho}$  the average dislocation density,  $\gamma$  the grain boundary surface energy,  $b$  the Burgers vector and  $\mu$  the shear modulus. The critical Bailey-Hirsch nucleus size noted  $r_{BH}^*$  is reached when the Gibbs free energy change is maximal. The resulting expression of  $r^*$  is the equation 5.10, so-called the Bailey-Hirsch criterion [110]:

$$r_{BH}^* = \frac{4\gamma}{\bar{\rho}\mu b^2} \quad (5.10)$$

This nucleation criterion has been extensively used for mean-field recrystallization models within the last decades [30, 96, 29]. However it neglects the effect of the elimination of pre-existing grain



boundaries on the energy balance of Equation 5.9, which may leads to an overestimation of the nucleus size.

This omission can be corrected by considering one of the cases presented in Figure 5.8. For the nucleation on a plane boundary, corresponding to the conventional concept of bulging [97], the nucleation of a grain of radius  $r$  consumes a pre-existing grain boundary area equal to  $\pi \cdot r^2$ . In the case of the nucleation at a triple boundary, an area  $3\pi \cdot r^2/2$  is removed. As a consequence, the Bailey-Hirsch criterion can be reformulated by:

$$r_{BH}^* = \frac{4K\gamma}{\bar{\rho}\mu b^2} \quad (5.11)$$

with  $K=1$  in the case of the Bailey-Hirsch criterion (equation 5.10 and Figure 5.8a),  $K=0.75$  at plane boundaries (Figure 5.8b) and  $K=0.625$  at triple boundaries (Figure 5.8c).

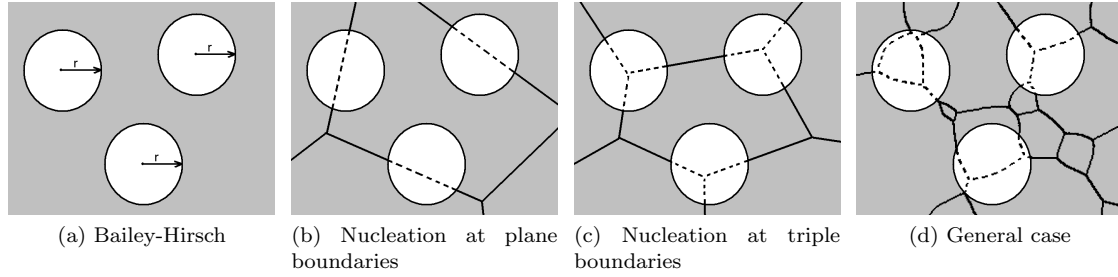


Figure 5.8: The different models of nucleation: 5.8a Bailey-Hirsch, 5.8b At a plane grain boundary (conventional), 5.8c At a triple boundary, 5.8d Complex nucleation on a combination of plane and triple boundaries

However, the general case is a combination of the different types of Figure 5.8, and  $K$  takes a value depending on the average grain size of the material (Figure 5.8d). A more complete reformulation of the equation 5.9 can be obtained as follows. The material is assumed to be constituted of identical grains with a mean size  $R$ . Thus the material contains a density of grain boundary surface energy equal to the Laplace pressure  $2\gamma/R$ . During the nucleation process, the pre-existing grain boundary surface is erased, and replaced by the boundary surface of the nucleus (Figure 5.8d). Therefore the equation 5.9 becomes:

$$\Delta G = -\frac{4}{3}\pi r^3 \cdot \frac{1}{2}\bar{\rho}\mu b^2 + 4\pi r^2\gamma - \frac{4}{3}\pi r^3 \cdot \frac{2\gamma}{R} \quad (5.12)$$

The nucleation criterion corresponding to a maximal Gibbs free energy change is  $r^*$ :

$$r^* = \frac{4\gamma}{\bar{\rho}\mu b^2 + \frac{4\gamma}{R}} \quad (5.13)$$

In this equation, if we consider a very large initial grain size, the term  $4\gamma/R$  can be neglected and the usual Bailey-Hirsch criterion is recovered. The following approach is equivalent to assume in the



usual Bailey-Hirsch criterion an effective grain boundary energy  $\gamma^*$  which is:

$$\gamma^* = \frac{\gamma}{1 + \frac{r_{BH}^*}{R}} \quad (5.14)$$

The ration between the two critical sizes obtained in equations 5.10 and 5.13 is:

$$\frac{r^*}{r_{BH}^*} = \frac{\gamma^*}{\gamma} = 1 - \frac{r^*}{R} \quad (5.15)$$

If we assume the grain boundary surface energy is  $\gamma \approx \mu b/10$  [136, 31], then the critical sizes ratio reduces to:

$$\frac{r^*}{r_{BH}^*} = \frac{\gamma^*}{\gamma} = \frac{1}{1 + \frac{4}{10\rho b R}} \quad (5.16)$$

Figure 5.9a represents a map of the ratio  $r^*/r_{BH}^*$  evolution with dislocation density and mean grain diameter. If this ratio is close to the unit, then the Bailey-Hirsch criterion estimates properly the nucleus size. If grain size is above 1mm and dislocation density is higher than  $10^{14} \text{ m}^{-2}$ , the Bailey-Hirsch criterion is equivalent to its extended formulation. For grain size smaller than  $100\mu\text{m}$  and dislocation density below  $10^{13} \text{ m}^{-2}$ , the ratio is low and the extended criterion (equation 5.13) should be used instead of the usual Bailey-Hirsch criterion. These conditions are very common in usual deformed microstructures; therefore the extended criterion is required for general cases.

Figure 5.9b illustrates an example of numerical application of equations 5.10 and 5.13. The Bailey-Hirsch criterion provides an estimation of nucleus size independent of mean grain size. As a consequence, for ultrafine grains the nucleus size becomes larger than the mean size, and microstructure is unstable. Small grain materials would recrystallize by involving nucleus larger than their parent grains, which is quite unexpected. Extended criterion is equivalent to Bailey-Hirsch criterion for large grains materials, and deviate for smaller grains to reach the mean grain size value. As a result, the critical size of nucleates for ultrafine grain materials is equal to the mean grain size. This means that recrystallization does not require formation of new grains, and proceed by simple grain growth of pre-existing small grains. To conclude, equation 5.13 captures the transition between the recrystallization process in large grains materials, and the grain growth process in small grain materials.

The critical nucleus size was calculated in the case of L-605 alloy using the equations 5.10 ( $K=1$ ), 5.11 ( $K<1$ ) and 5.13 ( $K=f(d)$ ). For the generalized criterion, the average grain size  $\bar{D}=2R$  was taken equal to the volumic average grain size. Indeed, when the nucleus forms, it removes the pre-existing boundaries in the volume affected by the nucleation, and therefore the grain boundary density  $4\gamma/R = 8\gamma/\bar{D}$  has to be calculated from the volumic average grain size and not the number average grain size in the equation 5.13. The different critical nucleus sizes are illustrated as a function of the average dislocation density in Figure 5.10, and compared with the volumic average grain size.



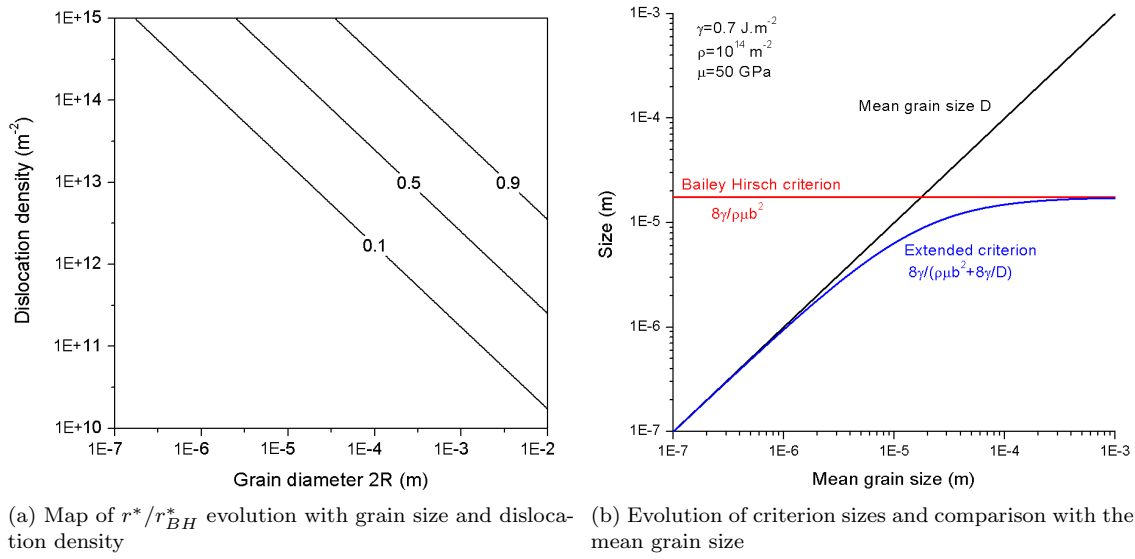


Figure 5.9: Comparison of criterion sizes and selection of the suitable criterion depending on the grain size and dislocation density

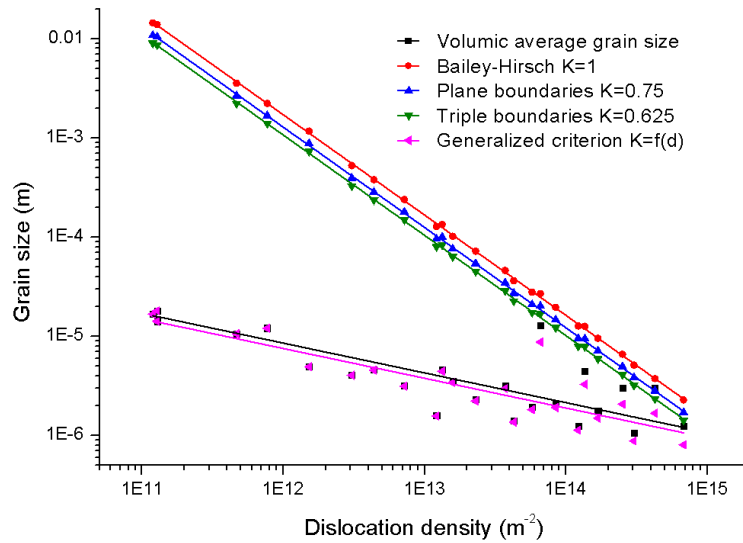


Figure 5.10: Comparison of the different nucleation criteria with the volumic average grain size as a function of dislocation density

The change in the coefficient  $K$  on the equation 5.11 is found to affect very weakly the nucleus size. For the Bailey-Hirsch criterion ( $K=1$ ) and its variants ( $K_1$ ), the nucleus size always 1 to 3 orders of magnitude larger than the volumic average grain size. This is quite surprising, as the recrystallized grains are supposed to reach the critical value at some time to become stable grains. However if the mean size is lower than the critical size, it would mean that none of the recrystallized grains have reach a stable state, and recrystallization would be unlikely to occur, which is in contradiction



with the experimental data (Figure 4.21). As a consequence, the Bailey-Hirsch criterion and its variants overestimate the critical size. For all the experimental range on L-605 alloy, the situation corresponds to the area  $r^*/r_{BH}^* \ll 1$  on Figure 5.9a, and the Bailey-Hirsch criterion is inadequate due to the small average grain size of the material. As illustrated in Figure 5.10, considering the nucleation at plane or triple boundaries is also insufficient to correct the criterion. On the other hand, the generalized criterion (equation 5.13) provides always a critical size lower than the average grain size. As a conclusion, the situation met experimentally is corresponding to Figure 5.8d: several triple boundaries can be consumed by the nucleation event, and the area consumed depends on the grain size. Therefore the generalized criterion proposed here provides a more reliable estimation while keeping the same simplicity as the Bailey-Hirsch criterion, and is applicable for a larger range of mean grain size and dislocation density conditions.

### 5.2.2 Gibbs energy hysteresis during recrystallization

Equation 5.12 provides the Gibbs free energy change during the lifetime of a grain. From the model developed in the section 5.1.1, the evolution of grain size and dislocation density with time are known at steady state, and therefore the Gibbs free energy change  $\Delta G$  can be calculated as a function of grain size. Figure 5.11a illustrates the contributions of the dislocation density change (red line) and of the surface energy (blue line) to  $\Delta G$  (black line). The surface energy path is reversible and do not induce any dissipation phenomenon. On the other hand, the contribution by dislocations storage is not a reversible path, because the growing grain contains a lower dislocation density than the shrinking grain. This results into a dissipative process, well known as the boundary migration induced softening (BMIS). As a result, the sum of these contributions is an hysteresis with an area representative of the dissipated energy during the lifetime of a grain. The more the hysteresis is open, and the more the recrystallization process dissipates energy and induces a macroscopic softening of the material.

Figure 5.11b shows the schematic evolution of  $\Delta G$ : the curve forms a loop starting from  $d=0$  corresponding to the birth of the grain, and ending to 0 corresponding to its disappearance. The curve increases until a maximum corresponding to the nucleation: at this point the volumic energy change is equal to the surface energy of the nucleus, and growth becomes stable. Beyond that point, the Gibbs energy plummets due to the stable growth process. Because of the accumulation of dislocations inside the grain, its stability is progressively reduced and the growth speed decreases. At the vertical tangent  $d(d(t))/d\Delta G=0$ , the grain boundary speed is null, and beyond this point the shrinkage step starts. Energy increases, illustrating the stability loss and the resulting shrinkage process. The curve passes to a maximum of  $\Delta G$ , that could be identified as a 'disappearance criterion' point, by analogy with the nucleation criterion. From this point, the shrinkage is a stable process and pursues until the grain completely disappears.



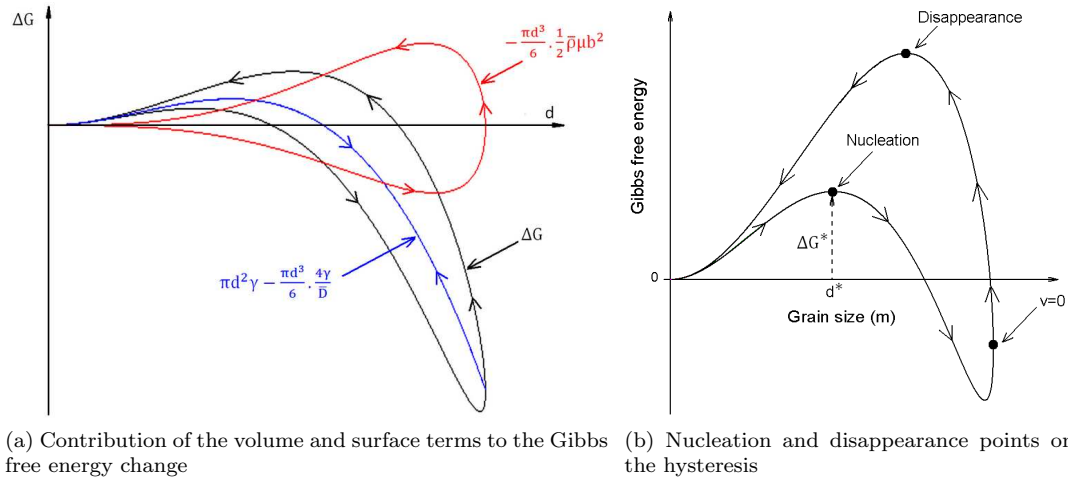


Figure 5.11: Gibbs free energy hysteresis loop during the lifetime of a grain at steady-state

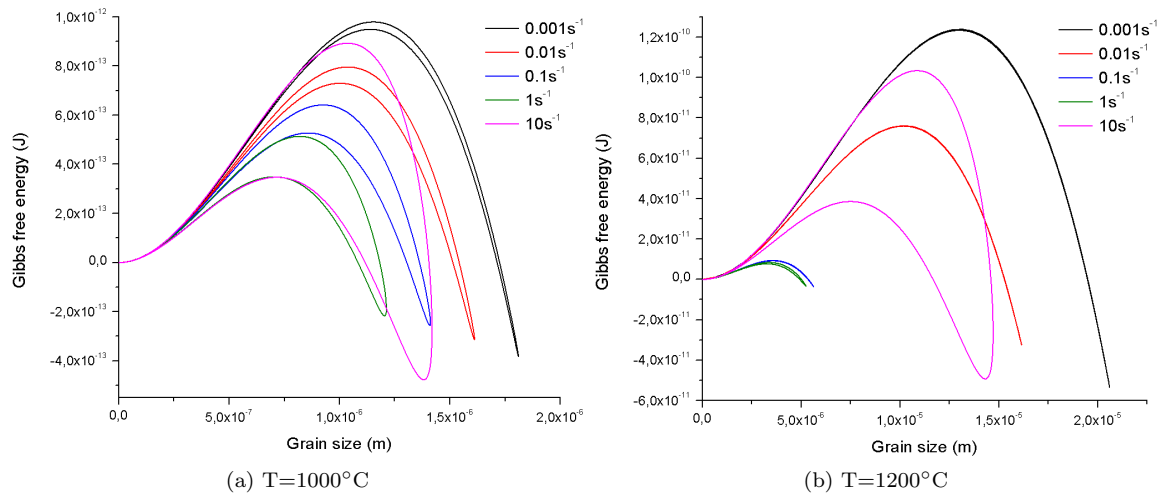


Figure 5.12: Evolution of Gibbs free energy during the lifetime of a grain

Figure 5.12 illustrates the  $\Delta G$  hysteresis curves for  $T=1000^\circ\text{C}$  and  $T=1200^\circ\text{C}$ . The area inside the loop increases with strain rate and decreases with temperature. This variation is due to the dislocation density change: when dislocation density is larger, the volumic stored energy in the material is higher and the growth of a grain leads to a larger dissipation than for low dislocation density conditions. Therefore a high dislocation density is necessarily associated with a highly efficient dissipative recrystallization process. That is why the flow softening  $\Delta\sigma$  is usually found to increase with flow stress  $\sigma$  [27]: strongly hardened material leads to a large dissipation for each new grain formed, and therefore to a large flow softening.



### 5.2.3 Frequency of nucleation

To achieve the modeling of the complete recrystallization process, the nucleation criterion is not sufficient, and the frequency of nucleation must be determined as well. The nucleation process occurs when a crystallite grows beyond the point  $d(t)=d^*$  noted on Figure 5.11b. This process requires that the nucleus overcomes the energy barrier  $\delta G^*$  to grow until it becomes a grain. The magnitude of the barrier can be determined from the equation 5.12, however the jump frequency of the barrier is unknown and cannot be determined in a trivial way.

We propose the following approach to determine the nucleation frequency. The number of crystallites able to overcome the energy barrier  $\delta G^*$  is assumed to be linked to the time required for a grain to grow until the critical size  $d^*$ . Indeed, if the time to reach  $d^*$ , called the incubation time  $\Delta t^*$  is very long, then during this period there is some chance that the crystallite disappears due to the competition with other grains. On the other hand, if the incubation time is short, then most of the crystallites formed by plasticity will manage to reach the critical size before being vanished by boundary migration or coalescence. Therefore the nucleation frequency is assumed to be proportional to the 'incubation frequency'  $1/\Delta t^*$ .

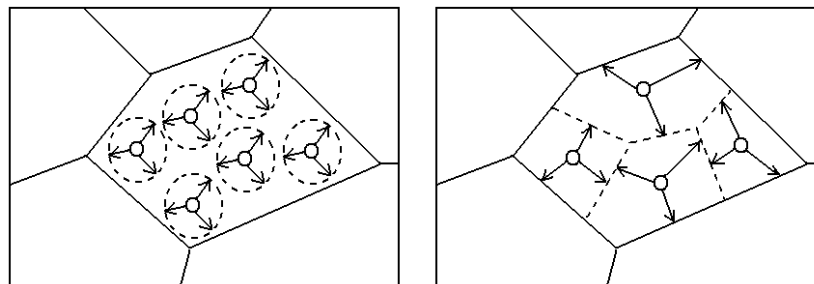


Figure 5.13: Effect of the critical size on the nucleus density

In addition, the nucleation frequency can be extracted from the modeling data of the section 5.1.1. At the steady-state, it is known that the number of grains and the grain size are constants. Therefore each recrystallized grain can give birth in average to a single nucleus only, so the total number of grains remain constant. As a consequence, the density of nucleus is one nucleus per grain. This amount of nucleus must be reported to the amount of grain boundary available, since the nucleation is known to occur mainly at grain boundaries [99]. Also the influence of the nucleus size must be taken into account: if the nucleus process involves very large nucleus size, then there would be a lower number of nucleus per boundary area. Figure 5.13 illustrates the effect of the critical size  $d^*$ : if  $d^*$  is very large, the number of nucleus is limited by the boundary available, and the excessive number of nucleus would be eliminated by competition or coalescence before reaching the critical size.



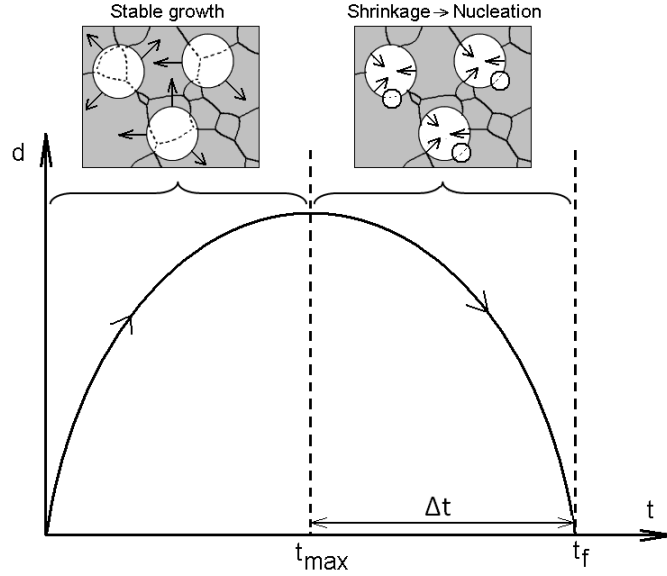


Figure 5.14: Nucleation of a single grain per parent grain during the shrinkage step at steady-state

The nucleation is likely to occur when the grain becomes unstable and shrinks. In this case, the shrinkage can be interpreted by the growth of the nucleus at the expense of the parent grain. The situation is represented in a diagram in Figure 5.14. From the time  $t_{\max}$  corresponding to a maximal grain size to the final time  $t_f$ , the nucleation occurs with a rate of one nucleus by parent grain, leading to a shrinkage and a progressive replacement of the parent grains. In this case, the frequency of nucleation per time unit is  $1/(t_f - t_{\max}) = 1/\Delta t$ . This frequency must be normalized by the grain boundary area and by the area consumed to take into account the effect of the grain size  $\bar{d}$  and of the critical size  $d^*$  like mentioned in Figure 5.13. Therefore the normalized frequency is  $N \cdot d^{*2}/(\Delta t \cdot \bar{d}^2)$ , with  $N$  the number of nucleus per parent grain set to  $N=1$  at the steady-state. This frequency is assumed to be proportional to the 'incubation frequency'  $1/\Delta t^*$ , as mentioned previously. Therefore the nucleation frequency is given by:

$$\frac{N \cdot d^{*2}}{\Delta t \cdot \bar{d}^2} = \frac{k_n}{\Delta t^*} \quad (5.17)$$

with  $\Delta t = t_f - t_{\max}$ ,  $\Delta t^*$  the incubation time and  $k_n$  a constant. The grain boundary migration speed is given by the equation 5.1:  $v = M\tau\bar{\rho}$ , therefore the incubation time is estimated to be about  $\Delta t^* \approx d^*/(2v) \approx d^*/(2M\tau\bar{\rho})$ . Therefore the equation 5.17 becomes dimensionless:

$$\frac{N \cdot d^*}{\Delta t \cdot \bar{d}^2} = 2 \cdot k_n \cdot M\tau\bar{\rho} \quad (5.18)$$

with  $k_n$  a parameter to determine by fit, and  $d^*$  the critical nucleus size given by the extended criterion (equation 5.13). The calculation is carried out for the data obtained by modelling on the L-605, and is illustrated in Figure 5.15. A linear relationship is effectively observed, with a



coefficient  $k_n \approx 1$ . The same fit was applied to the case of pure copper (Figure 23b) and pure cobalt (Figure 28b), and is illustrated in the Appendix 3. However the fit is hardly confirmed due to the accumulation of errors during the data processing and to the limited amount of experimental data available from literature, especially concerning the grain size. The coefficient  $k_n$  was determined as a guide, and values are summarized in the Table 5.5.

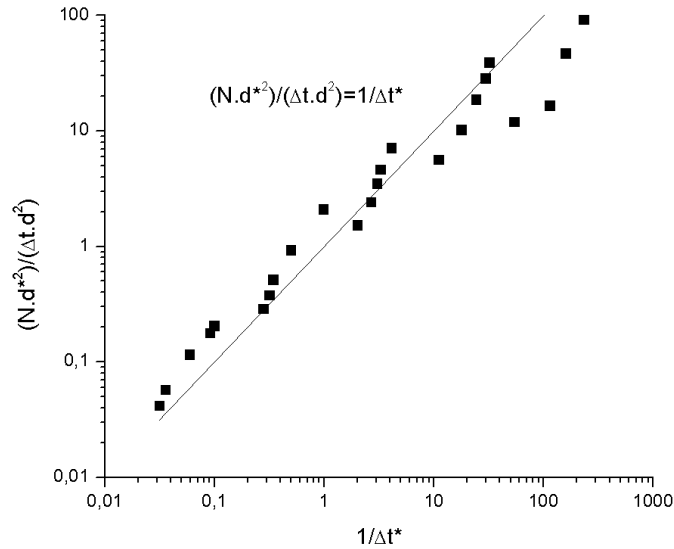


Figure 5.15: Normalized nucleation frequency  $N.d^{*2}/\Delta t.d^2$  as a function of nucleation incubation frequency  $1/\Delta t^*$

Material	$k_n$
L-605	1
ETP pure copper	$\approx 0.1$
Pure cobalt	$\approx 0.2$

Table 5.5: Nucleation frequency coefficient  $k_n$

To conclude, a new semi-empirical expression was proposed to determine the nucleation frequency at the steady-state. It can be attempted to use this expression for the whole deformation range, and may provide also a fair estimation of the nucleation during the transient step. The next section proposes to combine the mobility determined by the Turnbull estimation (Table 5.4) and the nucleation frequency obtained here to establish a complete model of dynamic recrystallization in L-605 superalloy.



### 5.3 Class modeling of dynamic recrystallization

The current sections attempts to gather the data collected from the study of steady-state in a complete model of dynamic recrystallization. The calculation is carried out in the framework of the mean-field modeling: each grain is assumed to grow in an homogeneous matrix, in order to simplify the interaction between grains. Moreover, the grain size distribution is considered and its evolution is predicted with deformation. To achieve this goal, class modeling is used: the grain size distribution is split up into classes, and each class is treated separately. This method enable to run the calculation in the case of an heterogeneous polycrystalline material, while keeping a fair simplicity and with minimizing the computing time.

#### 5.3.1 Principle

The initial material is defined by a set of  $10^5$  grains assigned into 1000 classes. Each class is a bundle of identical grains with a given grain size and dislocation density. The initial grain size distribution is following a Log-normal law with a mean grain size  $\mu_1 = 100\mu m$  and a standard deviation  $\sigma_1 = 0.5$ . This distribution is very close to the distribution experimentally measured by EBSD on the initial material (Figure 2.4).

The initial dislocation density is attributed randomly to each class by a Log-normal distribution with parameters  $\mu_2 = 10^9 m^{-2}$  and  $\sigma_2 = 0.5$ . To account for the heterogeneity of deformation, the Taylor factor  $M_T$  is taken following a normal distribution with a mean value  $\mu_3 = 3$  (FCC material) and a standard deviation  $\sigma_3 = 0.5$ . The material parameters are summarized in the Table 5.2.

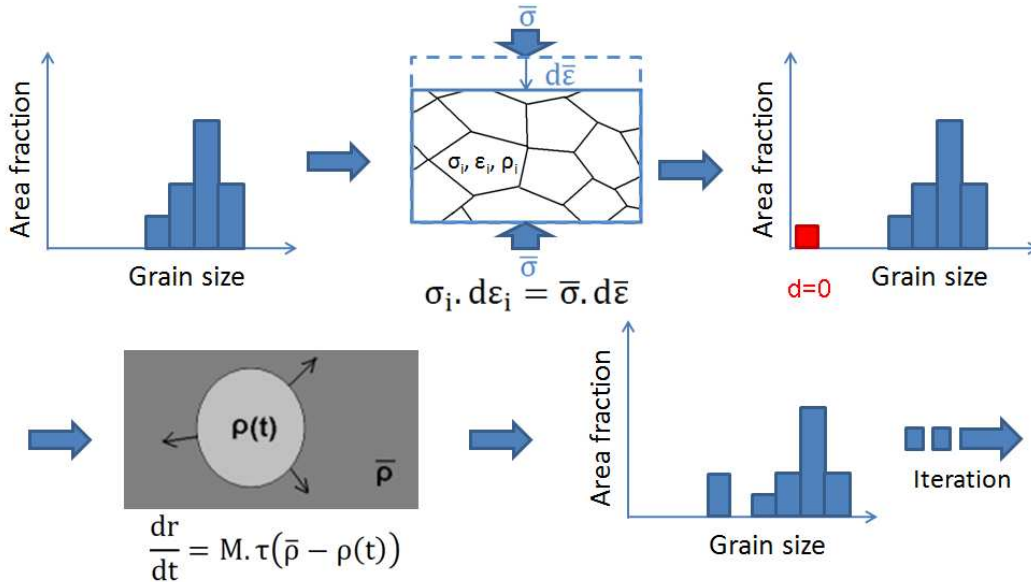


Figure 5.16: Schematic view of the dynamic recrystallization modeling steps



The calculation procedure is represented schematically in Figure 5.16. Most of the equations remain unchanged compared to the previous model at steady-state. The stress increment is calculated by the Voce law (equation 5.2) and using the parameters from the constitutive equations 3.3. To account for the heterogeneity of plasticity, the isowork assumption is applied (equation 5.3). The dislocation density is deduced by the Taylor formula (equation 5.3).

Then nucleation frequency is calculated with the equation 5.18 with the parameter  $k_n=1$  (Table 5.5). The number of nucleus created during a step is summed on the whole system, and a new class is created with the number of grains and an initial size equal to 0. Then the grain growth is calculated with a driving force equal to the dislocation density difference (equation 5.1). The boundary migration softening is taken into account by the equation 5.4. The mobility of grain boundaries is determined by the Turnbull estimation (equation 5.6), with the parameters of the Table 5.4.

Using directly the difference of dislocation density at the boundary interface does not respect the conservation of volume. This effect perturbs strongly the calculation and must be corrected. A method proposed by Montheillet et al. [99] and successfully applied by Cram et al.[30] consists into the modification of the driving force to keep the system volume constant. The average dislocation density  $\bar{\rho}$  taken for the calculation of boundary migration speed in the equation 5.1 is replaced by:

$$\bar{\rho}_{surf} = \frac{\sum \rho_i d_i^2}{\sum d_i^2} \quad (5.19)$$

where the summations are extended over all the grains of the system. Therefore the mean dislocation density  $\bar{\rho}_{surf}$  is the average dislocation density weighted by the surface area instead of the volume. The derivative of the overall system  $\Sigma d_i^3$  is  $\Sigma \dot{d}_i . d_i^2 = 2M\tau(\bar{\rho}\Sigma d_i^2 + \Sigma \rho_i . d_i^2)$ , which is equal to 0 when  $\bar{\rho} = \bar{\rho}_{surf}$ . Therefore the equation 5.19 is a convenient way to ensure the volume conservation with preserving the calculation simplicity.

The compression curves and the grain size distributions resulting from this model are presented in the next section, and are compared to the experimental data. The last section proposes a method to reproduce the microstructure based on the information from modeling, and the result can be compared directly with microscopy observations.

### 5.3.2 Evolution of nucleation frequency

Figure 5.17a illustrates the number of grains created per volume unit and per second for L-605 superalloy at  $T=1100^\circ\text{C}$  calculated from the equation 5.18. For comparison, Figure 5.17b illustrates the same nucleation frequency calculated from the nucleation criterion of Zurob et al. [29] and adapted to the dynamic recrystallization of copper by Cram, Hutchinson et al. The frequency evolution with strain is similar: at low strain the frequency is null as the recrystallization onset has not yet been reached. For a strain around 0.05 to 0.1, recrystallization starts and the frequency increases. Then the frequency stabilizes to a plateau for a strain above 0.3, corresponding to the



steady-state. For the two cases, some oscillations of the nucleation frequency are observed during the transient state at low strain rate (e.g.  $\dot{\epsilon} = 0.001s^{-1}$ ). This observation is in agreement with the literature [107, 31]: at low strain rate the nucleation is jerky and leads to some oscillations on the compression curve, while at high strain rate the nucleation is even and the compression curve exhibits a single peak stress. However in the case of L-605 alloy, the oscillations are extremely weak and are not observed experimentally on the stress-strain curves, but the model shows that at low strain rate ( $\dot{\epsilon} \approx 0.001s^{-1}$ ) the system is not far from the jerky flow conditions.

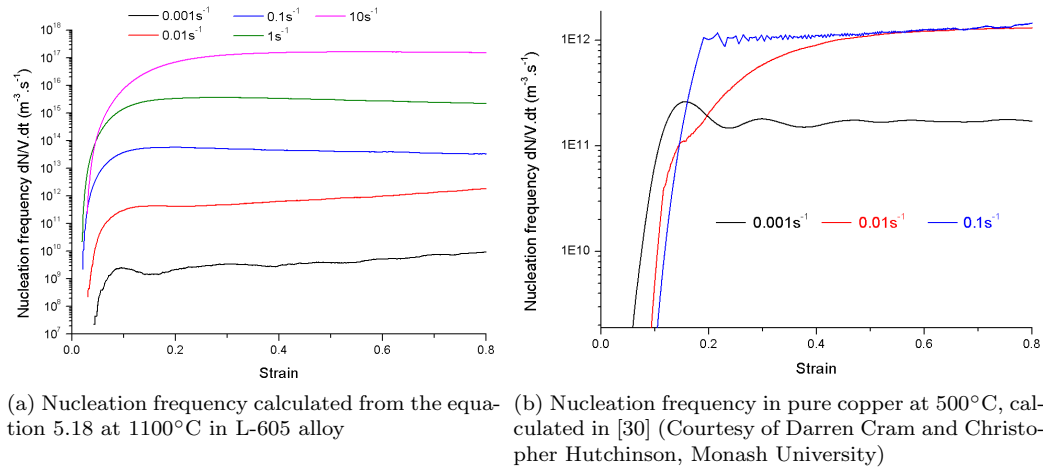


Figure 5.17: Nucleation frequency as a function of strain

### 5.3.3 Compression curves

Experimental compression curves obtained by hot compression with the Thermecmaster-Z device are illustrated in Figure 5.18. The calculated compression curves from the class model are shown in Figure 5.19. The two data set exhibit a similar deformation behavior: compression curves show a single stress peak, followed by a slow decay of stress at large strain due to dynamic recrystallization. As a result, the class model reproduces very well the deformation behavior during hot working. At high strain rate and low temperature, the model predicts a very weak flow softening, however the experimental stress-strain curves shows a significant flow softening, with a decrease of about 10% of the peak stress at  $\epsilon = 0.8$ . Therefore the model shows some slight discrepancy with the compression curves at low temperature and high strain rate. This difference may be due to some error on the driving force or the mobility, or on the nucleation frequency in the class model. Another explanation is the occurrence of adiabatic heating. If the temperature raises during the compression, the mobility increases and the boundary migration is promoted. As a consequence, some additional softening generated by boundary migration (BMIS) may occur during the experiment, and this softening would not be captured by the model.



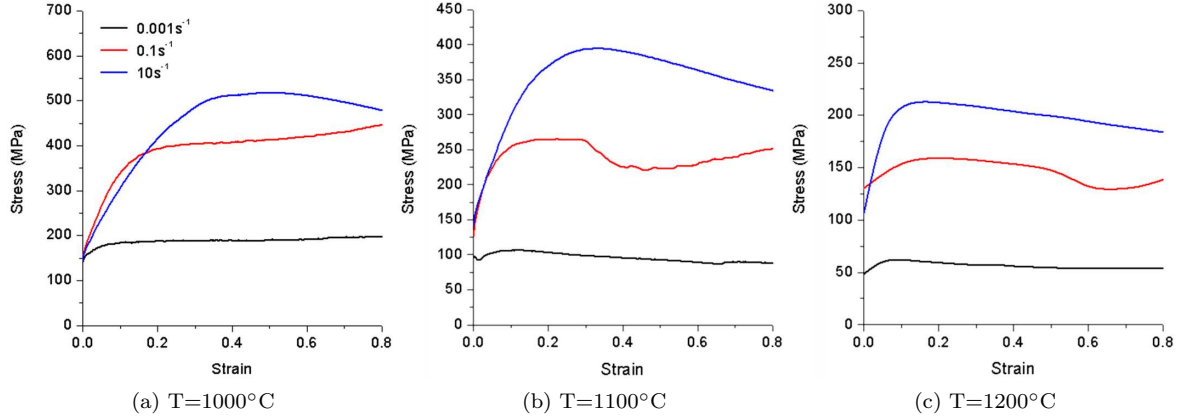


Figure 5.18: Experimental compression curves of L-605 alloy

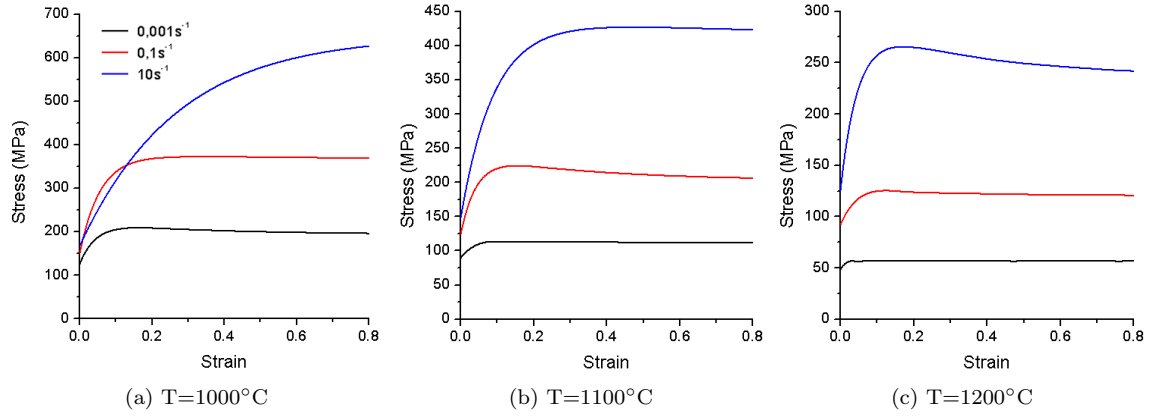


Figure 5.19: Calculated compression curves of L-605 alloy

### 5.3.4 Mean grain size and grain size distribution

Average grain size was determined after calculation until a strain  $\epsilon = 0.8$ , and the results are gathered in Figure 5.20a. The recrystallized fraction was calculated as the surface fraction of new grains divided by the total surface of grains in 2D, and is represented in Figure 5.20b. It can be concluded that the model predicts a regular decay of grain size and recrystallized fraction with decreasing temperature and increasing strain rate (=increasing the Zener-Hollomon parameter). This behavior is usually reported in the literature [31], and confirms that the model predicts reasonable trends.

Figure 5.21 shows the comparison between the grain size distribution obtained by EBSD at  $\epsilon = 0.8$  (red), and the calculated grain size distribution (blue). We find a very good agreement for high temperature and high strain rate. At high temperature and low strain rate, the good trend is predicted and the two distributions have the same shape, however the calculated distribution is shifted to larger sizes. This discrepancy can be attributed to some error on the grain boundary



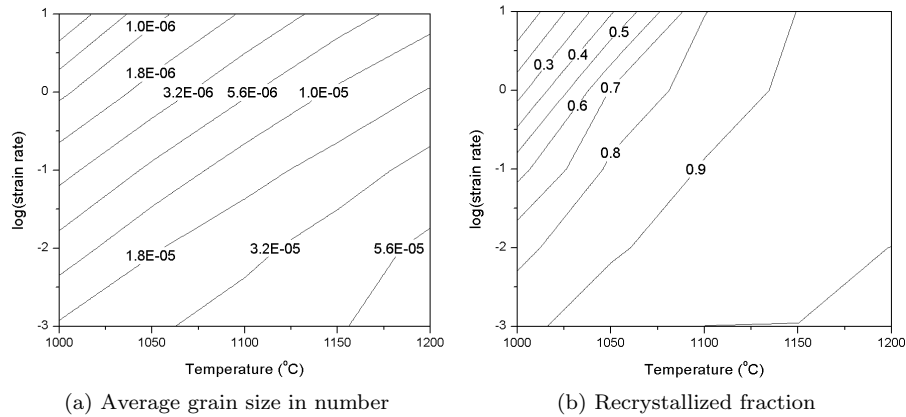


Figure 5.20: Average grain size and recrystallized fraction maps calculated for  $\epsilon = 0.8$

mobility, that might be overestimated. As a consequence, the overestimation would have practically no effect at high strain rate, so we have a good agreement at  $10s^{-1}$ , but would lead to a grain size overestimation at low strain rate where recrystallization is mainly driven by grain growth. For low temperature and high strain rate, the model predicts the formation of very small grains ( $< 1\mu m$ ) and a recrystallized fraction about 1%, while a grain size of  $1\mu m$  and a fraction of 30% are observed experimentally. This time, the discrepancy is strong at high strain rate only, and cannot be attributed to an error on the grain boundary mobility. The error may come from an error on the evaluation of the dislocation density, and therefore of the driving force for growth. Also the effect of adiabatic heating could be a an explanation: at low strain rate and high speed, the risks to have adiabatic heating is high due to the high work value. The model does not account for this effect and underestimates the size of new grains due to a lack of mobility.

On the experimental section 4.4, it was shown that the recrystallized fraction and the mean grain size exhibit a minimum at low temperature for intermediate strain rate (Figure 4.21). This behavior is not reproduced by the class model, and therefore one could attribute the discrepancy between the model and experiment to the occurrence of meta-dynamic recrystallization and to the effect of adiabatic heating that are not considered in the calculation. However, if we compare the grain size provided by the model and by the experiment at high strain rate, we find a pretty good agreement (e.g. Figure 5.21c). If meta-dynamic recrystallization and adiabatic heating had a strong effect on grain size, the model should fail mainly for high strain rate, which is not the case. Therefore these two phenomenon provide only a partial explanation of experimental results, and some contradictions remain unexplained.

Another possibility to explain the discrepancy between the model predictions and the experiment can be proposed. It was shown in Figure 3.5 of the section 3.1 that normalized hardening rate increase for a given value of  $g$  due to dynamic strain aging. As illustrated in Figure 3.5a, for intermediate strain rate at low temperature, a maximum of the hardening rate occurs and attests of the operation



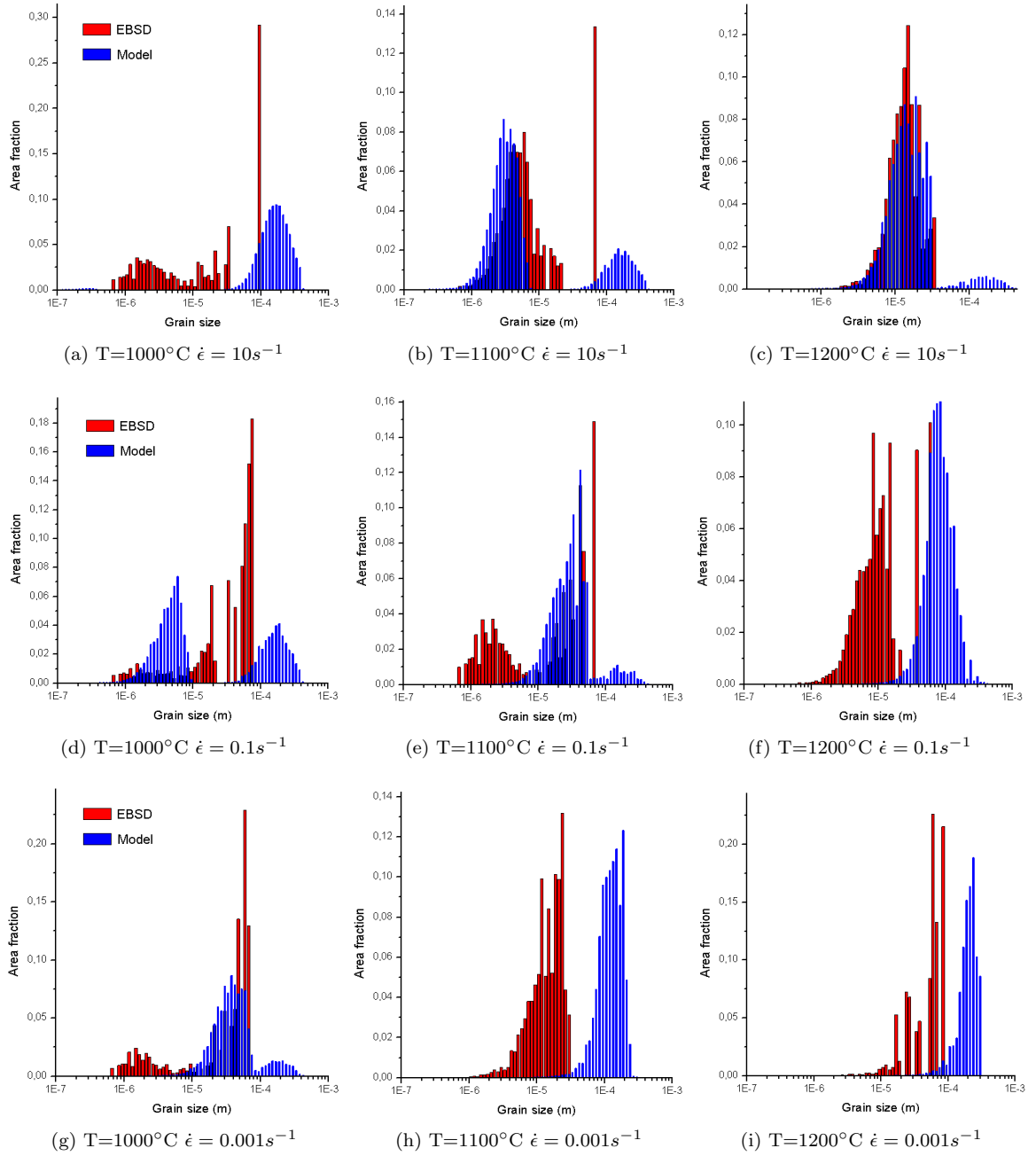


Figure 5.21: Grain size distribution: experimental distribution from EBSD (red), and calculated distribution (blue)

of dynamic strain aging. This condition range matches with the grain size minimum at intermediate strain rate on the map 4.21a. Therefore dynamic strain aging might hinder the grain boundary migration and lead to a smaller grain size, or affect the nucleation rate. However the interactions between dynamic strain aging and dynamic recrystallization are still unclear today, and the exact result of this interactions remain to investigate.



### 5.3.5 Prediction of the conditions for half and full recrystallization

From this point, it is possible to run the class model with calculating for each step the recrystallized fraction, and stop the calculation when this fraction has reached a given value. This process was run for a limit fraction of 0.5 and 1. Strain is fixed to a maximal value of  $\epsilon = 3$  to limit the computing time. The required strain to reach the given recrystallized fraction is illustrated on Figure 5.22.

To obtain a half-recrystallized microstructure, low deformation level about  $\epsilon = 0.2$  is sufficient for most conditions. However at high strain rate and low temperature, the required stress value increase until 3. To obtain a fully recrystallized microstructure, a deformation below  $\epsilon < 1$  is sufficient at high temperature and low strain rate only. For most of the deformation conditions, a deformation  $\epsilon \gg 1$  is required to completely erase the initial microstructure.

These calculations are valid for the material considered here, with an initial grain size about 100  $\mu\text{m}$ . Figure 5.22 may change with another initial grain size. These maps may be very helpful for industrial applications: it is possible to know the strain level to apply to reach the microstructure desired. Such maps could not be produced from experimental data, or at least would require a very large number of tests and would be very time consuming. Therefore the prediction of the strain level required is an illustration of the capacities of modeling to select the suitable deformation conditions to obtain the targeted microstructure.

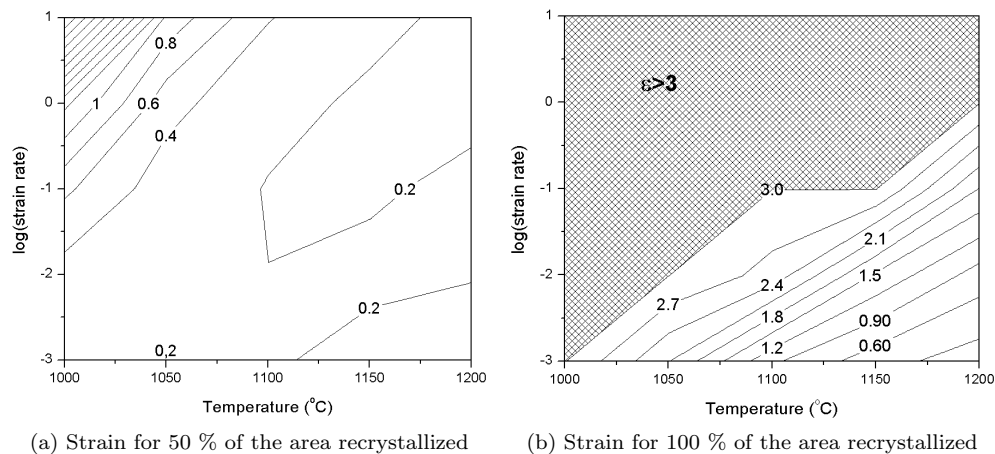


Figure 5.22: Maps of the strain required to obtain a recrystallized fraction of 50% and 100%

### 5.3.6 Microstructure generation from the size distribution

To provide a better visualization of the microstructure calculated from the class model, a program was built to generate microstructure pictures from the grain size distributions. The method used is detailed in the Appendix 3 (Figure 29 page 207). The resulting pictures are gathered in Figure 5.6.

The microstructure computed at 1000°C 10s<sup>-1</sup> did not reproduce the grain size distribution represented on the Figure 5.21 due to computing issues. The grain size is smaller than the step size



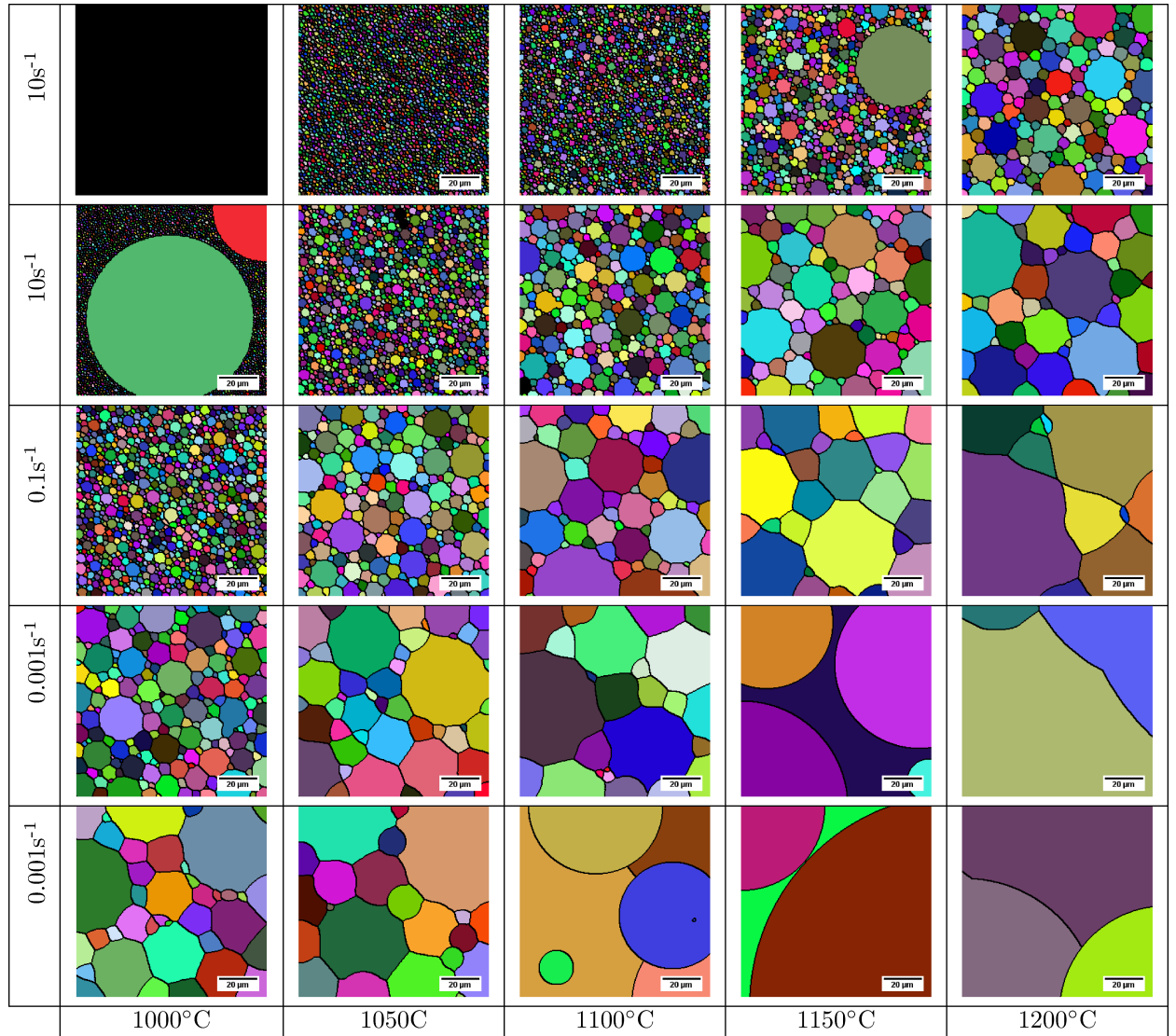


Table 5.6: Microstructure of L-605 deformed at  $\epsilon = 0.8$  generated by growth of a compact circles layout

used in the calculation, so the recrystallized grains were not visible on the picture. Reducing the step size would increase dramatically the computing time. Therefore the microstructure was not generated properly for this specific deformation condition.

On the Figure 5.6 it is easy to visualize the decay of grain size and of recrystallized fraction with increasing strain rate and decreasing temperature. For intermediate Zener-Hollomon parameter, the microstructure is in very good agreement with experiments. For low strain rate the grain size is overestimated, and at high strain rate and low temperature the grain size is overestimated, as mentioned previously. However the global trend is properly described, and the model can be fairly used for predictive calculations of microstructure.



### 5.3.7 Conclusion

A class model of dynamic recrystallization was established based on the mobility and nucleation frequency determined previously. The model predicts the correct trend both in terms of compression curves and grain size. For low temperature and high strain rate ( $T < 1050^{\circ}\text{C}$   $\dot{\epsilon} > 1\text{s}^{-1}$ ), the model underestimates the size of new grains and the recrystallized fraction, leading to an underestimated flow softening on the compression curve. For low strain rate and high temperature, the grain size is overestimated, however it has little incidence on the mechanical behavior. For all the other conditions, the model is in very good agreement with experimental data, and provides a fair estimation of the stress-strain curves and the grain size distributions.

The model does not reproduce the minimum of grain size and recrystallized fraction that was observed at intermediate strain rate on the experimental section. One could explain this discrepancy by the occurrence of meta-dynamic recrystallization and adiabatic heating. However the discrepancy conditions do not match with the conditions favorable to these two phenomenon. Moreover it was shown on the experimental section that meta-dynamic recrystallization and adiabatic heating are not sufficient to explain the recrystallization behavior. Another effect due to the interaction between dynamic recrystallization and dynamic strain aging is suggested. However the exact effect of dynamic strain aging on the growth of new grains is not very well-known, and further investigation would be required to confirm this assumption and clarify the nature of this interaction.



## Chapter 6

# Conclusions







# Conclusions

Mechanical behavior of L-605 alloy is investigated in the range 1000-1200°C and 0.001s<sup>-1</sup> to 10s<sup>-1</sup>. L-605 alloy follows a usual viscoplastic deformation behaviour at high temperature: stress increases with strain rate and decreases with temperature. Compression curves exhibit a peak stress followed by flow softening, and then stabilizes to a plateau at the steady-state. Flow softening is attributed to the occurrence of dynamic recrystallization at large strain. Fits of experimental data provide the normalized hardening rate  $\theta_0/\mu$  and the extrapolated steady-state stress  $\sigma_V$ . Normalized hardening rate increases at low temperature and intermediate strain rate, and this effect is attributed to the operation of dynamic strain aging. From these two fundamental parameters, the constitutive equation of the material is determined by the Kocks-Mecking method. Flow stress is properly described by the Kocks-Mecking model, and the estimations remain correct even for complex deformation situations such as speed jump tests.

Deformation behavior is determined by applying the Dynamic Materials Model, and by construction of processing maps. Flow is stable at strain rate lower than  $\dot{\epsilon} < 0.1s^{-1}$ , and unstable at large strain rate. However the agreement with experimental data is partial only, and this method provides little information on the effective deformation mechanisms at stake. Another method to study the mechanical behaviour is developed based on the analysis of Kocks-Mecking: fractional flow softening is calculated at large strain and plotted into a 2D map, similarly to processing map. The agreement with experimental data is correct, and provides some predictive information on the microstructural changes. This parameter is considered as an indicator of the recrystallization process in the current case, and may also be used to follow some other structural changes such as shear bands or cracks formation.

Precipitation behavior of L-605 alloy during aging treatment is investigated. Precipitates form at a temperature below 1100°C for several minutes to several hours holding time. Precipitates are M<sub>6</sub>C carbides and form a network along the grain boundaries. It is concluded that the hot working process of L-605 might involve the precipitation of carbides for 1000°C and very low strain rate ( $\dot{\epsilon} = 0.001s^{-1}$ ). For higher strain rate, the precipitation is not expected due to the short processing



time. For higher temperature, precipitation is sluggish and is not expected during the hot deformation process.

Grain growth kinetics is very fast for temperature above  $1100^{\circ}\text{C}$  ( $>0.78 T_f$ ), and produces a coarse microstructure after several minutes annealing only at  $1200^{\circ}\text{C}$ . The coarsening of the microstructure leads to a loss of strength and an improvement of ductility. The gain in ductility may be a serious advantage for stent manufacture, and despite the slight strength loss, it may be worth to apply an annealing treatment after forging to ensure to fulfil the maximal elongation requirement. The occurrence of abnormal grain growth was detected at intermediate annealing time, and produce an interesting bimodal grain size distribution. Grain growth can be properly estimated with the Hillert model by considering the grain boundary surface energy as the main driving force for boundaries migration.

Static recrystallization is observed during the annealing of cold rolled 23% L-605 alloy. This phenomenon is very brief and results into the high instability of deformed ultrafine microstructure at high temperature. Hillert model is shown to be inadequate to predict microstructure evolution during static recrystallization, because the nucleation is not considered. Moreover the driving force for recrystallization is the dislocation density and not any more the grain boundary surface energy. This example illustrates that simple models do not hold any more in the case of recrystallization. As a consequence, the grain growth law and the nucleation process must be thoroughly determined by modeling to predict the microstructure change in the specific case of recrystallization.

The occurrence of dynamic recrystallization is observed for all the deformation conditions tested. For temperature higher than  $1100^{\circ}\text{C}$  and strain rate lower than  $0.1\text{s}^{-1}$  or higher than  $1\text{s}^{-1}$ , dynamic recrystallization leads to an homogeneous equiaxial microstructure with a grain size about  $10\text{ }\mu\text{m}$ . Deformation at  $T < 1100^{\circ}\text{C}$  and strain rate in the range  $0.1\text{-}1\text{s}^{-1}$  results in an heterogeneous microstructure with grain size lower than  $1\text{ }\mu\text{m}$ . Dynamic recrystallization operates following a discontinuous mechanism by bulging from grain boundaries. A second nucleation mechanism involving annealing twins was highlighted for  $T > 1100^{\circ}\text{C}$ . In the first step,  $\Sigma 3$  annealing twins rotate from  $60^{\circ}$  to  $55^{\circ}$ , and then in a second step bulging can operate. The recrystallized fraction was shown to evolve inversely with dynamic recrystallized grain size and misorientation parameter.

The grain boundary mobility of L-605 alloy is determined by analytical modeling. In parallel, data extracted from the literature is analyzed and provides the mobility of pure copper and pure cobalt. Mobility increases with temperature, in agreement with the Turnbull estimation. By comparing the results on L-605 alloy and pure cobalt, it is deduced that solute elements decrease the grain boundary mobility. Solute-drag effect explains the relatively low boundary motion in L-605, and can be described by the theory of Cahn. However, for the sake of simplicity the Turnbull estimation



is used in the next steps as it provides the same estimated values as the Cahn theory that is more complex to handle.

The criterion of nucleation by bulging from boundaries is reformulated to account for the effect of the pre-existing boundaries. The new criterion makes the transition between recrystallization and grain growth process, and is applicable even in the case of ultrafine grain materials. Nucleation is extracted from modeling data at steady-state, and is extrapolated for other values of strain based on a new semi-empirical formula. From this point, both grain growth and nucleation are completely determined in a quantitative way, and the basis for a complete model are settled.

The mobility of boundaries and the nucleation frequency are injected in a class model to calculate the grain size evolution during the dynamic recrystallization process. The model reproduces very well the mechanical behavior at high temperature, and provides a fair estimation of the grain size distribution. However the model does not predict the minimum of grain size and recrystallized fraction for intermediate strain rate at low temperature. Meta-dynamic recrystallization and adiabatic heating at high strain rate may be responsible of the formation of this minimum. Therefore the model does not reproduces exactly the experimental data as it does not account for these phenomenon. A possible interaction between dynamic strain aging and recrystallization is also suggested as an interpretation of the grain size observed, but requires further investigation to be confirmed and fully understood.







# Appendix 1

ISO standard	Test name
ISO 10993-1:2003	Evaluation and testing
ISO 10993-2:2006	Animal welfare requirements
ISO 10993-3:2003	Tests for genotoxicity, carcinogenicity and reproductive toxicity
ISO 10993-4:2002	Selection of tests for interaction with blood
ISO 10993-5:1999	Tests for in vitro cytotoxicity
ISO 10993-6:2007	Tests for local effects after implantation
ISO 10993-7:1995	Ethylene oxide sterilization residuals
ISO 10993-9:1999	Framework for identification and quantification of potential degradation products
ISO 10993-10:2002	Tests for irritation and delayed-type hypersensitivity
ISO 10993-11:2006	Tests for systemic toxicity
ISO 10993-12:2002	Sample preparation and reference materials
ISO 10993-13:1998	Identification and quantification of degradation products from polymeric devices
ISO 10993-14:2001	Identification and quantification of degradation products from ceramics
ISO 10993-15:2000	Identification and quantification of degradation products from metals and alloys
ISO 10993-16:1997	Toxicokinetic study for degradation products and leachables
ISO 10993-17:2002	Establishment of allowable limits for leachable substances
ISO 10993-18:2005	Chemical characterization of materials
ISO 10993-19:2006	Physicochemical, morphological and topographical characterization of materials
ISO 10993-20:2006	Principles and methods for immunotoxicological testing of medical devices

Table 1: Detail of the tests required for the ISO 10993 norm [47]

Material designation	Aubert Duval designation	European standard	UTS (MPa)	Y (MPa)	A (%)
Engineering austenitic steels					
Austenitic stainless steels	M30NW	X4CrNiMoN21-9-4	860	450	40
Austenitic stainless steels	SC2104	X2CrNiMoN17-13-3	630	300	45
Austenitic stainless steels	SC2118	X2CrNiMo17-12	550	240	40
Austenitic stainless steels	X18BC	X2CrNi19-11	550	190	60
Austenitic stainless steels	X18MBC	X2CrNiMo17-12-2	550	200	60
Austenitic stainless steels	X18PA	X6CrNiTi18-10	600	220	50

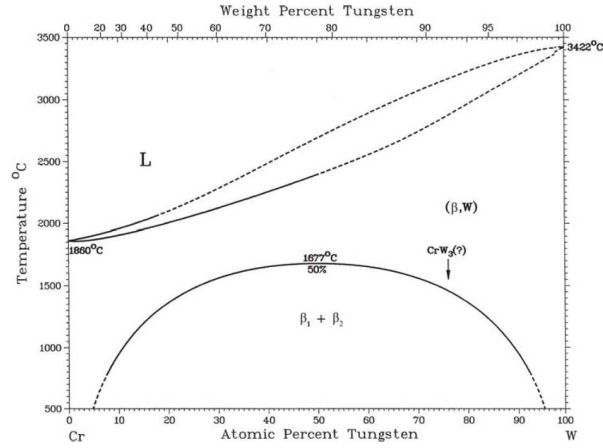


Austenitic stainless steels	M25W	X2CrNiMo18-14-3	540	210	60
Austenitic stainless steels	NYB66	X1CrNiMoWN24-22-6	800	420	50
Austenitic stainless steels	SC2109	X2CrNi18-9	550	220	45
Nickel superalloys					
Nickel alloys	NY625	NiCr22Mo9Nb	840	430	40
Nickel alloys	NY690	NiCr30Fe	586	240	30
Nickel alloys	NY925	NiCr20FeMo3TiCuAl	1150	795	28
Nickel alloys	PER2X	NiCr20TiAl	1000	620	39
Nickel alloys	PER3	NiCr20Co13Mo4Ti3Al	1270	850	25
Nickel alloys	PER5	NiCr19Co18Mo4Ti3Al31310	840	20	
Nickel alloys	PER5	NiCr19Co18Mo4Ti3Al31200	750	35	
Nickel alloys	PER625	NiCr22Mo9Nb	850	450	40
Nickel alloys	PER625	NiCr22Mo9Nb	750	350	65
Nickel alloys	PER706	NiFe38Cr16Nb	1260	1000	18
Nickel alloys	PER72	NiCr18Co15TiMoAl	1530	1150	14
Nickel alloys	PER75	NiCr20Ti	740	280	41
Nickel alloys	PYRAD49D	NiCr21Fe18Mo9	790	390	54
Nickel alloys	PYRAD53NW	NiCr19Fe19Nb5Mo3	1360	1120	18
Nickel alloys	PER718	NiCr19Fe19Nb5Mo3	1360	1120	18
Cobalt superalloys					
Cobalt alloys	M64BC	CoCr28Mo	1160	650	35
Cobalt alloys	XSH	CoCr20W15Ni	1005	460	45
Titanium alloys					
Titanium alloys	T40	Pure titanium	460	350	20
Titanium alloys	TA4DE	Ti-4Al-4Mo-2Sn-0,5Si	1150	1050	12
Titanium alloys	TA5CD4	Ti-5Al-2Sn-2Zr-4Mo-4Cr	1150	1060	6
Titanium alloys	TA6E4Zr	Ti-5,8Al-4Sn-3,5Zr-0,7Nb-0,5Mo-0,35Si-0,06C	1050	980	10
Titanium alloys	TA6V	Ti-6Al-4V	1100	1040	10
Titanium alloys	TA6V ELI	Ti-6Al-4V	860	790	10
Titanium alloys	TAD6Zr4E	Ti-6Al-2Sn-4Zr-6Mo	1100	1000	7
Titanium alloys	TA6Zr5D	Ti-6Al-5Zr-0,5Mo-0,2Si	1050	900	9
Titanium alloys	TA6Zr4DE	Ti-6Al-2Sn-4Zr-2Mo	1000	940	15
Titanium alloys	TAV6E	Ti-6Al-6V-2Sn	1100	1000	8
Titanium alloys	TV10A3Fe2	Ti-10V-2Fe-3Al	1150	1050	9

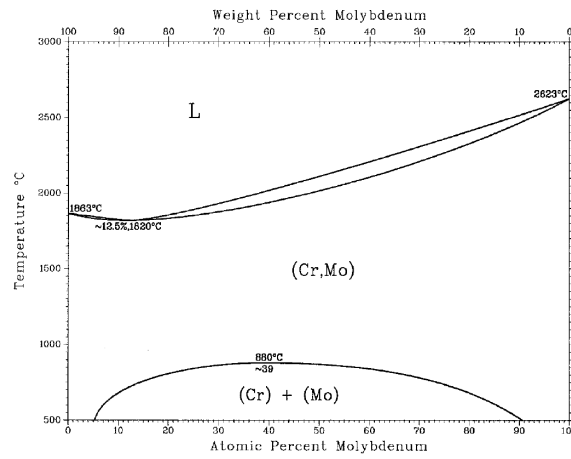
Table 2: Mechanical properties data from Aubert&Duval (Eramet) materials datasheets: Ultimate Tensile Stress (UTS), Yield stress (Y) and maximal elongation (A)



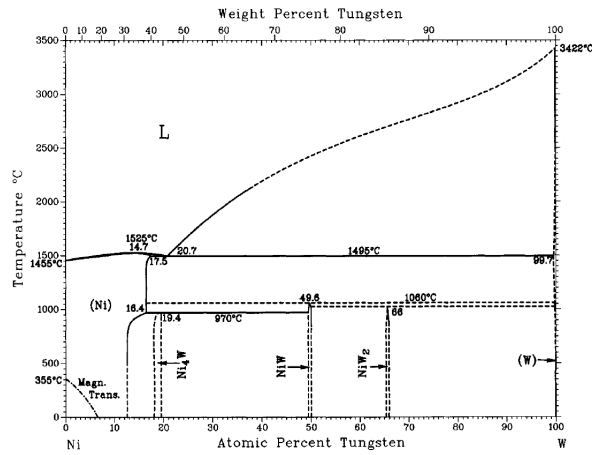
## Binary phase diagrams of Cr-W, Cr-Mo and Ni-W systems



(a) Phase diagram of the Cr-W system [56]



(b) Phase diagram of the Cr-Mo system [54]

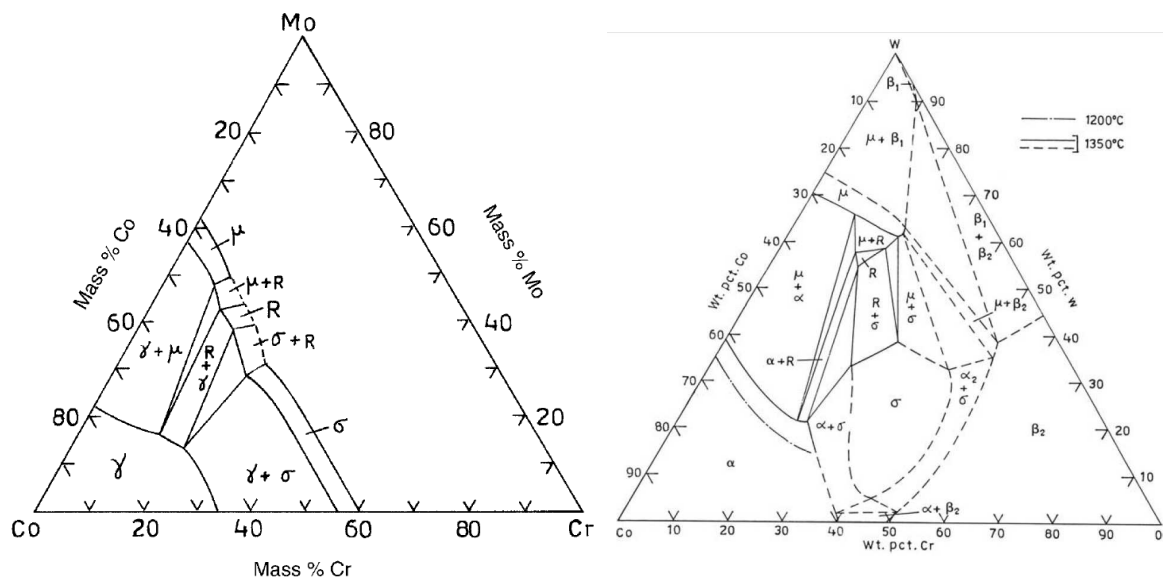


(c) Phase diagram of the Ni-W system [55]

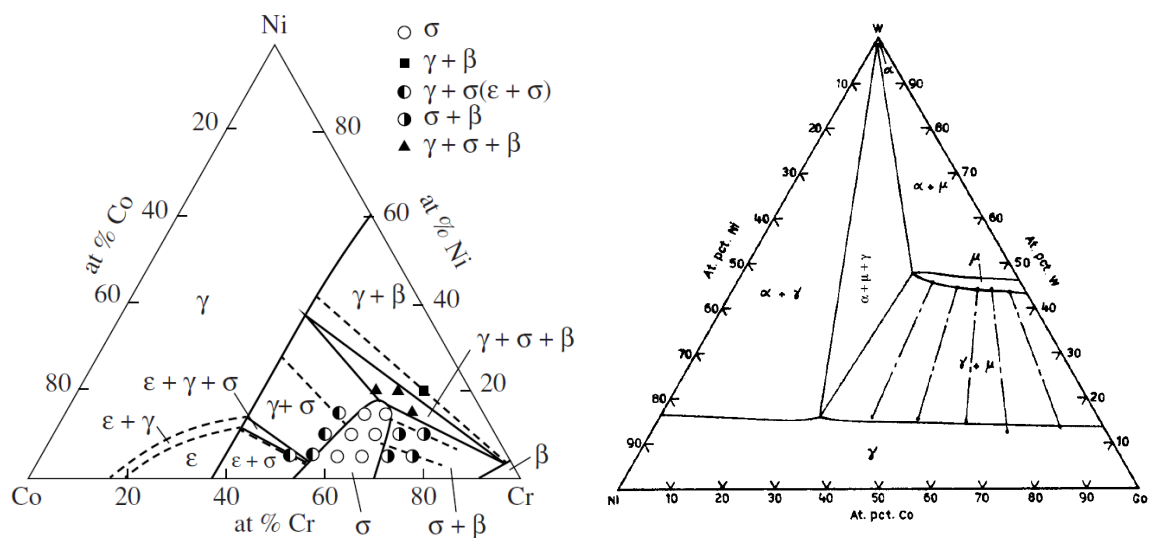
Figure 1: Phase diagrams of 1a Cr-W, 1b Cr-Mo and 1c Ni-W systems



## Ternary phase diagrams of usual cobalt-based systems



(a) Phase diagram of the Co-Cr-Mo system at 1200°C [54] (b) Phase diagram of the Co-Cr-W system at 1350°C [56]



(c) Phase diagram of the Co-Cr-Ni system at 800°C [57] (d) Phase diagram of the Co-Ni-W system at 1100°C [55]

Figure 2: Ternary phase diagrams of Co-Cr-W-Mo-Ni systems: 2a Co-Cr-Mo at 1200°C, 2b Co-Cr-W at 1350°C, 2c Co-Cr-Ni at 800°C, 2d Co-Ni-W at 1100°C



# Appendix 2

## High-temperature compression tests: compression curves

### Treatment of compression curves

The following part presents the treatment applied on data coming from mechanical tests at high temperature. Uniaxial compression tests carried out on Thermecmaster-Z and Gleeble forging simulators provide data under the form of a displacement and a force applied to the sample. The data must be converted to strain and stress in a first time. Assuming that strain is homogeneous in the sample, strain is calculated from displacement by using the following expression:

$$\epsilon = -\ln\left(1 - \frac{\Delta l}{l_0}\right) \quad (1)$$

with  $l_0$  the initial length of the sample, and  $\Delta l$  the displacement of the ram. The stress can be obtained from applied force by the relation:

$$\sigma = \frac{4F.(l_0 - \Delta l)}{\pi D_0^2 l_0} \quad (2)$$

The initial force-displacement curve and the converted stress-strain curve for 1100°C  $\dot{\epsilon} = 1s^{-1}$  are illustrated in Figure 4. Raw stress-strain data are represented in Figure 3 for T=1000°C and 1200°C. Strain noted  $\epsilon$  must be converted to plastic strain  $\epsilon_p$  to remove the effect of elastic strain  $\epsilon_e$  on the stress-strain diagram. This conversion is operated by the following formula:

$$\epsilon_p = \epsilon - \epsilon_e = \epsilon - \frac{\sigma}{E_a} \quad (3)$$

with  $E_a$  the apparent Young modulus corresponding to the initial slope of stress-strain curve. The conversion to stress- plastic strain is illustrated in Figure 4. This transformation affects slightly the shape of the curve [137], and is not simply a shift of the curve on the strain axis like we can find sometimes in the literature. The yield stress can be determined accurately graphically on stress - plastic strain diagram and corresponds to the y-intercept for  $\epsilon_p = 0$ .

Some irregularities on the compression curves are observed, and are attributed to the stick-slip sliding between the sample and the anvils. This phenomenon leads to very sharp variations on the flow stress not related to the material properties, and must be subtracted. Therefore, Smooth process is finally applied on the curves to remove the irregularities using the adjacent-averaging method, and an example of curve treatment is illustrated in Figure 5.



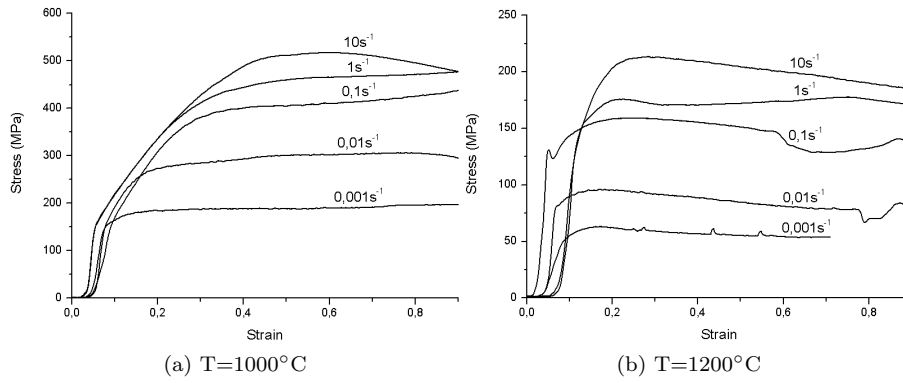


Figure 3: Raw stress-strain curves of L-605 from Thermecmaster-Z experiments before treatment

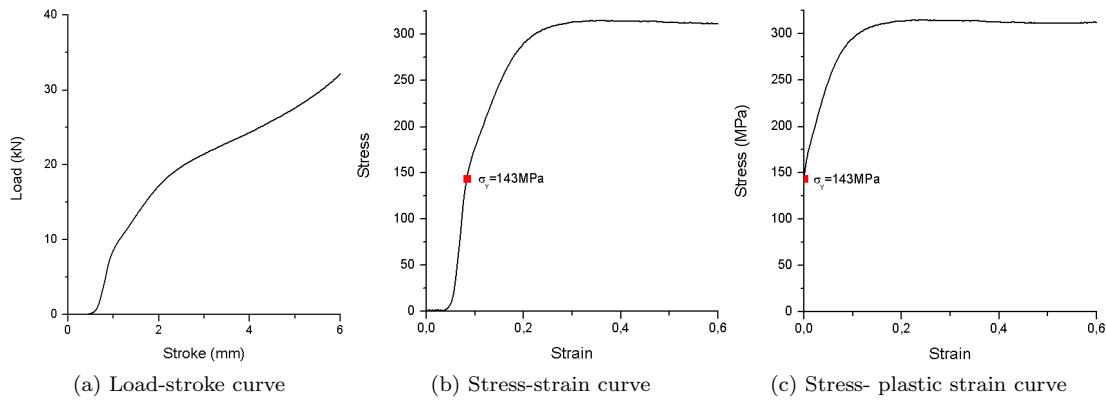


Figure 4: Conversion of load-stroke to stress-strain curve at  $1100^{\circ}\text{C}$   $\dot{\epsilon} = 1\text{s}^{-1}$ , and determination of yield stress  $\sigma_y$

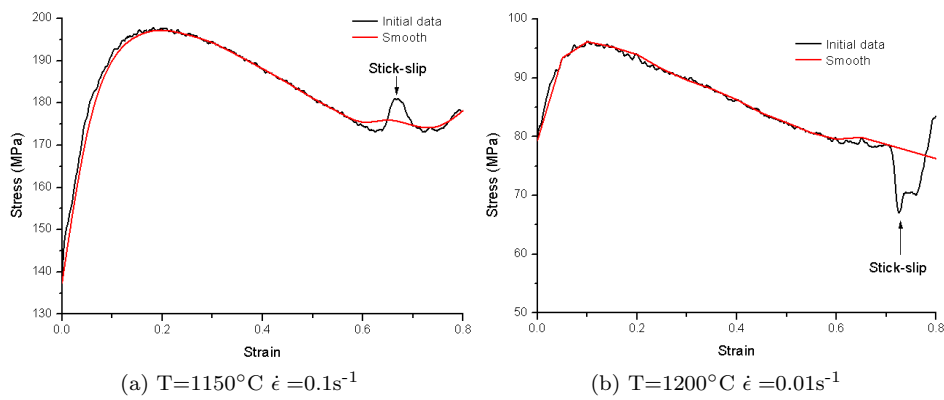


Figure 5: Smooth of the compression curve by adjacent-averaging smoothing method to remove the variations due to friction



## Compression curves data set after elastic correction

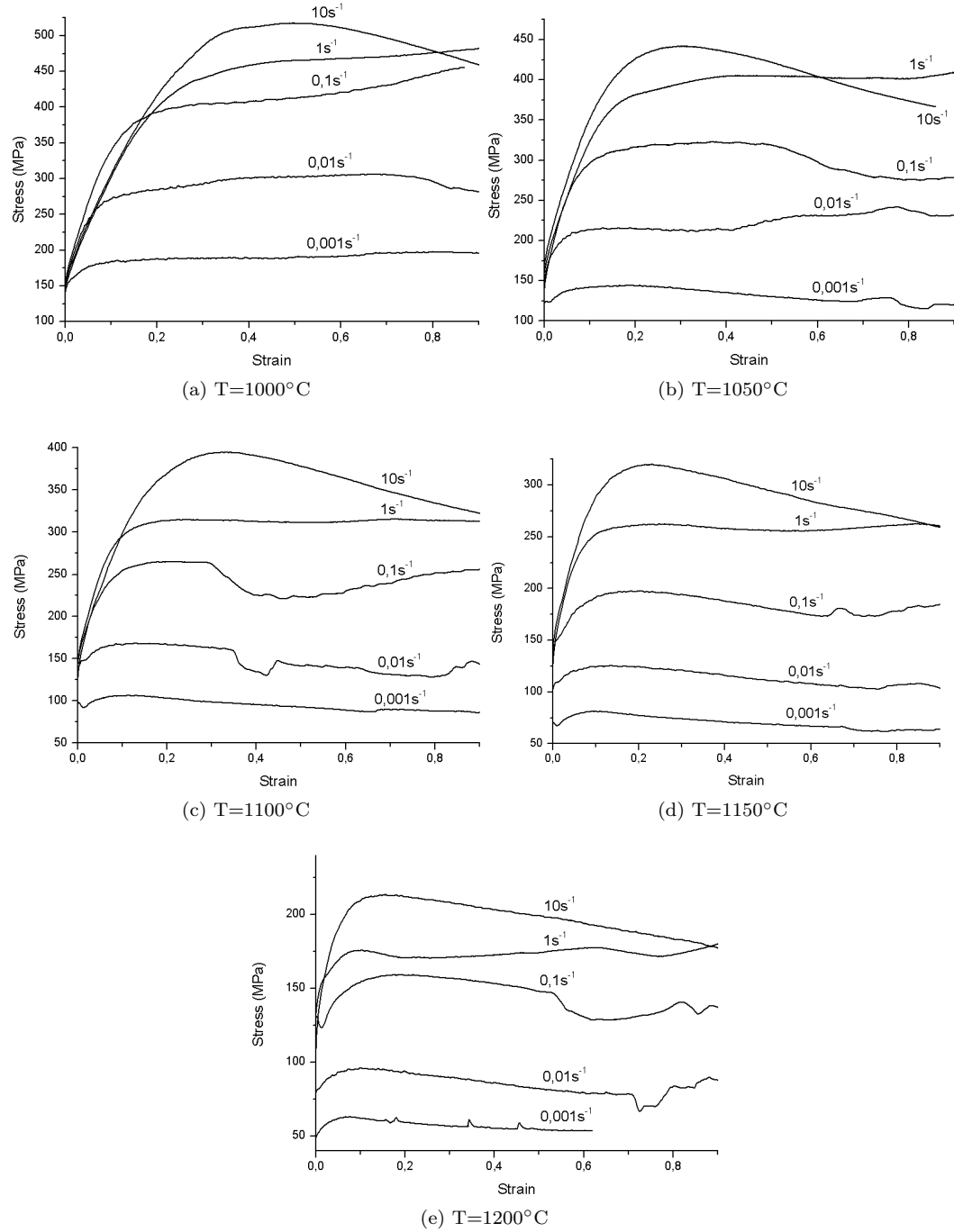


Figure 6: Plastic stress-strain curves of L-605 from Thermecmaster-Z experiments



Tables of steady-state stress  $\sigma_{ss}$ , extrapolated steady-state stress  $\sigma_V$  and yield stress  $\sigma_y$

Strain rate ( $s^{-1}$ )	Temperature ( $^{\circ}C$ )				
	1000	1050	1100	1150	1200
$0.001s^{-1}$	189	125	88	63	54
$0.01s^{-1}$	301	213	129	104	78
$0.1s^{-1}$	406	276	224	174	136
$1s^{-1}$	468	405	312	256	171
$10s^{-1}$	455	367	318	254	178

Table 3: Steady-state stress  $\sigma_{ss}$  (MPa)

Strain rate ( $s^{-1}$ )	Temperature ( $^{\circ}C$ )				
	1000	1050	1100	1150	1200
$0.001s^{-1}$	187	142	107	83	64
$0.01s^{-1}$	289	216	169	126	97
$0.1s^{-1}$	410	318	269	198	162
$1s^{-1}$	473	408	316	267	182
$10s^{-1}$	636	461	410	331	218

Table 4: Steady-state extrapolated stress  $\sigma_V$  (MPa)

Strain rate ( $s^{-1}$ )	Temperature ( $^{\circ}C$ )				
	1000	1050	1100	1150	1200
$0.001s^{-1}$	141	121	95	70	49
$0.01s^{-1}$	149	149	127	102	79
$0.1s^{-1}$	151	138	127	138	130
$1s^{-1}$	145	158	143	126	132
$10s^{-1}$	147	168	143	143	107

Table 5: Yield stress  $\sigma_y$  (MPa)



## Compression curves obtained with Gleeble device

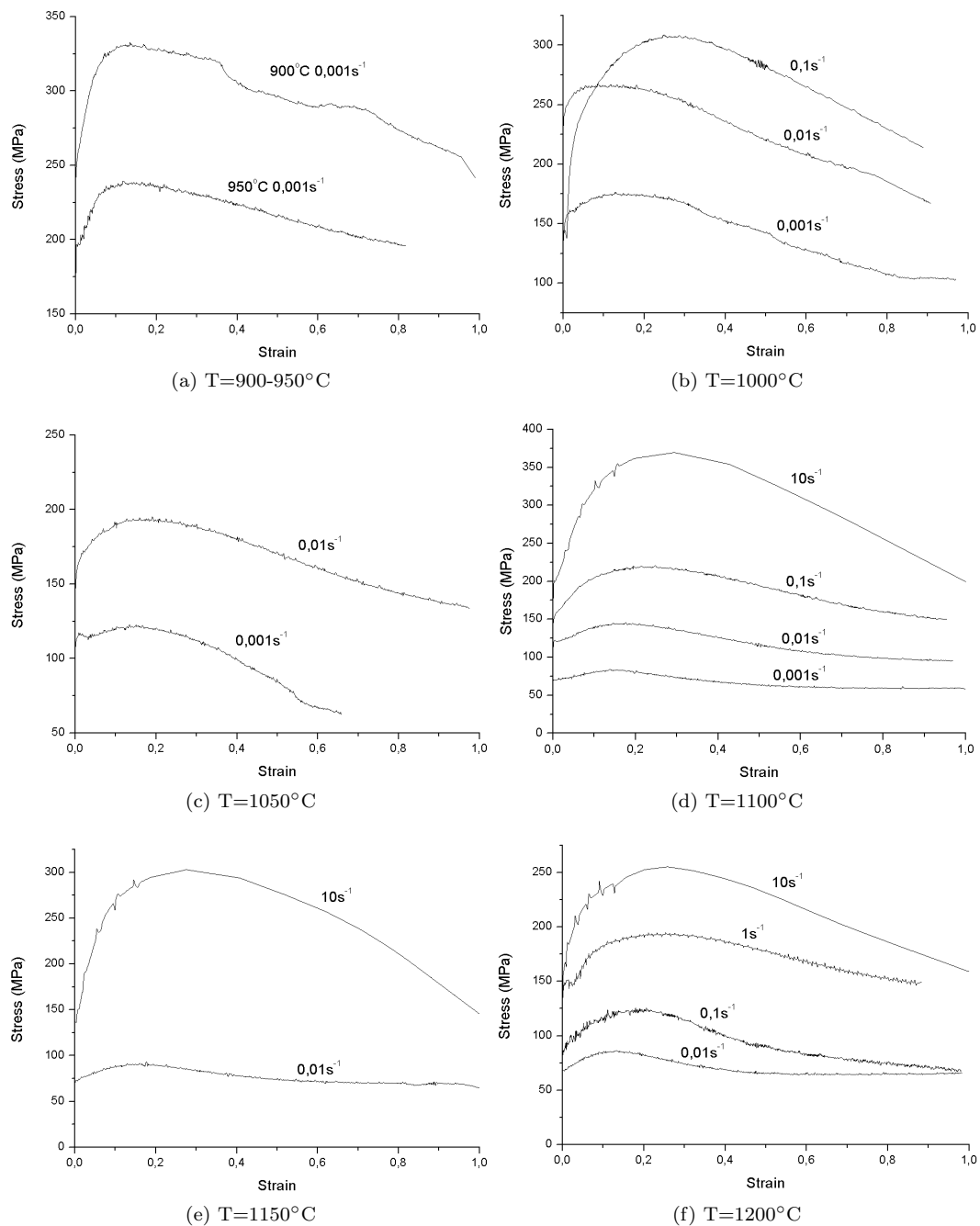


Figure 7: Plastic stress-strain curves of L-605 from Gleeble experiments



## Observation of microstructure by EBSD at low magnification

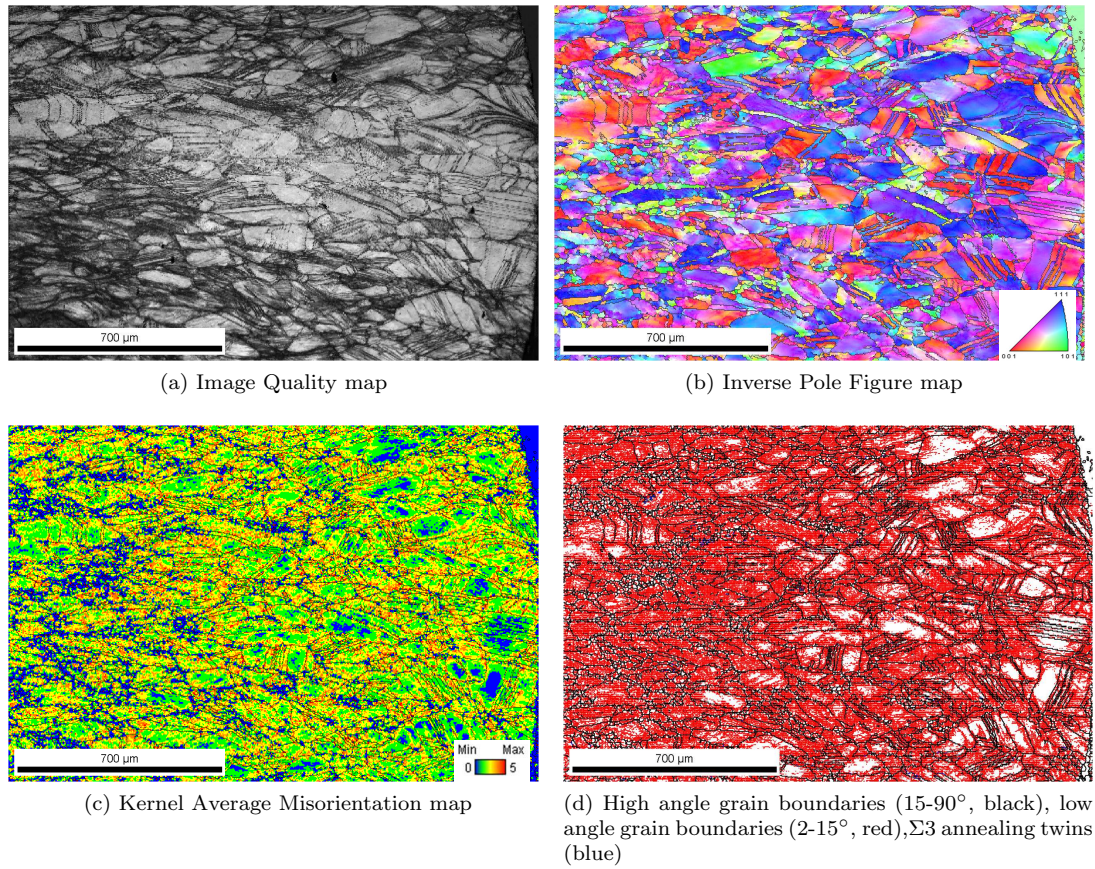


Figure 8: Observation of microstructure after deformation of  $\epsilon = 0.8$  at  $1000^\circ \text{ s}^{-1}$



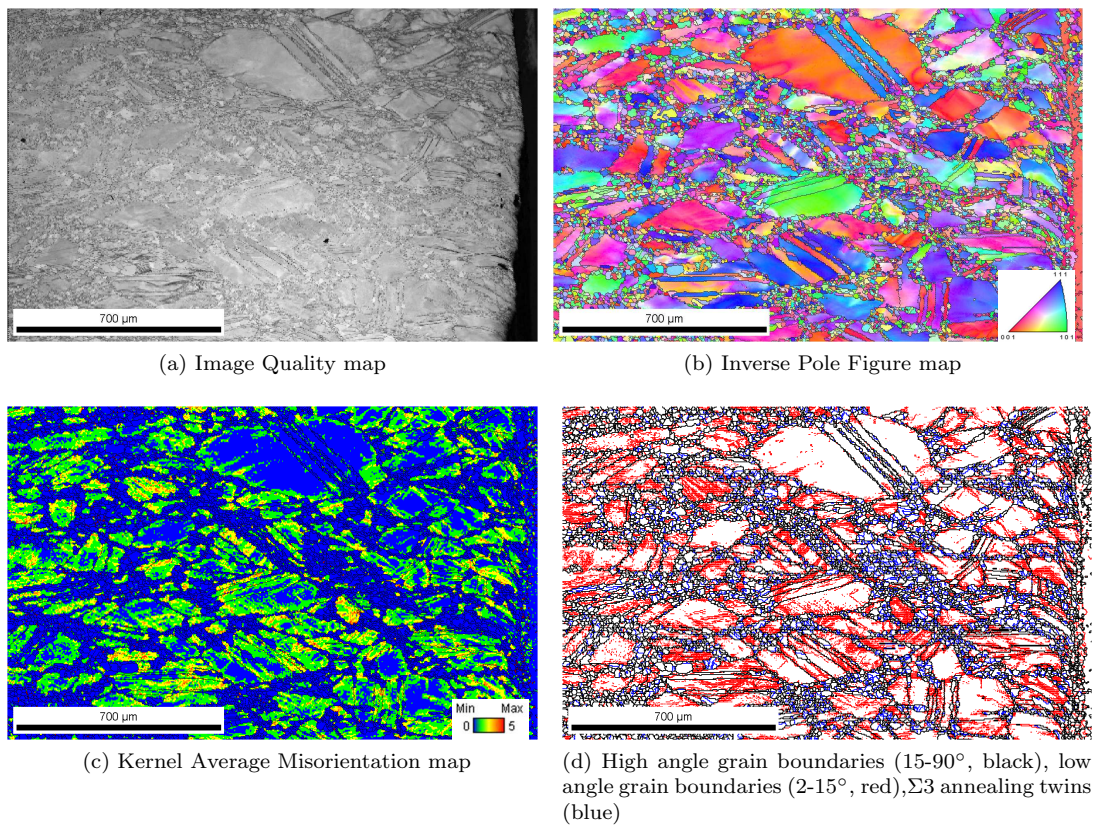
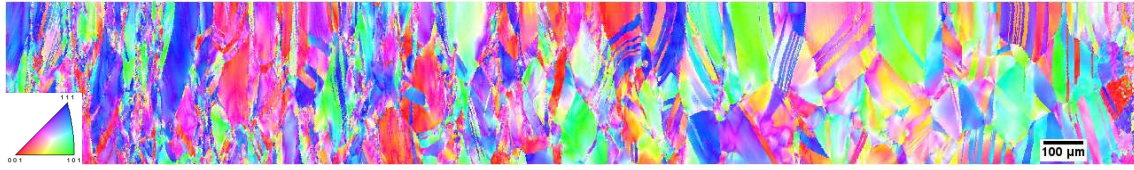
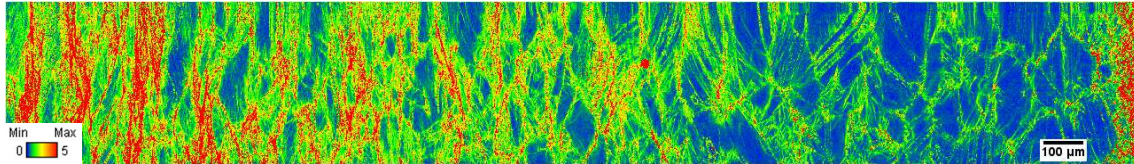


Figure 9: Observation of microstructure after deformation of  $\epsilon = 0.8$  at  $1000^\circ \text{ 1s}^{-1}$



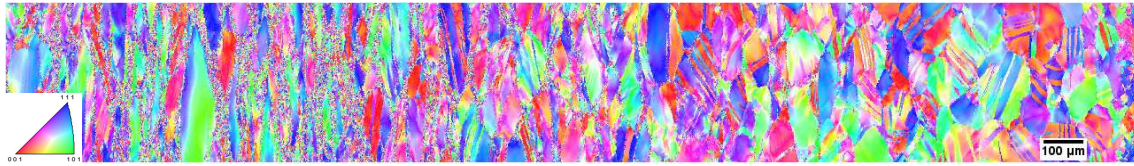


(a) IPF map along the longitudinal axis: left=middle of the sample, right=edge of the sample

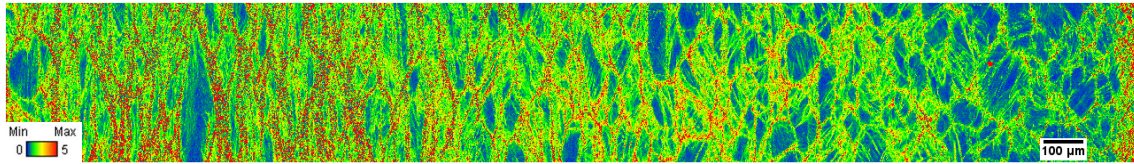


(b) KAM map along the longitudinal axis: left=middle of the sample, right=edge of the sample

Figure 10: Microstructure after deformation at  $1000^{\circ}\text{C}$   $0.1\text{s}^{-1}$  with Thermecmaster-Z device

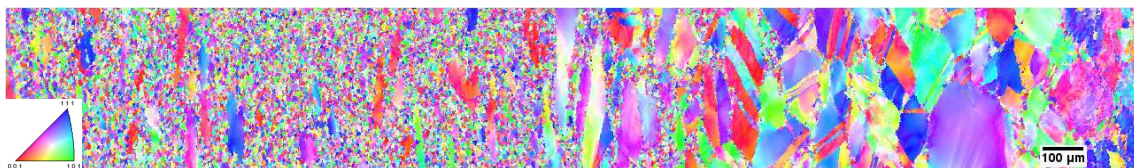


(a) IPF map along the longitudinal axis: left=middle of the sample, right=edge of the sample

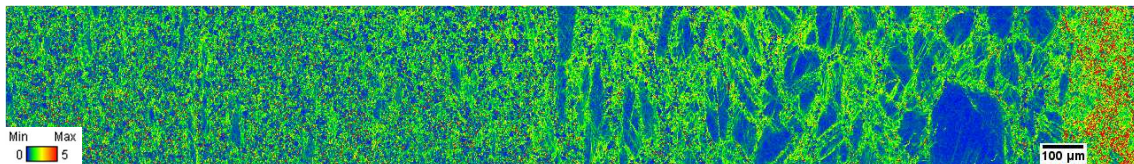


(b) KAM map along the longitudinal axis: left=middle of the sample, right=edge of the sample

Figure 11: Microstructure after deformation at  $1100^{\circ}\text{C}$   $0.1\text{s}^{-1}$  with Thermecmaster-Z device



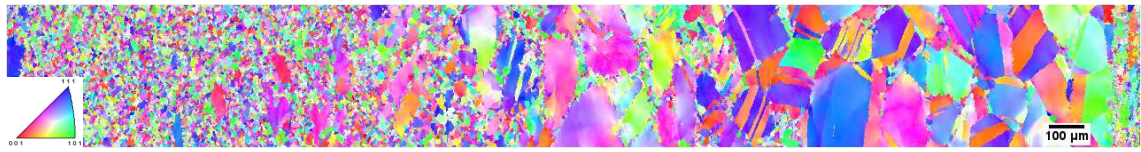
(a) IPF map along the longitudinal axis: left=middle of the sample, right=edge of the sample



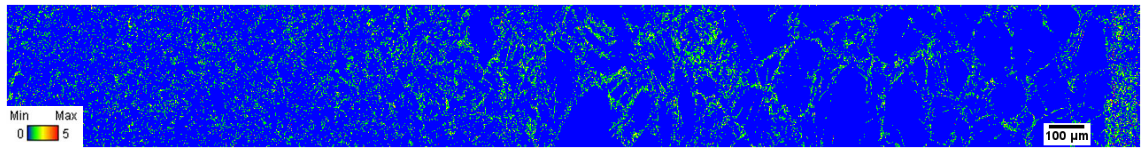
(b) KAM map along the longitudinal axis: left=middle of the sample, right=edge of the sample

Figure 12: Microstructure after deformation at  $1200^{\circ}\text{C}$   $0.1\text{s}^{-1}$  with Thermecmaster-Z device



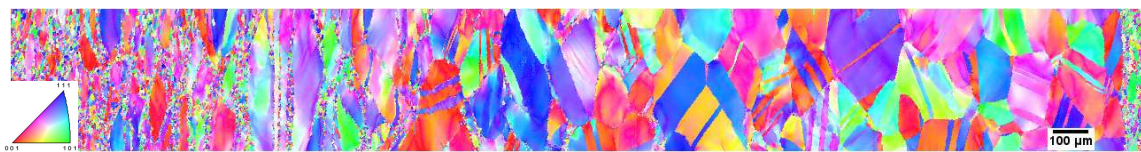


(a) IPF map along the longitudinal axis: left=middle of the sample, right=edge of the sample

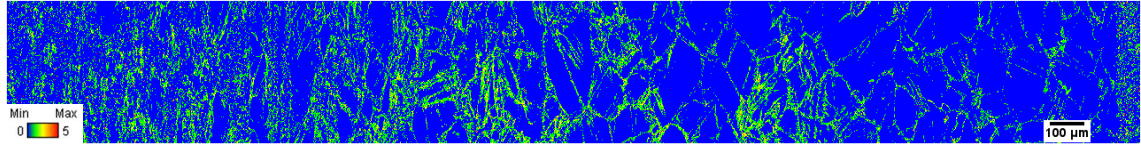


(b) KAM map along the longitudinal axis: left=middle of the sample, right=edge of the sample

Figure 13: Microstructure after deformation at  $1100^{\circ}\text{C}$   $0.1\text{s}^{-1}$  with Gleeble device



(a) IPF map along the longitudinal axis: left=middle of the sample, right=edge of the sample

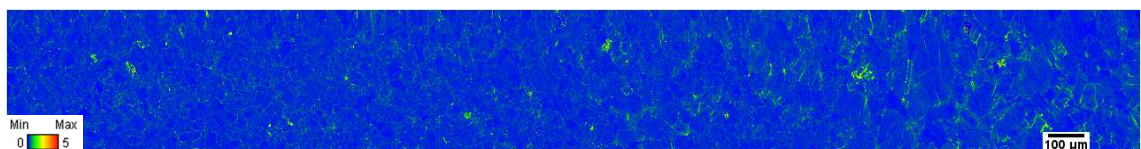


(b) KAM map along the longitudinal axis: left=middle of the sample, right=edge of the sample

Figure 14: Microstructure after deformation at  $1100^{\circ}\text{C}$   $0.1\text{s}^{-1}$  with Gleeble device



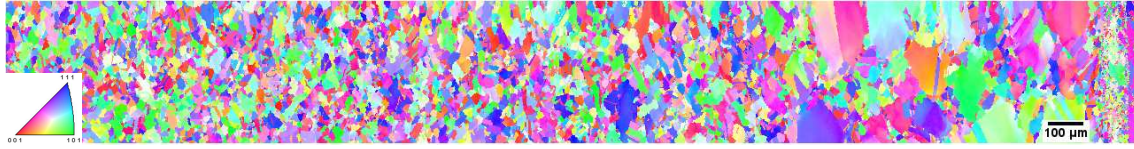
(a) IPF map along the longitudinal axis: left=middle of the sample, right=edge of the sample



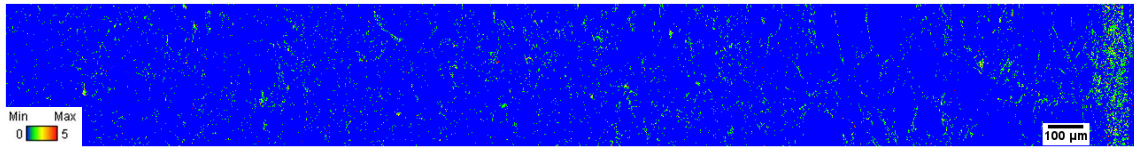
(b) KAM map along the longitudinal axis: left=middle of the sample, right=edge of the sample

Figure 15: Microstructure after deformation at  $1200^{\circ}\text{C}$   $0.1\text{s}^{-1}$  with Gleeble device



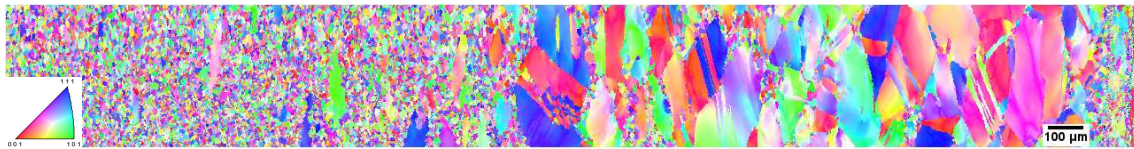


(a) IPF map along the longitudinal axis: left=middle of the sample, right=edge of the sample

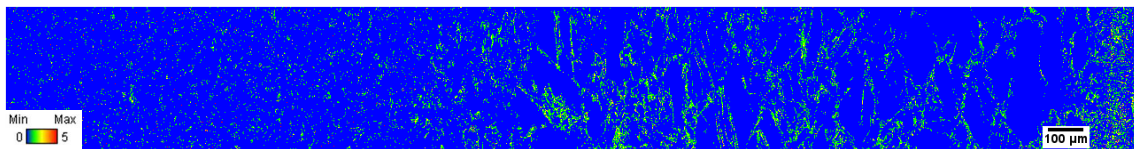


(b) KAM map along the longitudinal axis: left=middle of the sample, right=edge of the sample

Figure 16: Microstructure gradient after compression at 1100°C with a variable strain rate  $\dot{\epsilon} = 0.1 \rightarrow 0.01 \rightarrow 0.001 s^{-1}$



(a) IPF map along the longitudinal axis: left=middle of the sample, right=edge of the sample



(b) KAM map along the longitudinal axis: left=middle of the sample, right=edge of the sample

Figure 17: Microstructure gradient after compression at 1100°C with a variable strain rate  $\dot{\epsilon} = 0.001 \rightarrow 0.01 \rightarrow 0.1 s^{-1}$



# Appendix 3

## Treatment of pure copper hot deformation experimental data

### Raw data from literature

Pure copper was extensively studied in the literature as it constitutes a simple case of FCC metal convenient for understanding the fundamental deformation mechanisms. Large work was dedicated to pure copper during the last decade by Prasad et al. on electrolytic tough pitch copper (ETP) copper (oxygen concentration=100-650 ppm) [138, 139, 76], and on oxygen-free high conductivity (OFHC) copper (oxygen concentration<3040 ppm) [140, 141, 142]. The authors aimed at comparing these two materials to determine the effect of oxygen concentration on the deformation behaviour. We propose here to analyse in detail the data concerning the ETP copper, which correspond to the most common type of pure copper, containing oxygen as an impurity. The compression curves available from references [138, 139, 76] are illustrated in Figure 18. As illustrated in Figure 18f, the average grain size was measured by linear intercept, and fitted linearly versus Zener-Hollomon parameter ( $Z$  is expressed by equation 1.6).

### Treatment of compression curves by the Kocks-Mecking model

Compression curves are extracted and treated following the Kocks-Mecking method. Flow stress is derived with strain to obtain the hardening rate  $\theta$ . Curves of  $\theta=f(\sigma)$  present a linear domain corresponding to the Voce law (equation 1.16), and the linear fits are illustrated in Figure 19a. The linear domain is extrapolated to the large stress, and the steady-state extrapolated stress  $\sigma_V$  can be identified by the intersection point with the x-axis. The shear modulus used to calculate  $g$  parameter is  $\mu = 35.8 - 0.01303.T(^{\circ}C)$  (GPa) [30].  $\log(\sigma/\mu)$  is found to follow a linear decay for a reference strain rate  $\dot{\epsilon}_0 = 10^6 \text{s}^{-1}$ . Figure 19b shows the dependence of extrapolated stress  $\sigma_V$  and of the effective steady-state stress  $\sigma_{ss}$  with  $g$  parameter. Initial hardening rate  $\theta_0$  is the hardening rate corresponding to a stress equal to yield stress. Normalized initial hardening rate  $\theta_0/\mu$  is quite constant with temperature and strain rate, with an average value of 0.04.

The yield stress is weakly dependent with strain rate, and this dependence can be neglected in a first order approximation. Yield stress decreases linearly with temperature, as illustrated in Figure



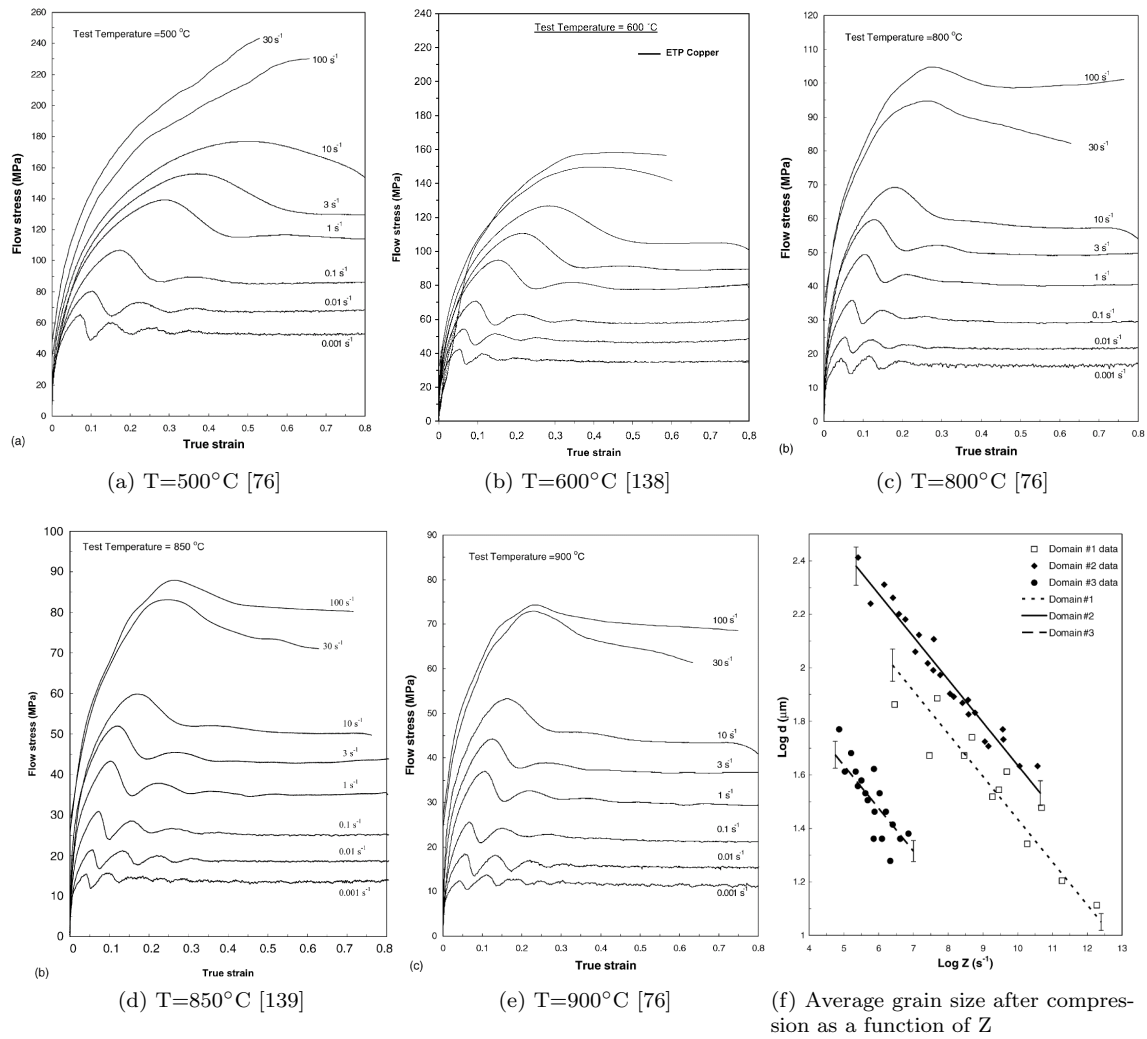


Figure 18: Stress-strain curves of pure ETP copper deformed in compression, and average grain size as a function of Zener-Hollomon parameter



19c. From the equations  $\text{Log}(\sigma_V/\mu)=f(g)$  and  $\sigma_y=f(T)$ , and using the coefficient  $\theta_0/\mu=0.04$ , the compression curves can be extrapolated by the Voce law using the equation 1.17. The experimental curves at 600°C and the corresponding extrapolated curves are illustrated in Figure 19d. Extrapolated curves show a good agreement with the experimental data for low strain, then a discrepancy occurs at large strain due to the onset of recrystallization.

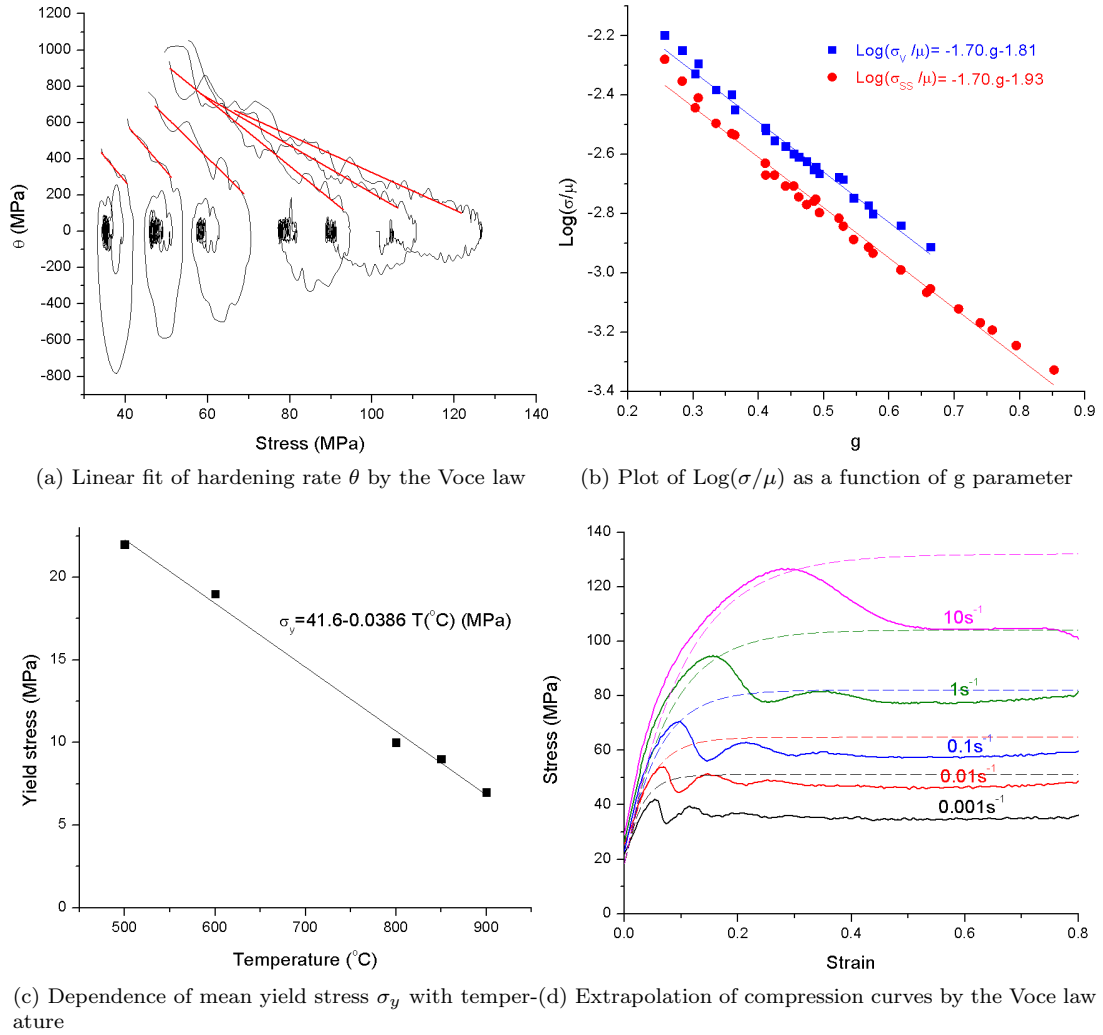


Figure 19: Treatment of compression curves: determination of  $\sigma_V$ ,  $\sigma_y$ , and extrapolation of curves by the Voce law using the calculated parameters

### Fit of the grain size by an unique equation: the Derby law

Prasad et al. proposes a set of three power laws to describe the dependence of grain size with Zener-Hollomon parameter [76]. For each equation, the Zener-Hollomon parameter was calculated with a different value of activation energy. Therefore the whole experimental data set is split into



three distinct domains of forging conditions, and it is assumed that the deformation mechanisms are different for each domain. Such an approach is quite inconvenient due to the large amount of parameters (3 parameters for each domain  $\rightarrow$  sum-total 9 empirical parameters), and not necessarily physically justified. Figure 21a represents the map of grain size obtained from the three empirical equations of Prasad et al. One can see the three distinct domains, each one with its specific activation energy for calculating  $Z$ . However, as there is no specific justification to have an abrupt transition between each domain, it is rather likely to have curved iso-value boundaries on this map with a continuum between each domain.

We propose to re-process the data by fitting with the empirical Derby law [32] (equation 1.40 page 56). Figure 20 provide an excellent fit of the average grain size with steady-state flow stress, and requires only two parameters to calculate the grain size. The equation indicated on Figure 20 is then combined with the equation of Figure 19b to calculate grain size for any condition. Thereof the map of grain size on Figure 21b was calculated. This map shows a very good agreement with Figure 20. As expected, the iso-value boundaries calculated are curved, and the three equations provided by Prasad et al. are just a local simplification each domain. The same comment can be made on flow stress: the Kocks-Mecking model manage to gather the whole flow stress data set in a single curve, while the use of power laws fail to provide a single equation. We can conclude that considering three domains with three activation energies is rather an artefact while plotting data than a real change of deformation mechanisms.

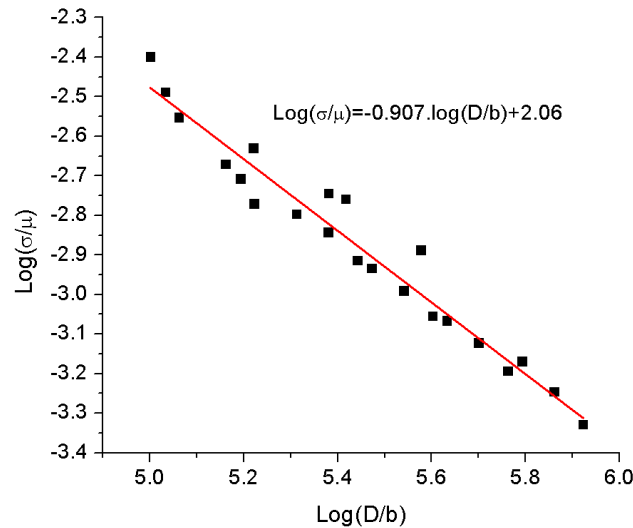


Figure 20: Fit of the average grain size with flow stress by the Derby law [32]

## Determination of grain boundary motion and nucleation



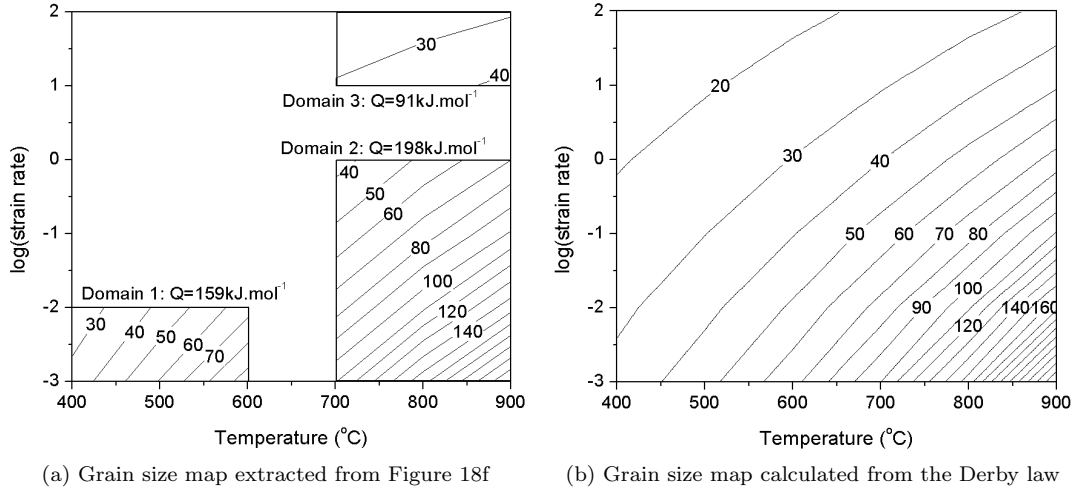


Figure 21: Determination of the average grain size as a function of flow stress, and comparison with the Zener-Hollomon dependent grain size

The grain boundary mobility is deduced from the stress and grain size using the optimization method described in the section 5.1.2 and the parameters of the Table 5.2. The map of the grain boundary mobility determined is illustrated in Figure 22a. Mobility increases with temperature, in agreement with the work of Turnbull et al. [101]. However, mobility also increases with strain rate, which is quite unexpected. Indeed, this phenomenon would rather be an effect of adiabatic heating and/or meta-dynamic recrystallization than an effective change in boundaries motion with strain rate. At high strain rate, the heat generated by compression has no time to be evacuated by dissipation, and the sample temperature raises. This heat can lead to an increase of the mobility, in agreement with the Turnbull estimation. If we assume that only adiabatic heat is contributing to the increase of mobility with strain rate, then the temperature raise  $\Delta T$  can be calculated by the equation 4:

$$\left. \begin{aligned} M_0 &= \frac{\beta \delta \cdot D_{GB} V_m}{b^2 R T} \quad (\text{Turnbull}) \\ D_{GB} &= D_0 \cdot \exp\left(\frac{-Q}{RT}\right) \quad (\text{Arrhenius}) \end{aligned} \right\} \rightarrow \ln\left(\frac{M}{M_0}\right) = \frac{Q}{R} \left(\frac{1}{T_0} - \frac{1}{T}\right) \rightarrow \Delta T = \frac{1}{\frac{1}{T_0} - \frac{R}{Q} \ln\left(\frac{M}{M_0}\right)} - T_0 \quad (4)$$

with  $M_0$  the mobility calculated from the Turnbull estimation (equation 1.29),  $D_{GB}$  the self-diffusivity along a grain boundary and  $Q$  its activation energy,  $T_0$  the initial temperature and  $T$  the effective temperature including the adiabatic heat effect. The parameters  $D_{GB}$  and  $Q$  are estimated at low strain rate, as illustrated in Figure 23a. A fit for  $\dot{\epsilon} = 0.001 \text{ s}^{-1}$  gives:  $\beta = 1$ ,  $D_{GB} = 0.5 \text{ m}^2 \cdot \text{s}^{-1}$  and  $Q = 170 \text{ kJ} \cdot \text{mol}^{-1}$ .

From the Turnbull estimation, the maximal adiabatic heat  $\Delta T$  is calculated and is represented in Figure 22b. The maximal value found is about  $180^\circ \text{C}$  for a compression at  $1000^\circ \text{C}$   $10 \text{ s}^{-1}$ . This value is credible, however it should be reminded that the post-dynamic phenomenon were not taken



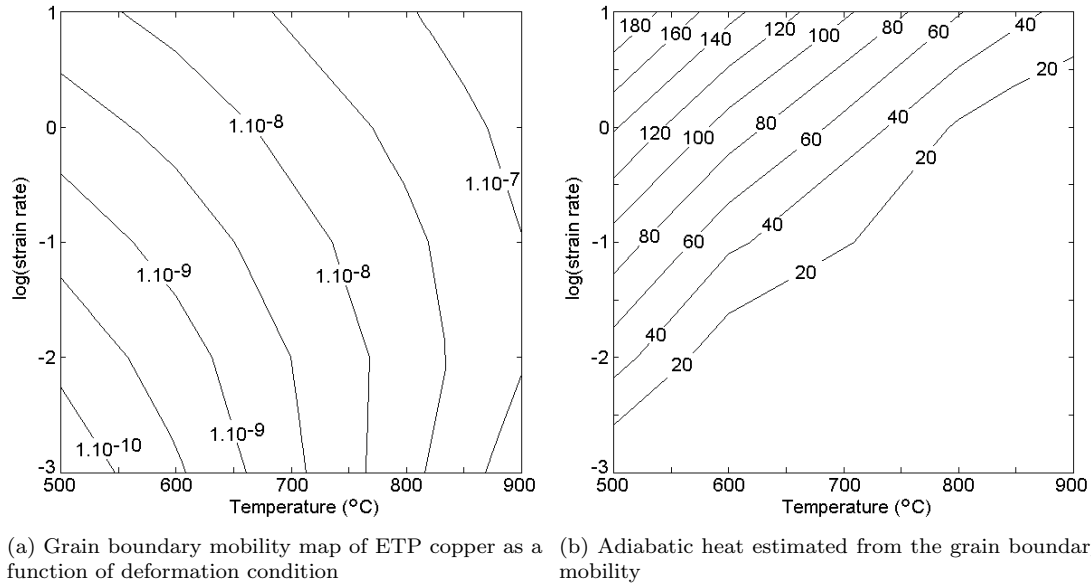


Figure 22: Determination of mobility and estimation of adiabatic heat from experimental data

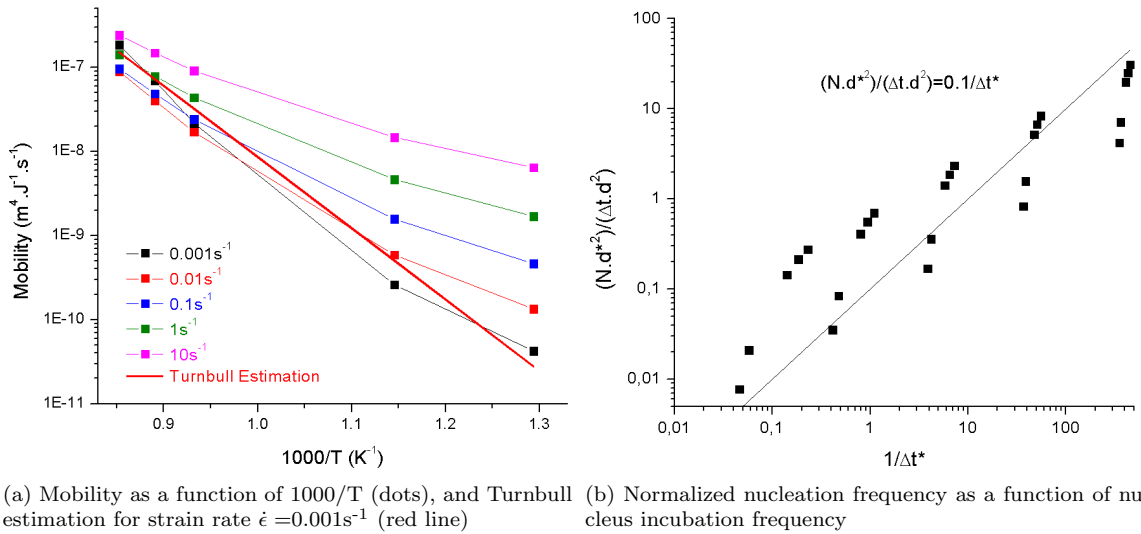


Figure 23: Determination of mobility and nucleation frequency from experimental data and modeling

into account, so this value is probably overestimated. The heat  $\Delta T$  is the upper bound of the effective temperature increase: it is not likely to have a adiabatic heat above this value, otherwise the calculated mobility would be further affected at high strain rate.

Meta-dynamic recrystallization can operate just after the deformation process, and leads to an increase of grain size. This effect is reflected in the mobility through the optimization process: the model tries to fit the experimental grain size by raising the mobility, leading to a mobility overestimate. Therefore the heat  $\Delta T$  could also attest of the occurrence of meta-dynamic recrystallization.



However, in this case there would be no reason to have a maximum of  $\Delta T$  at 500°C. Meta-dynamic recrystallization would rather occur at higher temperature ( $T \approx 900^\circ\text{C}$ ) where the mobility is larger. As a consequence, the main contribution to the mobility increase with strain rate is probably mainly adiabatic heating, as it is maximal at low temperature where the power received by the workpiece is the maximal.

Figure 23b illustrates the evolution of normalized nucleation frequency with the nucleus incubation frequency. The linear relationship can be highlighted, however the accumulative errors due to the experimental data fits (Kocks-Mecking model and Derby law) affect significantly the quality of this fit. A better estimation of the nucleation frequency could be obtained from a larger experimental data set, especially concerning the mean grain sizes.

## Conclusion

The experimental data from [76] were treated using the modelling method described in the section 5.1.2. Mobility was extracted, and is found to increase with temperature, in agreement with the literature. A dependence with strain rate was also highlighted, and was attributed mainly to the adiabatic heating. Probably the post-dynamic microstructural evolution may also contribute significantly to this dependence. The nucleation frequency was estimated and fitted with the incubation frequency. The results could be used for modelling the recrystallization of pure copper.

## Treatment of pure cobalt hot deformation experimental data

### Raw data from literature

Pure cobalt is a relevant example to compare with L-605 alloy in order to understand the effect of alloying elements on the recrystallized grain size. Experimental data were published by Kapoor et al. in [66, 109]. Some compression curves showing stress oscillations are illustrated in Figure 24a. These oscillations correspond to the transient regime of the discontinuous dynamic recrystallization, and can be observed for low strain rate ( $\dot{\epsilon} < 0.1\text{s}^{-1}$ ) and high temperature. ( $T > 750^\circ\text{C}$ ). For higher strain rate and lower temperature, compression curves with a single peak stress are observed. The microstructure undergoes a martensitic transformation during the cooling step. Microstructure is observed after etching: the martensite-fcc interface is coherent and is not revealed by etching [66]. Therefore the grain size measured corresponds to the high-temperature FCC grains formed before quenching. The average grain size is found to decrease with the Zener-Hollomon parameter, calculated with an apparent activation energy  $Q = 254\text{kJ.mol}^{-1}$ , and is illustrated in Figure 24b.

### Treatment of compression curves by the Kocks-Mecking model

Compression curves were extracted from [109] and derived versus strain to obtain the hardening rate  $\theta$ . Hardening rate was plotted as a function of stress to determine the parameters of the Voce



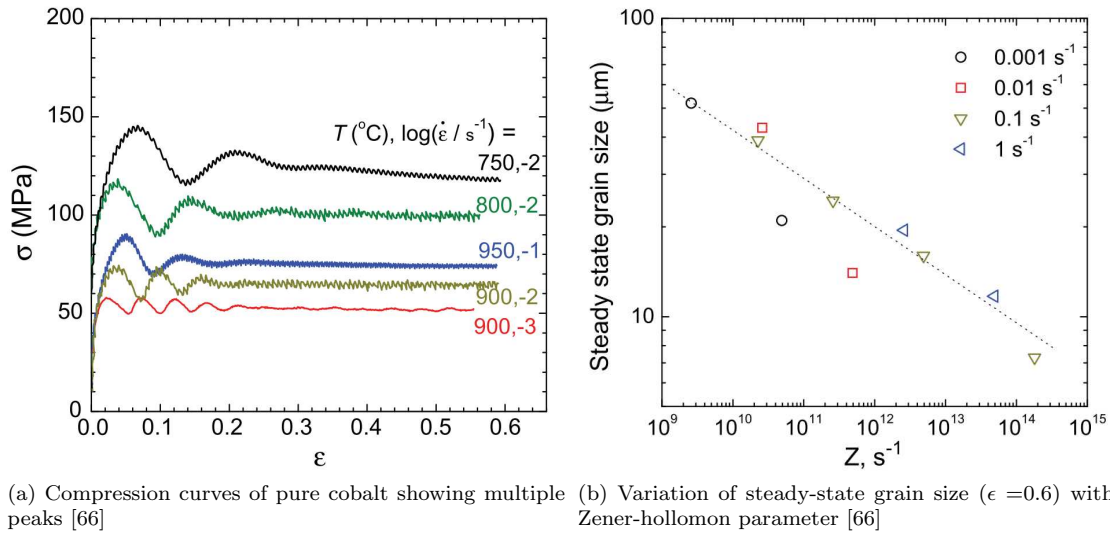


Figure 24: Compression curves and steady-state grain size of pure cobalt

law, and the linear fit of  $\theta = f(\sigma)$  is illustrated in Figure 25a. Extrapolated steady-state stress  $\sigma_V$  is identified as the intercept of linear fit with the x-axis. Effective steady-state stress  $\sigma_{ss}$  is taken as the stress at  $\epsilon = 0.6$ . However, for  $T \leq 750^\circ\text{C}$   $\dot{\epsilon} = 1\text{s}^{-1}$  and  $T = 600^\circ\text{C}$   $\dot{\epsilon} = 0.1\text{s}^{-1}$ , the compression curve do not reach the steady-state, therefore  $\sigma_{ss}$  is undetermined. The shear modulus used to calculate  $g$  parameter is  $\mu = 91.3 - 0.05253.T(^{\circ}\text{C})$  (GPa) [122]. A linear decay of  $\text{Log}(\sigma_V/\mu)$  and  $\text{Log}(\sigma_{ss}/\mu)$  with  $g$  is obtained for a fitting parameter  $\dot{\epsilon}_0$  set to  $10^3\text{s}^{-1}$ , and the fit is illustrated in Figure 25b. The normalized hardening rate  $\theta_0/\mu$  is quite constant with strain rate and temperature, with a mean value of 0.05. Yield stress depends mainly on temperature; while the dependence with strain rate leads to variations lower than 15%, and is neglected in a first approximation. The variation of yield stress with temperature is illustrated in Figure 26a. Steady-state grain size is obtained from [109] and is fitted by the Derby law in Figure 26b.

### Determination of grain boundary motion and nucleation

The experimental data analyzed previously are used to determine the grain boundary mobility based on the method described in the section 5.1.2. The mobility values calculated are gathered in Figure 27. The mobility increases with temperature, as illustrated also on Figure 28a. The mobility is fitted by the Turnbull estimation, with the parameters  $\beta = 1$ ,  $D_{GB} = 1.10^{-3}\text{m}^2.\text{s}^{-1}$  and  $Q = 150\text{kJ}.\text{mol}^{-1}$ .

Following the example of copper, some variations of mobility with strain rate are also observed. On Figure 28a, an increase of mobility with strain rate at low temperature is noted, and can be identified as the effect of adiabatic heating, by analogy with pure copper (Figure 23a). However, a second



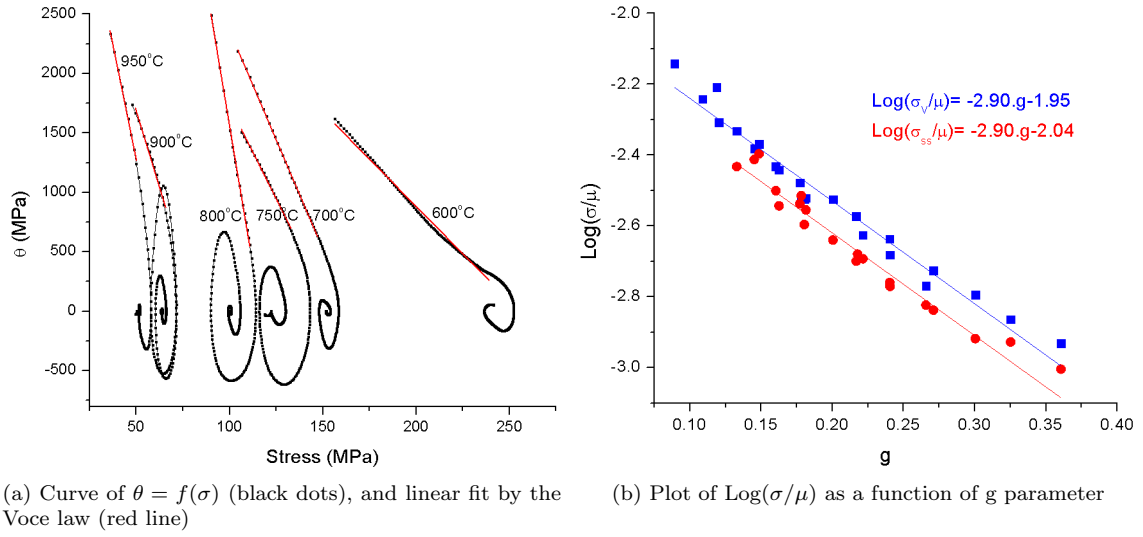


Figure 25: Determination of extrapolated steady-state stress  $\sigma_V$ , and fit by the  $g$  parameter with  $\dot{\epsilon}_0 = 10^{-3}\text{s}^{-1}$

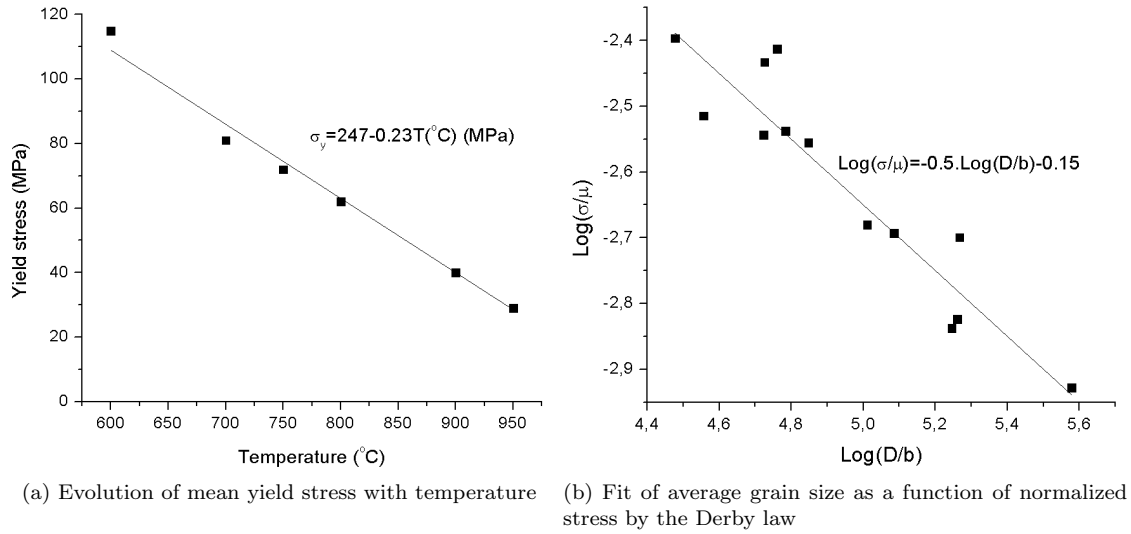


Figure 26: Yield stress as a function of temperature, and grain size dependence with normalized stress

type of mobility raise is observed for high temperature and low strain rate. For these conditions, grain growth is very active and rules the grain size. Therefore, the excessive increase of mobility may be due to the occurrence of abnormal grain growth: a few grains may gain the upper hand on other grains and grow until a size unexpected by the model employed here. The model tries to fit the experimental size, and introduce an overestimated mobility to achieve the fit. Therefore in the case of pure cobalt, adiabatic heating and post-dynamic microstructural evolution may explain the increase of mobility at high strain rate, while on the other hand abnormal grain growth leads to a



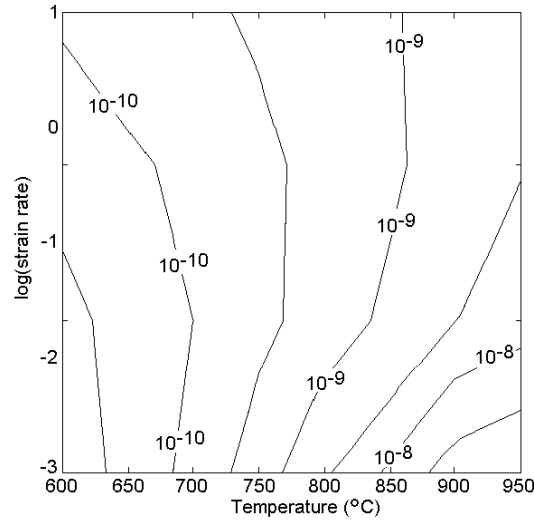
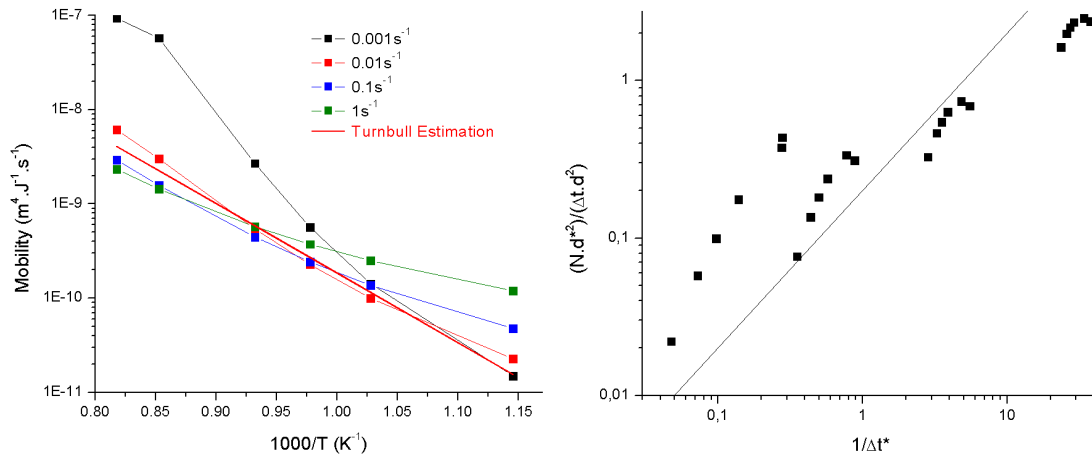


Figure 27: Grain boundary mobility map of pure cobalt as a function of deformation condition



(a) Evolution of mobility with temperature (dots), and (b) Normalized nucleation frequency as a function of nucleus incubation frequency

Figure 28: Determination of mobility and nucleation frequency from experimental data and modeling



similar overestimate but at low strain rate.

The normalized nucleation frequency is fitted with the nucleus incubation frequency, and is illustrated in Figure 28b. However this fit is very poor and the proportional coefficient is given only as a guide. The poor accuracy of the fit is probably due to some error on the grain size. The data available from [109] is very limited, and the fit by the Derby law is insufficient to give an accurate estimation of the normalized nucleation frequency.

## Conclusion

The experimental data from [109] were treated using the modelling method described in the section 5.1.2. Mobility was extracted, and is found to increase with temperature, in agreement with the literature. The dependence of mobility with strain rate was attributed to adiabatic heat and post-dynamic processes at high strain rate, and to abnormal grain growth at low strain rate. The nucleation frequency was estimated and fitted with the incubation frequency, but the fit lacks of accuracy due to the limited grain size data available. The results could be used for modelling the recrystallization of pure cobalt.

## Generation of microstructure from a grain size distribution

From the grain size distribution calculated by analytical class modeling in the section 5.3 (Figure 5.21), it is possible to generate a picture representative of the microstructural observation. To generate a microstructure, a method based on the layout of circles was used, and the different steps are illustrated on the Figure 29.

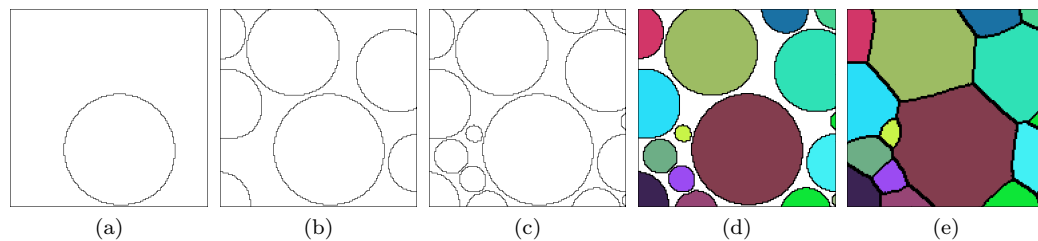


Figure 29: Microstructure generation process by growth of a compact layout of spheres

A box is formed with a square matrix of 300x300 numbers. The spacing between two cells on this matrix corresponds to a step size of  $0.3\mu\text{m}$ , therefore the box size is  $100\mu\text{m}$ . A set of circles is generated from the grain size distribution: each circle has the size of a class in the model, and is represented by an area fraction close to the area fraction of the class. The circles are then arranged into a compact layout in the box. To achieve this step, the circles are ranked from the larger to the smaller one. The program puts the circles in the box by starting with the larger ones (Figure 29 steps (a)-(c)). For each circle, the program tries all the positions possible, and choose the one leading to a minimal overlapping between grains. After a certain filling level, overlapping cannot be



avoided. Once the filling finished, a random colour is attributed to each circle to discriminate them, and also for aesthetic reasons. The program proceeds then to the growth of each circle to remove the blank spaces. If a pixel is white and has a neighbour with a colour attributed, then the white pixel takes the same color as his neighbour. Finally, the grains are highlighted by plotting grain boundaries with black lines: if a colour change occurs in the matrix, then at the interface the pixels become black. Finally the matrix is converted into a RVB image and saved. The resulting images are illustrated in Figure 5.6 of the section 5.3.



# References

- [1] KJ Klumb, TJ Fogarty, KP Kamdar, and B Hill. Endoluminal prosthesis placing method, 2002.
- [2] J Palmaz, EA Sprague, and CE Banas. Methods and apparatus for manufacturing an intravascular stent, 2001.
- [3] E Andersen and EP Strecker. Medical stent for body lumens exhibiting peristaltic motion, 1997.
- [4] C Gianturco. Percutaneous endovascular stent and method for insertion thereof, 1986.
- [5] HS Wallstn and C Imbert. Self-expanding prosthesis, 1991.
- [6] C Dumoulin and B Cochelin. Mechanical behaviour modelling of balloon-expandable stents. *Journal of Biomechanics*, 33:1461–1470, 2000.
- [7] JC Hornez, A Lefevre, D Joly, and HF Hildebrand. Multiple parameter cytotoxicity index on dental alloys and pure metals. *Biomolecular Engineering*, 19:103–117, 2002.
- [8] AS Al-Hiyasat and H Darmani. The effects of recasting on the cytotoxicity of base metal alloys. *The Journal of Prosthetic Dentistry*, 93:158–163, 2005.
- [9] M Niinomi. Recent metallic materials for biomedical applications. *Metallurgical and Materials Transactions A*, 33A:477–486, 2002.
- [10] Betzalel Avitzur. *Handbook of metal-forming processes*. J. Wiley, 1983.
- [11] RJ Saunders. Method and apparatus for direct laser cutting of metal stents, 1998.
- [12] T Trozera. Method of manufacturing a stent, 2004.
- [13] O Globerman. Medical stents, apparatus and method for making the same, 1998.
- [14] JR Davis. *ASM Speciality Handbook: Nickel, Cobalt, and their alloys*. ASM International, 2000.



- [15] GB Olson and M Cohen. A general mechanism of martensitic nucleation: Part I general concepts and the FCC-HCP transformation. *Metallurgical Transactions A*, 7A:1897–1904, 1976.
- [16] K Yamanaka, M Mori, and S Kurosu. Ultrafine grain refinement of biomedical Co-29Cr-6Mo alloy during conventional hot-compression deformation. *Metallurgical and Materials Transactions A*, 40A:1980–1994, 2009.
- [17] T Ericsson. The temperature and concentration dependence of the stacking fault energy in the Co-Ni system. *Acta Metallurgica*, 14:853–865, 1966.
- [18] K Yamanaka, M Mori, and A Chiba. Mechanical properties of as-forged Ni-free Co-29Cr-6Mo alloys with ultrafine-grained microstructure. *Materials Science and Engineering A*, 528:5961–5966, 2011.
- [19] JP Shingledecker, DB Glanton, RL Martin, BL Sparks, and RW Swindeman. Tensile and creep-rupture evaluation of a new heat of haynes alloy 25. Oak Ridge National Laboratory report - ORNL/TM-2006/609, February 2007.
- [20] YVRK Prasad, HL Gegel, SM Doraivelu, JC Malas, JT Morgan, KA Lark, and DR Barker. Modeling of dynamic material behavior in hot deformation: forging of Ti-6242. *Metallurgical Transactions A*, 15A:1883–1892, 1984.
- [21] YVRK Prasad. Processing maps: A status report. *Journal of Materials Engineering and Performance*, 12:638–645, 2003.
- [22] UF Kocks and H Mecking. Physics and phenomenology of strain hardening: the fcc case. *Progress in Materials Science*, 48:171–273, 2003.
- [23] H Mecking and UF Kocks. Kinetics of flow and strain-hardening. *Acta Metallurgica*, 29:1865–1875, 1981.
- [24] JJ Jonas, X Queleennec, L Jiang, and E Martin. The avrami kinetics of dynamic recrystallization. *Acta Materialia*, 57:2748–2756, 2009.
- [25] Y Estrin and H Mecking. A unified phenomenological description of work hardening and creep based on one-parameter models. *Acta Metallurgica*, 32:57–70, 1984.
- [26] A Belyakov, H Miura, and T Sakai. Dynamic recrystallization under warm deformation of a 304 type austenitic stainless steel. *Materials Science and Engineering A*, 255:139–147, 1998.
- [27] T Sakai. Dynamic recrystallization microstructures under hot working conditions. *Journal of Materials Processing Technology*, 53:349–361, 1995.



- [28] AM Wusatowska-Sarnek, H Miura, and T Sakai. Nucleation and microtexture development under dynamic recrystallization of copper. *Materials Science and Engineering A*, 323:177–186, 2002.
- [29] HS Zurob, Y Brechet, and J Dunlop. Quantitative criterion for recrystallization nucleation in single-phase alloys: Prediction of critical strains and incubation times. *Acta Materialia*, 54:3983–3990, 2006.
- [30] DG Cram, HS Zurob, Y Brechet, and CR Hutchinson. Modelling discontinuous dynamic recrystallization using a physically based model for nucleation. *Acta Materialia*, 57:5218–5228, 2009.
- [31] FJ Humphreys and M Hatherly. *Recrystallization and related annealing phenomena*. Pergamon, 1995.
- [32] B Derby. The dependence of grain size on stress during dynamic recrystallization. *Acta Metallurgica and Materialia*, 39:955–962, 1991.
- [33] X Kleber, L Simonet, F Fouquet, and M Delnondedieu. Thermoelectric power of a two-dimensional metal/metal composite: a numerical approach. *Institute of Physics Publishing - Modelling and Simulation in Materials Science and Engineering*, 13:341–354, 2005.
- [34] R Balcon, R Beyar, S Chierchia, I De Scheerder, PG Hugenholtz, F Kiemeneij, B Meier, J Meyer, JP Monassier, and W Wijns. Recommendations on stent manufacture, implantation and utilization. *European Heart Journal*, 18:1536–1547, 1997.
- [35] VB Kolachalama, AR Tzafriri, DY Arifin, and ER Edelman. Luminal flow patterns dictate arterial drug deposition in stent-based delivery. *Journal of Controlled Release*, 133:24–30, 2009.
- [36] RV Marrey, R Burgermeister, RB Grishaber, and Ritchie RO. Fatigue and life prediction for cobalt-chromium stents : A fracture mechanics analysis. *Biomaterials*, 27:1988–2000, 2006.
- [37] CL Zollikofer, F Antonucci, G Stuckmann, P Mattias, and Salomonowitz EK. Historical overview on the development and characteristics of stents and future outlooks. *Cardiovascular and Interventional Radiology*, 15:272–278, 1992.
- [38] J Palmaz. Balloon-expandable intravascular stent. *American Journal of Roentgenology*, 150:1263–1269, 1988.
- [39] K Tesdal, T Roeren, C Weiss, W Jaschke, and C Dueber. Metallic stents for treatment of benign biliary obstruction: A long-term study comparing different stents. *Journal of Vascular and Interventional Radiology*, 16:1479–1487, 2005.



- [40] KH Barth, R Virmani, J Froelich, T Takeda, SV Lossef, J Newsome, R Jones, and D Lindisch. Paired comparison of vascular wall reactions to palmaz stents, strecker tantalum stents, and wallstents in canine iliac and femoral arteries. *Circulation*, 93:2161–2169, 1996.
- [41] MA Byadretdinova, RG Ivanova, NA Iofis, and BV Molotilov. Artificial heart valve made of Co-Cr-W-Ni alloy. *Biomedical Engineering*, 20:21–24, 1986.
- [42] J Teague, E Cerreta, and Stout M. Tensile properties and microstructure of Haynes 25 alloy after aging at elevated temperatures for extended times. *Metallurgical and Materials Transactions A*, 35A:2767–2781, 2004.
- [43] C Larsson, TM Holden, MAM Bourke, M Stout, J Teague, and LE Lindgren. Measurement and modeling of residual stress in a welded Haynes 25 cylinder. *Materials Science and Engineering A*, 399:49–57, 2005.
- [44] M Hamdi and A Mohammed. High strength, ductile cobalt-base dental alloy, 1972.
- [45] J Pourcher, K Vang, and P Poncin. Standard for surgical implants. *Minitubes specifications*, PRD018:1–10, 2005.
- [46] F Etave, G Finet, M Boivin, JC Boyer, G Rioufol, and G Thollet. Mechanical properties of coronary stents determined by using finite element analysis. *Journal of Biomechanics*, 34:1065–1075, 2001.
- [47] G Schmalz and Arenholt-Bindslev D. *Biocompatibility of Dental Materials*. Springer-Verlag Berlin, 2009.
- [48] MF Ashby, Y Brechet, D Cebon, and L Salvo. Selection strategies for materials and processes. *Materials and Design*, 25:51–67, 2004.
- [49] KT Park, YS Kim, JG Lee, and DH Shin. Thermal stability and mechanical properties of ultrafine grained low carbon steel. *Materials Science and Engineering A*, 293:165–172, 2000.
- [50] HS Kim. Ductility of ultrafine grained copper. *Applied Physics Letters*, 79:4115–4117, 2001.
- [51] Y Wang, M Chen, F Zhou, and E Ma. High tensile ductility in a nanostructured metal. *Nature*, 419:912–915, 2002.
- [52] CT Sims. A contemporary view of cobalt-base alloys. *Journal of Metals*, 21:27–42, 1969.
- [53] W Betteridge. *Cobalt and its alloys*. Chichester, 1982.
- [54] KP Gupta. The Co-Cr-Mo (cobalt-chromium-molybdenum) system. *Journal of Phase Equilibria and Diffusion*, 26:87–92, 2005.



- [55] KP Gupta. The Co-Ni-W (cobalt-nickel-tungsten) system. *Journal of Phase Equilibria*, 21:396–401, 2000.
- [56] KP Gupta. The Co-Cr-W (cobalt-chromium-tungsten) system. *Journal of Phase Equilibria and Diffusion*, 27:178–183, 2006.
- [57] GP Zhmurko, EG Kabanova, VN Kuznetsov, and AV Leonov. Phase equilibria in the co-cr-ni system. *Moscow University chemistry bulletin*, 63:234–235, 2008.
- [58] S Asgari. Anomalous plastic behavior of fine-grained MP35N alloy during room temperature tensile testing. *Journal of Materials Processing Technology*, 155-156:1905–1911, 2004.
- [59] A Chiba, SH Lee, H Matsumoto, and M Nakamura. Construction of processing map for biomedical Co-28Cr-6Mo-0.16N alloy by studying its hot deformation behavior using compression tests. *Materials Science and Engineering A*, 513-514:286–293, 2009.
- [60] S Karimi, T Nickchi, and A Alfantazi. Effects of bovine serum albumin on the corrosion behaviour of AISI 316L, Co-28Cr-6Mo, and Ti-6Al-4V alloys in phosphate buffered saline solutions. *Corrosion Science*, 53:3262–3272, 2011.
- [61] PJ Ferreira and P Mullner. A thermodynamic model for the stacking-fault energy. *Acta Materialia*, 46:4479–4484, 1998.
- [62] S Allain, JP Chateau, O Bouaziz, S Migot, and N Guelton. Correlations between the calculated stacking fault energy and the plasticity mechanisms in Fe-Mn-C alloys. *Materials Science and Engineering A*, 387-389:158–162, 2004.
- [63] TS Byun. On the stress dependence of partial dislocation separation and deformation microstructure in austenitic stainless steels. *Acta Materialia*, 51:3063–3071, 2003.
- [64] CT Sims, NS Stoloff, and WC Hagel. *Superalloys II*. Wiley-Interscience, 1987.
- [65] BS Lee, H Matsumoto, and A Chiba. Fractures in tensile deformation of biomedical co-cr-mo-n alloys. *Materials Letters*, 65:843–846, 2011.
- [66] B Paul, R Kapoor, JK Chakravartty, Bidaye AC, IG Sharma, and AK Suri. Hot working characteristics of cobalt in the temperature range 600-950C. *Scripta Materialia*, 60:104–107, 2009.
- [67] Y Sato, N Nomura, S Fujinuma, and A Chiba. Microstructure and mechanical properties of hot-pressed co-cr-mo alloy compacts. *Advanced Materials Research*, 26-28:769–772, 2007.
- [68] AA Karimpoor, U Erb, Aust KT, and G Palumbo. High strength nanocrystalline cobalt with high tensile ductility. *Scripta Materialia*, 49:651–656, 2003.



- [69] GP Zheng. Grain-size effect on plastic flow in nanocrystalline cobalt by atomistic simulation. *Acta Materialia*, 55:149–159, 2007.
- [70] RK Gupta, MK Karthikeyan, DN Bhalia, BR Ghosh, and PP Sinha. Effect of microstructure on mechanical properties of refractory Co-Cr-W-Ni alloy. *Metal Science and Heat Treatment*, 50:175–179, 2008.
- [71] N Yukawa and K Sato. The correlation between microstructure and stress rupture properties of a Co-Cr-Ni-W (H-25) alloy, proc. int. conference on strength of metals and alloys. *Transactions of the Japan Institute of Metals*, 9:680–686, 1968.
- [72] ST Wlodek. Embrittlement of a Co-Cr-W (L-605) alloy. *Transactions of the ASM*, 56:287–303, 1963.
- [73] JC Malas. *Methodology for design and control of thermodynamical processes*. PhD thesis, Ohio University, 1991.
- [74] YVRK Prasad and S Sasidhara. *Hot Working Guide - A Compendium of Processing Maps*. ASM International, 1997.
- [75] H Ziegler, IN Sneddon, and R Hill. Progress in solid mechanics. *Wiley, New-York*, 4:91–193, 1965.
- [76] YVRK Prasad and KP Rao. Processing maps and rate controlling mechanisms of hot deformation of electrolytic tough pitch copper in the temperature range 300-950C. *Materials Science and Engineering A*, 391:141–150, 2005.
- [77] YVRK Prasad and KP Rao. Materials modeling and finite element simulation of isothermal forging of electrolytic copper. *Materials and Design*, 32:1851–1858, 2011.
- [78] F Montheillet, JJ Jonas, and KW Neale. Modeling of dynamic material behavior: A critical evaluation of the dissipator power co-content approach. *Metallurgical and Materials Transactions A*, 27A:232–235, 1996.
- [79] GI Taylor. The mechanism of plastic deformation of crystals. part I. theoretical. *Proceedings of the Royal Society of London A*, 45:362–387, 1934.
- [80] X Lemoine. Behavior laws and their influences on numerical prediction. *Proceedings of the 10th ESAFORM conference*, 907:269, 2007.
- [81] DU Furrer and SL Semiatin. *Metals Process Simulation*. ASM International, 2010.
- [82] Y Estrin, LS Toth, A Molinari, and Y Brechet. A dislocation-based model for all hardening stages in large strain deformation. *Acta Materialia*, 46:5509–5522, 1998.



- [83] AH Cottrell and RJ Stokes. Effects of temperature on the plastic properties of aluminium crystals. *Proceedings of the Royal Society of London A*, 233A:17–34, 1955.
- [84] ZS Basinski. Forest hardening in face centred cubic metals. *Scripta Metallurgica*, 8:1301–1308, 1974.
- [85] UF Kocks. *Constitutive Behavior Based on Crystal Plasticity*. Kluwer Academic Publishers, 1987.
- [86] O Bouaziz and P Buessler. Iso-work increment assumption for heterogeneous material behavior modeling. *Advanced Engineering Materials*, 6:79–83, 2004.
- [87] F Montheillet and G Damamme. Simple flow rules for modeling the behavior of inhomogeneous viscoplastic materials. *Advanced Engineering Materials*, 7:852–858, 2005.
- [88] A Molinari, GR Canova, and S Ahzi. A self-consistent approach of the large deformation polycrystal viscoplasticity. *Acta Metallurgica*, 35:2983–2994, 1987.
- [89] P Van Houtte, S Li, M Seefeldt, and L Delannay. Deformation texture prediction: from the taylor model to the advanced lamel model. *International Journal of Plasticity*, 21:589–624, 2005.
- [90] L Delannay, JJ Pascal, and SR Kalidindi. Finite element modeling of crystal plasticity with grains shaped as truncated octahedrons. *International Journal of Plasticity*, 22:1879–1898, 2006.
- [91] M Hillert. On the theory of normal and abnormal grain growth. *Acta Metallurgica*, 13:227–238, 1965.
- [92] J Burke and D Turnbull. Recrystallization and grain growth. *Progress in Metal Physics*, 3:220–244, 1952.
- [93] J Jeppsson, J Agren, and M Hillert. Modified mean field models of normal grain growth. *Acta Materialia*, 56:5188–5201, 2008.
- [94] R Sandstrom and R Lagneborg. A controlling factor for dynamic recrystallization. *Scripta Metallurgica*, 9:59–66, 1975.
- [95] T Sakai, M Ohashi, K Chiba, and JJ Jonas. Recovery and recrystallization of polycrystalline nickel after hot working. *Acta Metallurgica*, 36:1781–1790, 1988.
- [96] R Sandstrom and R Lagneborg. A model for hot working occuring by recrystallization. *Acta Metallurgica*, 23:387–398, 1975.



- [97] W Roberts and B Ahlblom. A nucleation criterion for dynamic recrystallization during hot working. *Acta Metallurgica*, 26:801–813, 1978.
- [98] R Ding and ZX Guo. Coupled quantitative simulation of microstructural evolution and plastic flow during dynamic recrystallization. *Acta Materialia*, 49:3163–3175, 2001.
- [99] F Montheillet, O Lurdos, and G Damamme. A grain scale approach for modeling steady-state discontinuous dynamic recrystallization. *Acta Materialia*, 57:1602–1612, 2009.
- [100] P Bernard, S Bag, K Huang, and RE Loge. A two-site mean field model of discontinuous dynamic recrystallization. *Materials Science and Engineering A*, 528:7357–7367, 2011.
- [101] D Turnbull. Theory of grain boundary migration rates. *Transactions of the AIME*, 191:661–665, 1951.
- [102] CR Hutchinson, HS Zurob, SW Sinclair, and Y Brechet. The comparative effectiveness of Nb solute and NbC precipitates at impeding grain-boundary motion in nb steels. *Scripta Materialia*, 59:635–637, 2008.
- [103] CW Sinclair, CR Hutchinson, and Y Brechet. The effect of Nb on the recrystallization and grain growth of ultra-high-purity  $\alpha$ -Fe: a combinatorial approach. *Metallurgical and Materials Transactions A*, 38A:821–830, 2007.
- [104] JW Cahn. The impurity-drag effect in grain boundary motion. *Acta Metallurgica*, 10:789–798, 1962.
- [105] CS Smith and C Zener. Grains, phases, and interfacesan interpretation of microstructure. *Transactions of the AIME*, 175:15–51, 1948.
- [106] M Hillert. Inhibition of grain growth by second-phase particles. *Acta Metallurgica*, 36:3177–3181, 1988.
- [107] T Sakai and JJ Jonas. Dynamic recrystallization: mechanical and microstructural considerations. *Acta Metallurgica*, 32:189–209, 1984.
- [108] S Gourdet and F Montheillet. A model of continuous dynamic recrystallization. *Acta Materialia*, 51:2685–2699, 2003.
- [109] R Kapoor, B Paul, S Raveendra, I Samajdar, and JK Chakravartty. Aspects of dynamic recrystallization in cobalt at high temperatures. *Metallurgical and Materials Transactions A*, 40A:818–827, 2009.
- [110] JE Bailey and PB Hirsch. The recrystallization process in some polycrystalline metals. *Proceedings of the Royal Society of London A*, 267:11–30, 1962.



- [111] H Miura, T Sakai, H Hamaji, and JJ Jonas. Preferential nucleation of dynamic recrystallization at triple junctions. *Scripta Materialia*, 50:65–69, 2004.
- [112] H Miura, T Sakai, R Mogawa, and G Gottstein. Nucleation of dynamic recrystallization at grain boundaries in copper bicrystals. *Scripta Materialia*, 51:671–675, 2004.
- [113] EI Poliak and JJ Jonas. A one-parameter approach to determining the critical conditions for the initiation of dynamic recrystallization. *Acta Materialia*, 44:127–136, 1996.
- [114] P Poelt, C Sommitsch, S Mitsche, and M Walter. Dynamic recrystallization of Ni-base alloys- experimental results and comparisons with simulations. *Materials Science and Engineering A*, 420:306–314, 2006.
- [115] T Sakai, H Miura, A Goloborodko, and O Sitdikov. Continuous dynamic recrystallization during the transient severe deformation of aluminum alloy 7475. *Acta Materialia*, 57:153–162, 2009.
- [116] F Montheillet, L Pallot, and D Piot. Hot deformation and dynamic recrystallization of the beta phase in titanium alloys. *Materials Science Forum*, 706-709:127–134, 2012.
- [117] I Kartika, H Matsumoto, and A Chiba. Deformation and microstructure evolution in Co-Ni-Cr-Mo superalloy during hot working. *Metallurgical and Materials Transactions A*, 40A:1457–1468, 2009.
- [118] FJ Blatt, PA Schroeder, CL Foiles, and Greig D. *Thermoelectric Power of Metals*. Springer, 1976.
- [119] N Lavaire, J Merlin, and V Sardoy. Study of ageing in strained ultra and extra low carbon steels by thermoelectric power measurement. *Scripta Materialia*, 44:553–559, 2001.
- [120] YP Li, E Onodera, and A Chiba. Friction coefficient in hot compression of cylindrical sample. *Materials Transactions*, 51:1210–1215, 2010.
- [121] KI Hirano, RP Agarwala, BL Averbach, and M Cohen. Diffusion in cobalt-nickel alloys. *Journal of Applied Physics*, 33:3049–3054, 1962.
- [122] PM Sargent, G Malakondaiah, and MF Ashby. A deformation map for cobalt. *Scripta Metallurgica*, 17:625–629, 1983.
- [123] DJ Embury, JD ANDLloyd. On the Bailey-Orowan equation for steady-state creep. *Scripta Metallurgica*, 3:821–826, 1969.



- [124] GR Rao, OP Gupta, and B Pradhan. Application of stress relaxation testing in evaluation of creep strength of a tungsten-alloyed 10% Cr cast steel. *International Journal of Pressure Vessels and Piping*, 88:65–74, 2011.
- [125] JH Holbrook, RW Rohde, and JC Swearingen. The continuity of plastic strain rate. *Acta Metallurgica*, 29:1099–1106, 1981.
- [126] O Ajaja. Determination of recovery rates during creep deformation. *Scripta Metallurgica et Materialia*, 24:1465–1470, 1990.
- [127] LF Bryant, R Speiser, and JP Hirth. Some interfacial properties of fcc cobalt. *Transactions of the metallurgical society of AIME*, 242:1145–1148, 1968.
- [128] BC Allen. The interfacial free energies of solid chromium, molybdenum and tungsten. *Journal of less-common metals*, 29:263–282, 1972.
- [129] EN Hodkin, MG Nicholas, and DM Poole. The surface energies of solid molybdenum, niobium, tantalum and tungsten. *Journal of the Less Common Metals*, 20:93–103, 1970.
- [130] GS Rohrer, EA Holm, AD Rollett, SM Foiles, J Li, and DL Olmsted. Comparing calculated and measured grain boundary energies in nickel. *Acta Materialia*, 58:5063–5069, 2010.
- [131] PA Mulheran. Mean field simulations of normal grain growth. *Acta Metallurgica and Materialia*, 8:1827–1833, 1992.
- [132] I Andersen and O Grong. Analytical modelling of grain growth in metals and alloys in the presence of growing and dissolving precipitates. *Acta Metallurgica and Materialia*, 43:2689–2700, 1995.
- [133] PR Rios. Abnormal grain growth development from uniform grain size distributions. *Acta Materialia*, 45:1785–1789, 1997.
- [134] R.L. Fullman and J.C. Fisher. Formation of annealing twins during grain growth. *Journal of Applied Physics*, 22:1350–1355, 1951.
- [135] P.J. Goodhew. Annealing twin formation by boundary dissociation. *Metal Science*, 13:108–112, 1979.
- [136] WT Read and W Shockley. Dislocation models of crystal grain boundaries. *Physical Review*, 78:275–289, 1950.
- [137] Anis Hor. *Simulation physique des conditions thermomecaniques de forgeage et d’usinage - caracterisation et modelisation de la rheologie et de l’endommagement*. PhD thesis, Arts et Metiers ParisTech, 2011.



- [138] YVRK Prasad and KP Rao. Influence of oxygen on rate-controlling mechanisms in hot deformation of polycrystalline copper: oxygen-free versus electrolytic grades. *Materials Letters*, 58:2061–2066, 2004.
- [139] YVRK Prasad and KP Rao. Mechanisms of high temperature deformation in electrolytic copper in extended ranges of temperature and strain rate. *Materials Science and Engineering A*, 374:335–341, 2004.
- [140] YVRK Prasad and KP Rao. Kinetics of high-temperature deformation of polycrystalline OFHC copper and the role of dislocation core diffusion. *Philosophical Magazine*, 84:3039–3050, 2004.
- [141] YVRK Prasad and KP Rao. Kinetics and dynamics of hot deformation of OFHC copper in extended temperature and strain rate ranges. *Zeitschrift fur Metallkunde*, 96:71–77, 2005.
- [142] YVRK Prasad and KP Rao. Effect of oxygen content on the processing maps for hot deformation of ofhc copper. *Transactions of the ASME*, 128:158–162, 2006.



## FOLIO ADMINISTRATIF

### THESE SOUTENUE DEVANT L'INSTITUT NATIONAL DES SCIENCES APPLIQUEES DE LYON

NOM : Favre  
(avec précision du nom de jeune fille, le cas échéant)

DATE de SOUTENANCE : 25/09/2012

Prénoms : Julien, Jean, Gabriel

TITRE :

Recrystallization of L-605 cobalt superalloy during hot-working process  
(Recristallisation du superalliage base cobalt L-605 pendant la déformation à chaud)

NATURE : Doctorat

Numéro d'ordre : 2012ISAL0112

Ecole doctorale : Matériaux de Lyon

Spécialité : Science et Génie des Matériaux

RESUME:

L'alliage L-605 est un superalliage base cobalt combinant une haute résistance et une bonne ductilité, de plus il est biocompatible et présente une bonne résistance à la corrosion. Du à son inertie chimique dans le corps humain, ce matériau a été utilisé avec succès pour fabriquer des valves cardiaques et des stents. Le contrôle de la microstructure peut influencer grandement les propriétés mécaniques : notamment un raffinement des grains est susceptible d'augmenter d'avantage la résistance et serait intéressant pour permettre de fabriquer des stents selon une architecture plus fine. L'ajustement de la distribution de taille de grains à travers le phénomène de recristallisation lors de la déformation à chaud apparaît comme une solution pratique pour ajuster les propriétés mécaniques du matériau. Pour contrôler la microstructure et choisir les conditions de procédé optimales, les mécanismes mis en jeu lors de la recristallisation dynamique et l'effet des conditions de déformation sur la taille de grain doivent être compris et prévisibles par des outils théoriques.

Les propriétés mécaniques du matériau à haute température sont déterminées par des essais de compression à chaud. L'évolution microstructurale du matériau lors de la compression est analysée par microscopie optique et électronique (EBSD, TEM). Le phénomène de recristallisation dynamique discontinue est mis en évidence, et procède par nucléation de nouveaux grains aux joints de grain. La corrélation entre le comportement mécanique à chaud et l'évolution microstructurale est déterminée expérimentalement. Les conditions optimales de déformation impliquant la recristallisation dynamique sont déterminées, et la microstructure résultante est étudiée en détail. De nouveaux outils théoriques permettant de prévoir les conditions de recristallisation et d'extraire les paramètres physiques du matériau à partir des données expérimentales sont proposés. Enfin, la recristallisation dynamique est modélisée analytiquement, et permet de prédire le comportement mécanique et l'évolution de la taille de grain lors de la déformation.

MOTS-CLES : cobalt, superalliage, recristallisation, déformation à chaud, microscopie EBSD, modélisation analytique

Laboratoire (s) de recherche :

Laboratoire MATEIS, INSA de Lyon  
Laboratoire Chiba, Institute for Materials Research, Tohoku University

Directeur de thèse: Eric Maire, Akihiko Chiba

Président de jury : Tadashi Furuhashi

Composition du jury : Akihiko Chiba, Toyohiko Konno, Chris Hutchinson, Eric Maire, Damien Fabrègue